THE UNIVERSITY OF QUEENSLAND

AUSTRALIA

Wideband Microwave Imaging System for Brain Injury Diagnosis

Ahmed Toaha Mobashsher

B. Sc., M. Sc.

A thesis submitted for the degree of Doctor of Philosophy at

The University of Queensland in 2016

The School of Information Technology and Electrical Engineering

Abstract

Brain injury is a major cause of disability and mortality worldwide. This medical emergency occurs when the brain is damaged as a result of various traumatic and non-traumatic incidences including accidents, strokes, drug abuses, tumours, infections and various diseases. As the devastating disorder of brain injury deteriorates rapidly, fast diagnosis and management is critically important for the treatment and recovery of the affected patient. Therefore, on-the-spot accurate detection by means of head imaging is the governing factor of the timely medication to ensure complete recovery of the injured patient. Although some existing imaging technologies, like CT and MRI, are capable for brain injury diagnosis, they are time-consuming, expensive, bulky and mostly stationary. Thus they cannot be carried by first response paramedic teams for the diagnosis purpose or be used for monitoring the patient to observe concurrent brain injury over periods of time without moving the patient. A compact and mobile technology that can be applied to monitor the patient continuously in real time, either at the bedside or in emergency room, would be a significant advantage comparing to the existing imaging techniques. This thesis aims to develop wideband microwave imaging systems for brain injury diagnosis and in doing so makes seven main contributions to the field of microwave imaging systems.

As the efficacy of the microwave imaging systems relies on the sensing antennas, emphasize is given in the developments of compact, wideband antennas with directional radiation patterns for low microwave frequencies, which is the first contribution of this thesis. Three-dimensional (3D) antennas are proposed relying on multiple folding and slot-loading techniques. Nevertheless, a novel generalized miniaturization technique is proposed for compact antennas. The antennas are found to be efficient in both near- and far-fields for both frequency- and time-domain characterizations.

The second contribution is the development of artificial human head phantom with realistic heterogeneous tissue distributions and actual wideband frequency-dispersive dielectric properties. The phantom is fabricated from artificial tissue emulating materials which are contained and structured by using 3D printed structures and castes. This realistic 3D human head phantom significantly improves the reliability of the experimental validation process of wideband microwave imaging compared to the reported validations with existing simple and stylized head phantoms.

The contribution third contribution is the performance comparison of directional and omni-directional antennas for wideband microwave head imaging systems. A novel near-field time-domain characterization technique is proposed that enables the comparative analysis of antennas for near-field applications. Application of this technique demonstrates that for microwave imaging systems directional antennas are more effective than omni-directional antennas. In terms of imaging performance, it is observed that directional antennas yields better images with higher accuracy

compared to the omni-directional antennas. This conclusive evidence significantly assists the decision making of practical wideband microwave imaging solutions.

The fourth contribution is the development of microwave imaging system for brain injury diagnosis, which is made portable by using a compact unidirectional antenna and a wideband transceiver. The system is prototyped and the imaging performance is validated by using a realistic 3D human head phantom. The developed confocal imaging algorithm is seen to successfully locate the position of brain injuries.

The fifth contribution is the improved back-projection algorithm relying on a novel approach of effective head permittivity model which overcomes the limitations of constant permittivity based existing imaging algorithms. The efficacy of the algorithm is verified in realistic brain injury scenarios in both simulation and measurement environments.

The sixth contribution is the design and experimental evaluation of an automated head imaging system which utilizes a single miniaturized wideband antenna with directional radiations. Based on the determinations of the numerical results, the imaging performances of the system are improved by considering the surface waves for both forward and scattered wave propagations. The experimental results positively validates the applicability of the imaging system for brain injury diagnosis.

The last but not least contribution of the array-based portable wideband microwave imaging system with multi-level scanning capabilities. The system, developed from 3D printing parts and custom made components, is flexible to be adjusted for different head shapes and sizes. The fast data acquisition technique and imaging algorithm relying on threshold normalization approach efficiently performs 3D localization of the position of brain injuries when applied on a realistic head phantom. The system meets the safety requirements of electromagnetic devices. The reliability of the imaging performance of pilot volunteer tests demonstrates the potential of this system be for preclinical trials for brain injury diagnosis.

The developed devices, techniques, systems and other advances reported in this thesis positively contribute to microwave imaging domain and are expected to encourage a low-cost, compact and portable wideband microwave head imaging system in near future that can proceed for mass production and significantly reduce human sufferings due to brain injuries.

Declaration by author

This thesis is composed of my original work, and contains no material previously published or written by another person except where due reference has been made in the text. I have clearly stated the contribution by others to jointly-authored works that I have included in my thesis.

I have clearly stated the contribution of others to my thesis as a whole, including statistical assistance, survey design, data analysis, significant technical procedures, professional editorial advice, and any other original research work used or reported in my thesis. The content of my thesis is the result of work I have carried out since the commencement of my research higher degree candidature and does not include a substantial part of work that has been submitted to qualify for the award of any other degree or diploma in any university or other tertiary institution. I have clearly stated which parts of my thesis, if any, have been submitted to qualify for another award.

I acknowledge that an electronic copy of my thesis must be lodged with the University Library and, subject to the policy and procedures of The University of Queensland, the thesis be made available for research and study in accordance with the Copyright Act 1968 unless a period of embargo has been approved by the Dean of the Graduate School.

I acknowledge that copyright of all material contained in my thesis resides with the copyright holder(s) of that material. Where appropriate I have obtained copyright permission from the copyright holder to reproduce material in this thesis.

Publications during candidature

Peer-reviewed Journal Papers

1. **Ahmed Toaha Mobashsher** and Amin Abbosh. 2016. *Compact three-dimensional slot-loaded folded dipole antenna with unidirectional radiation and low impulse distortion for head imaging applications*. IEEE Transactions on Antennas and Propagation. *(In Press)* doi: *10.1109/TAP.2016.2560909*

2. **Ahmed Toaha Mobashsher**, K. S. Bialkowski and Amin Abbosh. 2016. *Design of compact cross-fed three-dimensional slot-loaded antenna and its application in wideband head imaging system*. IEEE Antennas and Wireless Propagation Letters. *(In Press)* doi: *10.1109/LAWP.2016.2539970*

3. **Ahmed Toaha Mobashsher** and Amin Abbosh. 2016. *Performance of directional and omnidirectional antennas in wideband head imaging*. IEEE Antennas and Wireless Propagation Letters. (*In Press*) doi: *10.1109/LAWP.2016.2519527*

4. **Ahmed Toaha Mobashsher**, K.S. Bialkowski, A.M. Abbosh and S. Crozier. 2016. *Design and experimental evaluation of a non-invasive microwave head imaging system for intracranial haemorrhage detection*. PloS One, 11(4): e0152351. doi: *10.1371/journal.pone.0152351*

5. **Ahmed Toaha Mobashsher**, A. Mahmoud and Amin Abbosh. 2016. *Portable wideband microwave imaging system for intracranial hemorrhage detection using improved back-projection algorithm with model of effective head permittivity*. Nature - Scientific Reports, 6, 20459. doi: *10.1038/srep20459*

6. A. Zamani, A. Abbosh, and **A. T. Mobashsher**. 2016. *Fast frequency-based multistatic microwave imaging algorithm with application to brain injury detection*. IEEE Transactions on Microwave Theory and Techniques, 64(2):653-662. doi: *10.1109/TMTT.2015.2513398*

7. **Ahmed Toaha Mobashsher** and Amin Abbosh. 2015. *Near-field time-domain characterisation of wideband antennas*. Electronics Letters, 51(25): 2076 – 2078. doi: *10.1049/el.2015.2763*

8. **Ahmed Toaha Mobashsher** and Amin Abbosh. 2015. *Artificial human phantoms: human proxy in testing microwave apparatuses that have electromagnetic interaction with the human body*. IEEE Microwave Magazine, 16(6): 42 – 62. doi: *10.1109/MMM.2015.2419772*

9. **Ahmed Toaha Mobashsher** and Amin Abbosh. 2015. *Utilizing symmetry of planar ultra-wideband antennas for size reduction and enhanced performance*. IEEE Antennas and Propagation Magazine, 57(2): 153 – 166. doi: *10.1109/MAP.2015.2414488*

10. **Ahmed Toaha Mobashsher**, Amin Abbosh and Yifan Wang. 2014. *Microwave system to detect traumatic brain injuries using compact unidirectional antenna and wideband transceiver with verification on realistic head phantom*. IEEE Transactions on Microwave Theory and Techniques, 62(9): 1826 – 1836. doi: *10.1109/TMTT.2014.2342669*

11. **Ahmed Toaha Mobashsher** and Amin Abbosh. 2014. *Three dimensional human head phantom with realistic electrical properties and anatomy*. IEEE Antennas and Wireless Propagation Letters, 13: 1401 – 1404. doi: *10.1109/LAWP.2014.2340409*

12. **Ahmed Toaha Mobashsher** and Amin Abbosh. 2014. *Development of compact directional antenna utilising plane of symmetry for wideband brain stroke detection systems*. Electronics Letters, 50(12): 1 – 2. doi: *10.1049/el.2014.0616*

13. **Ahmed Toaha Mobashsher** and Amin Abbosh. 2014. *Slot-loaded folded dipole antenna with wideband and unidirectional performance for L-band applications*. IEEE Antennas and Wireless Propagation Letters. 13: 798 – 801. doi: *10.1109/LAWP.2014.2318035*

14. **Ahmed Toaha Mobashsher** and Amin Abbosh. 2014. *CPW-fed low-profile directional antenna operating in low microwave band for wideband medical diagnostic systems*. Electronics Letters, 50(4): 246 – 248. doi: *10.1049/el.2013.3909*

15. **Ahmed Toaha Mobashsher** and Amin Abbosh. 2014. *Three-dimensional folded antenna with ultra-wideband performance, directional radiation and compact size*. IET Microwaves, Antennas & Propagation, 8(3): 171 – 179. doi: *10.1049/iet-map.2013.0374*

Peer-reviewed Conference Papers

1. **Ahmed Toaha Mobashsher** and A. Abbosh. 2016. *Performance comparison of directional and omnidirectional ultra-wideband antennas in near-field microwave head imaging systems*. IEEE International Conference on Electromagnetics in Advanced Applications (ICEAA 2016), 19-23rd September 2016, Cairns, Australia. *(Accepted)*

2. **Ahmed Toaha Mobashsher** and A. Abbosh. 2015. *Developments of tomography and radar-based head imaging systems*. IEEE International Symposium on Antennas and Propagation (ISAP2015), 9-12th November 2015, Hobart, Tasmania, Australia.

3. **Ahmed Toaha Mobashsher** and A. Abbosh. 2015. *Development of compact three-dimensional unidirectional ultra-wideband antennas for portable microwave head imaging systems*. IEEE International Symposium on Antennas and Propagation and USNC-URSI Radio Science Meeting, 19-25 July 2015, Vancouver, British Columbia, Canada. doi: *10.1109/APS.2015.7304561*

4. A. M. Abbosh, A. Zamani and **A. T. Mobashsher**. 2015. *Real-time frequency-based multistatic microwave imaging for medical applications*. IEEE 2015 International Microwave Workshop Series on RF and Wireless Technologies for Biomedical and Healthcare Applications (IMWS-BIO, 2015), pp. 127-128, 21-23 September, Taipei. doi: *10.1109/IMWS-BIO.2015.7303811*

5. **Ahmed Toaha Mobashsher** and A. Abbosh. 2015. *Development of three-dimensional unidirectional ultra-wideband antennas for portable microwave head imaging systems*. Fourteenth Australian Symposium on Antennas (ASA 2015), Sydney, Australia, 18 - 19 Feb. 2015, Sydney, Australia.

6. A. Zamani, **A. T. Mobashsher**, B. J. Mohammed and A. Abbosh. 2014. *Microwave imaging using frequency domain method for brain stroke detection*, IEEE MTT-S International Microwave Workshop Series on RF and Wireless Technologies for Biomedical and Healthcare Applications 2014 (IMWS-Bio 2014), 8-10 December 2014, London. doi: *10.1109/IMWS-BIO.2014.7032452*

7. U.T. Ahmed, **A.T. Mobashsher**, K.S. Bialkowski, A.M. Abbosh. 2014. *Convex optimization approach for stroke detection in microwave head imaging*, IEEE Makassar International Conference on Electrical Engineering and Informatics (MICEEI) 2014, 26–30 November 2014, Makassar, South Sulawesi, Indonesia. doi: *10.1109/MICEEI.2014.7067308*

8. **Ahmed Toaha Mobashsher** and A. Abbosh. 2014. *Compact wideband directional antenna with three-dimensional structure for microwave-based head imaging systems*. IEEE International Symposium on Antennas and Propagation and USNC-URSI Radio Science Meeting, pp. 1141-1141, 6–11 July 2014, Memphis, Tennessee, USA. doi: *10.1109/APS.2014.6904897*

9. **Ahmed Toaha Mobashsher** and A. Abbosh. 2014. *Microwave imaging system to provide portable-low-powered medical facility for the detection of intracranial hemorrhage*. 1st Australian Microwave Symposium, 26-27 June 2014, Melbourne, Australia. doi: *10.1109/AUSMS.2014.7017347*

10. **Ahmed Toaha Mobashsher** and A. Abbosh. 2014. *Low profile ultra-wideband directional antenna operating in low microwave band for brain stroke diagnostic system*. The International Workshop on Antenna Technology (iWAT 2014), pp. 186-188, 4-6 March 2014, Sydney, Australia. doi: *10.1109/IWAT.2014.6958632*

11. **Ahmed Toaha Mobashsher**, P.T. Nguyen and A. Abbosh. 2013. *Detection and localization of brain strokes in realistic 3-D human head phantom*. IEEE International Microwave Workshop Series on RF and Wireless Technologies for Biomedical and Healthcare Applications (IMWS-Bio 2013), pp. 1-3, 9-11 December 2013, Singapore. doi: *10.1109/IMWS-BIO.2013.6756149*

12. **Ahmed Toaha Mobashsher**, B.J. Mohammed, S. Mustafa and A. Abbosh. 2013. *Ultra wideband antenna for portable brain stroke diagnostic system*. IEEE International Microwave Workshop Series on RF and Wireless Technologies for Biomedical and Healthcare Applications (IMWS-Bio 2013), pp. 1-3, 9-11 December 2013, Singapore. doi: *10.1109/IMWS-BIO.2013.6756163*

13. **Ahmed Toaha Mobashsher**, B.J. Mohammed, A. Abbosh and S. Mustafa. 2013. *Detection and differentiation of brain strokes by comparing the reflection phases with wideband unidirectional antennas*. International Conference on Electromagnetics in Advanced Applications (ICEAA) 2013, pp. 1283 - 1285, 9-13 September 2013, Torino, Italy. doi: *10.1109/ICEAA.2013.6632455*

14. **Ahmed Toaha Mobashsher** and A.M. Abbosh. 2013. *Wideband unidirectional antenna for head imaging system*. IEEE Antennas and Propagation Society International Symposium (APSURSI) 2013, pp. 674-675, 7-13 July 2013, Orlando, Florida. doi: *10.1109/APS.2013.6710997*

Publications included in this thesis

Peer-reviewed Journal Papers

1. **Ahmed Toaha Mobashsher**, K.S. Bialkowski, A.M. Abbosh and S. Crozier. 2016. *Design and experimental evaluation of a non-invasive microwave head imaging system for intracranial haemorrhage detection*. PloS One, 11(4): e0152351. doi: *10.1371/journal.pone.0152351* – Partly incorporated as paragraph in Chapter 5.

Contributor	Statement of contribution
Ahmed Toaha Mobashsher (Candidate)	Designed experiments (70%) Wrote the paper (55%)
K.S. Bialkowski	Designed experiments (15%) Wrote and edited paper (10%)
A.M. Abbosh	Designed experiments (10%) Wrote and edited paper (25%)
S. Crozier	Designed experiments (5%) Wrote and edited paper (10%)

2. **Ahmed Toaha Mobashsher** and Amin Abbosh. 2016. *Compact three-dimensional slot-loaded folded dipole antenna with unidirectional radiation and low impulse distortion for head imaging applications*. IEEE Transactions on Antennas and Propagation. *(In Press)* doi: *10.1109/TAP.2016.2560909* – Partly incorporated as paragraph in Chapter 6.

Contributor	Statement of contribution
Ahmed Toaha Mobashsher (Candidate)	Designed experiments (80%) Wrote the paper (70%)
A.M. Abbosh	Designed experiments (20%) Wrote and edited paper (30%)

3. **Ahmed Toaha Mobashsher**, K. S. Bialkowski and Amin Abbosh. 2016. *Design of compact cross-fed three-dimensional slot-loaded antenna and its application in wideband head imaging system*. IEEE Antennas and Wireless Propagation Letters. *(In Press)* doi: *10.1109/LAWP.2016.2539970* – Partly incorporated as paragraph in Chapter 3.

Contributor	Statement of contribution
Ahmed Toaha Mobashsher (Candidate)	Designed experiments (70%) Wrote the paper (65%)
K. S. Bialkowski	Designed experiments (20%) Wrote and edited paper (10%)
Amin Abbosh	Designed experiments (10%) Wrote and edited paper (25%)

4. **Ahmed Toaha Mobashsher** and Amin Abbosh. 2016. *Performance of directional and omnidirectional antennas in wideband head imaging*. IEEE Antennas and Wireless Propagation Letters. (*In Press*) doi: *10.1109/LAWP.2016.2519527* – Partly incorporated as paragraph in Chapter 5.

Contributor	Statement of contribution
Ahmed Toaha Mobashsher (Candidate)	Designed experiments (80%) Wrote the paper (70%)
Amin Abbosh	Designed experiments (20%) Wrote and edited paper (30%)

5. **Ahmed Toaha Mobashsher**, A. Mahmoud and Amin Abbosh. 2016. *Portable wideband microwave imaging system for intracranial hemorrhage detection using improved back-projection algorithm with model of effective head permittivity*. Nature - Scientific Reports, 6, 20459. doi: *10.1038/srep20459* – Partly incorporated as paragraph in Chapter 5.

Contributor	Statement of contribution
Ahmed Toaha Mobashsher (Candidate)	Designed experiments (75%) Wrote the paper (65%)
A. Mahmoud	Designed experiments (5%) Wrote and edited paper (5%)
Amin Abbosh	Designed experiments (20%) Wrote and edited paper (30%)

6. **Ahmed Toaha Mobashsher** and Amin Abbosh. 2015. *Near-field time-domain characterisation of wideband antennas*. Electronics Letters, 51(25): 2076 – 2078. doi: *10.1049/el.2015.2763* – Partly incorporated as paragraph in Chapter 3.

Contributor	Statement of contribution
Ahmed Toaha Mobashsher (Candidate)	Designed experiments (80%) Wrote the paper (70%)
Amin Abbosh	Designed experiments (20%) Wrote and edited paper (30%)

7. **Ahmed Toaha Mobashsher** and Amin Abbosh. 2015. *Artificial human phantoms: human proxy in testing microwave apparatuses that have electromagnetic interaction with the human body*. IEEE Microwave Magazine, 16(6): 42 – 62. doi: *10.1109/MMM.2015.2419772* – Partly incorporated as paragraph in Chapter 4.

Contributor	Statement of contribution
Ahmed Toaha Mobashsher (Candidate)	Designed experiments (80%) Wrote the paper (70%)
Amin Abbosh	Designed experiments (20%) Wrote and edited paper (30%)

8. **Ahmed Toaha Mobashsher** and Amin Abbosh. 2015. *Utilizing symmetry of planar ultra-wideband antennas for size reduction and enhanced performance*. IEEE Antennas and Propagation Magazine, 57(2): 153 – 166. doi: *10.1109/MAP.2015.2414488* – Partly incorporated as paragraph in Chapter 3.

Contributor	Statement of contribution
Ahmed Toaha Mobashsher (Candidate)	Designed experiments (80%) Wrote the paper (70%)
Amin Abbosh	Designed experiments (20%) Wrote and edited paper (30%)

9. **Ahmed Toaha Mobashsher**, Amin Abbosh and Yifan Wang. 2014. *Microwave system to detect traumatic brain injuries using compact unidirectional antenna and wideband transceiver with verification on realistic head phantom*. IEEE Transactions on Microwave Theory and Techniques, 62(9): 1826 – 1836. doi: *10.1109/TMTT.2014.2342669* – Partly incorporated as paragraph in Chapter 5.

Contributor	Statement of contribution
Ahmed Toaha Mobashsher (Candidate)	Designed experiments (70%) Wrote the paper (50%)
Amin Abbosh	Designed experiments (10%) Wrote and edited paper (30%)
Yifan Wang	Designed experiments (20%) Wrote and edited paper (20%)

10. **Ahmed Toaha Mobashsher** and Amin Abbosh. 2014. *Three dimensional human head phantom with realistic electrical properties and anatomy*. IEEE Antennas and Wireless Propagation Letters, 13: 1401 – 1404. doi: *10.1109/LAWP.2014.2340409* – Partly incorporated as paragraph in Chapter 4.

Contributor	Statement of contribution
Ahmed Toaha Mobashsher (Candidate)	Designed experiments (80%) Wrote the paper (70%)
Amin Abbosh	Designed experiments (20%) Wrote and edited paper (30%)

11. **Ahmed Toaha Mobashsher** and Amin Abbosh. 2014. *Development of compact directional antenna utilising plane of symmetry for wideband brain stroke detection systems*. Electronics Letters, 50(12): 1 – 2. doi: *10.1049/el.2014.0616* – Partly incorporated as paragraph in Chapter 3.

Contributor	Statement of contribution
Ahmed Toaha Mobashsher (Candidate)	Designed experiments (80%) Wrote the paper (70%)
Amin Abbosh	Designed experiments (20%) Wrote and edited paper (30%)

12. **Ahmed Toaha Mobashsher** and Amin Abbosh. 2014. *Slot-loaded folded dipole antenna with wideband and unidirectional performance for L-band applications*. IEEE Antennas and Wireless Propagation Letters. 13: 798 – 801. doi: *10.1109/LAWP.2014.2318035* – Partly incorporated as paragraph in Chapter 3.

Contributor	Statement of contribution
Ahmed Toaha Mobashsher (Candidate)	Designed experiments (80%) Wrote the paper (70%)
A.M. Abbosh	Designed experiments (20%) Wrote and edited paper (30%)

13. **Ahmed Toaha Mobashsher** and Amin Abbosh. 2014. *CPW-fed low-profile directional antenna operating in low microwave band for wideband medical diagnostic systems*. Electronics Letters, 50(4): 246 – 248. doi: *10.1049/el.2013.3909* – Partly incorporated as paragraph in Chapter 3.

Contributor	Statement of contribution
Ahmed Toaha Mobashsher (Candidate)	Designed experiments (80%) Wrote the paper (70%)
Amin Abbosh	Designed experiments (20%) Wrote and edited paper (30%)

14. **Ahmed Toaha Mobashsher** and Amin Abbosh. 2014. *Three-dimensional folded antenna with ultra-wideband performance, directional radiation and compact size*. IET Microwaves, Antennas & Propagation, 8(3): 171 – 179. doi: *10.1049/iet-map.2013.0374* – Partly incorporated as paragraph in Chapter 3.

Contributor	Statement of contribution
Ahmed Toaha Mobashsher (Candidate)	Designed experiments (80%) Wrote the paper (70%)
Amin Abbosh	Designed experiments (20%) Wrote and edited paper (30%)

Peer-reviewed Conference Papers

1. **Ahmed Toaha Mobashsher** and A. Abbosh. 2015. *Developments of tomography and radar-based head imaging systems*. IEEE International Symposium on Antennas and Propagation (ISAP2015), 9-12th November 2015, Hobart, Tasmania, Australia. – Partly incorporated as paragraph in Chapter 2.

Contributor	Statement of contribution
Ahmed Toaha Mobashsher (Candidate)	Designed experiments (80%) Wrote the paper (70%)
A. Abbosh	Designed experiments (20%) Wrote and edited paper (30%)

2. **Ahmed Toaha Mobashsher**, P.T. Nguyen and A. Abbosh. 2013. *Detection and localization of brain strokes in realistic 3-D human head phantom*. IEEE International Microwave Workshop Series on RF and Wireless Technologies for Biomedical and Healthcare Applications (IMWS-Bio 2013), pp. 1-3, 9-11 December 2013, Singapore. doi: *10.1109/IMWS-BIO.2013.6756149* – Partly incorporated as paragraph in Chapter 5.

Contributor	Statement of contribution
Ahmed Toaha Mobashsher (Candidate)	Designed experiments (70%) Wrote the paper (50%)
P.T. Nguyen	Designed experiments (20%) Wrote and edited paper (30%)
A. Abbosh	Designed experiments (10%) Wrote and edited paper (20%)

3. **Ahmed Toaha Mobashsher**, B.J. Mohammed, S. Mustafa and A. Abbosh. 2013. *Ultra wideband antenna for portable brain stroke diagnostic system*. IEEE International Microwave Workshop Series on RF and Wireless Technologies for Biomedical and Healthcare Applications (IMWS-Bio 2013), pp. 1-3, 9-11 December 2013, Singapore. doi: *10.1109/IMWS-BIO.2013.6756163* – Partly incorporated as paragraph in Chapter 5.

Contributor	Statement of contribution
Ahmed Toaha Mobashsher (Candidate)	Designed experiments (60%) Wrote the paper (50%)
B.J. Mohammed	Designed experiments (20%) Wrote and edited paper (10%)
S. Mustafa	Designed experiments (10%) Wrote and edited paper (20%)
A. Abbosh	Designed experiments (10%) Wrote and edited paper (20%)

Contributions by others to the thesis

Assoc. Prof. Amin Abbosh contributed closely in defining research problem, overall conception and direction of the thesis. Dr. Konstanty Bialkowski provided valuable advices on time-domain characterization and at various stages of the work. Dr. Beadaa Mohammed shared her knowledge and experiences in characterization of artificial tissue emulating materials.

Statement of parts of the thesis submitted to qualify for the award of another degree

None

Acknowledgements

I would like to express my sincerest gratitude to my principal advisor, Associate Professor Dr. Amin Abbosh, for his encouragement, guidance and feedback during the course of my PhD. I am also grateful to Associate Professor Vaughan Clarkson for his technical advice and support in his role as my associate advisor. My research would not have been possible without their invaluable technical insight and continuous guidance.

I thank my colleagues at Microwave group, in particular Dr. Konstanty Bialkowski and Dr. Yifan Wang for their technical suggestions. I would like to recognize my office mates for their enjoyable company and both academic and non-academic discussions. I also thank Dr. Beadaa Mohammed, of Microwave Group and Dr Philip Sharpe, of the School of Chemistry and Molecular Bioscience for their valuable suggestions regarding the development of artificial tissue mimicking materials.

I would like to thank the technical staff members of the Electronics Engineering Lab and Mechanical Workshops, especially Denis Bill, Richard Newport, John Kohlbach, Ian Daniel, Mark Lynne, Keith Lane, for their excellent services and technical support.

I would like to thank the Australian Research Council (ARC) and the School of Information Technology and Electrical Engineering (ITEE), The University of Queensland for the scholarship support.

Last but not least, I would like to thank my family for their continuous encouragement and moral support throughout my PhD journey.

Keywords

wideband microwave imaging, head imaging system, brain injury, wideband directional antenna, ultra-wideband antenna, near field, time-domain characterization, artificial phantoms, realistic human phantoms, head permittivity model.

Australian and New Zealand Standard Research Classifications (ANZSRC)

ANZSRC code: 090699 Electrical and Electronic Engineering not elsewhere classified 100%

Fields of Research (FoR) Classification

FoR code: 0906, Electrical and Electronic Engineering, 100%

Table of Contents

List of Figures

List of Tables

List of Abbreviations

2D	Two Dimensional
3D	Three Dimensional
CLL	Capacitive Loaded Loop
CPW	Co-planar Waveguide
CT	Computer Tomography
DDD	Dual Disk Dipole
DHDD	Dual Half Disk Dipole
EIT	Electrical Impedance Tomography
FEM	Finite Element Method
HPB	Half Power Beamwidth
ICH	Intracranial Hemorrhage
IEEE	Institute of Electrical and Electronics Engineers
ITEE	Information Technology and Electrical Engineering
MIS	Magnetic Induction Spectroscopy
MIT	Magnetic Induction Tomography
MoM	Method of Moments
MRI	Magnet Resonance Imaging
MT	Microwave Tomography
OA	Original Antenna
PSSMI	Phase Shift Spectroscopy of Magnetic Induction
SAR	Specific Absorption Ratio
SNR	Signal to Noise Ratio
TCD	Transcranial Doppler
TCM	Theory of Characteristic Modes
USB	Universal Serial Bus
UWB	Ultra-Wideband
VNA	Vector Network Analyser
WHO	World Health Organization

This thesis is dedicated to

my parents,

to whom I owe everything.

Chapter 1 - Introduction

This introductory chapter presents the background and underlying motivation of this research for utilizing wideband microwave imaging system for brain injury diagnosis. A description of the typical wideband microwave imaging system is provided along with its advantages and applications. The aims and original contributions of the thesis are also described. The organization of the thesis is outlined at the final section of this chapter.

1.1 Background and Motivation

Traumatic and non-traumatic brain injury is a major cause of disability and mortality worldwide [1-3]. Severe brain injuries include traumatic and acquired brain injuries, which happen when an external force traumatically injures the brain, such as in vehicular accidents, sports, or some other intentional and unintentional casualties or internal incidences, like stroke and tumors [1-4]. Intracranial hemorrhage (ICH), which refers to the accumulation of blood inside human head, is the most common form of such brain injury. It happens when a blood vessel inside the intracranial chamber bursts or is abruptly torn as a result of hypertensive damage, physical trauma, and other venous infections and malfunctions. As blood delivers necessary nutrition and oxygen to brain, deficiency of adequate blood supply prevents the proper brain function. As a result, brain cells start dying. From the onset of the brain injury, millions of brain's cells die every second, damaging the control links with different body parts which can result in a loss of memory, movement or speech and can lead to death [5]. At the same time blood swelling elevates the intracranial pressure which compresses the adjacent tissues and causing permanent brain damage [4]. It is estimated that ICH (which includes intra-parenchymal, subarachnoid, subdural and extradural hemorrhage) leads to brain deformation and a huge number of death (mortality rate of 30-50%) and disability (74% survivors) worldwide [6, 7], which makes it a crucial public health issue. Moreover, worldwide stroke is the second leading cause of death claiming a life in every six seconds [8]. Only in 2012, about 50,000 Australians suffered new and recurrent strokes – that is 1000 strokes every week or one stroke every 10 minutes [9]. As the devastating disorder of brain injury deteriorates rapidly, fast diagnosis and management is critically important for the treatment and recovery of the affected patient. Therefore, On-the-spot accurate detection by means of head imaging is the governing factor of the timely medication to ensure complete recovery of the injured patient [10, 11].

Although there are some highly sensitive imaging technologies (like CT scan and MRI) exist for brain injury diagnosis, they are expensive; hence, not accessible at rural hospitals and hardly affordable for all patients. According to World Health Organization (WHO), about three-quarter of the world population does not have access to reliable and affordable medical imaging systems [12]. More

importantly the existing imaging solutions are mostly bulky and cannot be carried by first response paramedic teams for the diagnosis purpose [13]. Time is crucial for the brain injury affected patients for fast and complete recoveries. Nevertheless, till now there is no monitoring technology to observe concurrent brain injury over periods of time without moving the patient. A compact and mobile technology that can be applied to monitor the patient continuously in real time, either at the bedside or in emergency room, would be a significant advantage comparing to the existing imaging techniques.

1.2 Wideband Microwave Imaging – Advantages and Applications

The non-invasive, non-ionizing, cost-effective and painless features of microwave imaging systems attracted numerous researchers to image the interior of human body. Two main approaches are commonly adopted as microwave-based imaging domain: microwave tomography and wideband microwave imaging. Microwave tomography approach seeks to estimate the complex dielectric profiles by solving a non-linear inverse scattering problem. On the other hand, wideband microwave imaging method is based on radar techniques which directly looks for the location of the significant scatterers (hemorrhage, in this scenario) utilizing the scattered signals across a wide span of microwave frequencies. Wideband microwave imaging is well preferred over microwave tomography in head imaging system due to its advantages in such ill-conditioned non-linear problem inside heterogeneous human head, where tomography approach becomes very complex and takes longer time to reconstruct a map of head interior [14, 15].

Wideband microwave imaging technique exhibits great potential in terms of cost, detection speed and portability of brain injury detection system. This kind of imaging methods utilizes the discrepancy of electrical properties of imaged scenario and look for potential scatterers, whose positions are calculated from the time differences of the pulses received by different antennas.

Wideband microwave imaging systems have been widely applied in breast cancer detection systems [16-19]and recently they are proposed to detect the abnormalities of human brain [20, 21]. The physical basis of this technique comes from the fact that from the moment the inception, the accumulation of hemorrhagic (bleeding) changes the electrical properties of the affected part of brain, creating a considerable dielectric contrast between the targeted affected portion and its surroundings. The investigation is done by exposing the brain to a low-level electromagnetic energy at microwave frequencies and acquiring the scattered radiated energy. The position of brain injury is estimated by calculating the path-time differences of the scattered signals that are received from different angles through antennas. The research works conducted in this thesis is intended towards the design and

development of a compact, portable and low cost head imaging system for accurate and effective detection of brain injury inside human head.

1.3 Aim of the Thesis

This project aims to develop a wideband microwave imaging system that is portable, of low cost and will effectively identify and locate the position of the brain injury. The following approaches are taken into account to achieve the goals of this project:

1) Antenna design: compact, wideband antenna has to be designed with uni-directional radiation patterns in order to transmit/receive more electromagnetic energy to/from the imaged body.
2) Design and construction of antenna array: an array of antennas has to be designed using the wideband antenna elements. Depending on the image reconstruction algorithm, a circular, elliptical or 3D shaped array will be proposed to construct the whole diagnostic system in compact shape.
3) Realistic head simulation model: a realistic head model has to be constructed with high resolution to simulate the realistic brain injury scenario in electromagnetic simulators like HFSS/CST.
4) Imaging: image has to be constructed from known and modified imaging algorithms to detect and locate the brain injury in simulation.
5) Fabrication of realistic human head model: realistic human head phantom will be constructed mimicking the electrical properties of real human head.
6) Verification: the proposed microwave system will be examined on the fabricated human head phantom and verified by detecting the presence of brain injury.

1.4 Original Contributions of the Thesis

The research works undertaken to attain the aims of this thesis result the following original contributions:

1) Design and development of several wideband antennas with compact size are proposed. This includes:
    a. A miniaturization technique based on the planes of symmetry which can be generalized for both microstrip and co-planar waveguide feeding, is explained with the help of characteristics modes.
    b. Design and development of a compact unidirectional folded 3D antenna which attained superior performances compared to the previously reported antennas.

c. Both directional and omni-directional antennas are designed utilizing the plane of symmetry approach.
d. A near-field time-domain characterization technique is proposed and performances of both directional and omni-directional antennas are compared.
e. Several slot-loaded folded dipole antennas are proposed with multiple novelties in terms of compact, low-profile, wideband and unidirectional (in near and far-field regions) features.
f. Multi-folded 3D antennas are introduced that attain wideband operation with directional radiation patterns in both near- and far-fields (in both frequency and time-domains) having compact size and low-profiles.

2) Realistic human head phantom is introduced. The contributions include:
   a. A detailed literature review of the existing types of artificial human phantoms and the fabricating materials.
   b. Elaborated discussions on the features and functions of different materials that are used in various human phantoms, along with a list of developed human head phantoms from the literature.
   c. The design and development of a 3D human head phantom with realistic anatomical tissue distributions and electrical properties proposed for head imaging systems.
3) Design and developments of single antenna based head imaging systems which are applied on human head phantoms.
   a. The simulations of realistic human head phantoms with brain injuries in realistic environment are performed with experimental verifications and the images are reconstructed.
   b. An imaging performance comparison of the head imaging system using both directional and omni-directional antennas is done to find out the superior one.
   c. A portable head imaging system is prototyped and successfully validated with on the realistic 3D human head phantom.
   d. Image reconstruction improvements are done by using an improved back-projection algorithm with a model effective head permittivity.
   e. A compact head imaging system with automated scanning capabilities is prototyped and imaging improvements are performed by considering the surface waves along the sir-skin interface.
4) Array based head imaging systems are simulated, analyzed and prototyped. The contributions include:

a. Full-wave wave electromagnetic simulations of a compact head imaging platform which is checked for radiation safety and image reconstruction accuracy with the simulations results.
b. An array based head imaging system with multi-level scanning capabilities is designed and fabricated using 3D printing and custom made mounting parts.
c. The head imaging system is numerically analyzed in simulation environment and is successfully validated with the realistic human head phantom to locate the 3D position of brain injury.
d. Pilot human tests are performed using the wideband microwave imaging system and the imaging results are compared with those of phantom data. The results confirm the future application of the prototyped microwave imaging system in preclinical trials.

1.5 Thesis Organization

The research works undertaken in this thesis are organised as follows:

Chapter 1 presents the background and underlying motivation behind current research. A brief discussion of microwave imaging is provided with a discussion of the advantages of using wideband microwave imaging compared to the existing state-of-the-art imaging technologies for brain injury diagnosis and the challenges faced by this wideband technology for the intended application. The aims and original contributions of this thesis are also outlined in details.

Chapter 2 overviews the microwave-based head imaging systems for brain injury diagnosis. The existing medical imaging systems are discussed which is followed by a detailed discussion of the existing microwave-based head imaging systems. The chapter ends with an elaborated detail of the challenges that an advanced head imaging system faces to meet an effective diagnosis scenario.

Chapter 3 presents the design and development of compact antennas potentially applicable for wideband head imaging systems. Several directional and omni-directional antennas are designed, prototyped and measured in both near- and far-field regions for both frequency and time-domain scenarios.

Chapter 4 introduces a realistic 3D human head phantom with heterogeneous distribution of head tissues and frequency dispersive electrical properties of respective tissues. The chapter starts with the discussion of the necessities of realistic 3D phantoms for microwave imaging applications. Different types of artificial phantoms are also classified with the description of the features and functions of various ingredients utilized for phantom fabrications.

Chapter 5 presents the developments of single antenna based head imaging systems for brain injury diagnosis. Both simulation and experimental results of realistic brain injury scenario and the imaging performances are discussed in details. Nevertheless improved back projection algorithms relying on the model of effective head permittivity are also discussed with a comparative imaging and statistical analysis with the existing imaging algorithms.

Chapter 6 discusses the developments of a compact array based portable head imaging system with multi-level scanning capability. The experimental results from the imaging system is presented and compared with the imaging results of the pilot human tests of healthy volunteers.

Chapter 7 concludes the thesis with the suggestions for future works.

Chapter 2 - Overview of the Microwave-based Systems for Head Imaging

This chapter presents an overview of the microwave-based head imaging systems for brain injury diagnosis. It starts with an introduction and discussion of the limitations of existing medical imaging systems that are typically used or have the potential of using in brain injury detection. The state-of-the-art microwave-based head imaging systems, reported in the literature, are also detailed in the next section. The challenges of wideband head imaging systems are described afterwards with the concluding remarks.

2.1 Existing Brain Injury Diagnosis Techniques and Limitations

There are some highly sensitive existing diagnostic tests that are performed to determine location of brain injury. Among them computerized tomography (CT) scan, magnetic resonance imaging (MRI), carotid duplex scanning, cerebral angiography (angiogram), Transcranial Doppler (TCD) diagnosis are mostly performed to diagnose brain injury [22-24]. Popular imaging systems like CT scan and MRI are able to identify the location. However, these techniques do not offer a fast and portable system, nor are they accessible at rural medical clinics, or carried by first response paramedical teams [13]. Although CT scan is regarded as one of the primary diagnostic medical imaging techniques to be performed on a brain injured patient, this technique exposes the patient to X-ray in order to create detailed images of the head interior and this exposure to such ionizing radiation increases the risk of the patient to develop cancer later in life [25, 26]. MRI is considered as one of the safest and effective medical imaging technologies which is utilizes powerful magnetic fields with radio waves and do not require any sorts of ionizing X-ray exposures. However, their high costs (in Australia, for example, more than one thousand dollars per scan) limit their use as monitoring tools and their availability at rural medical clinics. According to World Health Organization (WHO), about three-quarter of the world population does not have access to reliable and affordable medical imaging systems [12]. Hence, a portable and low-cost imaging system is widely demanded for the detection of ICH. Several medical imaging modalities, like electrical impedance tomography (EIT) [27], magnetic induction tomography (MIT) [28], magnetic induction spectroscopy (MIS) [29], or phase shift spectroscopy of magnetic induction (PSSMI) [30] are recently explored by the researchers. However, these technologies are either invasive or cannot detect ICH in a realistic environment; hence their practical demonstration is scarce. On the other hand, in the wideband microwave imaging, the investigation of brain injuries is performed by exposing the human head to a low-level electromagnetic energy over a wide bandwidth of microwave frequencies and acquiring the scattered radiated energy to reconstruct the interior of the head. Considering all previously aforementioned limitations of the existing brain

injury diagnosis technologies, wideband microwave based imaging have the potential to provide a non-invasive, non-ionizing, cost-effective and painless system with high diagnostic accuracy.

2.2 Existing Microwave-based Head Imaging Systems

Microwave-based imaging refers to the image reconstruction process of an object using microwave frequencies (1-30 GHz) [31]. As mentioned earlier, numerous researchers have been involved in investigating different microwave techniques for head imaging due to its low-cost, fast, non-invasive, non-ionizing and portable features compared to the existing imaging systems like computerized tomography (CT) scan, magnetic resonance imaging (MRI) etc. In microwave-based head imaging system, a low-level of electromagnetic energy is emitted towards the head using an antenna array and the scattered signals are collected and processed to image the interior of the human head. The image reconstruction and the principle of detection mostly depend on the contrast of scattering or electrical properties (conductivity and/or permittivity) between normal and abnormal tissues of the human head at the band of operation. The scope of microwave head imaging extends to a diverse range of fields including antennas to capture the backscattered signals, digital signal processing to locate the target and for the image computation and software engineering for the collection of data and image output. However, this type of microwave systems was underdeveloped due to its unique hardware component requirements and limitation in data processing speed. Recent advancements of wireless communication and computing have opened new doors for further research and development of this technology towards various applications pertaining human head [32].

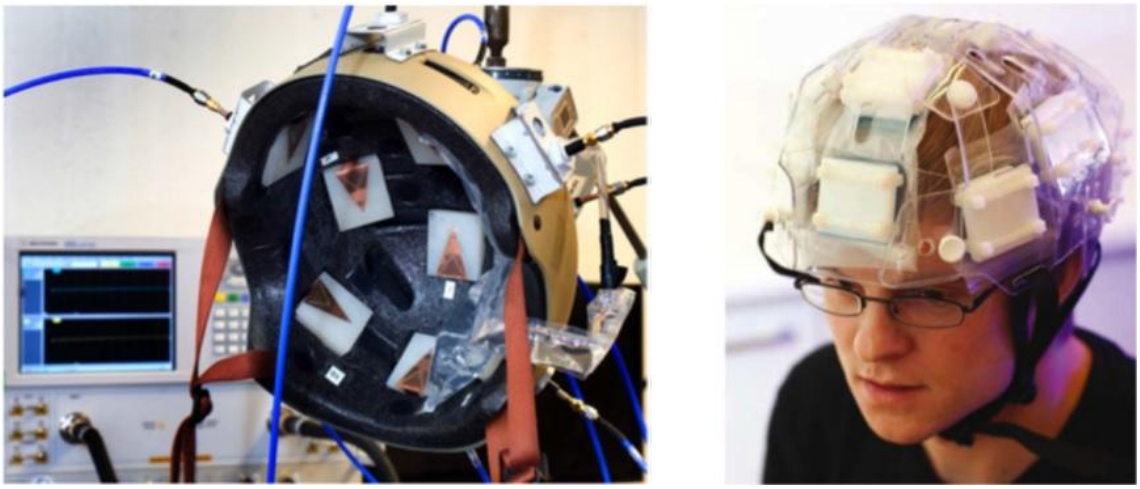

(a) (b)

Fig. 2.1 The developed microwave-based sensing prototypes [33]: (a) ten antenna based bicycle helmet prototype and (b) twelve antenna based mounting system on a custom-built supporting structure.

The head imaging systems can be applied on the detection of brain tumour [34]. However, among the numerous identified applications of the head imaging systems, researchers have concentrated more on the applications that are defined as life-threatening medical emergencies, which require rapid detection and medication for complete recovery. The detection of brain stroke, intracranial hemorrhage, subdural hematoma and so on [32], occurring from various traumatic and non-traumatic causes are some of the examples of such applications. In order to take a rapid medication procedure, the diagnosis is required to be on-site and fast. Microwave-based sensing system relying on a supervised learning-based classification algorithm using data from an antenna array was presented to be clinically applicable for stroke classification [33]. Fig. 2.1 illustrates two systems utilized for the sensing purpose. However, compared to microwave sensing, image based detection system provides more information regarding the position and size of the brain injury.

Owing to the combination of multiple technologies, the challenges of head imaging systems are multifold. Firstly, the detecting antennas are placed in close proximity of the human head where the lossy high permittivity head's tissues prevent the transmitted low powered signal from penetrating inside the head. The radiation and thermal safety of the human subject is one of the prime reasons restricting the transmission power, which is typically 1 mW or 0 dBm [35]. Low-microwave frequencies are less susceptible in lossy tissues and provide better penetration with the amount of utilized power, but may result in low resolution images due to the increased wavelength [36]. Attaining wide bandwidth can improve the image quality in this regard [37]. Most of the reported head imaging systems utilize frequencies between 0.5-4 GHz in narrowband or wideband manner, as a compromise between the image resolution and signal penetration [14, 15, 38-43]. The size of the antenna is the major design concern at these low frequencies, especially when wideband is demanded. Utilizing matching liquid in front of the antennas can reduce the relative size and improve matching with the head [32]; however, it may increase physical discomfort of the patient when applied. It is obvious that compact designs enable more elements in the sensing array within the available specific volume. This section reviews the recent developments in the microwave-based head imaging systems reported for diagnostic applications.

There are two major approaches that have become prevalent in microwave imaging literature are microwave tomography (MT) and wideband microwave imaging techniques. Both of them have advantages over each other. In MT technique the head is surrounded by an array of antennas operating at a single or multiple frequencies. Comparing the measured data from these antennas, MT approach seeks to estimate the complex dielectric profiles of the imaged domain (the head) by solving a non-linear inverse scattering problem. On the other hand, UWB radar method directly looks for the location of the significant scatterers (bleeding or clot target) by processing the scattered signals across

a wide span of microwave frequencies. UWB radar imaging is well preferred in microwave imaging due to its fast image processing in ill-conditioned non-linear problems, such as head imaging. However, due to the use of wide bandwidth the microwave hardware (transceiver, antenna) design, and signal acquisition and processing are more challenging.

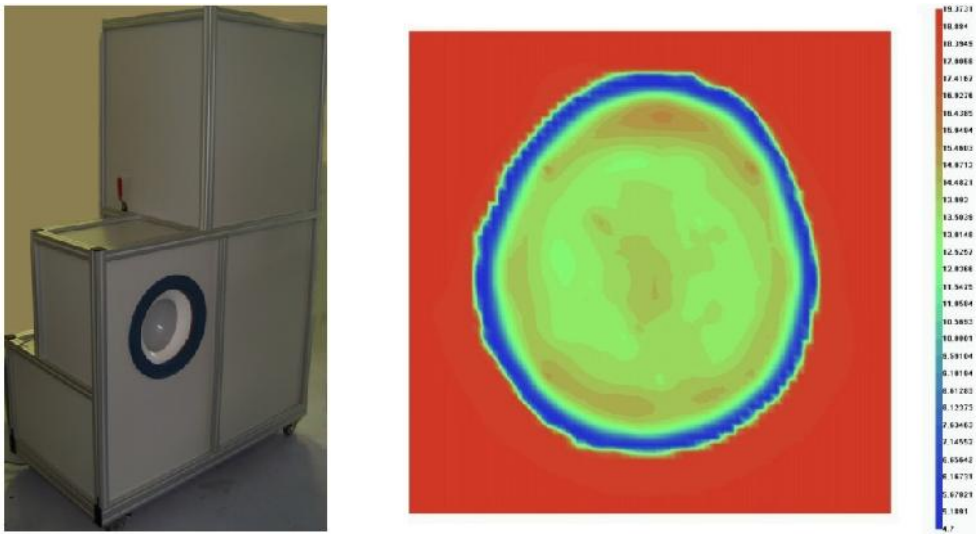

(a) (b)

Fig. 2.2 (a) Overall view of the EMTensor Brain Imaging System Generation 1 (EMT BRIM G1) and (b) MT image of a volunteer's head using the imaging system [40].

2.2.1 Microwave Tomography Imaging

MT is a form of quantitative imaging technique. The reconstructed image using MT illustrates the distribution of different tissues inside the human head. Typically, narrowband or multiband antennas are utilized in the imaging system which usually uses homogeneous matching medium to couple the transmitted energy and reduces reflections occurring at the skin layer. Among different reported MT studies for head imaging, variations of processing techniques, operating frequencies and utilized models are found. An MT system using 32 × 32 transmitters-receivers with simple inhomogeneous head model was proposed in [36]. Presuming high (40-60 dB) signal to noise ratio (SNR), the system attains good detection capability using multi-frequency approach at 0.5, 1 and 2 GHz. Images of virtual brain with ischemic stroke and edema was also detected using similar approach at 1 GHz [38]. Another study presents MT of realistic head models based on the Born iterative method [15]. It exhibits the feasibility of microwave imaging using 36 point sources operating at 850 GHz requiring lower SNR of 20 dB. The detection of ischemic strokes was performed through head imaging of 2D realistic head model using 24 ideal sources at 1 GHz using the nonlinear iterative Gauss–Newton algorithm [14]. All these studies promise the detection of stroke affected region through images. However, they are performed in simulation environment with transverse slices of the head. Recently,

an MT system was manufactured (Fig. 2.2) (EMTensor Brain Imaging System Generation 1 (EMT BRIM G1)) with 160 antennas operating from 0.9 to 1.1 GHz located in 5 rings [39, 40]. Images of healthy volunteers have demonstrated the detection of exterior layers of the head tissues. Although the interior portion of the head cannot be prominently layered and thus improvements of hardware and imaging algorithm are required, this is a significant milestone towards the practical implementation of MT for head imaging.

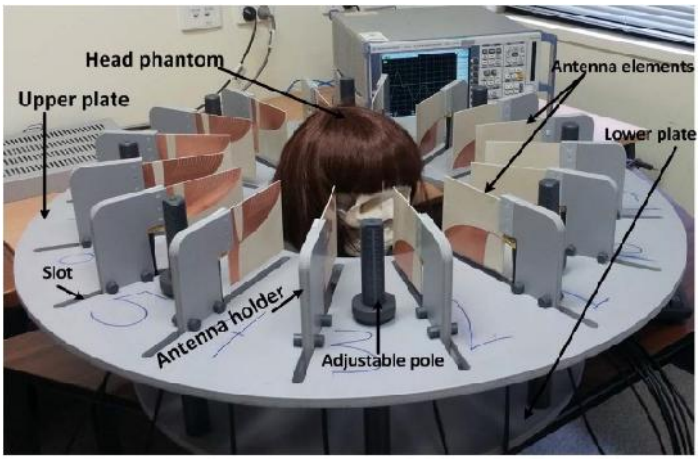

(a)

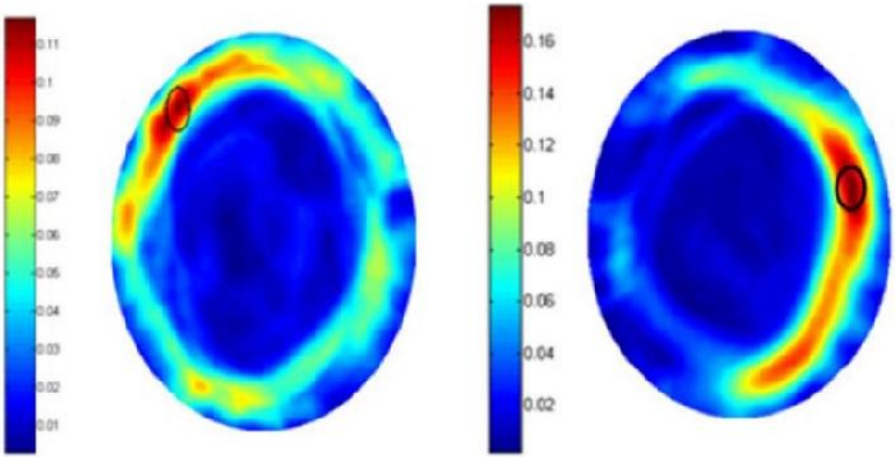

(b)

Fig. 2.3 (a) Configuration of the microwave imaging system and (b) reconstructed images with two different locations of a hemorrhagic stroke in a realistic head phantom [20].

2.2.2 Wideband Microwave Imaging

Wideband head imaging systems utilize the modality of qualitative imaging. In this case, the system transmits a wideband signal. The scattered signals are captured and processed to form a microwave image. The reconstructed image does not present the dielectric properties of the imaged domain or

the targeted region. However, it shows any significant scatterer within the imaged domain. Depending on the number of antennas used in the system, wideband radar imaging method can be utilized in three different approaches: mono static, bi-static and multi-static. Various numerical simulations of the head imaging systems are found using 2D head slices [41] as well as 3D simple head model [42, 44]. Although for microwave imaging, the properties of human tissues are fixed, in UWB scenario, the dispersive properties of the head has to be considered for realistic assumption. With the improvement of human tissue emulating materials and manufacturing techniques, phantoms are manufactured with anatomically and electrically realistic properties [45]. These phantoms play a vital role in the design, validation and safety precautions of head imaging systems. A complete microwave system (Fig. 2.3) was constructed using 16 antipodal antennas covering 1-4 GHz [20]. The system was experimentally verified by using a realistic human head phantom with hemorrhagic stroke. However, none of these systems is easily portable. Among the other limitations of these systems, the bulky vector network analyser and high profile antennas are vital for their operation [43]. Recently, a portable UWB imaging system with improved pre-processing technique has been reported using a compact unidirectional antenna and a small wideband transceiver for head imaging [21]. The system was validated using realistic head phantom and found efficient in detecting brain injuries. The use of small low cost software-defined radar system also recently being applied in medical head imaging applications [46, 47]. However, practically applicable head imaging system prototype is still found scarce.

This section has reviewed the recently developed head imaging systems that pose potential for preclinical or clinical implementation. The imaging of the head interior provides vital information about the location and impact of brain injury. In this section, most frequent microwave-based head imaging, namely tomography and wideband systems are discussed. Although numerous imaging techniques are examined for other applications, like breast cancer detection, synthetic aperture radar (SAR) applications and so on, many of these techniques are not valid, inefficient or unexplored for head imaging application. Nevertheless, more studies are yet to be reported for a practically applicable and clinically approved microwave-based head imaging system intended to the diagnosis of life-threatening medical emergencies.

2.3 Challenges of Wideband Microwave Imaging

Despite the potential methodological advantages of the wideband microwave imaging technique, there are several challenges that needs to be solved for an effective brain injury diagnosis system. It is worth to mention that the scope of wideband microwave imaging technology itself extends to a diverse range of fields including microwave and antenna theory to capture the backscattered signals, digital signal processing to locate the target and for the image computation and software engineering

for the collection of the data and image output [48]. Wideband microwave imaging for brain injury diagnosis was underdeveloped due to its unique hardware component requirements and limitation in data processing speed. Recent advancement of wireless communication and computing has opened new door for further research and development of wideband microwave imaging towards brain injury detection applications [32].

The size of the wideband microwave imaging system primarily depends on the construction of the antenna element and the array. High permittivity coupling medium is widely used in breast imaging to design antennas with compact size to overcome the array space limitation in imaging environment. In case of brain imaging system, constructing an array of antennas immersed in coupling medium creates physical discomfort to the patients and is considered difficult from the practical application viewpoint. However, computational research finding shows promising results of brain injury localization placing the imaged head in free space [49].

Operating frequency consideration is another big issue is brain injury diagnosis research. Researchers are trying to resolve this subject from different perspectives. From bio-electromagnetic point of view, the skin-depth (δ), which characterizes the penetration of electromagnetic fields inside human head, is an important issue for this non-invasive imaging application [50]. As δ is inversely proportional to the frequency, it is widely known that operating at microwave frequencies provides increased depth of penetration due to low signal attenuation [51]. However, the spatial resolution of image decreases at the same time. Thus, low microwave frequencies are more feasible for this application as a tradeoff to compensate these issues [52-54]. Nevertheless, in order to make the imaging system small, and thus, portable, wideband antenna elements with compact size is highly required. The design procedure becomes more thought-provoking when a wideband antenna with low cutoff frequency is desired for the wideband system. Another challenge of wideband microwave imaging system comes from the small scattered signal due to a target which is masked by a large reflected signal at the air-imaged head interface. Although some imaging algorithms are capable to subtract the reflection from the exterior of the head [49], antennas with increased directionality is required to enhance the received scattered signal from the target.

Another challenge comes from the most common assumption of constant permittivity in most radar microwave imaging systems relying on radar principle, while the fact is that the head tissues have frequency dispersive electrical properties. Thus a frequency dispersive model of human head is required for realistically locate the position of brain injury. Nevertheless, improvements of image processing algorithms are also required.

Validation process of the head imaging system is also challenging. Although it is comparatively easy to detect and locate the target location inside a simple phantom, in realistic heterogeneous scenario

this situation becomes very complex. However, before a system to be considered for preclinical trials realistic validation is also required. This calls for the validation of head imaging system on realistic 3D human head phantoms. In addition to these challenges, the head imaging system needs to be flexible for different sizes of heads, because the head sizes and shapes of different patients presumably vary from one to another. Nevertheless, multi-level scanning capability is also required for 3D localization of the brain injury position. In order to attain an effective head imaging diagnostic system the aforementioned challenges need to be overcome.

2.4 Conclusion

This chapter discussed the microwave-based head imaging systems for brain injury diagnosis. The existing state-of-the-art medical imaging systems and related technologies are described with their individual limitations and it is noted that wideband microwave imaging have the potential of overcoming these limitations. The existing microwave-based head imaging systems are discussed later. It is noted that in the literature most of the systems are studied numerically or with simplified head phantoms. Only handful of head imaging systems are prototyped and tested with realistic head phantom, not to mention tiny fraction of them have gone towards the preclinical trials. Despite the advantages, wideband microwave imaging systems have to face numerous challenges as the system relies on a diverse range of fields including electromagnetics, signal and image processing, instrumentations, material engineering, software development and so one. In order to make the head-imaging system compact, portable and low-cost which is as well effective in accurately detect the location of brain injury, the system has to meet all the challenges as discussed in Section 2.3.

Chapter 3 - Compact Wideband Antennas for Microwave Imaging Systems

The efficacy of microwave-based imaging systems depends strongly on the efficiency of the sensing antennas employed. The antennas capture scattering signals from the imaged body part. Hence, compact antennas with proper impedance matching are essential for a successful imaging system. This chapter describes the design challenges of designing an effective antenna for microwave based head imaging systems and introduces the developed antennas for the imaging systems.

3.1 Challenges of Designing an Effective Antenna for Head Imaging Systems and Literature Review

In order to design an effective antenna for head imaging system, there are several fundamental challenges that need to be considered. The tissues of the head are highly lossy due to their increased conductivity with frequency. Although relatively lower losses and higher penetration depth can be achieved at lower microwave frequencies [55, 56], the reconstructed image using these frequencies suffer from poor resolution. However, operating over a large bandwidth can improve image resolution [57]. Consequently, microwave frequencies are considered a trade-off between these criteria [58]. Nevertheless, the sensing antennas need to be compact and low profile to ensure a light-weight and portable imaging system. Omni-directional antennas appear to be the easiest solutions to meet the system's requirements. However, since only a tiny fraction of emitted power is scattered back from the head, the directional antennas might be more effective for microwave imaging systems. All these requirements increase the complexity of antenna design procedure.

The amount of research done on UWB antennas is in fact tremendous. The breakthrough of printed circuit board (PCB) technique vigorously changed the evolution of UWB antenna design. Most of the 3-D antennas were translated into their 2-D versions (see [59] and [60]). The PCB technique created a new domain in the field of antenna research, which resulted in low-cost and compact antenna structures that can be easily integrated into a circuit board and embedded into a portable device. Both omni- and directional patterns can be achieved by the PCB-fabricated antennas [61, 62].

Planar dipole antennas [63] and dipole-evolved monopole antennas [64-66] are mostly reported in the literature to attain improved operation of portable devices. Monopoles considerably decrease the required space to integrate into the system. UWB monopole antennas are primarily designed by meeting the electrical symmetry of dipole antennas. Afterward, some miniaturization measures, such as imposing slots [67, 68], truncations [69], fractals [70], ground modifications[71, 72], dielectric

resonators [73], impedance transformers [74], or capacitively loaded loop (CLL) resonators [75], are applied to realize smaller quasimonopole UWB structures.

It is worth mentioning that all the aforementioned miniaturization processes have some undesired effects on the radiation patterns generated by the antennas. Due to the planar orientation, the monopole antennas can be fed by microstrip lines, where the ground plane is situated at the opposite layer of the fed patch or by a coplanar-waveguide (CPW) structure, where all the antenna parts are printed on the same layer of the substrate. Fabricating the quasi-monopole antennas on high dielectric substrates can further miniaturize their size. However, the physical limitation still exists, and the manufacturing cost also increases.

Most of the reported monopole and quasi-monopole UWB antennas have symmetrical structures [69, 70, 73, 74, 76, 77]. Numerous band-notch UWB quasi-monopole antennas have also illustrated symmetrical shapes [77-80]. In those structures, two strong current paths exist on two symmetrical halves. It is noted that the patterns of the current distribution matches the conditions of magnetic mirror symmetry. Some researchers have shown that chopping off half of the symmetrical monopole antenna retains one strong current path and can operate over a wider bandwidth [81, 82]. Degradation in the cross-polarization level is reported as a limitation to this technique [35]. However, not all halfcut antennas can achieve wider bandwidth with suitable impedance matching right away. Hence, some literatures have reported that modifying the feeding structure provides better impedance matching [35, 82]. However, this method cannot be generalized since all these antennas are CPW fed, and a microstrip-fed bevel-shaped UWB antenna failed to provide proper impedance matching with 50-Ω input system impedance[83]. The reason might be attributed to the high input impedance that halved the microstrip feeding imposed on the antenna, resulting in an unstable impedance matching.

When directional radiation is sought, the choice of planar antennas becomes limited to two main types: quasi-Yagi and tapered slot antennas. For the former antenna to become directive, a reflector and at least one director are required at a certain distance from the fed dipole. Those factors consequently increase the antenna's profile [61, 84]. On the other hand, tapered slot antennas do not generally need a reflector to achieve its directionality. However, they need electrically long conductors or strips along the way of the electromagnetic radiation, making them inappropriate for the compact microwave imaging applications [85]. Moreover, the profile of both types of antennas becomes really large and impractical to use in microwave systems that operate at low-microwave bands [41, 86].

Dipole antennas naturally exhibit omnidirectional radiation patterns. However, several reported dipole-based antennas have a compact size or low-profile with directional radiation patterns by utilising some intelligent techniques. Examples of those techniques include using a dipole with a

composite E- and H-type corrugated reflector [87], reversed T-match dipole with a flat ground plane [88], cavity-backed folded triangular bowtie antenna with a rimmed circular reflector [89], a leaf-shaped bowtie array with a flat reflector [90], a dipole antenna on a mushroom-like electromagnetic bandgap structure [91].

The radiation and impedance matching of the antennas in [87-91] mostly depend on a large ground plane or reflector, which is undesirable for the light weight requirement of such portable application[92]. That undesired phenomenon is observed also in some other novel antennas. For instance, utilising an artificial high permittivity dielectric substrate lens significantly increases the front-to-back ratio, but the antenna size remains large [93]. Folded truncated metal plate antenna [94] or magneto-electric dipoles [95] can achieve wideband with low antenna profile. However, those antennas rely on relatively large ground plane for their performances. To the contrary, the coupled sectorial loop antenna [96] or cavity-backed monopole-like slot antenna [97] overcomes the small ground plane effect, but does not meet the low-profile criteria.

Recently, a self-grounded bowtie UWB antenna is introduced to achieve directional radiation patterns with low profile [98]. However, the acute bending of the thin copper plate of the antenna is difficult to construct precisely and vulnerable to use in sophisticated systems or rough environments, where slight pressure might change the shape of the antenna.

3.2 Utilization of Plane of Symmetry and Compact Omni-directional Antennas

The goal of this section is to examine the effects of miniaturizing a planar antenna along the magnetic and/or electric boundary line starting from dipole to monopole antennas. A generalized way to improve the impedance matching of the monopole and quasi-monopole antennas with different feedings is also described with an explanation of the characteristic modes of antennas. Consequences of miniaturization on the current distributions, and thus the radiation patterns, are also described from the characteristic mode perspective. Performances of applying the new miniaturization technique are also compared with other variations. Finally, the new miniaturization technique is applied on some sample antennas with different feeding techniques to demonstrate the effectiveness of the proposed approach.

3.2.1 Boundary Conditions in a Typical Symmetrical Dipole Antenna

A dual disk dipole (DDD) antenna, which represents a general shape of a dipole, in free space is shown in Fig. 3.1. The disks are of radius R = 15 *mm* and separated from each other by a distance 0.5 *mm*. It is to be noted that the selection of certain dimensions are needed in this and the following

examples to show the performance of the example antennas using the full-wave electromagnetic simulators. That specific selection does not limit the application of the presented approach. The antenna is excited from the mid-point. Image theory of electromagnetics suggests that when an electric current source is placed next to an infinitely large electric conductor, the conductor can be substituted with an out of phase current source of the same magnitude [99, 100]. On the contrary, an electrical symmetry line exists between two identical electric fields with a 180° polarity difference relative to each other. Observing this criterion for the currents flowing on the dipole, we can identify the electrical symmetry condition between the two disks. The dashed line along X axis represents this symmetry of the dual disk dipole, keeping one disk in each side of the line. Similarly, the in-phase current distributions along Y axis evoke the in-phase magnetic fields on the dipole. Nevertheless, the magnitude is seen to be identical along the center line. Thus according to the image theory, a magnetic symmetry exists along the center line of Y axis [101]. The solid line represents the magnetic boundary condition which divides the dipole into two parts where each portion have two half circular disks.

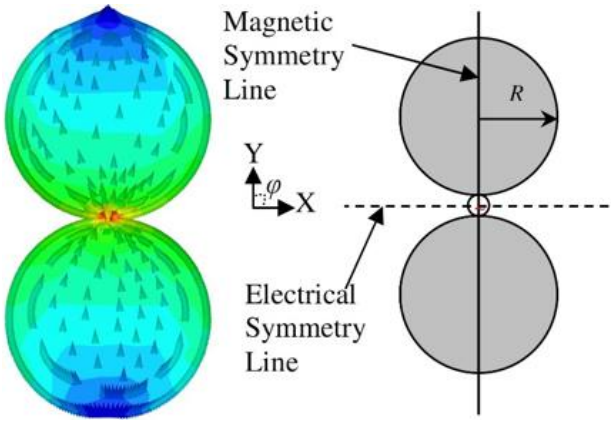

(a) (b)

Fig. 3.1 (a) Current distribution and (b) symmetry conditions of a typical dual disk dipole antenna.

Surface current distributions of an antenna at a certain frequency reveal the operating principle of the antenna at that particular frequency. As seen from Fig. 3.1, the currents are in mirror symmetry along the magnetic boundary line. Because of the symmetrical structure of the dual disk dipole, there exist two identical current paths in mirror. Each of those paths is reasonably enough to attain the resonance. This is why a dual half disk dipole (DHDD) antenna is constructed where the magnetic boundary condition is met to examine the effects on the antenna's performances after the cut. As anticipated, the direction of currents has not changed in the new DHDD antenna. However, when the DDD is shredded into two portions, the cut edge emits more radiation whereas the radiation from the middle part decreases. Thus, a significant amount of currents gather around the cut edge, while a slight decrement of current is observed in the inner portion.

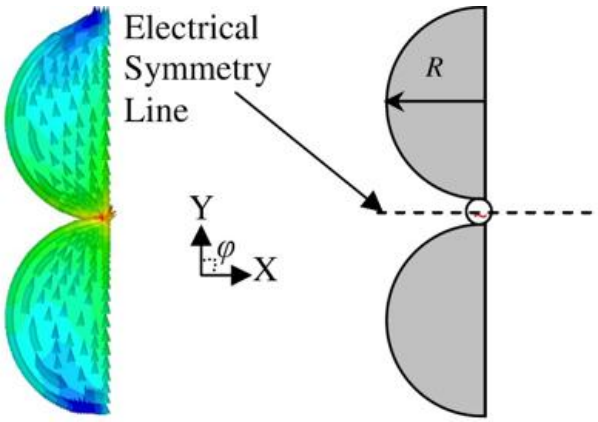

(a) (b)

Fig. 3.2 (a) Current distribution and (b) symmetry condition of dual half disk dipole.

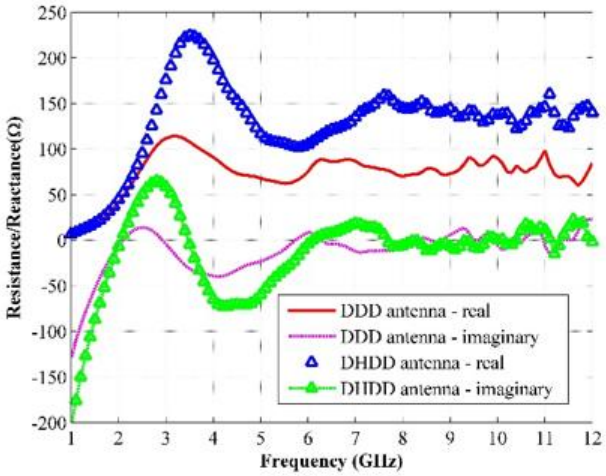

(a)

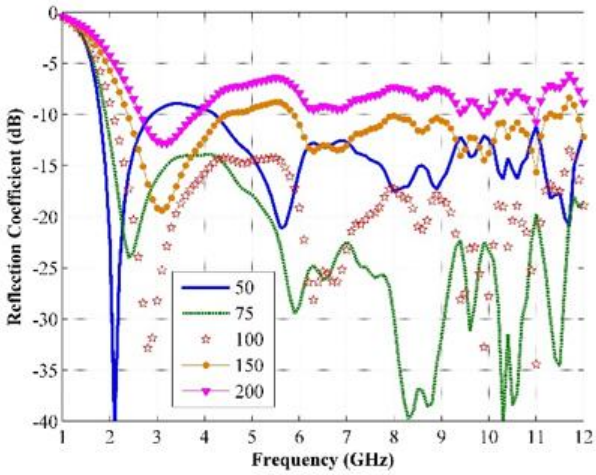

(b)

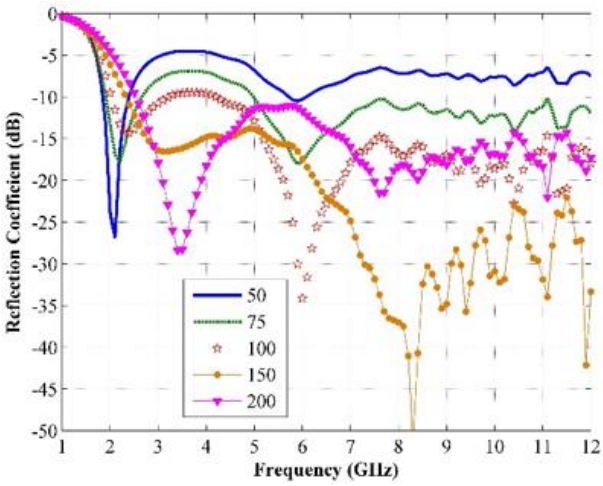

(c)

Fig. 3.3 (a) Real and imaginary parts of the input impedance of DDD and DHDD antennas; impedance matching of (b) DDD and (c) DHDD antennas with various reference impedances.

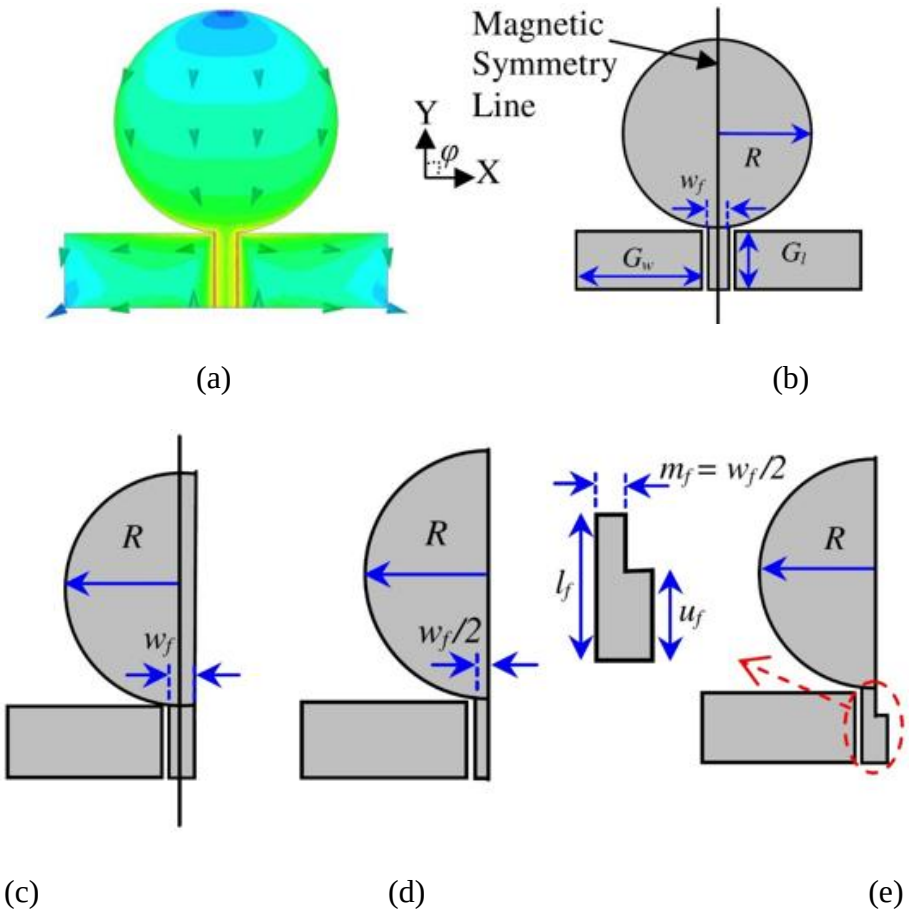

Fig. 3.4 (a) Surface current distribution and (b) magnetic symmetry condition of conventional monopole antenna; geometric configurations of (c) FUHM, (d) HM and (e) MHM antennas.

Cutting along the magnetic symmetry line of the antenna makes it an open-circuit. Hence the impedance increases significantly. This scenario is simulated using the finite element method based (FEM) electromagnetic tool HFSS. Fig. 3.3(a) illustrates that the resistance becomes almost double as the antenna is halved. Due to the inductive nature of the antenna, the reactive portion of the input impedance exhibits higher inductive values over the band of observation.

Figs. 3.3(b) and 3.3(c) illustrates the matching of the both DDD and DHDD antennas with respect to various reference impedances namely, 50, 75, 100, 150 and 200 Ω. It is seen that with 50 Ω reference, DDD shows wide but slightly interrupted -10 dB operating bandwidth; but best performance is achieved (from 2 to 12 GHz) when the reference impedance approximates to 75 Ω. On the other hand, in the case of DHDD, best matching is achieved when the reference impedance is twice the previous value, i.e. 150 Ω. Thus, it is possible to cut an antenna in the magnetic symmetry and adjust the impedance matching by changing its feeding mechanism in the new antenna. It is noted that for all respective impedance references, the resonating frequencies remain unchanged when DDD is cut along the magnetic symmetry line; only the values of reflection coefficients change due to the change in the input impedance.

3.2.2 Performance Enhancement of Monopole Antennas

It is well known that monopoles are constructed when the electrical symmetry condition of a dipole is met. Fig. 3.4 shows a conventional monopole (CM) antenna derived from DDD and operating in free-space. The monopole is fed with co-planar ground planes separated by 0.15 *mm* gap from the feeding line which has a width of w_f = 3 *mm*. The co-planar grounds are identical to each other with width, G_w = 20 *mm* and G_l = 10 *mm*. This feeding network is equivalent to 50Ω impedance. Dimensions of the 50Ω microstrip feeding line are calculated using well known microstrip line calculation. For general conceptual relevance, the antenna is analyzed by feeding it with a 50 Ω Sub-Miniature A (SMA) connector. As seen from Fig. 3.5, the antenna covers a wide bandwidth from 2.8 GHz to more than 11 GHz.

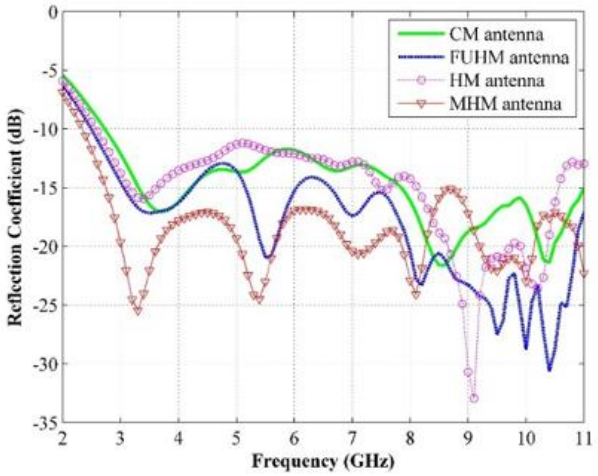

Fig. 3.5 Impedance matching of monopole antennas shown in Fig. 3.4 with respect to 50Ω input impedance.

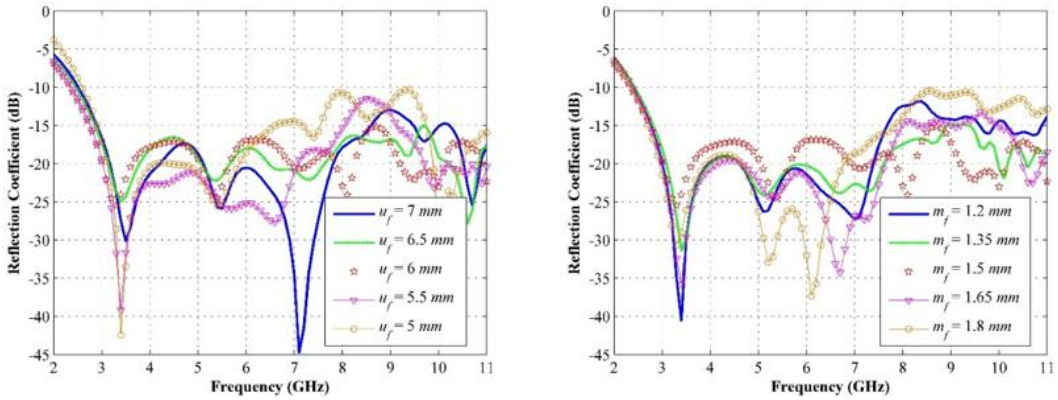

(a) (b)

Fig. 3.6 Effect on reflection coefficient versus frequency while changing (a) unmodified feeding length (u_f) and (b) modified feeding width (m_f).

From Fig. 3.4(a), it is observed that a magnetic symmetry line exists along the Y axis of this monopole. However, unlike the previous DHDD, meeting the symmetry condition also changes the feeding network of the antenna. For this reason, firstly two different quasi-monopoles, namely feed unmodified half monopole (FUHM) and half monopole (HM) antennas are built with slightly different feeding structures (Fig. 3.4 (c, d)). The FUHM antenna meets the symmetry condition up to the edge of the feeding line; thus the feeding line is unmodified (= w_f) as the CM antenna. However, the HM antenna properly satisfies the symmetry condition; hence the feeding line turns half (= w_f /2) of the CM antenna. Using the simulator HFSS, it is seen from Fig. 3.5 that the antennas achieve better impedance matching performance than the original monopole antenna. These results are in contrary to those of DHDD antenna, which can be attributed to the coupling effect of the ground plane in case of the antennas shown in Fig. 3.4. Due to the strong capacitive effect of the untouched ground side, the reactive portions of the input impedances of the modified antennas do not exhibit rapid increase of inductance. Moreover, unlike DHDD, due to the symmetrical feeding structure of CM antenna, the modified FUHM and HM antennas attain asymmetrical slot-line feeding network. As a result, the resistive portions of the input impedances of FUHM and HM antennas exhibit slight increments in their values. These combining effects consequently result in a marginal improvement in the impedance matching. Between these two designs, a slightly improved matching is achieved for FUHM when the main feeding line remains unaltered.

Combining these two (FUHM and HM) antennas, another modified half monopole (MHM) is designed (Fig. 3.4). The original feeding line is kept unchanged for u_f = 6 *mm*; then the feeding is halved to $m_f = w_f /2$ in order to increase the impedance of the feeding line which connects the halved patch at the end. It is noted from Fig. 3.5 that MHM antenna attains better impedance matching than the rest of the designs. MHM is basically the optimum derived design from DDD by using HFSS electromagnetic simulator defining u_f and m_f as variables and the other dimensions as constants in order to satisfy both the electrical and magnetic symmetry conditions; while the modified feeding network helps the antenna to reduce the impedance mismatch with the input signal and to achieve a broader radiation band.

It is observed from Fig. 3.6(a) that changing the unmodified feeding length (u_f) has a significant effect on the reflection coefficient performance of the antenna. On the other hand, the lower operating band does not dramatically change when the value of modified feeding width (w_f) is varied from the optimized value (Fig. 3.6(b)). However, the higher operating band is sensitive to the amount of feeding modification. As a general guideline of the modified feeding, it is recommended to maintain a truncated feeding width ratio (=w_f / m_f) and truncated feeding length ratio (=l_f / u_f) around 0.5. A modal analysis is performed next according to the theory of characteristic modes (TCM) to explain

the interest of meeting the electrical and magnetic boundary conditions and the mechanism behind the wider impedance matching of MHM antenna.

3.2.3 Characteristic Mode Analysis

Modal analysis is done by numerically calculating a weighted set of orthogonal current modes for a given arbitrarily shaped conducting structure. As described in [102], the characteristic modes or characteristics currents are obtained by solving a particular eigenvalue equation that is derived from the Method of Moments (MoM) impedance matrix,

$$X(\vec{J}_n) = \lambda_n R(\vec{J}_n) \qquad (3.1)$$

where λ_n are the eigenvalues, $\vec{J}_n$ are eigenfunctions or eigencurrents, and R and X are the real and imaginary parts of the MoM impedance operator, $Z = R + jX$.

3.2.3.1 Eigenvalue Analysis

Eigenvalues, λ_n range from -∞ to ∞. The magnitude of a particular eigenvalue represents how efficiently the characteristic mode radiates. Hence, modes with small values of $|\lambda_n|$ radiates efficiently and vice versa. When $|\lambda_n| = 0$, the mode reaches a resonating frequency. Again, if $\lambda_n > 0$, the modes have inductive contribution and stores magnetic energy; while $\lambda_n < 0$, the modes have capacitive contribution and stores electric energy [103]. To analyze the characteristics modes, firstly the eigenvalues are analyzed as they provide information of how the associated modes (J_n) radiate and how they are related to the resonance. It is proven that a few modes are required to characterize the mechanism of a small antenna [103, 104].

MoM electromagnetic tool FEKO is proven to implement TCM accurately [105]. Hence, this software is utilized to apply the theory and calculate the characteristic modes. However, the advanced tracking method mentioned in [106] is also adapted to deal with noisy modes and non-continuous behaviour of eigenvalues. Fig. 3.7(a-c) shows the variation of eigenvalues in different frequencies for the three monopole antenna types, namely the CM, HM and MHM antennas. The modal and resonance characteristics of FUHM are mostly similar to the HM antenna; hence it is not mentioned for the sake of brevity.

The first six eigenvalues are presented here. It is seen that all eigenvalues, except λ_0, start from the negative side, then crosses the zero level as they reach resonance and continues to increase in the positive side with a gradual slope. The zero eigenvalue, λ_0 that never reaches the resonance condition ($|\lambda_n| = 0$), holds a positive value in every frequency. This non-resonating mode is associated with the non-resonating current ($\vec{J}_0$) and only contributes to increasing the reactive magnetic power of the

antenna. The other modes related to the eigencurrents meet their resonances at some certain frequencies which are listed in table 3-I.

It is seen that the lower resonating frequency primarily depends on J_1 mode. As the monopoles are gradually modified from CM to MHM, to optimally match the antenna's input impedance, the resonating frequency of this J_1 mode shifts to lower values. This explains the reason behind the enhanced operation of MHM antenna in lower frequencies. In case of CM antenna, eigenvalue analysis shows that mode J_3 resonates at 5.50 GHz that is lower than the resonance of mode J_2. On the other hand, for HM and MHM antennas, J_2 resonates faster than J_3 and in a higher frequency compared to mode J_3 of CM antenna. It is also noted from Fig. 3.5 that the second resonance of CM antenna attains lower frequency compared to HM and MHM antennas because of the excitation and dominance of mode J_3 of CM antenna on the second resonance.

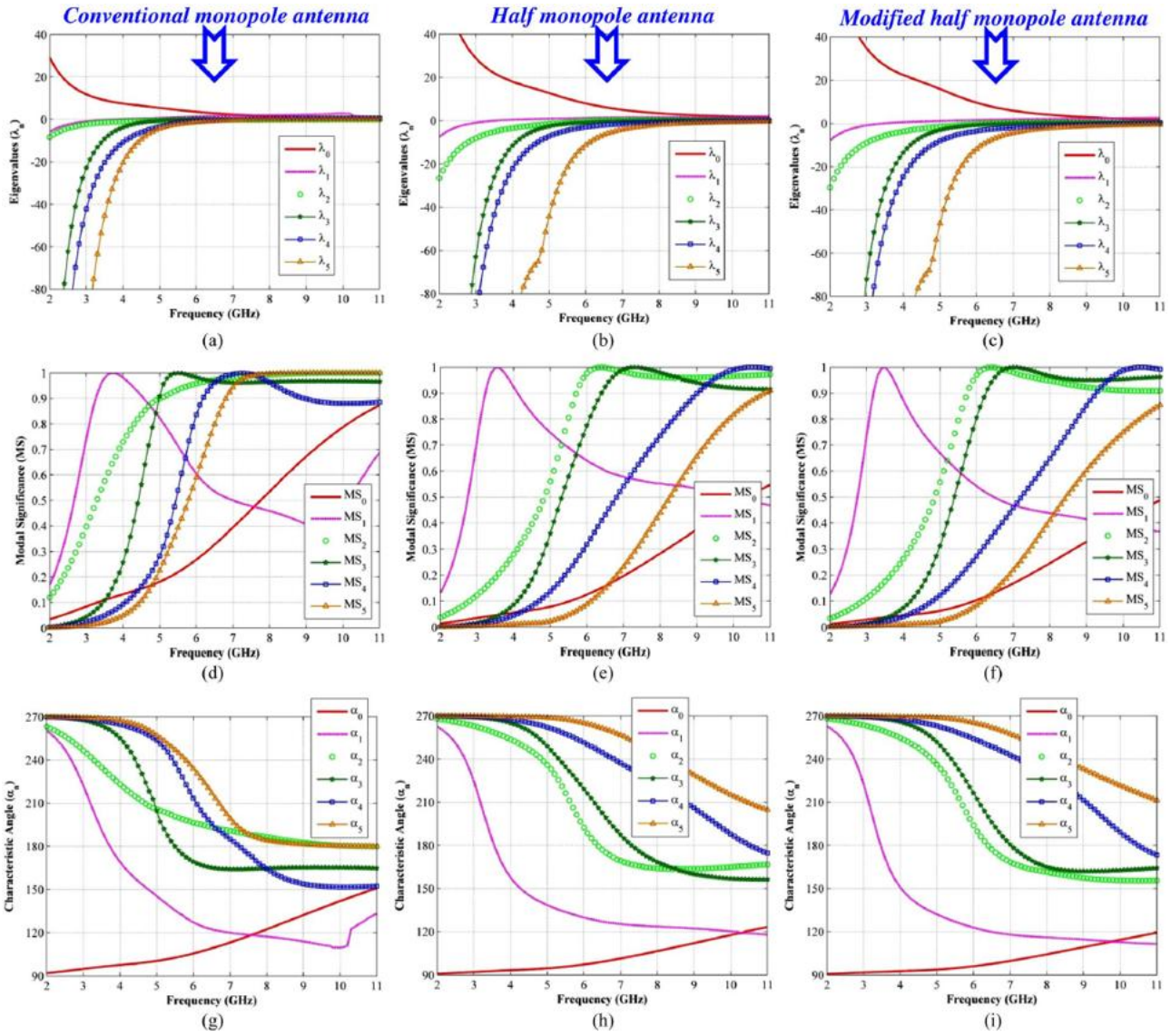

Fig. 3.7 (a-c) Eigenvalue, (d-f) modal significance, (g-i) characteristic angle curves of conventional monopole, half monopole and modified half monopole antennas respectively.

Table 3-I: Resonant frequency (f_r) for the characteristic modes of different monopole antennas

	Mode J_1	***Mode J_2***	***Mode J_3***	***Mode J_4***	***Mode J_5***
CM	3.75	10.90	5.50	7.30	10.70
HM	3.55	6.45	7.3	10.55	-
MHM	3.45	6.40	7.0	10.50	-

3.2.3.2 Modal Significance Analysis

In order to highlight the respective roles of characteristic modes, another representation named modal significance (MS_n) is preferred over the eigenvalues, which is defined as:

$$M_n = \left| \frac{1}{1+j\lambda_n} \right| \qquad (3.2)$$

MS_n represents the inherent normalized amplitude of the characteristic modes [107]. The values of MS state the importance of the respective mode on the scattering characteristics of the antenna. When the value of $MS = 1$, the mode meets the resonance condition. A mode closer to the highest MS_n curve suggests how effectively that mode is associated to the radiation at a specific frequency.

Figs. 3.7(d-f) exhibit modal significances of the first six modes for all the three discussed monopole antennas. It is seen that mode zero (MS_0) does not resonate over the frequency of operation due to its non-resonating nature. The values suggest that the inductive effect contributed by this mode increases as the modification of the monopole is done from CM to MHM antenna. Similar enhanced inductive effect in the input impedance can also be seen from Fig. 3.3(a), when the magnetic symmetry condition is considered. The first mode (MS_1) is most dominant in lower operating frequencies. It is noted that as the monopole antenna is cut to meet the magnetic symmetry condition, the contributions of other modes become less significant. For a conventional monopole antenna, all the modes have some impact on the operation of the antenna. Hence, the radiation behavior of this antenna is more complex to predict from the current modes. On the other hand, for HM and MHM antennas, the lower band is controlled by exciting mode J_1, middle portion by modes J_2 and J_3, and the last portion by modes J_4 and J_5. However, since multiple characteristic modes contribute to the high frequency resonances, it is difficult to separate the effects of individual current modes at these higher harmonics.

3.2.3.3 Characteristic Angle Analysis

The characteristic angle (α_n) is another term that is used to explain the operation of an antenna. This angle describes the phase difference between the eigencurrent, $\vec{J}_n$ and its associated characteristic field. It is defined as $\alpha_n = 180° - t\iota^{-1}(\lambda_n)$. The angle α_n is a measure of the radiation effectiveness of a structure. The modes associated with angle α_n=180° are at resonance and thus the related structure becomes a good radiator, minimizing stored energy in the reactive near field. However, the modes with α_n = 90° or 270° radiates poorly [108]. The nearer the characteristic angle is to 180°, the better is the radiating manner of the mode.

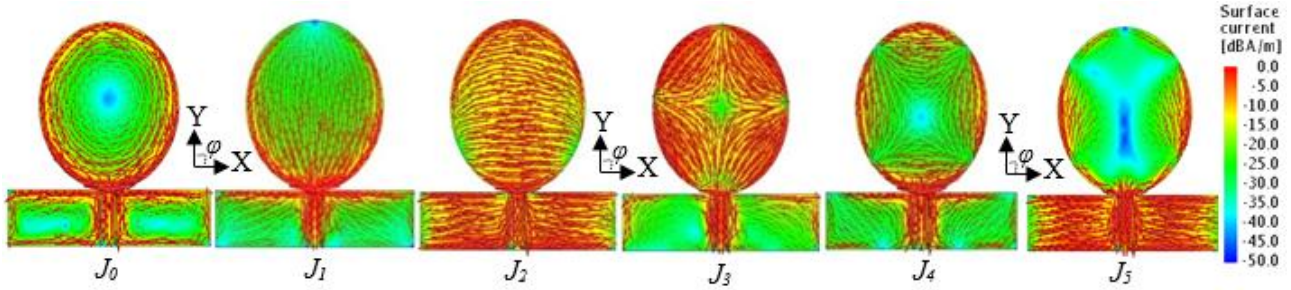

(a)

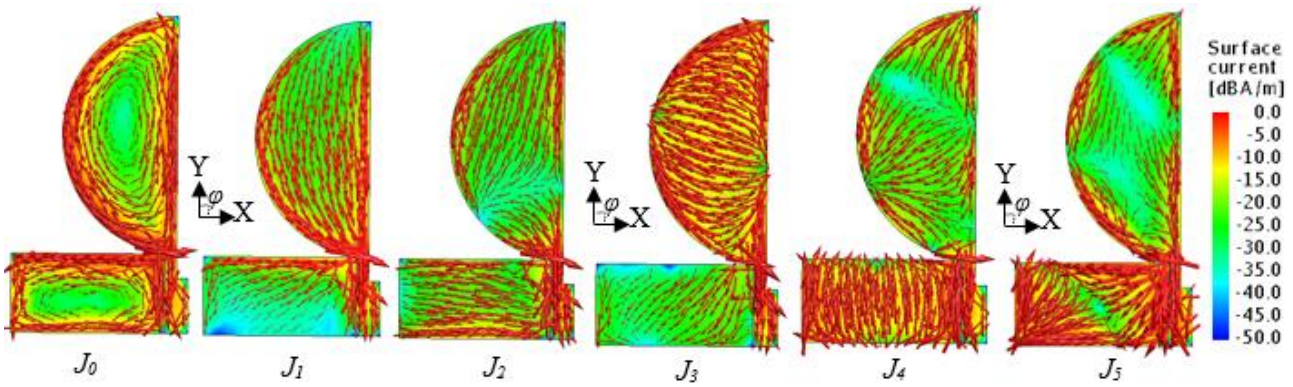

(b)

Fig. 3.8 Normalized magnitude of current distribution at resonance for the first six characteristic modes of (a) CM and (b) MHM antennas.

The characteristic angles of the first six modes of the three investigated antennas are illustrated in Figs. 3.7(g-i). Although these are other interpretations of Figs. 3.7(a-c) and 3.7(d-f), information extraction of resonances is much easier from this plot by merely considering points on α_n = 180° line. It is seen that as the CM antenna is minimized to a halved size by accomplishing the magnetic boundary condition, the lowest-order characteristic mode (J_1) resonates in lower frequencies and the slopes become smoother in high frequencies. The middle portion of the operating band of CM antenna is dominated by third (J_3) and forth (J_4) modes, while the upper band is dominated by J_2 and J_5. In case of both HM and MHM antennas, the middle and upper parts of the band are influenced by J_2 and

J_3. However, for MHM, these modes resonate in lower frequencies with smoother slopes resulting in better impedance matching over this frequency range.

3.2.3.4 Eigencurrent Analysis

The eigencurrents, $\vec{J}_n$ are independent of any specific source or excitation and depend only on the shape and dimensions of the structure and frequency of operation. The total current on the surface of an antenna can be calculated as a sum of $\vec{J}_n$ of the antenna. Similarly, the near and far fields can also be estimated from the independently radiating modal near- and far-fields, respectively. Thus, the modal analysis not only reveals the resonating mechanism of the antenna structure, but also provides an insight into the operation and radiation the antenna.

Fig. 3.8 exhibits the normalized surface current distributions of the first six characteristic modes of the CM and MHM antennas. All currents contribute in antenna resonances, except mode J_0, which is a non-resonating current mode forming a loop like current distribution on each part of the antennas. J_0 determines the inductive behaviors of the antennas and helps to store magnetic energy. It should be remembered that these eigencurrent distributions do not rely on the position of the feeding, but on the shape of the antenna. A proper feeding position excites the antenna modes and the exhibit optimum performance of the antenna. Extended simulations show that despite their different modal behavior, the HM antenna exhibits eigencurrent distributions similar to the MHM antenna; hence, they are not presented here.

In CM antenna, most of the currents of mode J_1 flow in vertical direction, along Y-axis, and currents of mode J_2 flow in horizontal direction, along X-axis. However, in case of mode J_3, multiple current nulls are observed with strong current distributions on the circular patch and less currents on the rectangular grounds. It is noted from the discussions of the previous section that most of the operating bandwidth of the antenna is dominated by these three modes. The other two modes, J_4 and J_5, contribute mostly in the higher frequencies. In case of modes J_1, J_3 and J_5, magnetic symmetry condition is observed along Y-axis. The other modes (J_0, J_2 and J_4) demonstrate electric boundary condition for the CM antenna. However, it is seen for this antenna that the modes (J_1, J_3 and J_5), which exhibit magnetic symmetry, are more significant than the other modes over the operating band (see Fig. 3.7(a, d, g)). Mode J_1 resonates first and is responsible for the lower operating frequencies of CM antennas.

As the CM antenna is halved and the feeding is modified, the proposed MHM antenna meets the magnetic boundary condition. It is seen from Fig. 3.8 that J_1, J_3 and J_5 modes do not change their characteristic currents after this modification. Most of the currents of these modes still flow vertically

along Y-axis. Mode J_0 creates a loop shape in the half circular patch. Currents on the remaining rectangular ground do not alter their directions. A significant change of current flow is observed in mode J_2. Most of the currents flow vertically, starting from the current null. As described later, vertical currents plays an important role on the radiation patterns of the antenna. Since mode J_2 resonates in a quicker manner than that of CM antenna, these currents help MHM antenna to improve its radiation characteristics over 5 to 7 GHz. In case of MHM antenna, the resonances of modes J_4 and J_5 shift to higher frequencies. Thus, these modes have lesser effect on MHM antenna performance than CM antenna.

Since the modal currents are independent to antenna excitation, suitable feeding position of antennas is critically important to excite specific characteristic modes. It is also noted from Fig. 3.8 that the CPW strip line consistently carries strong current vectors in both the structures of CM and MHM antennas. The areas having large current magnitude in regular manner, suggest that feeding the antennas from the strip line end will excite the eigencurrents and thus, the characteristic modes properly [109].

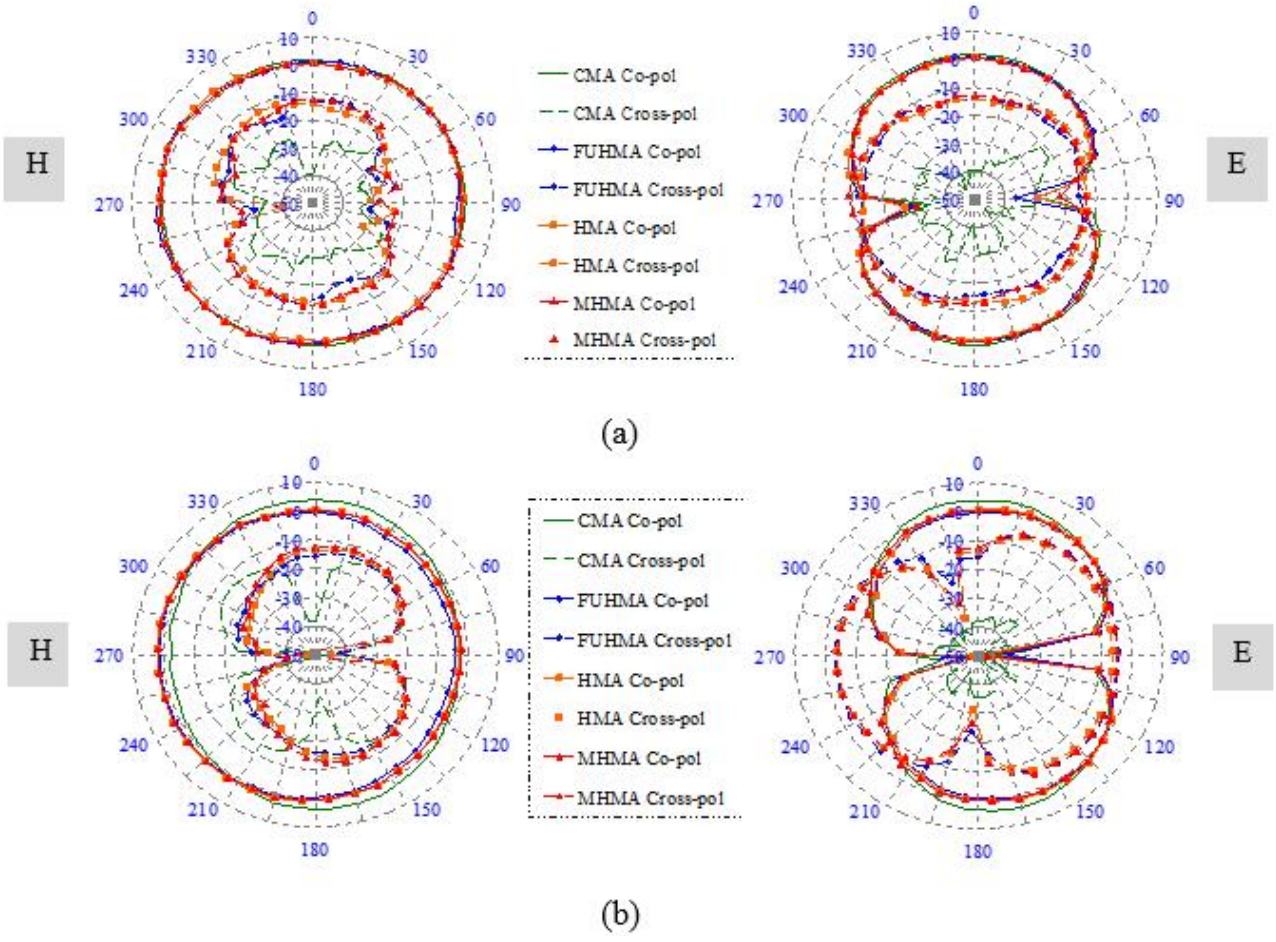

Fig. 3.9 H-(XZ) and E-(YZ) plane pattern of various monopole antennas extracted from HFSS at (a) 4 and (b) 8 GHz frequency.

3.2.3.5 Correlation between eigencurrents and radiation patterns

The radiation patterns of all four quasi-monopole antennas at 4 and 8 GHz are illustrated in Fig. 3.9. Good omnidirectional radiation patterns in H-(XZ) plane are achieved for all the antennas. In spite of the asymmetrical structures of the halved monopoles, they exhibit symmetrical radiation patterns in lower frequencies. With the increase of operating frequency, as the relative sizes of the asymmetric ground planes increase, the antennas tend to radiate slightly more along the X-direction. The main direction of radiation (Z-direction) still remains relatively high. Similar phenomena are observed in case of E-(YZ) plane radiation. However, for both planes, a significant increase in cross-polarization level is observed. This feature can be explained from the eigencurrents shown in Fig. 3.8, as the field distribution fully depends on the variation of current strength and direction.

Mode J_1 is mostly responsible for the lower operating frequencies of the monopole antennas. A strong current flows on the circular patch along Y-axis, while the rectangular ground carries the horizontal current components. It is worth to mention that since the antennas are fed from a CPW feeding point, the vertical (Y-axis) currents are responsible for the co-polar radiation. The horizontal (X-axis) currents contribute in building up the cross-polarization of the radiation patterns. For CM antenna, the X-axis currents are out of phase along Y-axis, creating a magnetic symmetry line. Hence, the fields generated by these currents cancel each other limiting the cross-polarization level to relatively low. On the other hand, for the halved monopoles the counter radiation of the horizontal currents is absent due to the size reduction. Hence, these horizontal currents create high cross-polarization level for the halved monopoles.

Mode J_2 is more significant in the halved antennas than in the conventional monopole antenna. The altered vertical currents of mode J_2 reduces the effect of increased horizontal currents in the middle portion of the band. The same mode also affects the antenna's radiation in higher frequencies along with mode J_3.

Although the impedance matching of the proposed MHM antenna improves quite well than the other halved antennas (FUHMA and HMA), they show similar radiation patterns and cross-polarization level. It is recommended that decreasing the width of the rectangular ground decreases the horizontal currents and, thus, the cross-polarization level. However, slight deficiency in the operating frequency band is observed.

The peak gain plots of the four antennas are illustrated in Fig. 3.10. The gain increases gradually with the increase in operating frequencies. A slight variation in the gain is observed from one antenna to another. Although the radiation slightly decreases along Z-direction for halved antennas, the peak gain level is still comparable to the CM antenna.

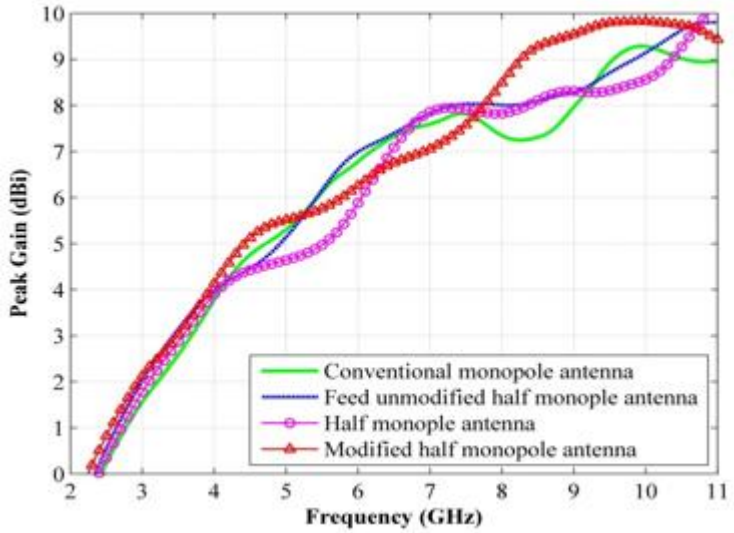

Fig. 3.10 Maximum gain patterns of different monopole antennas.

3.2.4 Design Examples

3.2.4.1 CPW Fed Quasi-monopole Antenna

The proposed modified feeding technique for half monopole antennas is applied for the miniaturization of compact CPW fed quasi-monopole antenna described in [110]. That antenna provides UWB performance by loading inverted L-strip over typical monopole radiator on one side of 1.6 mm thick FR4 substrate (permittivity of 4.4 and loss tangent of 0.024). The original design and our modified variations are illustrated in Fig. 3.11. All the dimensions given in this and subsequent antenna structures are in (mm). The FUHM and HM antennas are shaped by chopping half of the antenna while keeping the full and half of the feeding line respectively. The FUHM, HM and MHM antennas are designed following the findings of the previous discussions on the analysis of characteristics modes based on the antennas of Fig. 3.4. In the MHM antenna formation, the original feed remains up to 5.3 *mm* length and then the feed is cut into half of the width and extended and connected to the radiating patch 8.8 *mm* from the SMA connection point.

The results of the antenna miniaturization extracted from HFSS, are exhibited in Fig. 3.12. The miniaturized antennas (FUHM and HM) provide wider bandwidths than the conventional design. However, they lack in maintaining proper impedance matching level and impose instability. The MHM antenna, on the other hand, clearly overcomes these problems; it supports radiation from 2.2 GHz to over 11 GHz with respect to –10 dB reflection coefficient reference line. A 14% increase in impedance bandwidth is achieved in MHM antenna as a result of the new miniaturization technique with a 44% size reduction from the original quasi-monopole antenna.

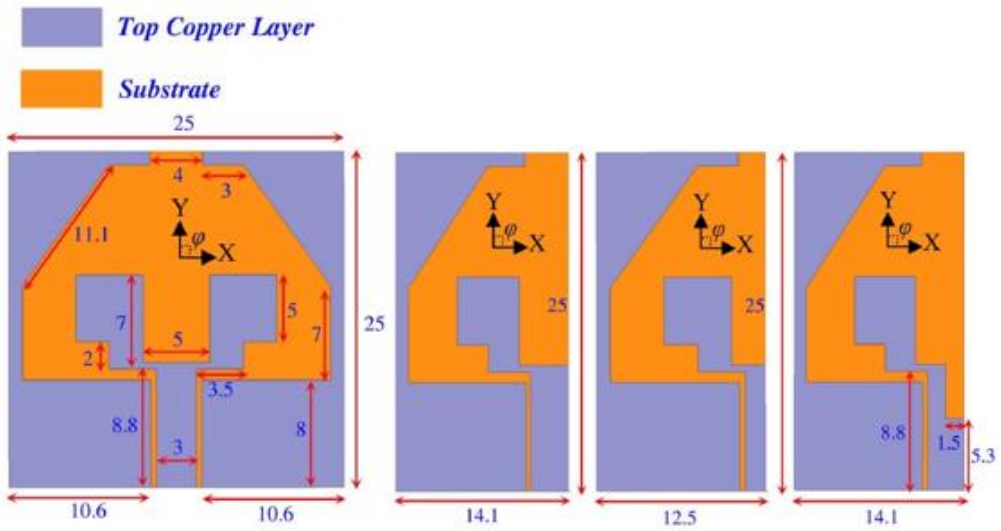

(a) (b) (c) (d)

Fig. 3.11 Schematic diagrams of (a) CM, (b) FUHM, (c) HM and (d) MHM version of the antenna in [110] .

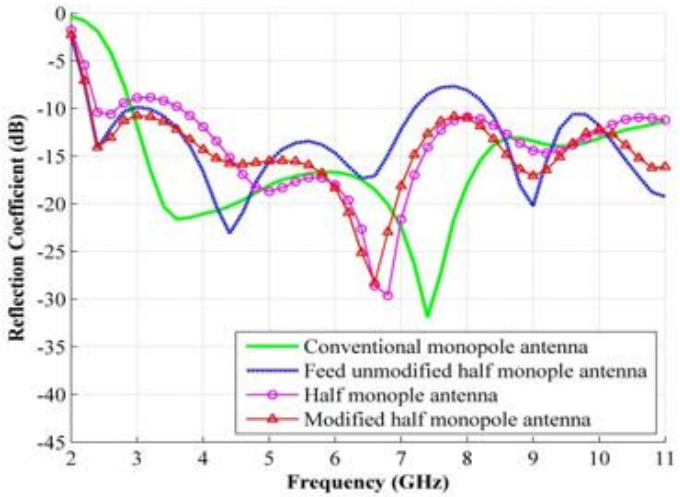

Fig. 3.12 Impedance matching of antennas shown in Fig. 3.11 with a 50Ω feed.

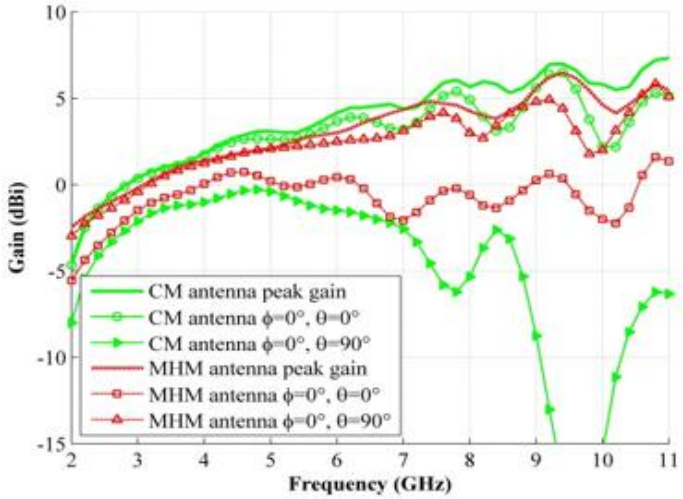

Fig. 3.13 Gain patterns of CM and MHM antennas of Fig. 3.11 in various directions.

Comparing the gains of CM and MHM antennas provides an insight into the change in the radiation characteristics due to the miniaturization. As shown in Fig. 3.13, the peak co-polar gain attained from MHM antenna slightly decreases compared to that of CM antenna due to the reduction in the radiating area. The negative gains at lower frequencies are due to the material loss of FR4 substrate which can be overcome by using low loss substrates. The co-polar gain curve of the MHM antenna along Z-axis direction (ϕ=0°, Θ=0°) tends to roam around 0 dBi, while for CM antenna, the gain matches well with peak gain as the CM antenna radiates better than the MHM antenna along this direction due to the symmetry of the CM antenna. However, it is noted that the co-polar gain plot of the MHM antenna along Y-axis direction (ϕ=0°, Θ=90°) corresponds to the maximum gain curve well. This concludes that the MHM antenna radiates mainly along ϕ=0°, Θ=90° direction. Comparing to the CM antenna, the gain values are much higher in this direction. If omni-directionality is of concern, it can be observed by looking at the gain curves that MHM antenna radiates better than the CM antenna in this manner.

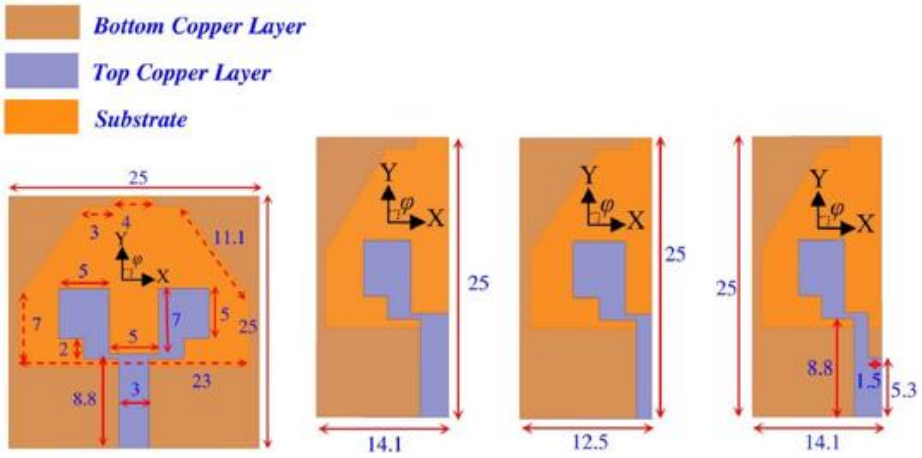

Fig. 3.14 Geometric configurations microstrip feed modifications of (a) CM, (b) FUHM, (c) HM and (d) MHM antennas shown in Fig. 3.11.

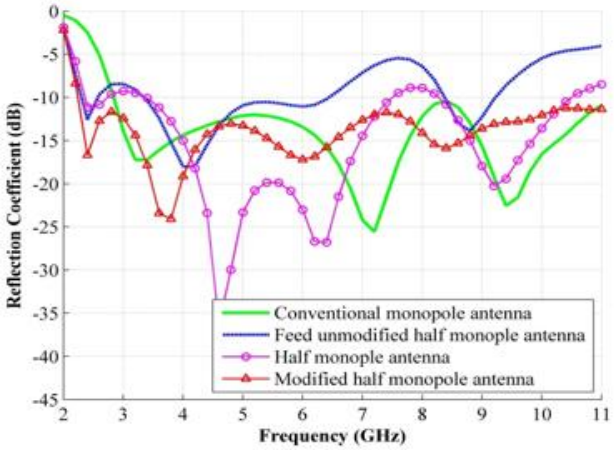

Fig. 3.15 Reflection coefficients of the antennas of Fig. 3.14.

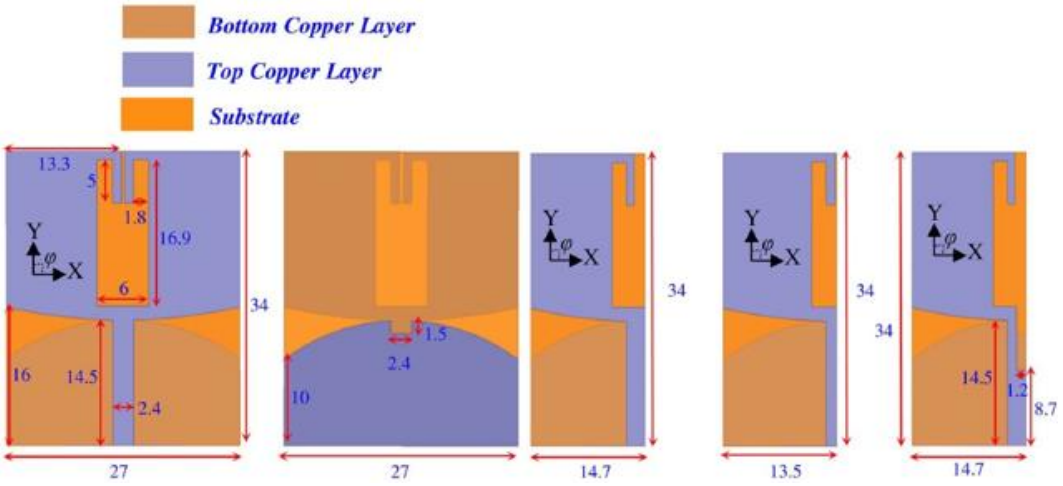

Fig. 3.16 Top and bottom views of microstrip fed (a) CM, (b) FUHM, (c) HM and (d) MHM antennas, modified from [75].

3.2.4.2 Microstrip Line Fed Quasi-monopole Antenna

The miniaturization technique is also applied to the microstrip fed antennas. In the first example, the aforementioned CPW antenna is converted to a microstrip fed UWB antenna and exhibited in Fig. 3.14. After simulating the structures using HFSS, similar characteristics were seen as antecedently discussed (Fig. 3.15). For the sake of brevity, the explanations are not repeated.

For the second example, a top capacitively-loaded loop UWB antenna [75] is chosen for the verification. This microstrip fed antenna is fabricated on 0.787 *mm* thick Rogers Duroid 5880 material with permittivity of 2.2 and loss tangent of 0.0009. The geometry of the antenna and the modified variations are exhibited in Fig. 3.16. The final MHM version of this antenna consists of half of the original structure along with the modified feeding which comprises of 8.7 *mm* long original feed line which is then truncated to half to feed the radiating patch. A truncation ratio of 0.6 is maintained in this case. It is seen from Fig. 3.17 that the HM antenna provides wider bandwidth than CM antenna with good impedance matching, but presents narrower operating band than MHM version. The MHM antenna covers an operating band from 2.4 to more than 11 GHz, which is around 10% fractional bandwidth improvement with 46% size reduction compared with the original CM edition.

Table 3-II summarizes the results of the proposed miniaturization technique for both CPW and microstrip fed symmetrical antennas. Distinct advantages are seen vividly upon the application of symmetry conditions and generalized modified feeding method on both types of antennas.

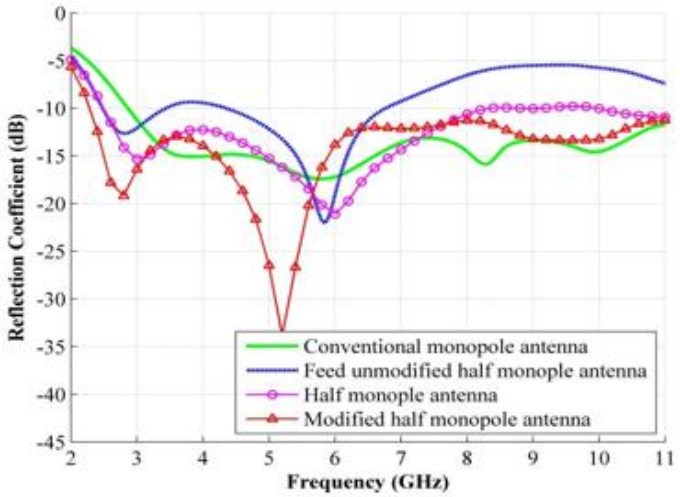

Fig. 3.17 Impedance matching characteristics of different antennas of Fig. 3.16.

Table 3-II: Summary of applying the proposed miniaturization techniques on various antennas

Antennas	***[110]***	***Microstrip Fed [110]***	***[75]***
Truncated width ratio (w_f / m_f)	1.5/3 = 0.5	1.5/3 = 0.5	1.2/2.4 = 0.5
Truncated length ratio (l_f / u_f)	5.3/8.8 = 0.61	5.3/8.8 = 0.61	8.7/14.5 = 0.6
Lowest operating frequency of CM antenna (GHz)	2.85	2.8	2.9
Lowest operating frequency of MHM antenna (GHz)	2.2	2.25	2.4
Fractional Bandwidth of CM antenna (%)	117	118	116
Fractional Bandwidth of MHM antenna (%)	133	132	128
Size reduction from CM to MHM antenna (%)	44	44	46

With the invention of printed circuit board (PCB) techniques, extensive research has been done to achieve wider bandwidth, low cost, compact and planar antenna designs, in past few decades. As a result, a huge number of ultra-wideband (UWB) antennas are reported. Most of the existing compact planar designs are monopole antennas with symmetrical structures which are derived by meeting the

electrical symmetry of their dipole version. In this section, a new half cut monopole antenna technique has been proposed by meeting the magnetic symmetry condition and feeding network modification. The modified feeding technique can be used as a general guideline to utilize the existing symmetrical designs for compact structures and wider bandwidths. In order to look deep into the physics behind the enhanced performance, modal analysis is adopted.. The main reason attributed to the effects of the modified structures is identified. It has been shown that the modes responsible for modified half monopole (MHM) antenna's operation resonate in lower frequencies with smoother slopes than the other feed unmodified half monopole (FUHM) and half monopole (HM) antennas. The excitation independent characteristic currents (eigencurrents) are also observed by the theory of characteristic modes and correlated to the radiation patterns of MHM antennas. It is seen that fields created by the horizontal currents, which loses their opposing counterpart from other half of the antenna, are responsible for the increased cross-polarization level. However, it is seen that the MHM antenna radiates in a similar manner as FUHM and HM antennas. Finally, some examples of the proposed feeding techniques have been illustrated for both coplanar waveguide and microwave feeding. Using the modified half monopole (MHM) structures, a fractional bandwidth improvement of 10-15% is accomplished with a size reduction of around 45%. It is also observed that the MHM radiates in a more omni-directional manner than their conventional monopoles counterparts.

3.3 Compact Omni-directional Antenna Operating in Low Microwave Frequencies

Imaging of dense vital organs, such as the head, requires enough penetration of the low-level signal which can be assured if the antenna operates at the low microwave bands [57]. A wideband monopole antenna with omnidirectional radiation is designed relying on the principle described in Section 3.2. The antenna is printed on FR4 substrate (ε_r=4.5, $\tan\delta$=0.02) and occupies a space of $0.32\lambda_0 \times 0.19\lambda_0 \times 0.006\lambda_0$. The monopole antenna's geometry is illustrated in Fig. 3.18(a) with the photographs of the fabricated antennas in Figs. 3.18(b). The antenna performance is presented in Fig 3.18(c). The compact omnidirectional antenna is designed to operate over the same band (1.25-2.4 GHz) with an average gain of 3.5 dBi along X-direction. The dimensions of the omnidirectional antenna are (in *mm*): R=33, W=45, L=85, w_f =3, w_l=9, g_l=15, g_w=21, gs_l=3, gs_w=6.

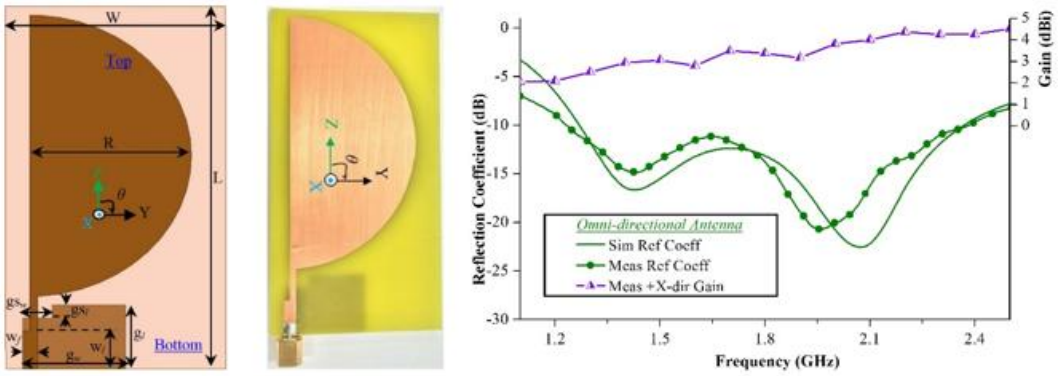

(a) (b) (c)

Fig. 3.18 (a) Schematic diagram of the omnidirectional antenna. (b) Photograph (top view) of the fabricated prototype of the omni-directional antenna. (c) The reflection coefficient and boresight gain performance of the antenna over the operating bandwidth.

3.4 Three-dimensional Folded Antenna with Directional Radiation

This section presents a novel design of low-profile UWB antenna which has a compact and rigid structure and provides unidirectional radiation patterns. The antenna uses a three-dimensional structure that is folded and properly shaped to achieve the required performance. The proposed design is validated by simulations and measurements.

3.4.1 Antenna Configuration

A diagram of the final design of the proposed antenna is shown in Fig. 3.19 with detailed dimensions listed in Table 3-III. The antenna is primarily printed on two parallel slabs of GIL GML 1032 substrate (dielectric constant ε_r=3.2, thickness h_s=1.52 mm). The proposed antenna is evolved from a folded dipole antenna, with a simplified feeding technique. The top slab consists of two layers of copper strips. The layout of the first layer is shown in Fig. 3.19(b). This is mainly a bowtie shaped flare, which is connected to an l_f long microstrip feeding line. The width w_f of the feeding strip corresponds to 50 Ω impedance. The strip is finally soldered with a 50 Ω Sub-Miniature-A (SMA) connector to excite the antenna using an external transmission system.

As shown in Fig. 3.19(c), the second layer of the top slab is basically the reflected version of the first layer without the feeding strip. The second layer backs up the feeding strip and acts as a ground for it. A distance of *g/2* is maintained from the Y-axis line for both layers. Thus, a total horizontal distance of *g* is set between the two bowtie like flares.

The bowtie shapes are constructed by etching triangular flares with width *b*, concentric along the X-axis. This cutting creates an angle of approximately 150° at the center for each bowtie layers. Two

open circular shaped slots with radius *R*, reinforced with an additional semi-circular slot of radius *r* are inserted in both layers. The slots are at *t* distance from one another. Two circular segments of radius r_s are incorporated from the side of each bowtie to increase the effective edge length of the flare.

The bottom substrate block consists of only a rectangular copper layer with length and width of *L* and *w*, respectively. The two opposite sides along the X-axis of the bottom layer are connected with the first and second layer of the top slab with the help of two 0.3 *mm* thick copper plates. The bottom block mainly provides wideband impedance matching with the very low antenna profile and directs the radiation towards the Z-direction. The overall dimension of the fabricated antenna is 70 *mm* × 60 *mm* × 15 *mm*.

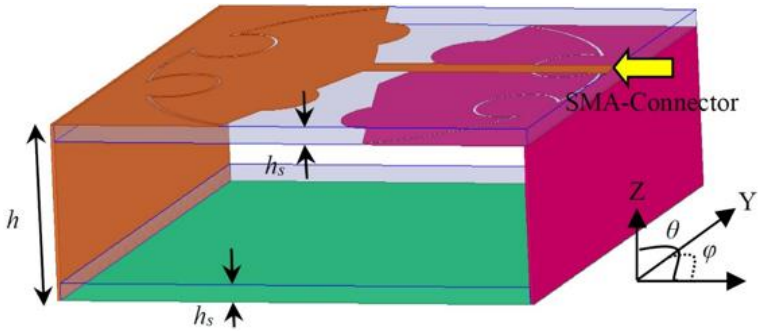

(a)

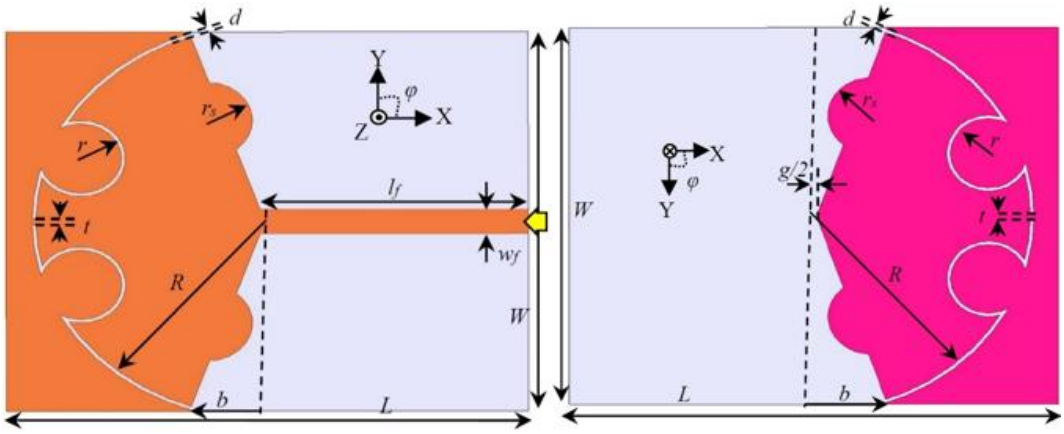

(b) (c)

Fig. 3.19 Schematic diagrams of the final design, (a) whole antenna, (b) top view of the first layer, and (c) view of the second layer from bottom side.

3.4.2 Design Strategy and Operation

3.4.2.1 Design Process

The design strategy of the proposed antenna is exhibited in Fig. 3.20. The commercial electromagnetic solver ANSOFT HFSS, which uses a finite element based method, is used for the

simulation purpose. Initially, Antenna A which is basically a slot loaded three dimensional (3D) folded dipole antenna, is chosen to start the designing process. Fig. 3.20(a) shows the schematic diagram of Antenna A printed on GML1032 substrate. The elements are of length L=70 *mm* with a gap of (g) for connecting the excitation source. The distance between the elements is h=15 *mm*; thus, the air-gap between the substrates is h_f=11.96 *mm*, whereas the width of the elements is W. It is well known that widths of elements of a folded dipole antenna influence the antenna impedance and increasing the width decreases the impedance. Thus, it is easier to match the antenna with low reference impedance. Nevertheless, increasing the width also increases the front to back ratio of the antenna along Z-direction. It is found in extended simulations that when W=60 *mm*, the front to back ratio reaches the saturation. Hence, despite the fact that the resonant frequency goes down while increasing W, considering the front to back ratio of the initial design, width, W=60 *mm* was taken as the optimized one.

Table 3-III: Values of geometric parameters of the proposed antenna

Parameters	***L***	***W***	***h***	h_s
Values (mm)	*70*	*60*	*15*	*1.52*
Parameters	***r***	r_s	***d***	***t***
Values (mm)	*6*	*6.5*	*0.5*	*1*
Parameters	***g***	***b***	l_f	w_f
Values (mm)	*1*	*10*	*35.5*	*3.8*

Four open-ended slots are added at distance l=30 *mm* from the center along the X-axis. As depicted in Fig. 3.20, the slots are d=1 *mm* wide and are separated by t=1 *mm* from each other along the Y-axis. Fig. 3.21 shows the impedance matching of the antenna when it is fed by the standard port impedance of 50 Ω. It is seen that a resonance evokes around 2.35 GHz due to the implementation of the slots. Dragging the slots to further distance than l=30 *mm* affects the impedance matching. Thus, this is taken as the optimized distance. However, the effects of slot lengths on the resonating frequencies are discussed later in details.

The bowtie-shaped dipoles typically give flatter impedance matching than the rectangular ones. Hence four flares of width b at the end are etched from the top element which constructs the shape of the antenna as bowtie (antenna B). The flare width is varied to examine the impedance matching (not

shown here). It was seen that the resonances tends go to lower values. However, some other resonances with good impedance matching appear as a result of this modification.

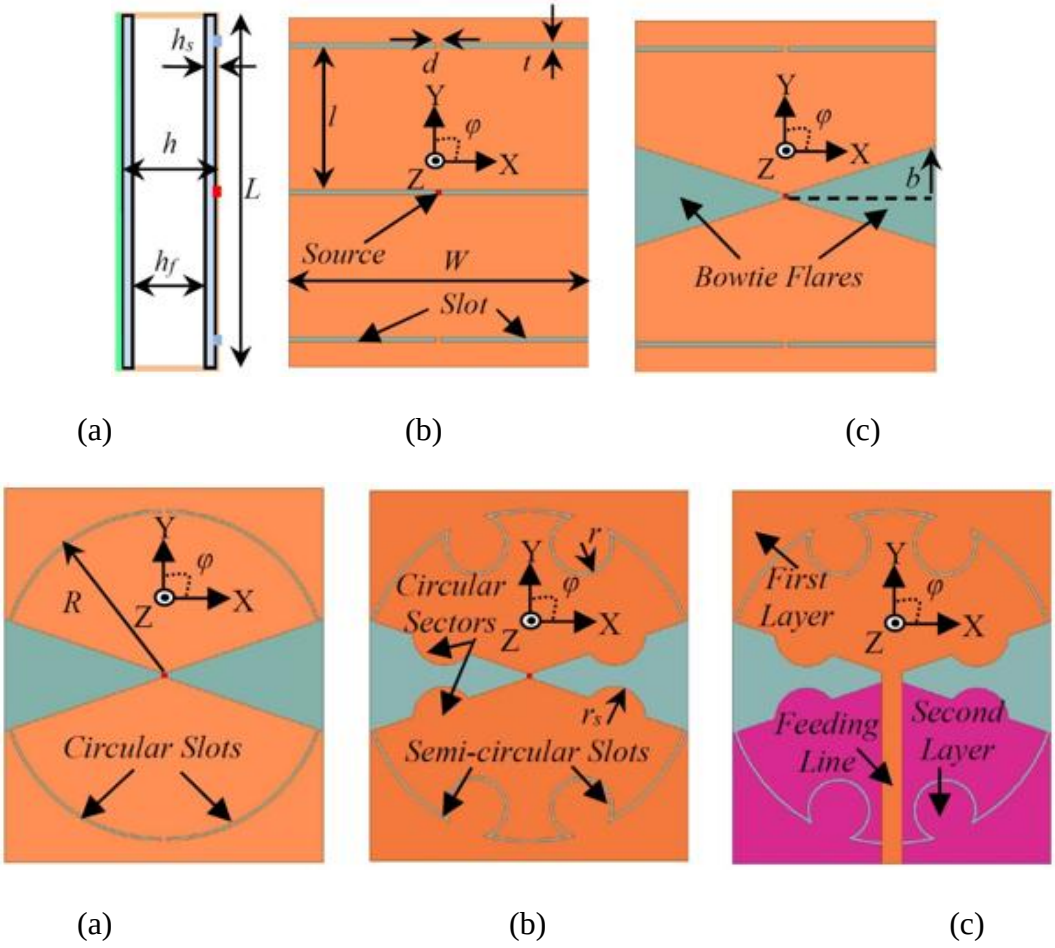

Fig. 3.20 Adopted design strategy and the geometrical diagrams of: side view of (a) antenna A, and top view of (b) antenna A, (c) antenna B, (d) antenna C, (e) antenna D, (f) final antenna design.

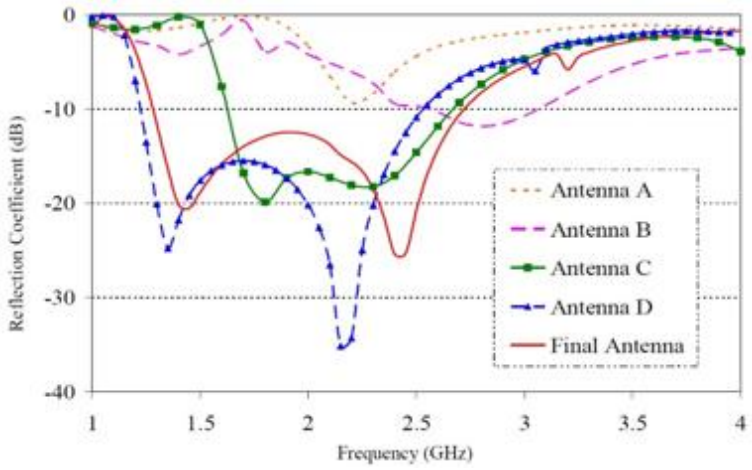

Fig. 3.21 Performances of various antennas

The slots have the most significant effect on the impedance matching of the antenna. In the next stage, antenna C was constructed by employing four circular slots instead of straight slots keeping the lower end fixed at the X-axis. The antenna achieves a fractional impedance bandwidth of 49.3% (1.62-2.68 GHz) with two vivid resonances. With circular-shaped slots, their actual length as well as the currents along their edges become longer [111]. Consequently, the resonant frequencies owing to the slot currents go down to lower values. Simultaneously, the ripples in the resistive part of the input impedance are reduced and become stable at around 50 Ω. Thus, a wide bandwidth is achieved. The effects of the radius of the slots are discussed in the parametric section.

It is seen through parametric studies that the slot lengths and the outer edges of the bowtie flares have influences on the resonating frequencies. In antenna D, an extra semi-circular slot was added to each circular slot to increase the length. It is observed that this change helps the first resonance of the antenna to go to lower values and did not alter the second resonating frequency. Moreover, two circular sectors of radius r_s are added on each bowtie flare to increase the length of edge currents flown through the flare edges. It is also possible to increase this length by etching some portion along the tilted flare-line; but this type of cutting alters the currents of the whole flare. It is noted that the highest resonance dramatically decreases with the increase in r_s. After optimization, antenna D accomplishes a wide bandwidth of 67.7% (1.27-2.57 GHz).

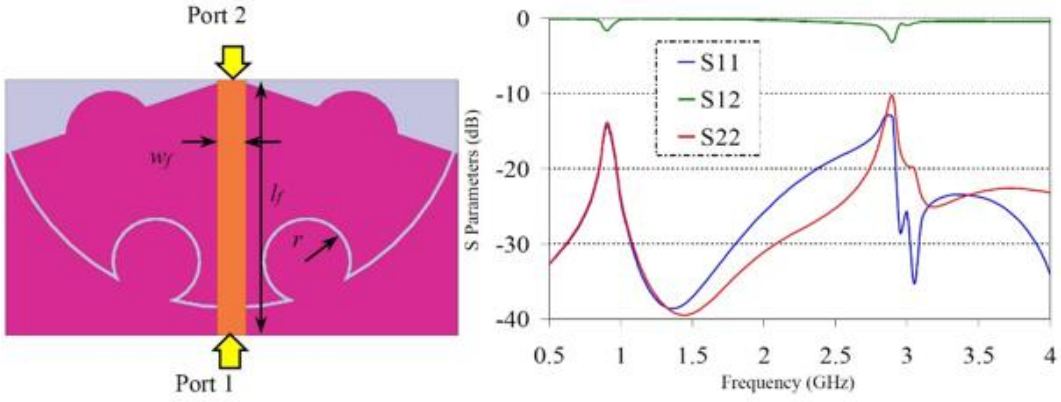

(a) (b)

Fig. 3.22 (a) Diagram of the feeding network separated for analysis. (b) Impedance characteristics of the feeding transmission line over one half of the flare.

Antenna D is developed from a 3D folded dipole and remains as a slotted modified version of this kind. Traditionally, coaxial cables are mainly used to feed the center of the dipoles. But, this is not a suitable option for this antenna due to the concern of embedding with compact devices. It is important

to understand that the symmetry of electrical currents also induces the symmetry in the electromagnetic field. Since the antenna D is symmetrical the generated field along the centerline of the Y-axis becomes null and insertion of a feeding transformer negligibly disturbs the surface currents or radiation patterns [112]. However, it is a complicated task to design proper feeding transformer and fit that in such a low profile. For these reasons, the antenna is fed using a simple 50 Ω transmission line. As shown in Fig. 3.22, the final structure is designed by lowering one half of the bowtie flare to the opposite side of the substrate slab so that it can support the feeding line. A simplified version of this feeding can be found in [113].

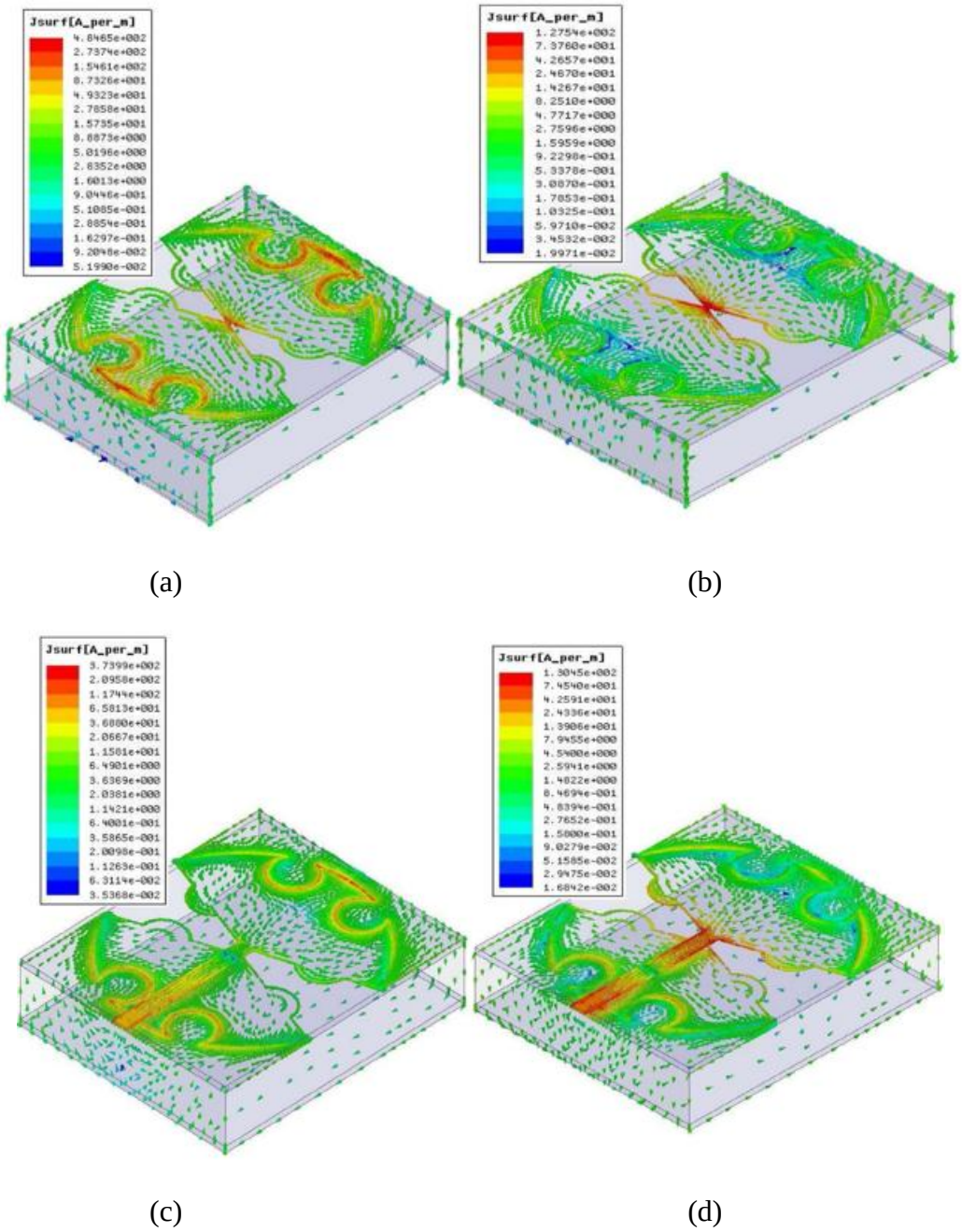

(a) (b)

(c) (d)

Fig. 3.23 Vector current distributions of antenna D at the first two resonant frequencies (a) 1.35 and (b) 2.20 GHz and final design at the first two resonances (c) 1.45 GHz and (d) 2.45 GHz.

The extended transmission line over the other half flare is also analyzed as depicted in Fig. 3.23(a). Two ports are used to see the transmission characteristics. Although the slots are narrowly distant from each other (t=1 *mm*), S_{12} is found to be less than -1 *dB* over the proposed band of operation as shown in Fig. 3.23(b). Hence, the line can transfer signal efficiently with low insertion loss. However, the position and magnitude of the two resonances that are created in the S_{12} curve by the feeding line can be controlled by adjusting the slot width, t and distance, d for the intended band of operation.

The effects of this feeding structure can be examined by comparing the impedance matching of antenna D to the final design from Fig. 3.22. When the extended line is incorporated with the antenna increases the inductive value (not shown here) of the antenna and thus, the reflection coefficient of the final design increases slightly. The high frequencies become more affected by this feeding strip. However, the shift in resonating frequencies can be attributed to the reduction in the electrical length of the antenna, as the bottom flare is less distant from the reflector in this orientation.

3.4.2.2 Current Distribution and Radiation of the antenna

In order to gain further understanding of the way resonances are excited and the radiation mechanism, the vector surface current distributions of the proposed antenna are extracted for realization. Antenna D and the final design are compared to understand the effect of the feeding line. Fig. 3.23 demonstrates the current distributions of these two antennas at respective upper and lower resonating frequencies. Making the top element of the antenna from one layer (antenna D) to two layers (final antenna design) and inserting the feeding line does not change the currents at individual resonances. As similar current distributions are observed on both antennas at the resonating frequencies, we can conclude that the working principle of these two antennas is the same.

From Fig. 3.23, it is observed that most of the currents are concentrated on the top element. Thus, the top element is the main source of antenna radiation. The currents are in resemblance along the center line of the X axis. For the first resonating frequency (1.35 GHz for antenna D and 1.45 GHz for the final design), strong current vectors are seen to circulate around the slot. The slots provide the necessary capacitances to simultaneously increase the path for the edge currents which eventually increases the inductive value. Thus, the slots attempt to neutralize the reactive portion of the input impedance. The bowtie shape provides a flatter impedance matching for the antennas. The feeding point and the tilted edges carry significant amount of currents over the whole bandwidth; nevertheless in the case of the second resonance (2.2 GHz for antenna D and 2.45 GHz for the final design), it is a vital section for radiation. In fact, this resonance can be controlled by the length of the flare edges.

The current distributions of the bottom element have a significant effect on the radiation mechanism of the proposed antenna. It is noted that on the top and bottom elements, most of the currents flow in

the opposite directions to each other. At the lower resonance (1.45 GHz), the currents at the opposite edges of the proposed antenna completely become out of phase which creates a rectangular loop of currents along the top and bottom of the substrates. Even though the phases are opposite, the magnitude of currents on the top radiator is slightly higher than the lower element. As a result, all the fields created by the top radiator toward the backward direction could not be neutralized by the bottom element. Still, these contrary currents promise high front to back ratio around this resonance. In case of the upper resonance (2.45 GHz), the direction of currents reverses except the middle portion of bowtie flare. Here, the currents on the flare edges flow in the same direction as the lower element. Thus the fields generated by this portion of top element are not effectively opposed by those of bottom element. Hence moderate front to back ratio can be predicted, creating quasi-directional radiation patterns around the second resonant frequency. Thus, the bottom conductor is seen to support the impedance matching and the directionality of radiation.

3.4.2.3 Parametric Analysis

A parametric analysis was carried out to elaborate the design and optimization process as well as the operation of the proposed antenna. For better convenience of the effect of the antenna performance upon changing the parameters, only one parameter was changed at a time, keeping others unchanged at the optimized value. The summary of the studies is mentioned in Table 3-VI.

The length *L* and width *W* of the antenna defines the operating frequencies of the antenna. Increasing the length and width eventually increases the current paths and thus helps the antenna to resonate at lower frequencies. However, increasing the width, *W* of the antenna improves the overall reflection coefficient and consequently the bandwidth, while raising the value of antenna length *L* deteriorates the impedance matching, causing the bandwidth to become narrower. In extensive simulations (not shown here), it is found that changing the antenna's height *h* has only a slight effect on its resonant frequency. It is noted that with the increase in *h*, the gain of the antenna in the Z-direction decreases slightly. However, the front-to-back ratio changes negligibly with *h*.

In extended investigation, we found that as long as $h_f >> 2h_s$, the substrate's thickness does not have significant impact on the design of the antenna as the effective dielectric constant of the structure will be close to that of free-space. The effective dielectric constant ε_{eff} can be roughly calculated using the following formula which is derived from the quasi-static model of the effective capacitance of the structure.

$$\varepsilon_{eff} = \frac{\varepsilon_r (h_f + 2h_s)}{\varepsilon_r h_f + 2h_s} \tag{3.3}$$

Table 3-IV: Summary of the parametric studies when varying geometric values

Param. (*mm*)	**Variation**	**First Resonance**		**Second Resonance**		**Overall BW**
		f_{c1}	$\|RC\|$	f_{c2}	$\|RC\|$	
L=70	>	▼	▲	▼	▼	▼
	<	▲	▲	▲	▼	▲
W=60	>	▼	▲	▼	▼	▲
	<	▲	~	▲	▼	▼
d=0.5	>	▲	~	▼	▼	▼
	<	▼	▲	▲	▼	▲
t=1	>	▲	▼	-	~	▼
	<	▼	▼	-	~	▼
R=30	>	▼	▼	-	▼	▼
	<	▲	▼	-	▼	▼
r=6	>	▼	▼	-	▲	▼
	<	▲	▼	-	▼	▼
b=10	>	▲	▼	▼	▲	▼
	<	~	~	▲	~	▼
r_s=6.5	>	-	▲	▼	▼	▼
	<	-	▼	▲	▼	▼

* '-' states the independent phenomenon upon the variation of a parameter; '~' represents the non-monotonic fluctuation of the criteria when varying the geometry; '▲' and '▼' represent the enhanced and deteriorated phenomenon of the antenna upon changing parameter-values, the first and second resonating frequencies are expressed as 'f_{c1}' and 'f_{c2}' respectively, $|RC|$ represents the absolute value of the reflection coefficients at the resonances.

In our investigations, it is found that ε_{eff} for the current final design is 1.2, which is close to the value (1.16) that can be obtained from (3.3). The effective dielectric constant calculated from (3.3) can be used to estimate the required overall dimensions of the antenna. As a general guideline, the area of

the elements of the antenna remains near ($\lambda_{eff}/3$) × ($\lambda_{eff}/4$) where λ_{eff} is the effective wavelength at the lowest resonant frequency calculated from $^{a}{}_{eff}\ Z\ c/(f\sqrt{£_{eff}})$, where c is speed of the field in free-space.

The circular slot creates appropriate current paths and supplies necessary capacitances for impedance matching of the antenna. Hence the increasing thickness of the circular slot, *d* affects both the resonances and the overall bandwidth and it is possible to increase the bandwidth by decreasing its value. However, the distance between two circular slots, t only has effects on the first resonance. Increasing the distance, *t* decreases the overall slot length. As the first resonance is mostly dependent on the length of this slot the resonating frequency increases with the increase of *t*. For the same reason, the increasing the radius of the circular slot, *R* and semi-circular slot, *r* decreases the first resonating frequency. But the fluctuation of *t*, *R* or *r* does not have any effect on the second resonance. This behaviour exhibits the independence of the second resonance and evokes the possibility to enhance the overall bandwidth by suitably adjusting the resonances.

The bowtie flare is an important factor to correct the second resonance. It is seen that the flare width, *b* slightly effects the first resonance, but has a prominent effect on second one. Also the radius of the circular segment, r_s increases the edge length of the flare and thus is able to reduce the second resonance. However, in this case careful measures should be taken to improve the impedance matching.

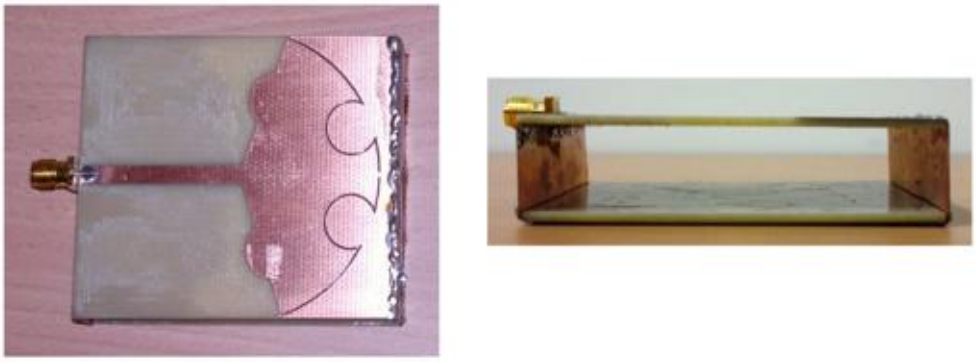

(a) (b)

Fig. 3.24 Photographs of the fabricated prototype: (a) Top view, and (b) side view

3.4.3 Experimental Results

A prototype of the proposed modified folded antenna is fabricated (shown in Fig. 3.24) and the performances are examined for verification. Fig. 3.25(a) shows the simulated and measured reflection coefficient of the antenna. A good agreement is observed between them. The antenna provides 77% fractional bandwidth centered at 2 GHz. The measured and simulated gain of the antenna along the

Z-axis (φ=0° and θ=0°) are exhibited in Fig. 3.25(b). An average gain of 5.2 dBi is found over the operating band. The deviation of the measured gain from the simulated one is mainly induced by the long coaxial cable which is used to feed the prototyped antenna.

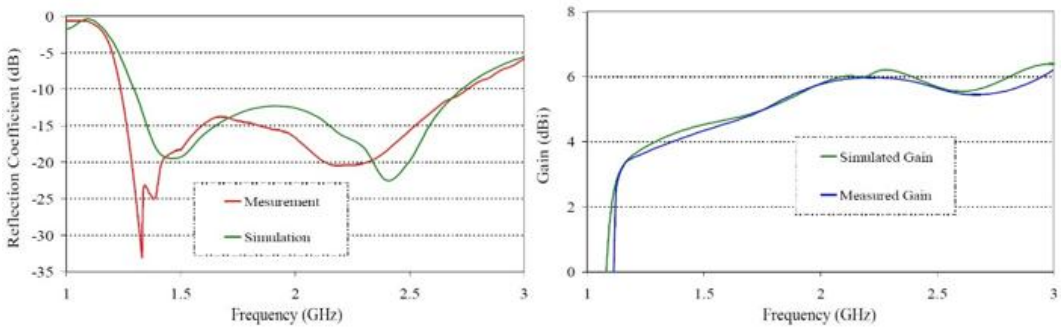

(a) (b)

Fig. 3.25 Comparison between the measured and simulated results of the prototype: (a) reflection coefficient, and (b) gain towards Z-direction.

The radiation pattern of the antenna is measured in an anechoic chamber to analyze its unidirectionality. The simulated and measured E-(XZ) and H-(YZ) plane radiation patterns of the antenna at frequencies of 1.3, 1.6, 1.9, 2.2 and 2.5 GHz are illustrated in Fig. 3.26. The maximum radiation points are around the Z-axis line which proves the antenna's unidirectional characteristics. A low cross polarization level of around -20 dB is achieved along the boresight direction in both the E- and H- planes. The main radiation of the antenna is located at the top element. The shorting walls connecting the top and bottom elements block most of the side radiation along the E-(XZ) plane [114]. On the other hand, there is no copper wall to block the side radiations along the H-(YZ) plane. Hence, the H-(YZ) plane patterns show broader beamwidths and the antenna radiates more along the sides in the H-(YZ) plane than the E-(XZ) plane.

Fig. 3.27 shows the simulated and measured front to back ratio of the prototyped antenna. The measured ratio fluctuates around 15 dB up to 2 GHz, after which the curve tends to decrease. At the end of the operating band, the front to back ratio becomes around 7 dB. As described in the current distribution section, this moderate front to back ratio is expected to be due to the current formation of the top and bottom element.

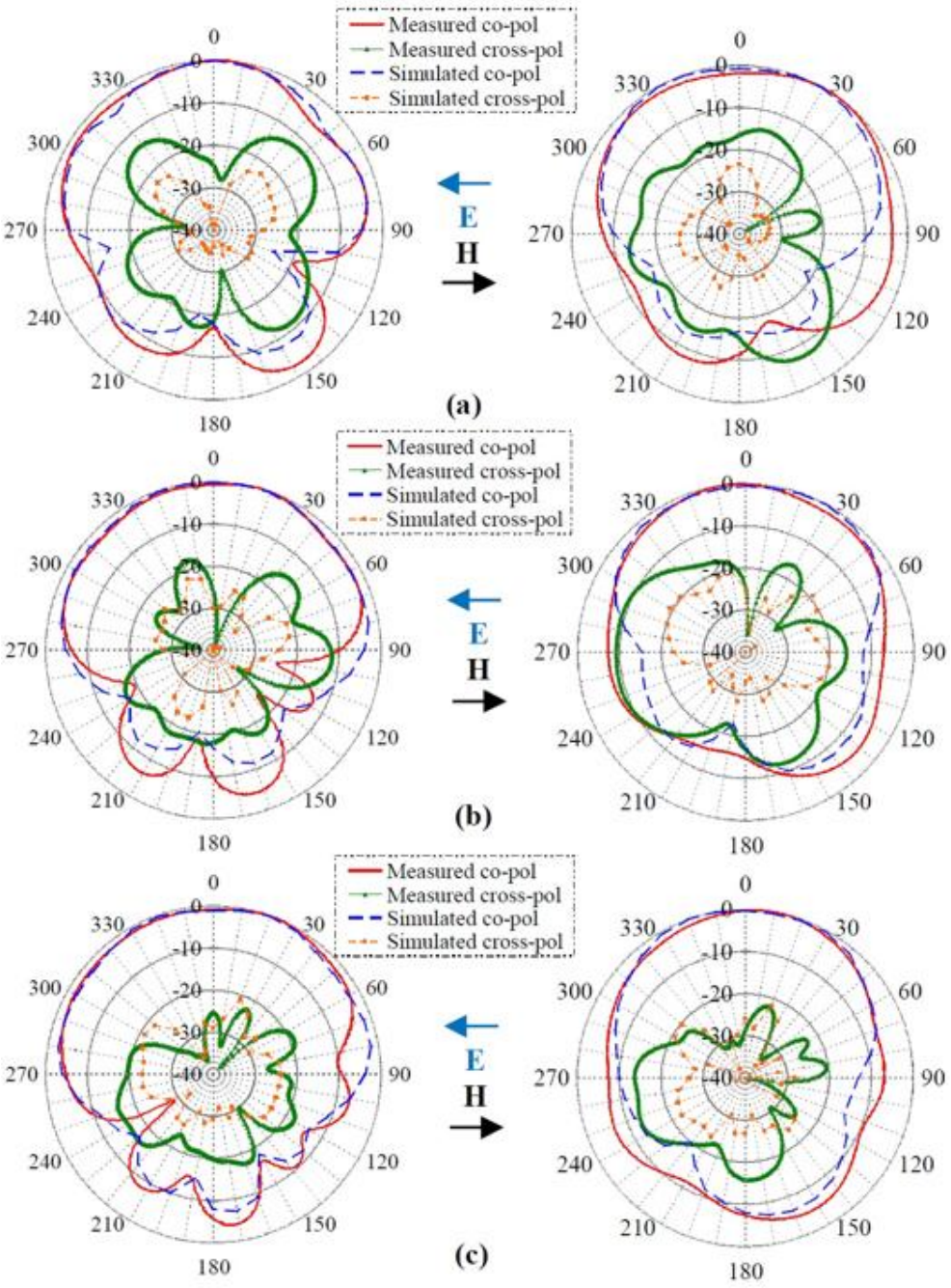

Fig. 3.26 Simulated and measured radiation patterns in both E-(XZ) and H-(YZ) planes at different frequencies: (a) 1.3 GHz, (b) 1.9 GHz, and (c) 2.5 GHz.

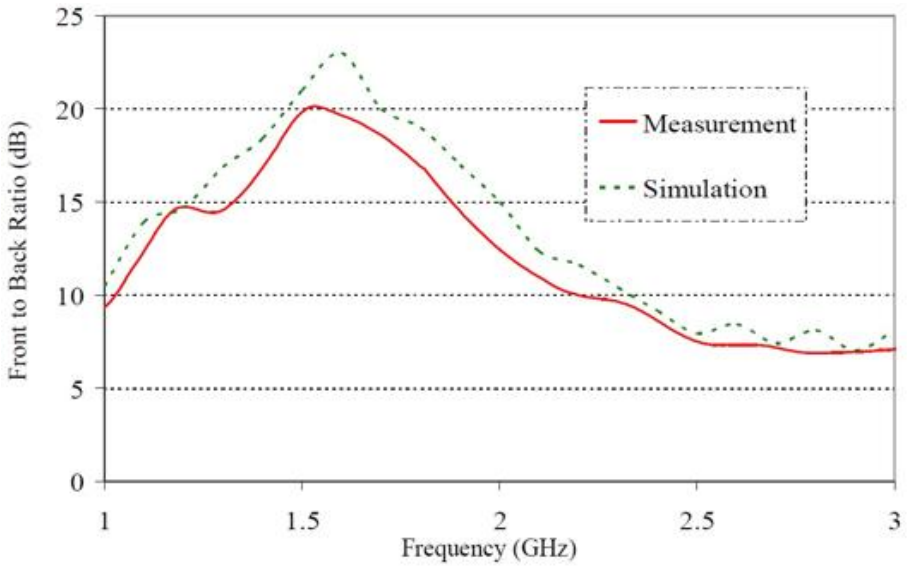

Fig. 3.27 Measured front to back ratio of the proposed antenna along Z-axis.

3.4.4 Comparison

The dimensions and performance of the antenna are compared with some recent compact wideband directional antennas in the literature as shown in Table 3-V. The proposed antenna is around 50% smaller in volume than the antenna of [115]. Moreover, to the contrary of the proposed antenna, a large reflector of more than one wavelength side length is needed in [115], which has seen to have significant effect on the impedance matching and unidirectionality of the antennas as used also in [116]. These types of antennas are not suitable for compact system applications. The antennas reported in [117, 118] can support ultra-wideband service without the help of a reflector behind it. But compared to the proposed antenna, they have a high profile and a volume that is five times the volume of the proposed antenna.

It is to be noted from Table 3-V that the bandwidths of the antennas presented in [117, 118], and are calculated assuming a high reference value for the reflection coefficient. If -10 dB of reflection coefficient is taken as the reference, both antennas of [117, 118] exhibit multi-band characteristics, providing 84.9% (2.1-5.2 GHz) and 14.6% (1.08-1.25 GHz) fractional bandwidths, respectively, at the lowest operating band. Moreover, high input port impedances, namely 150 Ω and 100 Ω are chosen to match those antennas. Feed baluns are designed to connect them with 50 Ω transmission networks, which increase antenna design complexity. On the other hand, the proposed antenna in this work is matched to 50 Ω and takes the advantage that it can be directly connected with the transceiver. Concerning the radiation characteristics of the antennas, the proposed antenna has the most stable boresight radiation as depicted in Table 3-V.

Table 3-V: Comparison of proposed antenna with some recent wideband antennas with unidirectional radiation patterns

Comparing Parameters	**[115]**	**[117]**	**[118]**	**This work**
Length (λ_{eff})	*0.66*	*0.46*	*0.57*	*0.33*
Width (λ_{eff})	*0.17*	*0.43*	*0.29*	*0.25*
Height (λ_{eff})	*0.08*	*0.19*	*0.19*	*0.07*
Overall Volume (λ_{eff}^3)	*0.009*	*0.038*	*0.031*	*0.006*
Separate Reflector used?	*Yes,* $1.1\ \lambda_{eff} \times 1.1\ \lambda_{eff}$	*No*	*No*	*No*
Return loss reference value (dB)	*9.5*	*7*	*7.4*	*10*
Fractional Bandwidth (%)	*83*	*153*	*128*	*77*
Gain Variation (dBi)	*Min: 2.5* *Max: 8*	*Min: 5* *Max: 8*	*Min: 5* *Max: 11*	*Min: 3* *Max: 6.2*
Comments on radiating beams	*Main beam in E-plane is at 45°*	*Main Beam squints at 7 GHz*	*Side lobes appear at high frequency*	*Stable Boresight at 0° with wide beamwidth*

* $\boldsymbol{\lambda_{eff}}$ is the effective wavelength of the corresponding lowest resonating frequency of the antenna

A three-dimensional folded antenna has been proposed. The antenna consists mainly of two bowtie-shaped slabs of printed substrates having copper walls connecting them to the ground bottom element. Semicircular slots are created at those slabs to achieve lower cutoff frequencies without increasing the size. The bottom element works mainly to support the impedance matching and reflects most of the radiations. The working mechanism and the optimization process of the antenna have been described in details. The designed antenna is prototyped and examined. The antenna provides 77% fractional impedance bandwidth centered at 2 GHz. The radiation patterns of the antenna in the E-

and H-planes show an average of 15 dB front-to-back ratio and -20 dB cross polarization over most of the operating band. Finally, the compactness of the antenna is compared with recent literature of unidirectional UWB antennas; it turns out that the antenna has the lowest volume and most stable radiation pattern, which makes it a strong candidate for compact applications that need directional and low-profile antenna operating at the low microwave bands.

3.5 Miniaturization of Directional Folded Dipole Antenna Using Plane of Symmetry

This section reports the development of a compact and low profile antenna by utilizing the idea of plane of symmetry on the original antenna (OA) reported in Section 3.4. Alike OA, the proposed antenna (PA) operates over a wide bandwidth with directional radiation patterns. The PA minimizes the space requirement to about 50% of the OA and permits twice the number of array-elements. The near and far-field radiation characteristics and radiation safety are also investigated to verify the suitability of the antenna in the head imaging application.

3.5.1 Antenna Geometry and Design Considerations

The OA describes a symmetrical modified folded structure that uses closed loop currents to achieve directive radiation over a wide bandwidth (Fig. 3.28(a)). Image theory of electromagnetics suggests that a magnetic symmetry line exists between two identical electric fields with a 0° polarity difference relative to each other, while identical magnitude of currents exists on the either sides of the line [117]. Observing this criterion for the currents flowing on the antenna along Y-direction (Fig. 3.28(a)), the plane of electrical symmetry, which divides the antenna into two identical halves, can be identified. Fig. 3.28 also demonstrates the transformation process and the geometry of the proposed antenna. Theoretically, cutting the original antenna into halves comprises a dominating current path and similar resonances can be achieved. However, this procedure also creates an open circuit condition that results in impedance mismatch. Hence, the half antenna (HA) leads to a dual band antenna (Fig. 3.29). Thus, some measures are taken to improve the impedance matching. The radius of circular slot, r_s is increased to 8 *mm* to decrease second resonance and improve the reflection coefficient. Similarly, the gap of semi-circular slot, d_2 is decreased to improve the matching of the first resonance. The feeding strip is moved accordingly to be inside the PA. The antenna is simulated using both HFSS and CST. The PA is designed on the same substrates as the OA with dimensions (in *mm*): L = 70, W = 30.5, h = 15, h_s = 1.5, d_1 = 0.5, d_2 = 0.3, w_f = 3.8, r = 6, l = 21, l_f = 35.5, f_w = 3.2.

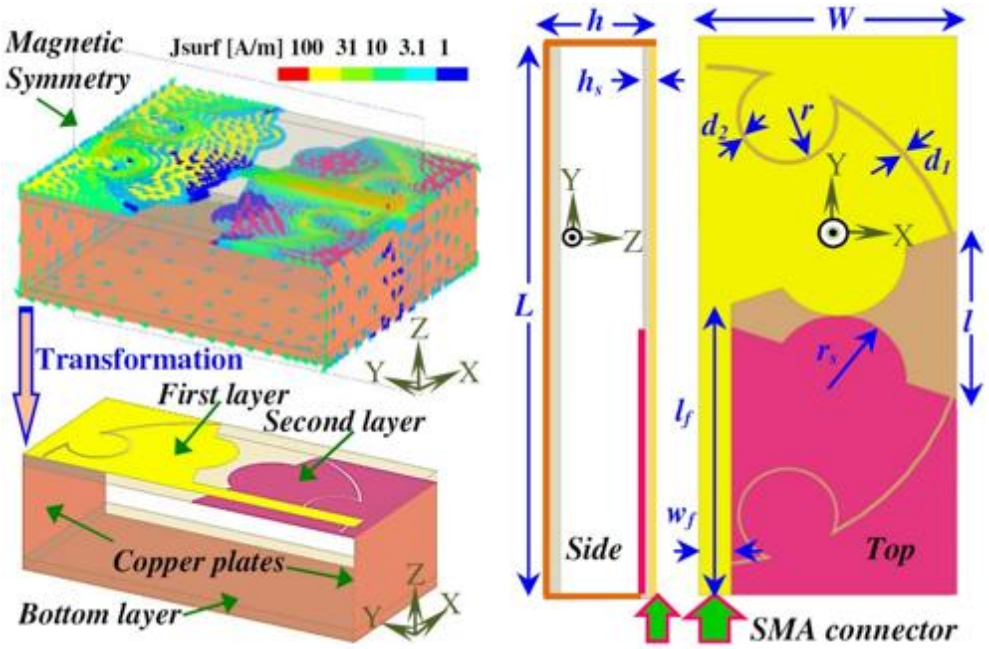

(a) (b)

Fig. 3.28 (a) Transformation process from the OA to PA (not to scale). (b) Schematic diagrams of the proposed antenna (not to scale)

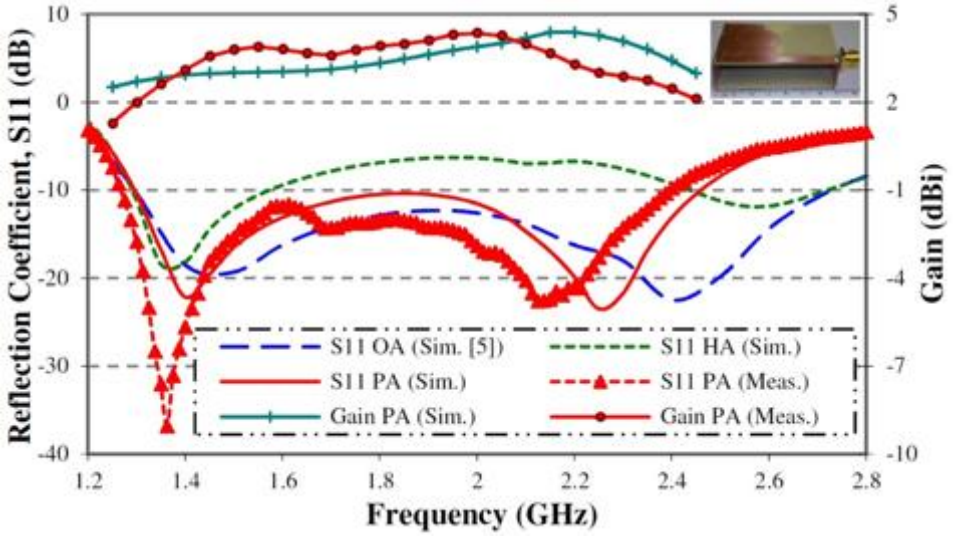

Fig. 3.29 Reflection coefficients of the OA, HA and PA, and the gain characteristics of the PA with a photograph of the prototype at inset.

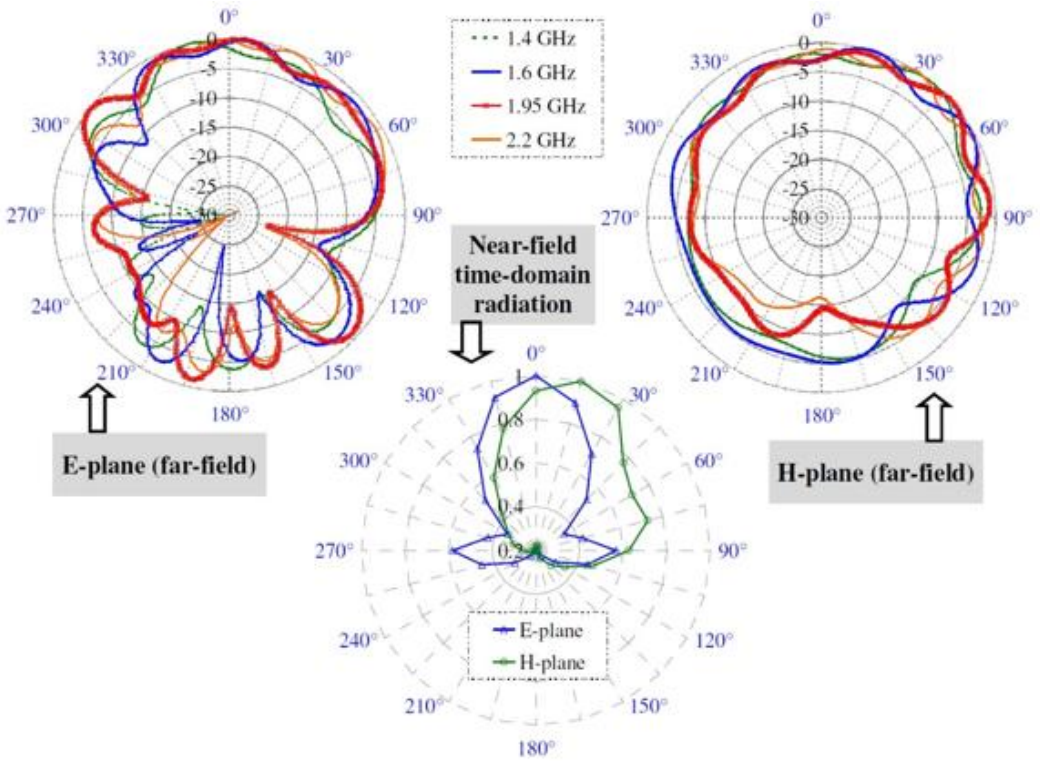

Fig. 3.30 Far and near-field radiation patterns of the antenna.

3.5.2 Results and Discussions

The proposed antenna is fabricated (Fig. 3.29) for verification. The reflection coefficient of the antenna presented in Fig. 3.29 indicates that the prototyped antenna covers the band from 1.25 GHz to 2.4 GHz, which is equivalent to 63% fractional bandwidth. It is noted that the PA does not compromise the penetration capacity of the OA which is related to the lowest operating frequency [20]. The radiation characteristics of the prototype are also examined. The prototype provides an average gain of 3.5 dBi along the main beam direction (Fig. 3.29). The E (-YZ) and H (-XZ) plane radiation patterns at 1.4, 1.6, 1.95 and 2.2 GHz are also measured and presented in Fig. 3.30. The prototype provides steady directional radiation patterns in E-plane. In H-plane the main beam is slightly tilted (~10˚) due to the asymmetrical structure of the antenna. However, as H-plane patterns have wide half power beamwidths (HPB), the asymmetry can be neglected. About 10 dB front to back (F/B) ratio is achieved along Z-direction at the high end of the band; while F/B ratio reduces in the lower end as the antenna is electrically small compared to the operating frequencies. High level of polarization purity (> 10 dB) is observed in the measurement.

To verify the performance of the antenna and related safety issues when operating in a stroke detection system, the antenna in CST Microwave Studio simulator 5 *mm* in front of an in-house built MRI-based realistic three-dimensional human head phantom with frequency dispersive electrical properties [41]. For the PA, as the maximum linear dimension, L < 0.32 λ_m, where λ_m is the operating wavelength

in the medium, by definition, the near field region extends up to 1.6 λ_m. Considering the average permittivity of the head as 35, the near field region inside the head extends from 33 *mm* (2.4 GHz) to 64 *mm* (1.25 GHz). Hence, in the stroke detection system, the antenna works both in near and far field regions. To characterize near-field in free space, time-domain co-polarized electric-field (E_y) probes are placed around the antenna at 20 *mm* distance from the surface. The presented results (Fig 3.30) demonstrate directional radiation along Z-direction. The HPB in E and H-planes are around 70˚ and 100˚ respectively. Moreover, a high F/B ratio of 5.2:1 is attained along Z-direction in both planes, which is comparatively high in near-field region for such a compact antenna [119].

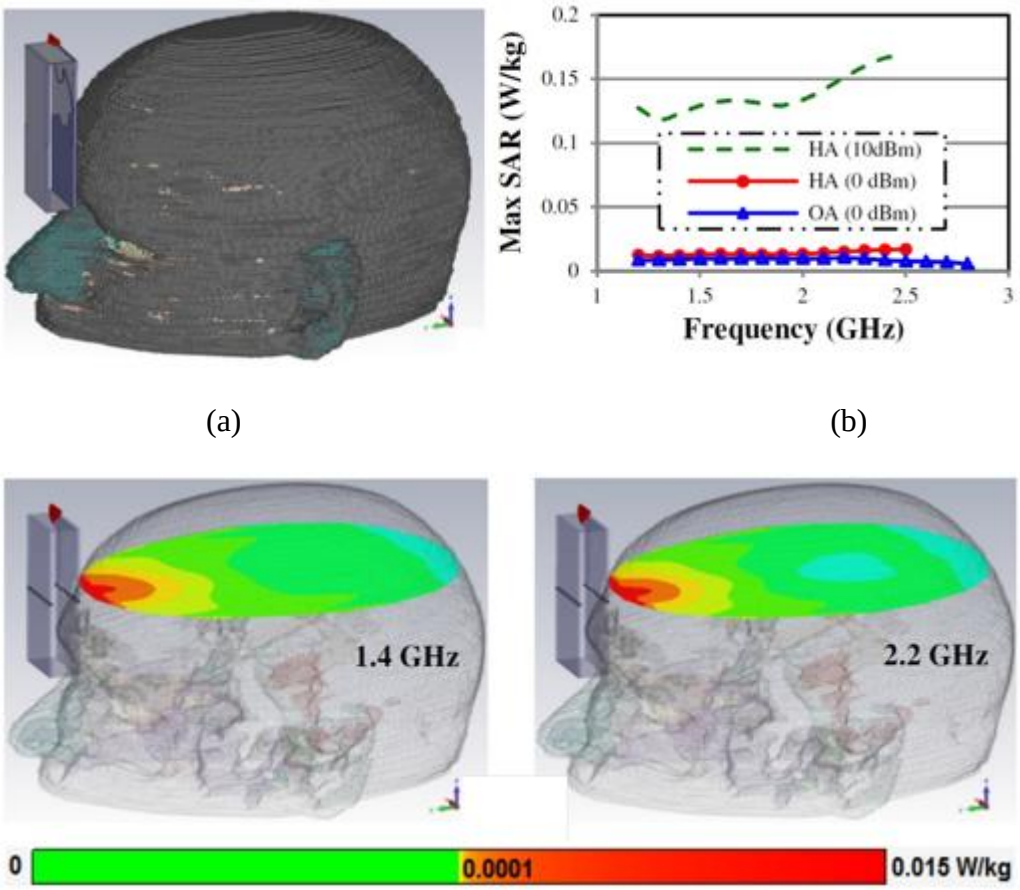

Fig. 3.31 SAR analysis of the proposed antenna: (a) Investigation model and maximum SAR for different power levels. (b) SAR distribution of XY-plane cut at different frequencies for 0dBm.

It is noted that the reduction of antenna aperture increases the transmitted power density. As, typically, the operational power is 0 dBm or 1 mW, the transmitted power density of the proposed antenna having 7 × 3 cm^2 aperture, increases to 0.05 mW/cm^2, which is still 20 times below the recommended safety limit of 1 mW/cm^2 [120]. The induced SAR of the antenna is also investigated to assure operational safety. Fig. 3.31(a) exhibits that the SAR of the proposed antenna is significantly less than the IEEE safety barrier [120]. Assessing SAR level, it can be concluded that it is possible to

increase the power level to 10 dBm in order to increase the signal to noise ratio (SNR) and receive stronger signals from the diagnosed head. Fig. 3.31(b) demonstrates that, at this power level, the maximum SAR stays below the approved limit and mainly situated at the exterior layers of the head.

A compact, wideband and directive antenna is presented for stroke diagnostic system by using the magnetic plane of symmetry obtained from the image theory of electromagnetics. The antenna attains 63% fractional bandwidth with 3.5 dBi average gain along the direction of radiation. It provides directional radiation in both near and far fields and meets the safety requirements for the application. The proposed antenna miniaturizes the space requirements to half allowing twice the number of antenna-elements surrounding the head which consequently results in improved image reconstruction ensuring early brain stroke detection.

3.6 Near-field Time-domain Characterization of Wideband Antennas and Performance Comparison

The efficacy of microwave near-field diagnostic systems essentially depends on the sensitivity and efficiency of the transmitted and received pulses. Different types of wideband antennas are proposed for those systems, which are being investigated for medical applications. To test the performance of those antennas, in most cases, only frequency domain characterization is performed, while the time-domain performances, especially in the near-field, are rarely mentioned [35, 58, 121]. Thus, it is hard to decide the most suitable antenna for time-domain based processing algorithms.

System fidelity factor (SFF), which suggests the level of transient distortion, is previously reported as a comparing tool of wideband antennas [122]. However, SFF ignores the pulse amplitude and only relies on the spatial characteristics and conveys signal correlations in different directions. Effective wideband systems require antennas that radiate short pulses with low distortion and high magnitudes, which consequently result in less distorted received pulses with higher amplitudes. Therefore, the utilization of the maximum magnitude of the transient response's envelope of the antenna to represent its time-domain radiation capability provides limited insight [123]. On the other hand, normalizing the peak responses individually cease the opportunity of relative studies between different antennas [124].

In this section, a pulse merit factor is proposed by generalizing a combined matrix in a comparable manner for antennas under consideration. The merit factor consists of near-field time-domain signal amplitude and fidelity factor, both normalized to the highest values attained from the antennas. As a proof of concept, this near-field characterization is utilized to examine the suitability of a unidirectional and an omnidirectional antenna for near-field diagnostic systems.

3.6.1 Near-field transient response and analysis

The transient characterization of antennas can be swiftly done using time domain measurements (transmitting and receiving ultra-short pulses). However, in this work, the characterization is performed by post-processing frequency domain measurements to time domain owing to the advantageous high dynamic range of frequency domain measurements and the flexibility of pulse selection [124]. In post-processing, the following time domain input pulse of choice is generated in MATLAB,

$$U(t) = -s\ (2\pi f_c t)e.\ (-2\pi t^2/\tau^2) \tag{3.4}$$

where $f_c = (f_h + f_l)/2$ is central frequency, f_l and f_h are respectively the lowest and highest operating frequencies, and τ is the Gaussian pulse width employed so that the pulse spectrum covers the operating band in the frequency domain. A time sampling rate, Δt in the scale of nano-seconds is considered for smoothing. A fast Fourier transformation (FFT) of the input pulse is multiplied with the transfer function of the antenna.

$$R(\omega, \theta, \varphi) = F\ (U(t))H(\omega, \theta, \varphi) \tag{3.5}$$

To improve the accuracy of the time domain signals, $H(\omega, \theta, \varphi)$ is complemented with zero paddings from 0 to f_l and f_h to f_m match highest frequency of transformed $U(t)$ of $f_m = 1/\Delta t$. Taking the inverse Fourier transformation (IFFT) of the resultant signal yields a complex function, of which the real part represents the transient response of the antenna [122].

$$R(t, \theta, \varphi) = \Re e\ \{I\ (R(\omega, \theta, \varphi))\} \tag{3.6}$$

The data is accordingly scaled using the fine time resolution of $\Delta\tau = 1/N\Delta f$, where N is the number of considered points. Owing to the imperfect pulse-shaping filtering capability of the wideband antenna and the channel, the transient response, $R(t)$ is the distorted and dispersed version of the input pulse. The level of distortion in the time domain pulse generated by the antenna can be quantified by calculating the fidelity factor, $F(\theta, \varphi)$ [58]. To accumulate both amplitude and correlation characterizations of the transient response, a combined matrix $C(\theta, \varphi)$ is defined as the pulse merit factor,

$$C(\theta, \varphi) = \frac{|P\ \ R(t)(\theta,\varphi)|F(\theta,\varphi)}{a\mathrm{m}_{,\theta,\varphi}|P\ \ R(t)(\theta,\varphi)|\ a\mathrm{m}_{,\theta,\varphi}F(\theta,\varphi)} \tag{3.7}$$

Here, peak amplitude and fidelity of individual received signal are normalized with the respective maximum values of all readings from the considered antennas for a comparative realization of the radiation capability. Values of $C(\theta, \varphi)$ close to unity indicate higher power transmission capability with low distortion in the time domain.

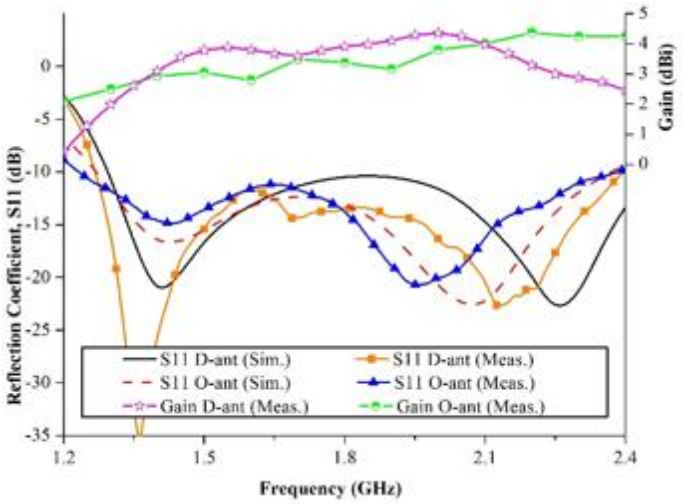

Fig. 3.32 Performance comparison of the prototyped omnidirectional (O) and directional (D) antennas: S11 and +Z-direction far-field gain performances of the antennas.

3.6.2 Antennas under consideration

The reported three-dimensional (3D) low profile unidirectional antenna with wideband performance for microwave head imaging of Section 3.5 is selected to verify the proposed method. The antenna covers the band 1.25-2.4 GHz with an average far-field gain of 3.5 dBi and occupies a space, with respect to lowest operating wavelength, of 0.29 × 0.12 × 0.06. The performance of this antenna is compared with a miniaturized monopole (MM) omnidirectional antenna designed for the same head imaging application by utilizing the symmetry of planar wideband antennas and introduced in Section 3.2. The MM antenna is designed to cover the same band (1.25-2.4 GHz) with the same average far-field gain along intended +Z-direction (θ = 0˚) (3.5 dBi). The omnidirectional MM antenna has the overall dimensions, with respect to lowest operating wavelength, of 0.32 × 0.19 × 0.006. Both antennas are prototyped and their performances are tested. Fig. 3.32(a) depicts the photographs and geometries of the two antennas. To limit the inherent near-field effect of the connector adjoining the system and antenna, small MXC connectors are used in both antennas. Fig. 3.32(b) demonstrates the reflection coefficient and gain performances along +Z-axis (θ = 0˚) of both antennas.

3.6.3 Measurement setup and simulation

To estimate the received pulse in the near-field region, each antenna is used as the transmitter in the anechoic chamber. A calibrated near-field E-probe (Aaronia-PBS-EP1) is applied to measure the complex E-field ($S_2\ (\omega, \theta, \varphi)$) over the band of interest using a vector network analyzer (R&S ZVA 24). $S_2\ (\omega, \theta, \varphi)$ is alternatively called the system transfer function ($H(\omega, \theta, \varphi)$), which quantifies the line-of-sight propagation [122]. The data is recorded across the band 1.2-2.4 GHz with 1001 equidistant sweeping points resulting in a frequency spacing of Δf = 1.2 MHz. The transmission

coefficients are calculated in different angles of E- (φ = 0˚) and H- (φ = 90˚) plane with an angular resolution of $\Delta\theta$ = 10˚. An identical polarization is maintained between the transmitting antenna and E-probe. To compare with the measurements, numerical simulations are performed in the three-dimensional electromagnetic software CST MWS using identical procedure.

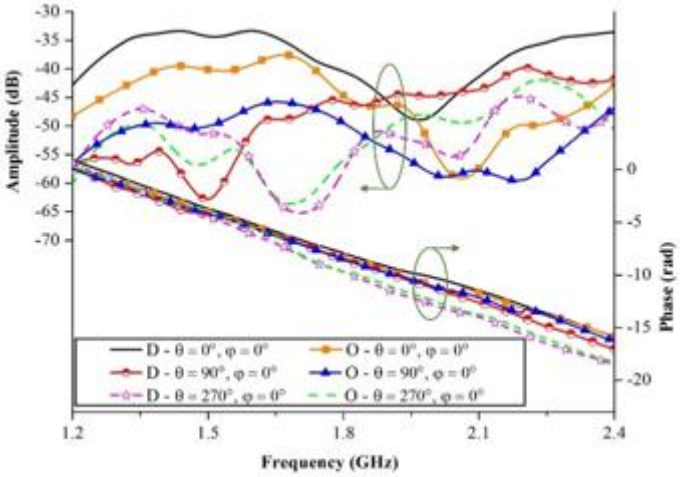

(a)

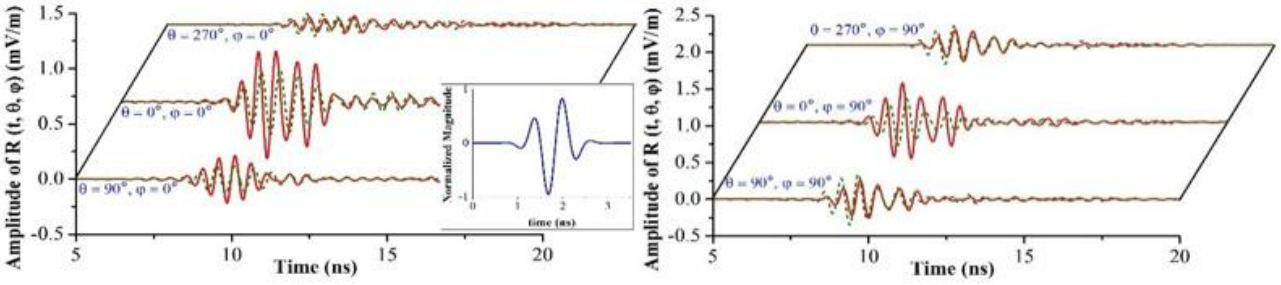

(b) (c)

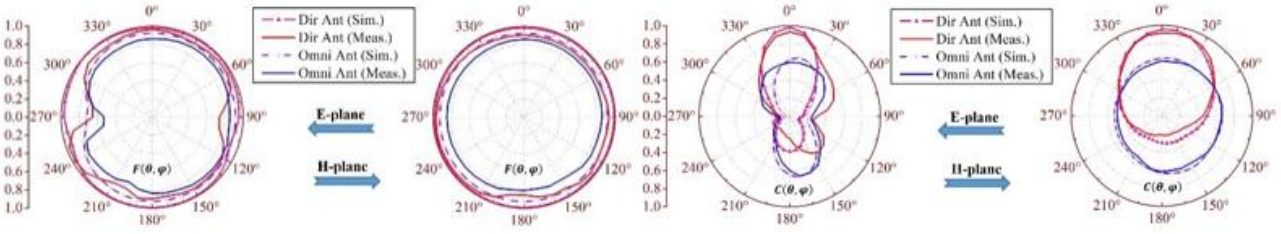

(d) (e)

Fig. 3.33 Measured and simulated results and analysis of the directional (D) and omnidirectional (O) antennas: (a) Measured transfer functions in different angles. (b) Measured transient responses in E-plane. (c) Measured transient responses of the antennas in H-plane. (d) Measured and simulated fidelity factor, $F(\theta,\varphi)$ patterns of the antennas. (e) Measured and simulated combined matrix, $C(\theta,\varphi)$ pattern comparisons.

3.6.4 Results and discussions

Fig. 3.33(a) illustrates the measured phases and magnitudes of transfer functions of the prototyped antennas in different directions. The directional antenna exhibits better phase linearity and less magnitude fluctuations along the broadside (+Z-axis) direction. However, the responses vary with the change in observation angles. Transient responses received from the antennas are compared in Fig. 3.33(b, c). It is noted that the response of the omnidirectional antenna includes more ringing owing to the rapid phase variations of its transient responses. Moreover, the directional antenna mostly demonstrates higher amplitudes of the time-domain responses. The quantitative analyses of the received time-domain data are performed in both of the simulation and measurement. The fidelity factor patterns of the antennas in E and H-planes are shown in Fig. 3.33(d). A low discrepancy is observed between the simulated and measured patterns. The soldering of the prototyped antennas increases their impulse distortion in the near-field and eventually affects their fidelity factors. It is noted that the 3D antenna has higher fidelity factors compared to the MM antenna. However, more than 80% of fidelity along the intended Z-axis direction (θ = 0˚) is observed in both planes of the antennas. This is an attractive outcome for near-field imaging purpose. Fig. 3.33(e) illustrates the pulse merit factor ($C(\theta, \varphi)$) patterns of E- and H-planes of simulated and measured antennas. The measured patterns quite thoroughly follow the simulated ones, while the slight differences can be attributed to the fabrication limitations. It is observed that in the near-field E-plane, the $C(\theta, \varphi)$ pattern of the MM antenna is bi-directional, whereas it is quasi-omnidirectional in near-field H-plane. However, the 3D antenna radiates in directional manner in the near-field. More importantly, it is noted that the MM antenna demonstrates 35% less pulse merit factor towards the intended Z-direction (θ = 0˚) due to the radiation mechanism of the MM antenna. In that antenna, different frequencies are radiated from different parts and the transient response spreads over a longer time [122]. On the other hand, the phase centers of the *3D* antenna are comparatively stable over the band of operation because of the symmetrical structure. Therefore, it radiates less distorted impulses with higher amplitudes.

A near-field time-domain characterization in terms of pulse merit factor is proposed in this section for comparative studies of wideband antennas. In order to demonstrate the usefulness, 3D unidirectional and omnidirectional MM antennas are utilized in this investigation. The near-field time-domain responses at different angles are post-processed from frequency-domain transient responses. Pulse merit factor patterns are measured and simulated in both E- and H-planes. It is observed that the directional antenna radiates 35% more along the direction of radiation with lower distortion than the MM omnidirectional antenna. This near-field characterization indicates that the 3D unidirectional antenna is more suitable in near-field transient applications, like microwave head imaging for brain stroke detection.

3.7 Slot-loaded Folded Dipole Antenna with Unidirectional Performance

From Section 3.6 it is evident that for these medical applications, directional wideband antennas are highly desirable to achieve the required signal penetration in the human body using the allowable levels of microwave power. The compact size of the antennas in such an application is also vital as the space available for the antennas, or the antenna array, is usually limited.

This section proposes a compact antenna which is motivated from the structure of a conventional microstrip 3D folded dipole antenna. It has a slot-loaded 3D folded structure with unidirectional radiation patterns and compact size compared to the reported literatures. The performance of the antenna is compared with conventional printed 3D-folded dipole counterparts to illustrate the antenna's operating principle. A parametric analysis is performed to have a deep understanding of its operation. The proposed antenna is fabricated and its performance is verified.

3.7.1 Design of the Antenna

The antenna consists of two main elements as depicted in Fig. 3.34. The top element is printed on GIL GML 1032 substrate with dielectric constant ε_r = 3.2, thickness h_s = 1.52 *mm*. The bottom structure is constructed with a rectangular copper plate having a length of L = 70 *mm* and width of W = 30 *mm* and two ($h \times W$ = 15 × 30 mm^2) rectangular vertical copper plates constructing a U-shaped structure. The antenna is fed at the top layer from the center of the wide slot (g_f = 1 *mm*) with the help of a coaxial cable connected to a 50Ω SMA connector (Fig. 3.34(d)). Two loaded slots of width (g_d = 1.3 *mm*) are symmetrically placed with respect to the feeding point. The distance between the two slots is l_d = 55.6 *mm*.

Based on our parametric study, the resonating frequencies can be approximated from the following equations:

$$f_l = {}^{c}\!/_{2\{(L - l_d + 10/g_d)\sqrt{\varepsilon_e} + 2h + L\}} \tag{3.8}$$

$$f_u = {}^{c}\!/_{2\{(L + l_d)/2 + W - 10 \square g_d + 2 \square g_f\}\sqrt{\varepsilon_e}} \tag{3.9}$$

where c is the speed of light in free space and ε_e is the effective permittivity which can be accurately calculated using the formula of suspended microstip lines [14]:

$$\varepsilon_e = \left[1 + \frac{h_s}{h_u}\left\{(0.86 - 0.13\ln\frac{h_s}{h_u})^4 - (0.5 - 0.14\ln\frac{h_s}{h_u})^4 \ln\frac{W}{h_u}\right\}\left(\frac{1}{\sqrt{\varepsilon_r}} - 1\right)\right]^{-2} \tag{3.10}$$

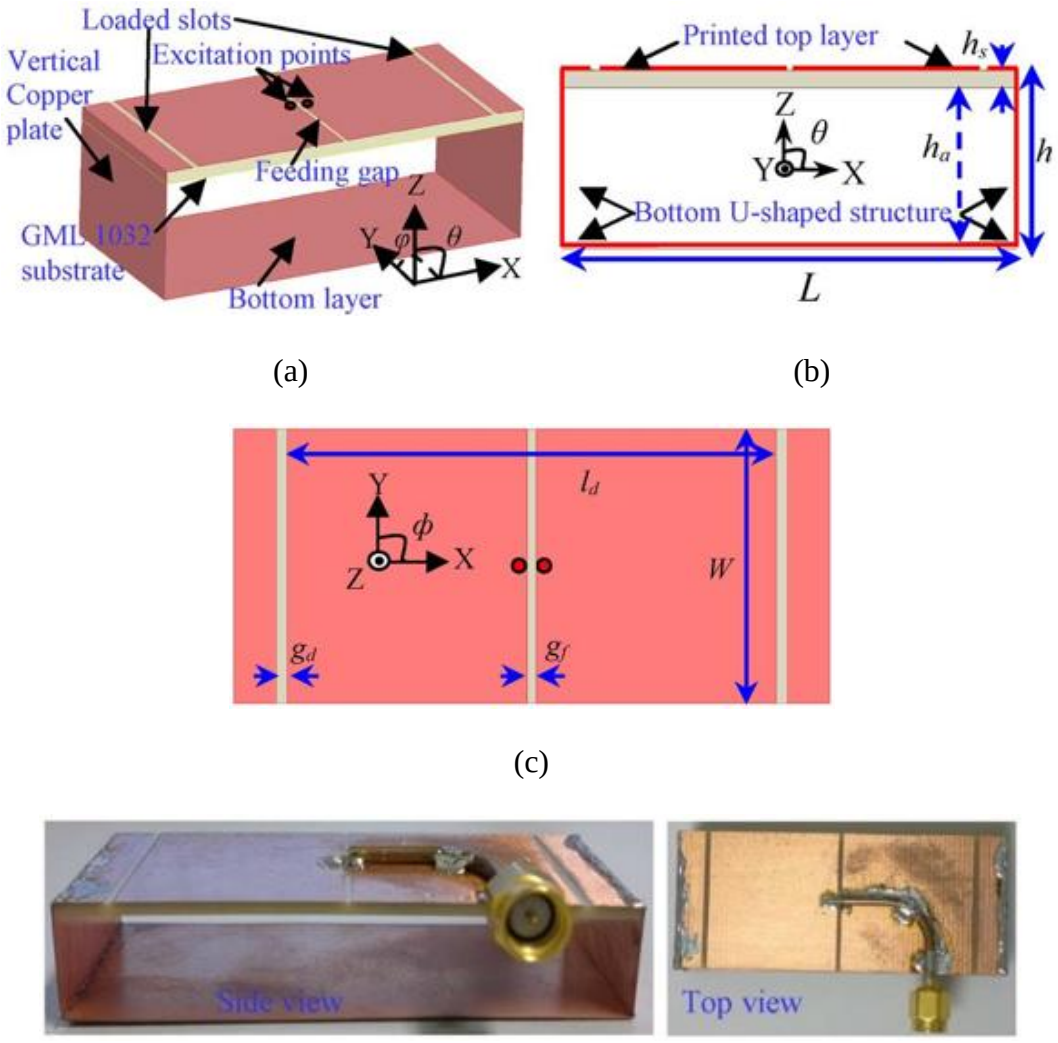

Fig. 3.34 Proposed slot-loaded 3D folded dipole antenna; (a) perspective view, (b) side view, (c) top view and (d) photographs of the fabricated prototype.

3.7.1.1 Antenna Development and Input Impedance

The outcomes of the proposed antenna evolution from the conventional 3D folded dipole antenna are illustrated in this section. Fig. 3.35 demonstrates the impedance characteristics of the conventional antenna having the same structure of the proposed antenna except the loaded slots. It is well known that typical thin folded dipole antennas have high input impedance. That impedance can be reduced, and the directivity can be increased, by increasing the width of the folded dipole. However, the reactive part of the impedance becomes the dominant part for the traditional folded dipole as depicted in Fig. 3.35(a). Thus, as seen from Fig. 3.35(b), the conventional antenna fails to provide a good impedance matching.

The impedance matching improves dramatically after the inception of the two slots (Fig. 3.35(a)). As a result of the slot loading, the resistive portion of the input impedance increases to 50Ω reference

impedance level. The reactive part also goes up due to the series capacitive effect of the loaded slots. It is also seen from the Smith chart of Fig. 3.35(b) that the complex input impedance travels toward the impedance locus upon the effective loading of the slots. Fig. 3.35(c) demonstrates that the proposed antenna provides wideband operation with good impedance matching. Apart from the resonance at 1.65 GHz, which is also seen for the conventional antenna, the proposed antenna exhibits an additional resonance at 1.15 GHz. The operation of the antenna is examined in the next section.

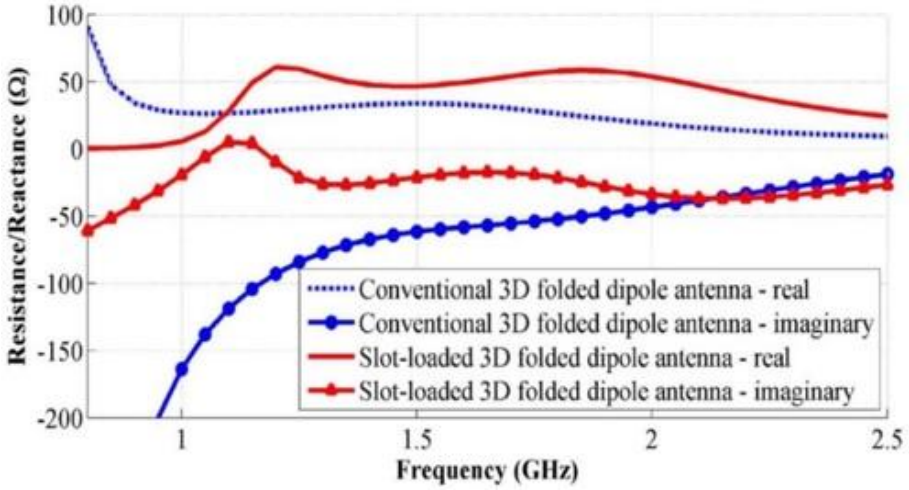

(a)

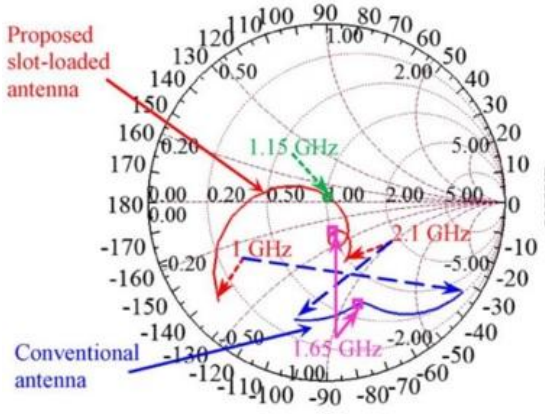

(b)

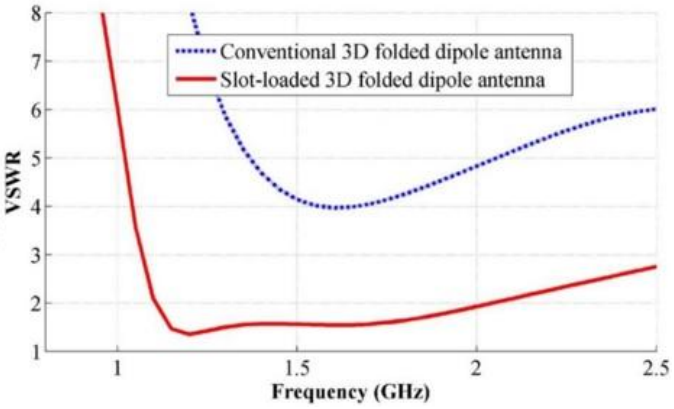

(c)

Fig. 3.35 (a) Input impedance, (b) complex input impedance in Smith chart and (c) impedance matching comparisons of conventional and slot-loaded 3D folded dipole antennas.

3.7.1.2 Current Distributions and Antenna Operation

The vector surface current distribution of the antenna is illustrated in Figs. 3.36(a-d) along with the respective E field distributions on XZ plane. The excited currents of the conventional folded dipole antenna at 1.15 and 1.65 GHz are shown in Figs. 3.36(a, b). In both cases, this antenna operates in the dipole mode; the currents on the top and bottom layers are seen to be in phase to each other. As a result, both the top and bottom layers radiate in the same manner. However, the top copper layer

carries marginally higher magnitude of currents. Consequently, the top layer radiates slightly more than the bottom one and thus a low front-to-back ratio (F/B ratio) is observed along Z-axis (Fig. 3.37).

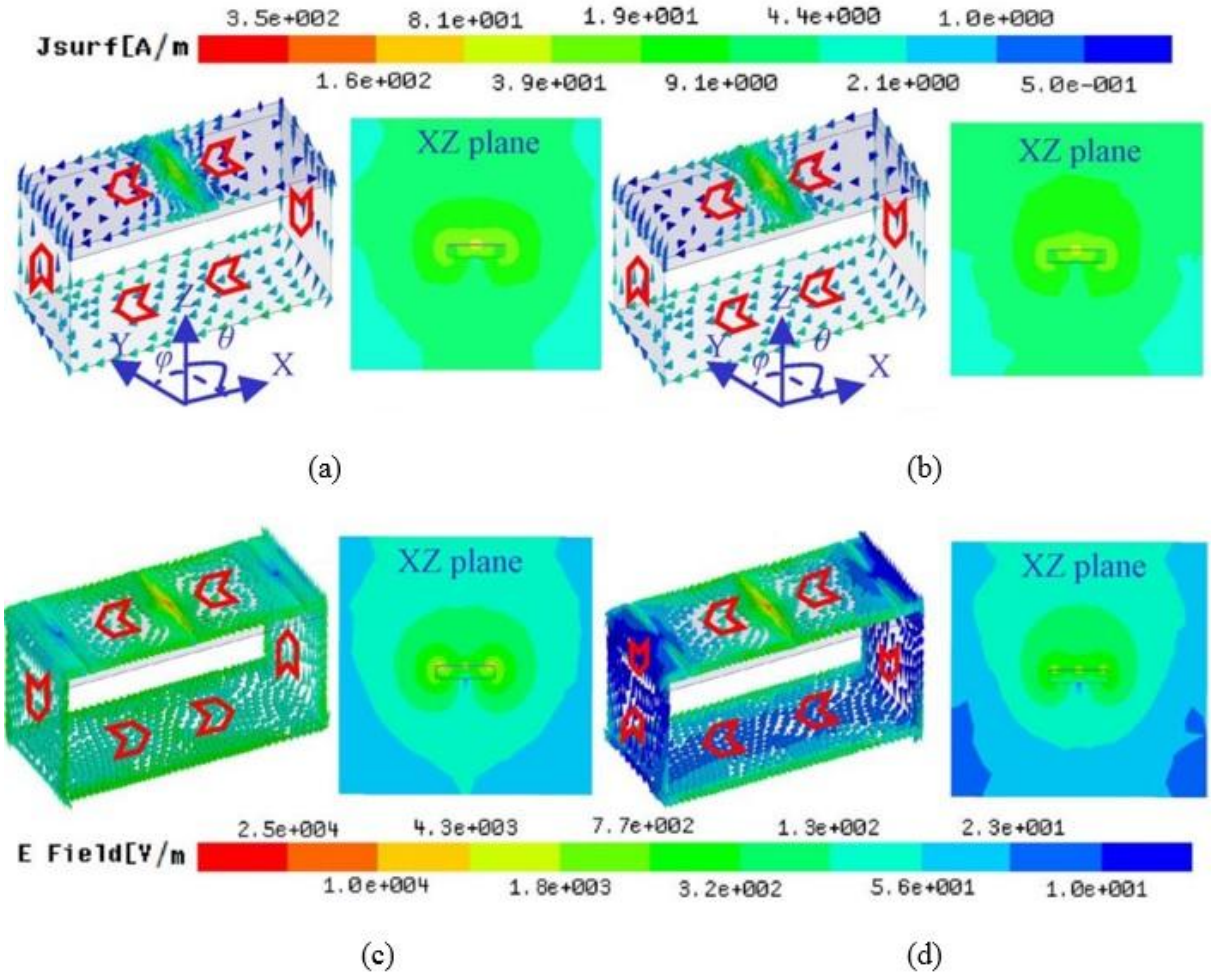

Fig. 3.36 Surface current and electric field distributions at resonance frequencies of (a, c) 1.15 and (b, d) 1.65 GHz of conventional and slotted 3D folded dipole antennas, respectively (not shown to scale).

Fig. 3.36(c, d) demonstrates the current distributions at the frequencies 1.15 GHz and 1.65 GHz of the proposed antenna. Compared to the conventional counterpart, this antenna carries denser currents on the top and less currents on the bottom layer. Hence, the F/B ratio of the proposed antenna is higher than the conventional antenna (Fig. 3.37).

It is clearly noted from Figs. 3.36(c, d) that the capacitive slots also contribute to radiation [125]. From the XZ plane field distribution, three distinct radiation dots are found on the top layer of the proposed antenna. These radiation points correspond to one excitation and two loaded slots. The loaded slots increase the current and electric field densities on the top radiator. The capacitive gaps are absent in the conventional antenna. Accordingly, the currents and produced fields are low

compared to the proposed antenna. The radiation nulls of the bottom layer also disappear (Figs. 3.36(a, b)) and the antenna radiates in an omni-directional manner. However, after loading the slots, the proposed antenna attains higher gain and F/B ratio along the Z-direction (shown in Fig. 3.37).

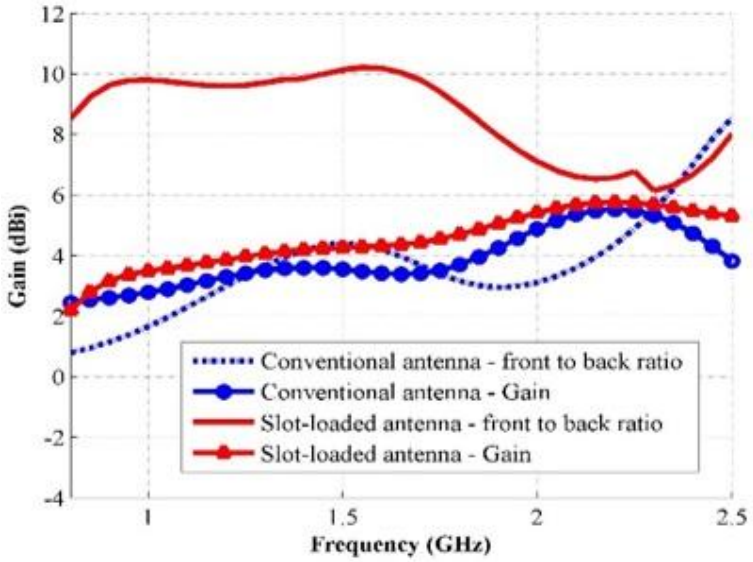

Fig. 3.37 The gain and front-to-back ratio characteristics along Z-direction (φ = 0°, θ = 0°) of the slot-loaded and conventional 3D folded dipole antennas in various frequencies.

3.7.1.3 Parametric Studies

A parametric analysis is performed to investigate the effect of varying different parameters from their optimum values on the performance of the proposed antenna. For the sake of simplicity, only one parameter is varied at each case while keeping others unchanged from their optimum values. The summary of the parametric synthesis is listed in table 3-VI.

The dimensions defining the size of the antenna, namely the length (*L*), width (*W*) and height (*h*) exhibit most significant effects on the resonances and impedance matching of the antenna. Both the resonating frequencies shift to lower values with the increase of length, *L* and contrariwise effects are observed for decreasing *L* conditions. This can be attributed to the improvement and decline of the dominant current paths due to the increase and decrease of *L* value, respectively. In case of *W* and *h*, likewise circumstances are noticed, although the first resonating frequency does not change its position in response to the variation of *W*, whereas the second resonance is insensitive to the change in *h*.

It is seen in extended simulations that the overall gain and F/B ratio of the antenna decreases for any modification in *L* from the optimized point. On the other hand, increasing *W* increases the amount of strong currents (as described in the previous section) on the top element antenna; thus the Z-directed gain and F/B ratio also increases, Nevertheless, the impedance matching of the antenna becomes

wretched. For decreasing *h* condition, similar increment in gain and F/B ratio is observed because the reduction of *h* brings the bottom reflector element in proximity to the top element resulting in an increase in Z-directed radiation. However, the bandwidth dramatically decreases as the height (*h*) is stepped down; hence, this measure is not taken.

Table 3-VI: Summary of the parametric studies when varying geometric values compared to the optimum values

Param.	**Variation**	**First Resonance**		**Second Resonance**		**Overall BW**
		f_{c1}	***VSWR***	f_{c2}	***VSWR***	
L	>	▼	▲	▼	▲	▼
	<	▲	▲	▲	▲	▼
W	>	-	▼	▼	~	~
	<	-	▲	▲	▲	▼
h	>	▼	▲	-	▲	▼
	<	▲	▼	-	▼	▼
g_f	>	-	▲	▼	~	~
	<	-	▼	▲	▲	▼
g_d	>	▲	▲	▲	▼	-
	<	▼	▲	▼	▲	▼
l_d	>	▲	~	▼	▲	▼
	<	▼	▼	▲	▲	▼

'>'and '<' represents the increment and decrement of the parameters' values from the optimized positions; '-' states the independent phenomenon upon the variation of a parameter; '~' represents the non-monotonic fluctuation of the criteria when varying the geometry; '▲' and '▼' represent the enhanced and deteriorated phenomenon of the antenna upon changing parameter-values.

The feeding gap, g_f is crucial for adequate impedance matching of the antenna. No change in the radiation pattern is observed due to the variation in g_f. In contrary, the slot gap, g_d is not only important

for the proper impedance matching, but also critical for the radiation characteristics. The resistance and capacitance of the antenna decrease with the increase in g_d. Consequently, the antenna experiences a lower radiation loss; hence a more Z-directive radiation pattern is observed. However, inappropriate increment in g_d cuts down the operating bandwidth of the antenna. Similar consequences are seen in l_d, the distance of the slot from the feeding edge. It is noted that alterations from the optimized parameters either tends to bring the resonances closer or increase the VSWR values which consequently leads to narrower bandwidths.

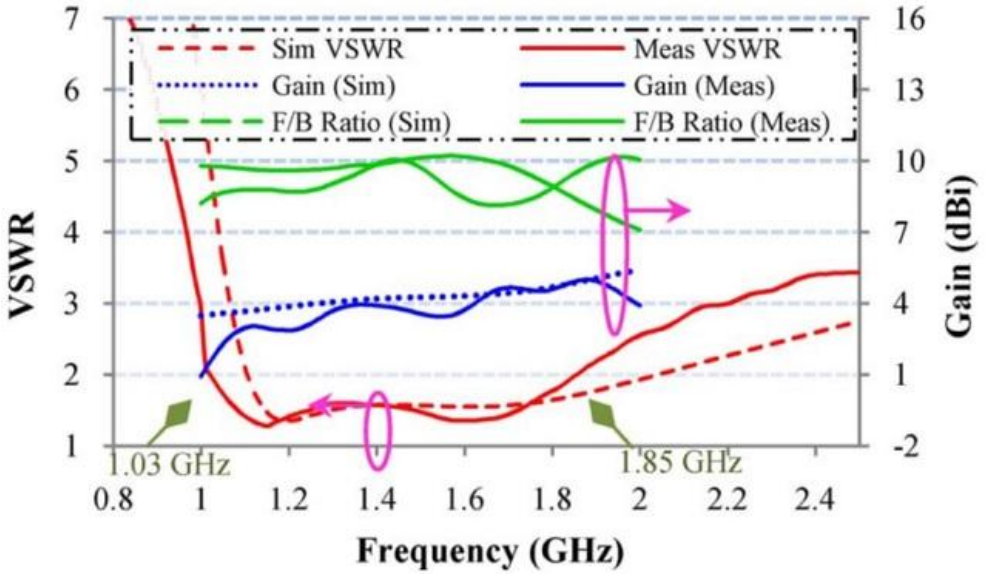

Fig. 3.38 Measured and Simulated VSWR, gain and front-to-back ratio (F/B ratio) along Z-direction ($\varphi = 0°$, $\theta = 0°$) of the proposed antenna.

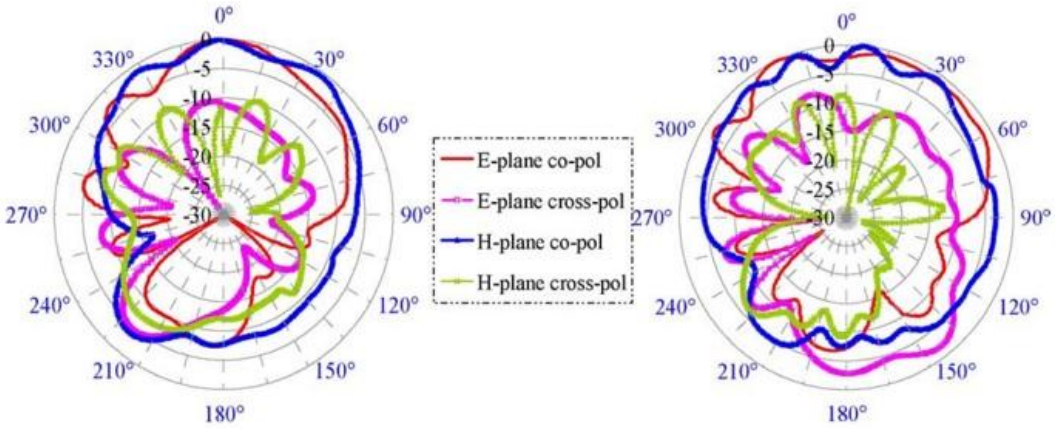

(a) (b)

Fig. 3.39 Measured E- (XZ) and H- (YZ) plane co- and cross-polarization radiation patterns of the fabricated antenna at (a) 1.15 and (b) 1.65 GHz.

3.7.2 Experimental Results

The designed antenna is prototyped and tested for performance verification. Proper ferrite beads are used around the coaxial feeder during the measurements to absorb any currents flowing back to the feeding cable. The simulated and measured VSWR of the antenna are presented in Fig. 3.38. A reasonable agreement is seen between the plots. The prototyped antenna exhibits a wide bandwidth below VSWR = 2 from 1.03 GHz to 1.85 GHz, which is equivalent to 57% fractional bandwidth. An average gain of 3.7 *dBi* is observed over the band of operation (Fig. 3.38). The measured gain tends to be slightly lower than the simulated gain due to the use of ferrite beads during the tests. We noticed that the difference between the measured gains with and without beads is around 0.3 dB at 1.4 GHz, which is close to the difference between the simulated and measured gain seen in Fig. 3.38. However, this difference is larger at low frequencies due to the increased effect of the ferrite beads. The F/B ratio of the antenna along Z-direction ($\varphi = 0°$, $\theta = 0°$) fluctuates around 9 *dBi* which is reasonable for its directional operation.

The radiation performances of the antenna are measured in an anechoic chamber. The measured E and H plane radiation patterns of the antenna at 1.15 GHz and 1.65 GHz are depicted in Fig. 3.39. The antenna provides unidirectional radiation patterns along Z-direction. The cross polarization is 10 dB below the co-polarization level along the boresight direction which ensures polarization purity of the propagated wave from this linear polarized antenna.

A slot-loaded 3-D folded antenna has been introduced. The main radiator is fabricated using low cost dielectric substrate. Rectangular copper plates are used to complete the loop like structure of the antenna. To address the performance enhancements over the conventional 3-D folded dipole, the significance of employing two slots, symmetrically placed with respect to the center line, has been described. It has been shown that the antenna operates in a loop like mode at the first resonance and in a folded dipole mode at the second resonance. The measured performance of the prototyped antenna has shown a 57% fractional bandwidth with stable directional radiation patterns over the band of operation. The compact antenna is prescribed for the utilization in a portable stroke diagnostic system operating across the L-band 1-2 GHz.

3.8 CPW-fed Low-profile Directional Antenna

In microwave-based medical diagnostic systems, wideband directional antennas operating in low microwave frequencies are demanded. However, the size of the antenna is a major design concern at these low frequencies. It is obvious that compact designs enable suitable positioning of the sensing array elements within the available volume and enable to construct portable diagnostic systems with

acceptable imaging results. Several antennas with directional wideband characteristics and compact size, such as quasi-Yagi, have been proposed in literature. However, these types of antennas present high profile along the direction of radiation.

Table 3-VII: Antennas' profile and bandwidth comparison

Antennas	[98]	[126]	[127]	[128]	[129]
Profile (λ)	0.11	0.1	0.1	0.07	0.08
FBW (%)	118	47	71	100	48

Several antennas reported to attain wideband directional radiation with low profile [98, 126, 127, 129]. A summary of the antennas' features in terms of profile and bandwidth are listed in Table 3-VII. Although [98, 127] provides wideband operation, the size of the ground plane is too large for array operation in a compact medical diagnostic system. Slot antennas are used to achieve directional radiations with the help of a compact reflector [126] and a graded index superstrate [128]. Both of the antennas manage to achieve stable radiation patterns. However, [126] does not provide enough bandwidth and [128] offers increased weight because of the utilized glass and polycarbonate. Recently, a folded antenna claims low profile and wideband behaviour with directional radiation patterns [129]. The microstrip feeding enables the antenna to be easily embedded with the circuitry. However, portable microwave diagnostic systems still require lower antenna profile and more compact size.

This section introduces a coplanar-waveguide (CPW) fed capacitive-slot-loaded folded structure. The antenna uses some basic features of [129]. By optimizing the width and position of the loaded slot, the proposed antenna provides an impedance bandwidth of 109% (from 0.75 to 2.55 GHz) for -10 dB reflection coefficient level. The antenna provides stable directional radiation patterns with a front to back ratio of around 9 dB.

3.8.1 Antenna Geometry and Design Considerations

The proposed directional antenna is exhibited in Fig. 3.40. The antenna is printed on two blocks of GIL GML 1032 dielectric substrate with ε_r = 3.32, tanδ = 0.003 and thickness, h_s = 1.53 mm. Two copper walls with height, h = 20 mm are utilized to connect both of the printed structures and create a closed loop like pattern. The antenna is excited from the top radiator by a CPW feeder at f_d = 6 mm away from the edge. Two capacitive slots are loaded at l = 36.5 mm away from the excitation edge. These slots are primarily responsible for the wideband impedance matching of the proposed design

as shown in Fig. 3.41, which also demonstrates the reflection coefficient behaviour of the antenna without the loaded slots.

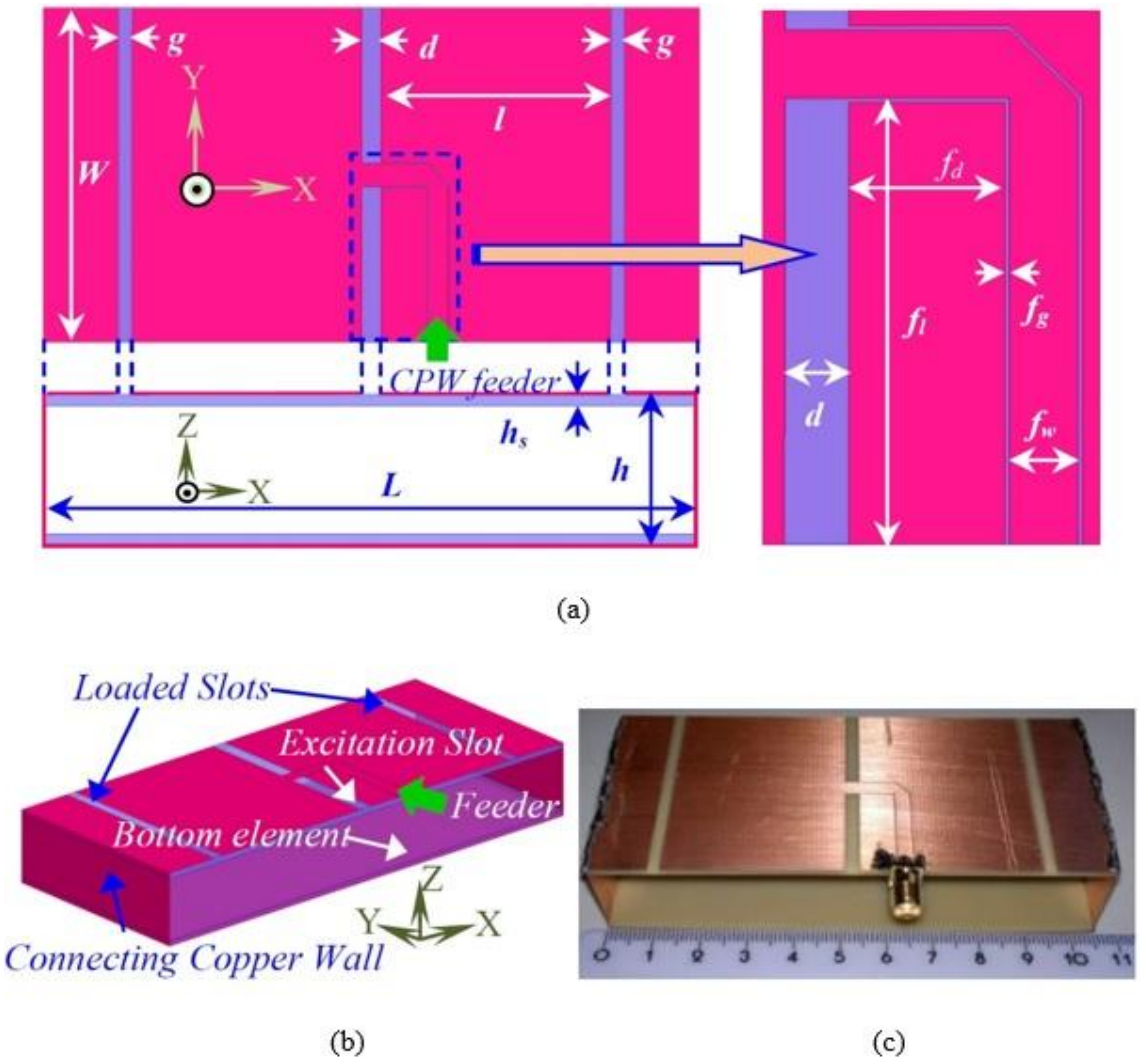

Fig. 3.40 Proposed antenna: (a) Geometry of the antenna with enlarged view of CPW feeding line. (b) Isometric view of the design. (c) Photograph of the fabricated prototype

Without slots, the antenna presents similar resonances in higher frequencies with low reflection coefficient values compared to the slot-loaded design. However, the first resonance is absent. This is because without the slots the antenna operates like a basic folded dipole. For the second and third resonances, the proposed antenna operates in folded dipole mode, where the currents on the both printed structures flows in phase. In these resonances, the currents on the top radiator are significantly high with less current flows in the bottom radiator. Hence, the antenna radiates more along the boresight direction and the antenna produces directional radiation patterns. The proposed antenna holds these modes in addition to the first resonance where the antenna creates a small current loop.

The currents flowing on the top radiator are out of phase with those flowing in the bottom radiator. However, the magnitudes of the flowing currents on the top radiator are higher than those of the bottom printed layer. This is why, the backward fields created by the top radiator are mostly neutralized by the fields generated by the bottom radiator and the antenna produces a directional radiation pattern around the first resonance. The antenna is simulated using the electromagnetic simulator HFSS. The final dimensions of the antenna (in mm) are: L = 105, W = 45, g = 2.6, d = 3, f_g = 0.2, f_l = 20.9, f_w = 3.2.

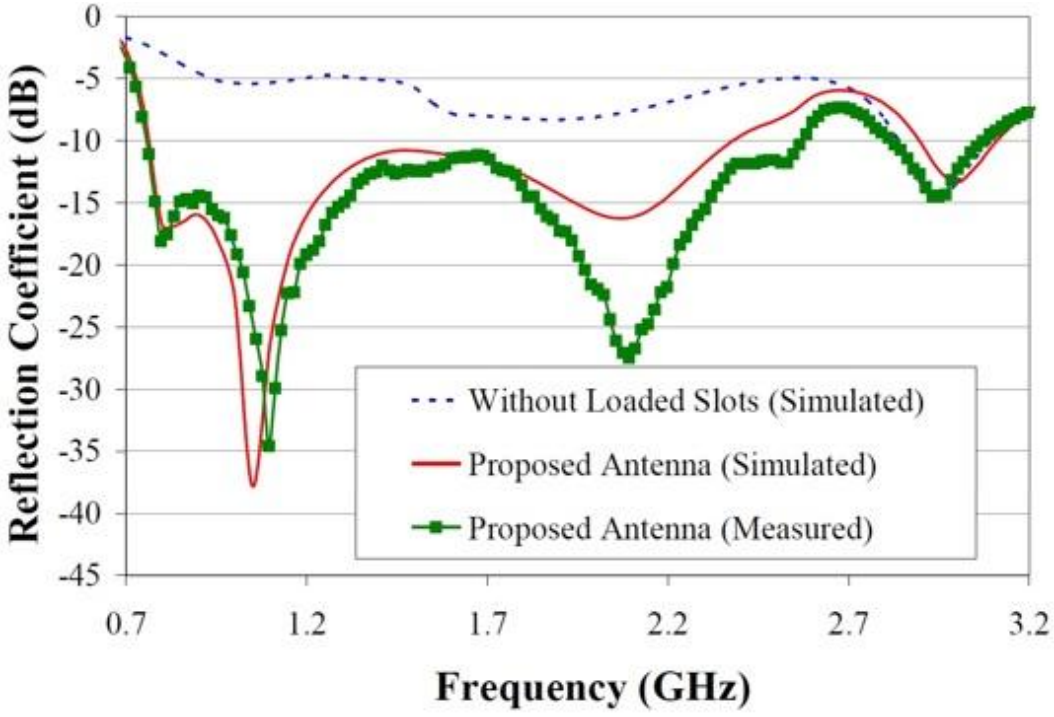

Fig. 3.41 Reflection coefficients with and without loaded slots.

3.8.2 Results and Discussions

The designed antenna is fabricated (Fig. 3.40(c)) and tested for verification. The reflection coefficient of the antenna is measured with a vector network analyser and presented in Fig. 3.41. The prototype has 109% fractional bandwidth covering the band from 0.75 to 2.55 GHz, which includes all the bands used in microwave-based head imaging. The normalized measured E (-XZ) and H (-YZ) plane radiation patterns at 0.85, 1.1, 1.5, 1.95 and 2.5 GHz are shown in Fig. 3.40. Moreover, the simulated and measured gain characteristics along with the front to back ratio (F/B) and half power beamwidths (HPB) of both E and H-planes in various frequencies are presented in Fig. 3.41. The prototype provides a steady Z-directed gain with an average of 3.5 dBi. It is noted that the prototyped antenna provides stable radiation patterns with about 9 dB F/B ratio over most of the operating band. The

HPB is relatively constant in E-plane than H-plane. Nevertheless, low cross-polarization levels of less than -10 dB are observed for both E and H-planes over the entire bandwidth.

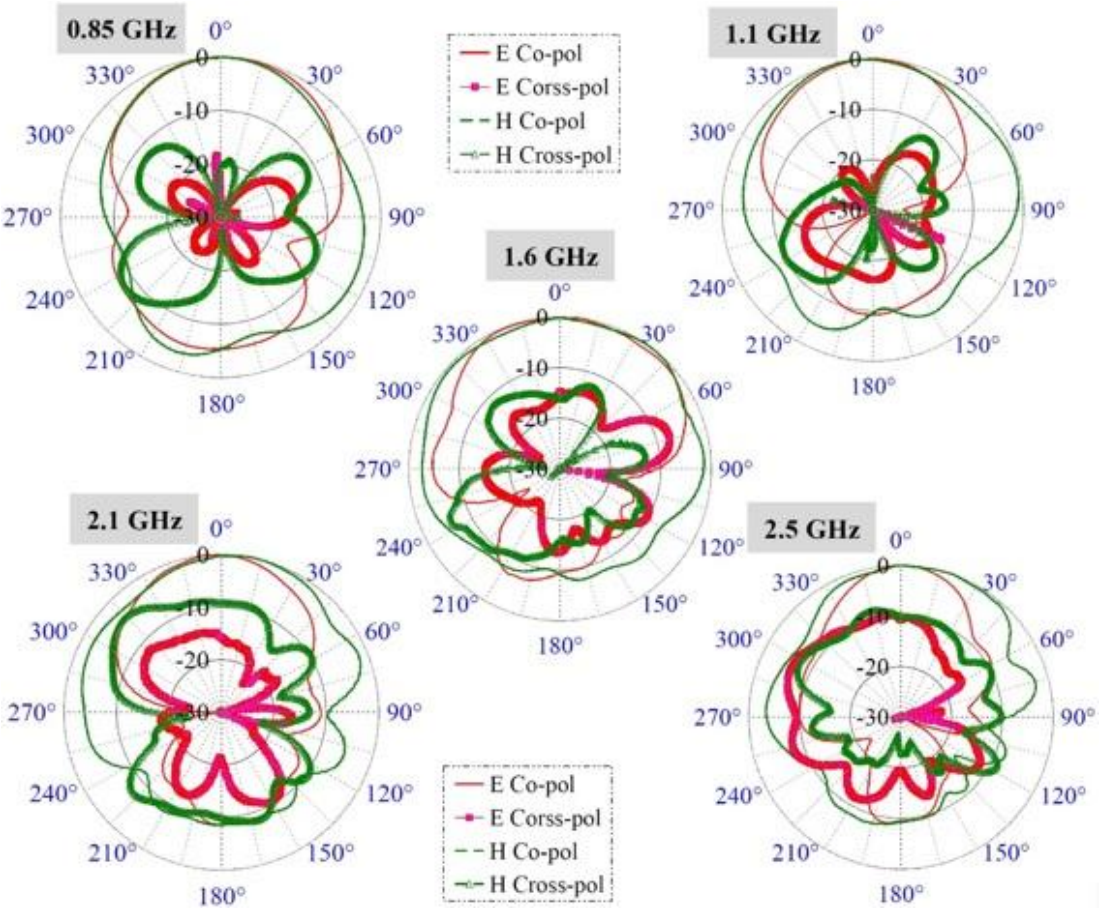

Fig. 3.42 Measured radiation patterns of the antenna.

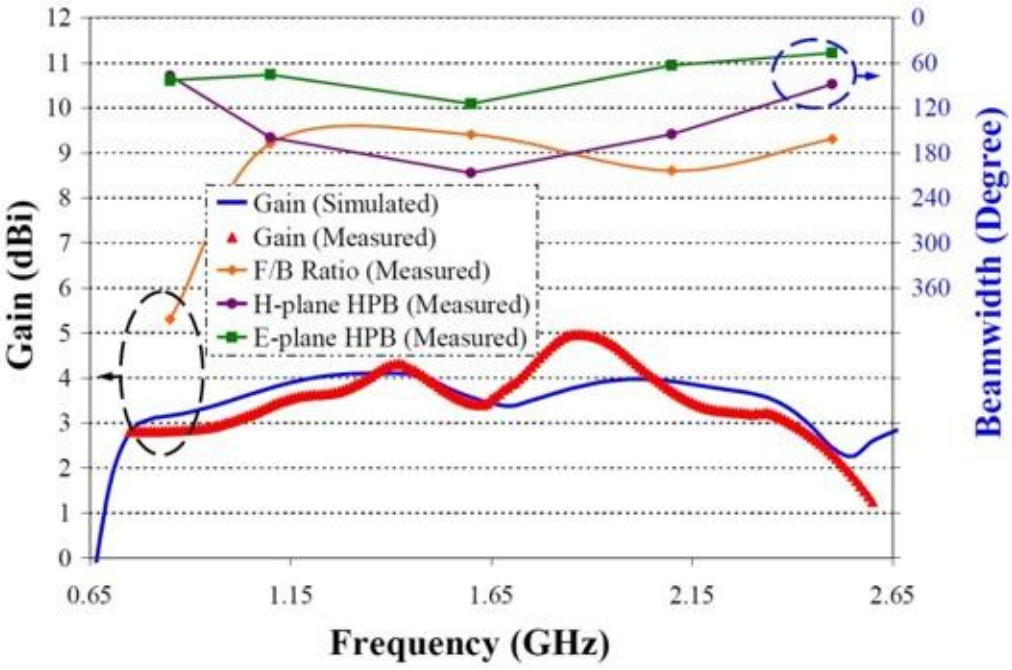

Fig. 3.43 Gain, F/B ratio, E and H-plane HPB of the antenna.

A wideband low profile compact antenna is presented. The antenna is composed of CPW-fed folded structure with two symmetrically placed capacitively loaded slots. The antenna achieves 109% bandwidth in low microwave frequencies. Stable directive radiation patterns in both E and H-planes are observed with about 9 dB front-to-back ratio and an average gain of 3.5 dBi. The overall dimensions of the proposed antenna are only 0.26 × 0.11 × 0.05 λ^3 (λ = wavelength at lowest frequency). The compact size and low profile of the antenna feature the potential application of it in portable wideband medical diagnostic systems operating in low microwave frequencies.

3.9 Bandwidth Enhancement using Additional Slots

In this section, a compact antenna is proposed for wideband microwave systems aimed to the head imaging applications. The antenna is composed of a microstrip-fed dipole structure with a folded parasitic element. Bandwidth enhancement is attained by optimizing folded dipole structure as well as by imposing multiple slots on the top surface of the structure. Moreover, the antenna provides directional radiation patterns without the use of any large reflector.

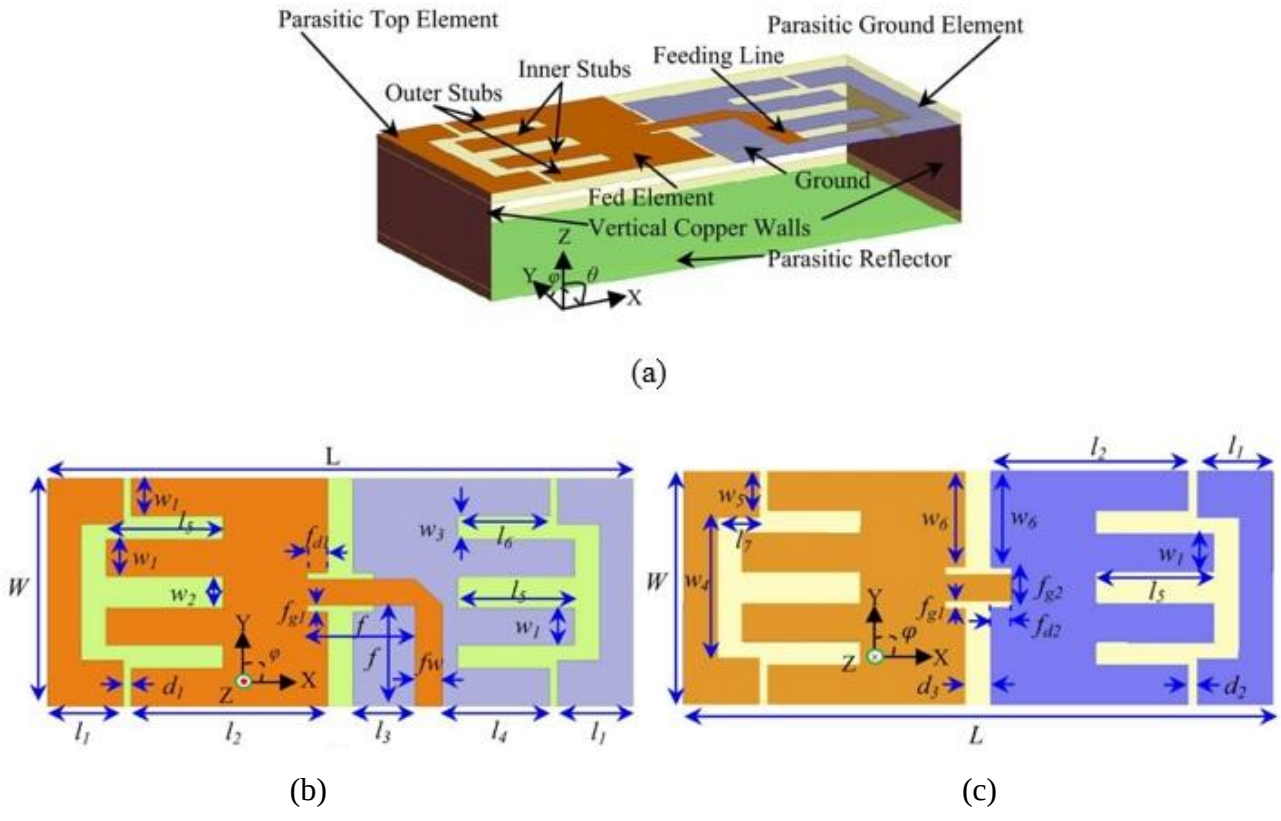

Fig. 3.44 Geometry of the designed antenna: (a) perspective view, (b) top view, and (c) bottom view of the top dielectric slab.

3.9.1 Antenna Configuration and Operation

The schematic diagram of the proposed antenna for the imaging system is exhibited in Fig. 3.44. The antenna is printed on two blocks of low cost GIL 1023 substrates (permittivity, $\varepsilon_r = 3.32$, loss tangent, $tan\delta = 0.003$, thickness, $h_s = 1.524\ mm$).

From metallization point of view, the antenna is composed of a slotted dipole element and a folded parasitic structure. The slotted basic dipole consists of two symmetrically positioned fed- and ground-elements. This dipole is responsible for the high resonant frequencies. The top element is fed by a microstrip line of width $f_w = 3.8\ mm$, which corresponds to 50 Ω equivalent impedance. The ground plane, having similar structure to the fed-element, is printed on the other side of the top substrate. Three slots are loaded on both of the fed- and ground elements resulting in two outer and two inner stubs. These stubs increase the electrical current paths of the excited signals. Nevertheless, the slots induce adequate capacitances to the input impedance for a proper impedance matching.

The folded parasitic structure, on the other hand, dominates the lower operating band and is responsible for the unidirectionality of the radiation characteristics of the antenna. This folded structure is constructed with two top and bottom parasitic elements, two vertical walls and a parasitic reflector. The top and ground parasitic elements are printed on the top block of GIL 1023 substrate and are connected to two 0.3 *mm* thick copper plates with width *W* and height *h*. These vertical copper walls are finally connected to the opposite ends of the parasitic reflector element that is printed on the second block of GIL 1023 substrate. Both of the dielectric slabs have the same size covering an area of $L \times W$. The top and ground parasitic elements couples with the fed and ground element of the antenna and drives currents onto the folded parasitic element. Thus, increasing the path of the flown current eventually results in lowering the operating frequencies.

The parasitic structure has a significant effect on the antenna performance. The effect of various parts of the parasitic structure on the antenna's scattering parameter and radiation characteristics is exhibited in Fig. 3.45. It is seen that without any parasitic elements the basic dipole provides a bandwidth from 1.7 to 3.3 GHz. Hence, this structure is responsible for the upper band operation. However, the basic dipole displays omni-directional radiation patterns. Adding the top and ground PE the antenna performance slightly enhanced; the bandwidth, overall reflection coefficients and gain increases. Adding both PE and VW improves antenna performance further due to the increase in electrical size. But the radiation patterns are still omni-directioanl. It is observed that adding a PR to the dipole structure produces uni-directional radiation patterns with higher gain. However, with this structure the antenna becomes narrow-band and is unable to produce good reflection coefficient performances. Finally, having the parasitic structure by adding all PR, VW and PR in a folded manner,

the proposed antenna achieves a wide bandwidth with directional radiation patterns. On the other hand, if the parts of the parasitic structure (PR, VW and PR) are added in a flat orientation (FO), the antenna also achieves wide bandwidth with low reflection coefficient values. However, the gain becomes deteriorated and the patterns are omni-directional which is not desired for the imaging application. Thus, the parametric structure extends the antenna performance to lower frequencies and provides directional radiation patterns with stable gain.

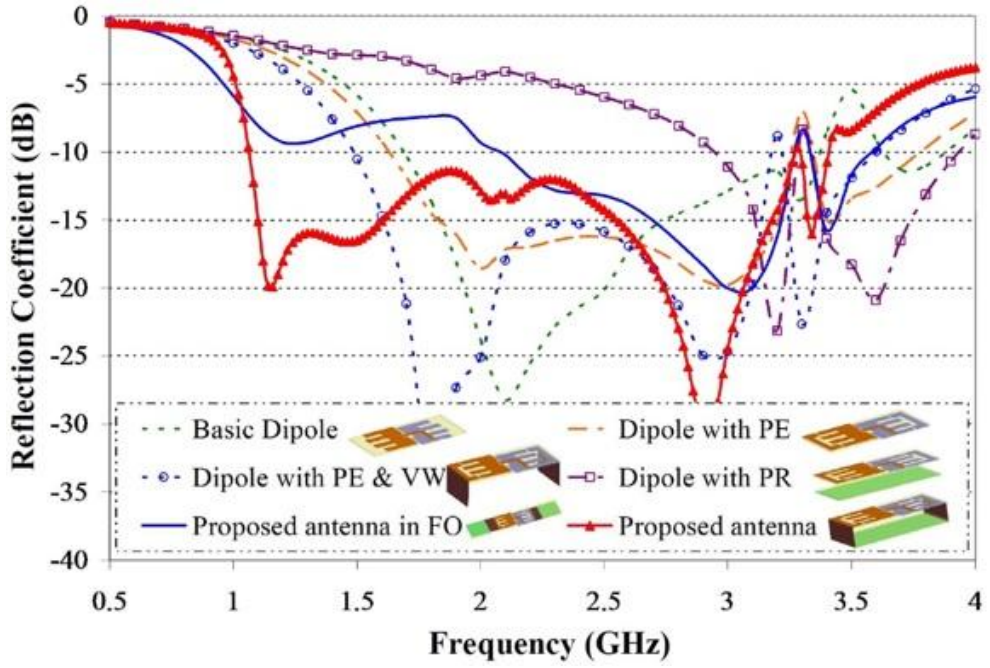

(a)

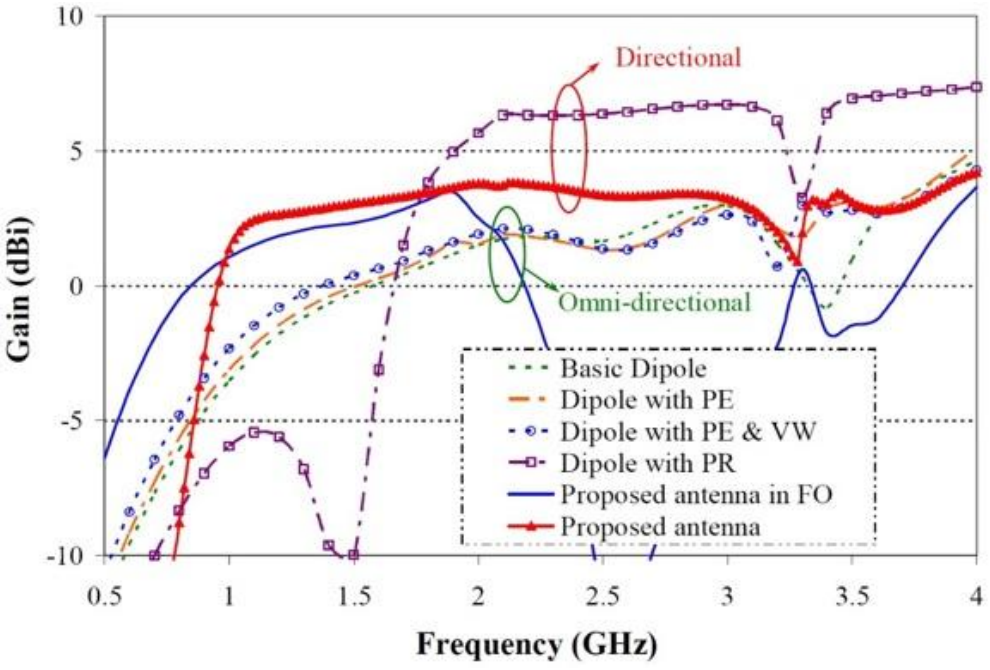

(b)

Fig. 3.45 Effects on (a) the reflection coefficients, and (b) the Z-directed radiated gain of introducing parametric elements (PE), vertical walls (VW) to the basic dipole in folded and flat orientation (FO).

The radiation mechanism of the antenna can be realized from the current distributions. Fig. 3.46 demonstrates the surface current distributions of the proposed antenna at 1.1, 1.5, 2.1 and 2.9 GHz. It is seen that most of the strong currents are located on the top substrate block of the antenna and the folded parasitic structure creates a loop like current distribution. The currents flowing on this parasitic structure are out of phase of those of the upper part. Thus, the backward radiations generated by the upper dipole element are counteracted by the fields generated by the lower parasitic reflector, due to the generated out of phase field distributions. Nevertheless, as the top substrate carries denser current distribution on it, the currents flowing on the top and bottom substrate blocks are unequal in magnitude. This is how, the antenna radiates most of its radiation along Z-direction ($\theta = 0°$, $\varphi = 0°$) and the antenna provides a good front to back ratio with a small size.

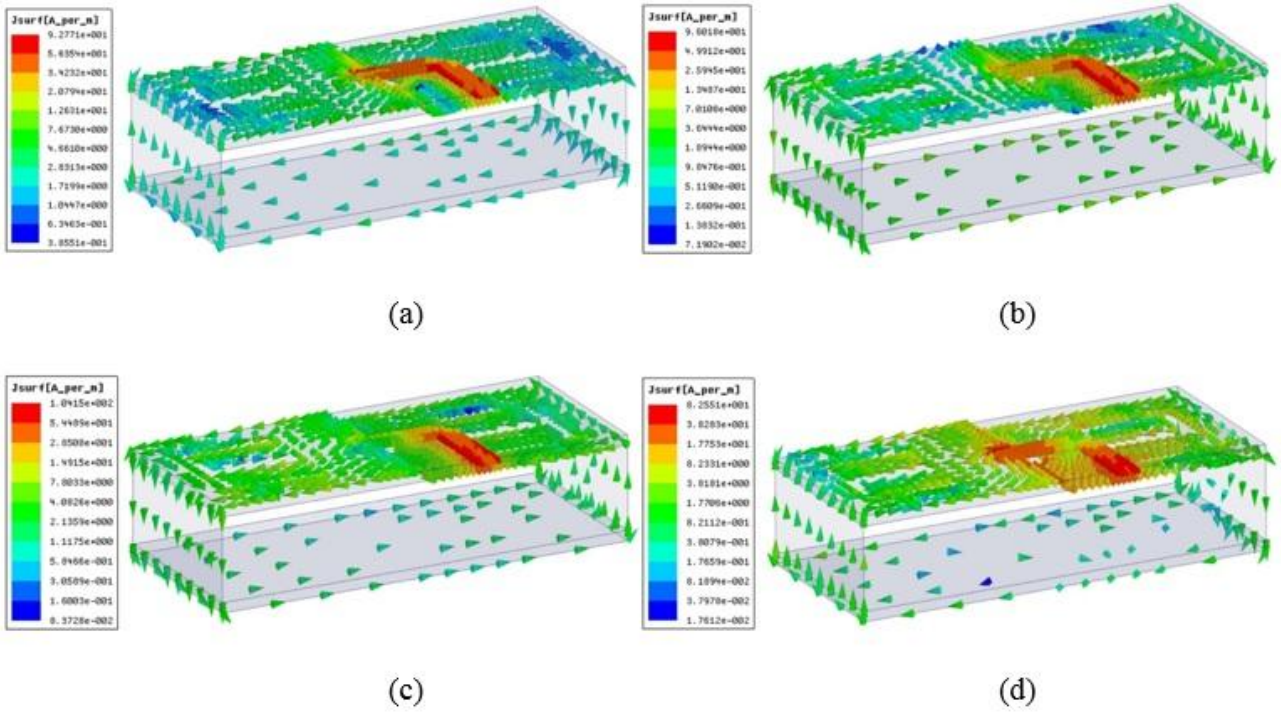

Fig. 3.46 Vector surface current distributions of the proposed antenna in (a) 1.1, (b) 1.5, (c) 2.1 and (d) 2.9 GHz.

Initially, the length of the slotted dipole ($L - 2 \times l_1$) is assumed as half of the effective wavelength at the center of the band (around 2 GHz) and the overall antenna length (L) as quarter of the effective wavelength at the first resonance (1.1 GHz). The inner stubs (l_5) are taken as quarter wavelength of the end resonance (around 3 GHz). Then, the antenna is optimized widest bandwidth with radiation unidirectionality by utilizing the 'Quasi Newton' algorithm in the finite element method based electromagnetic simulator HFSS. The final dimensions of antenna geometry are listed in Table 3-VIII.

Table 3-VIII: Values in (*mm*) of Geometric Parameters of the Antenna

Antenna Dimensional Parameters	Symbol	Value
Antenna length	L	70
Antenna width	W	30
Height of antenna	H	15
Substrate thickness	h_s	1.524
Air thickness	h_a	13.476
Microstrip feed-line width	f_w	3.2
Microstrip feed-line vertical length	f_1	13.4
Microstrip feed-line horizontal length	f_2	13
Gap width of fed-line inset	f_{g1}	1
Gap length of fed-line inset	f_{d1}	2.5
Ground inset width	f_{g2}	5.2
Ground inset length	f_{d2}	3
Width of the stub lines	w_1	5
Gap width, between third and fourth stubs	w_2	4
Gap width, between first and second stubs	w_3	3
Width of the inset of parasitic elements	w_4	18
Distance of parasitic element inset from edge	w_5	6
Distance of the insets of ground and fed element from the antenna edge	w_6	12.4
Length of parasitic element	l_1	9
Ground or fed element length	l_2	23.5
Distance of the feeding line from the inner edge	l_3	7.5
Distance of the feeding line from the outer edge	l_4	12.8
Length of the inner stub lines	l_5	14
Length of the outer stub lines	l_6	11

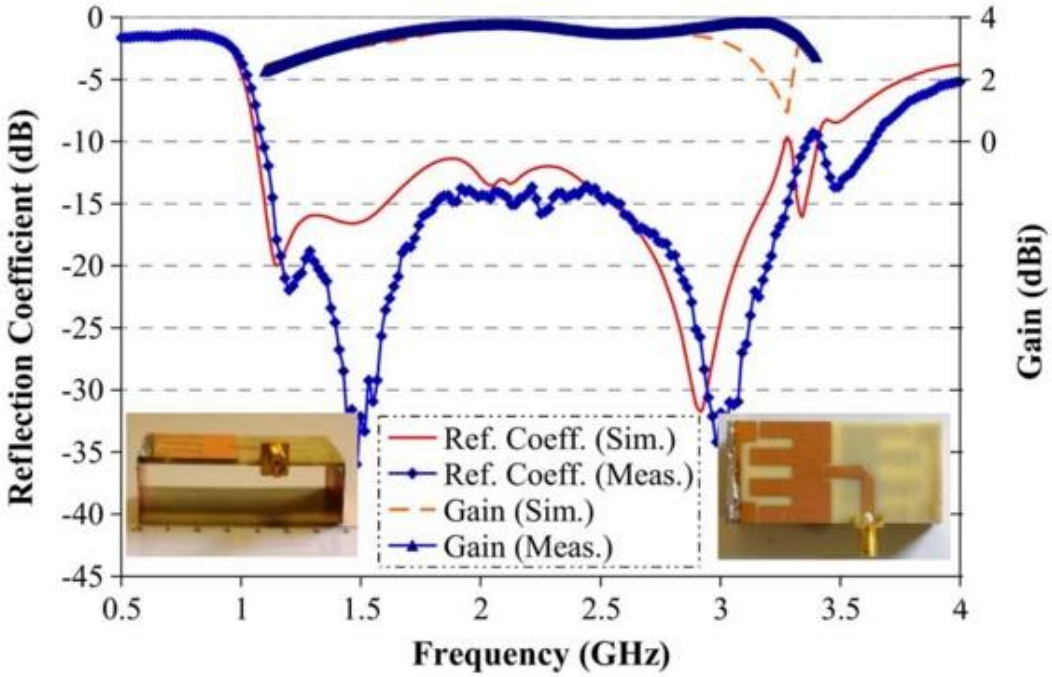

Fig. 3.47 Input reflection coefficient and Z-directed (θ = 0˚, φ = 0˚) gain comparisons between the simulated model and prototyped antenna with the photographs (3-D and top view) of the fabricated prototype at the inset.

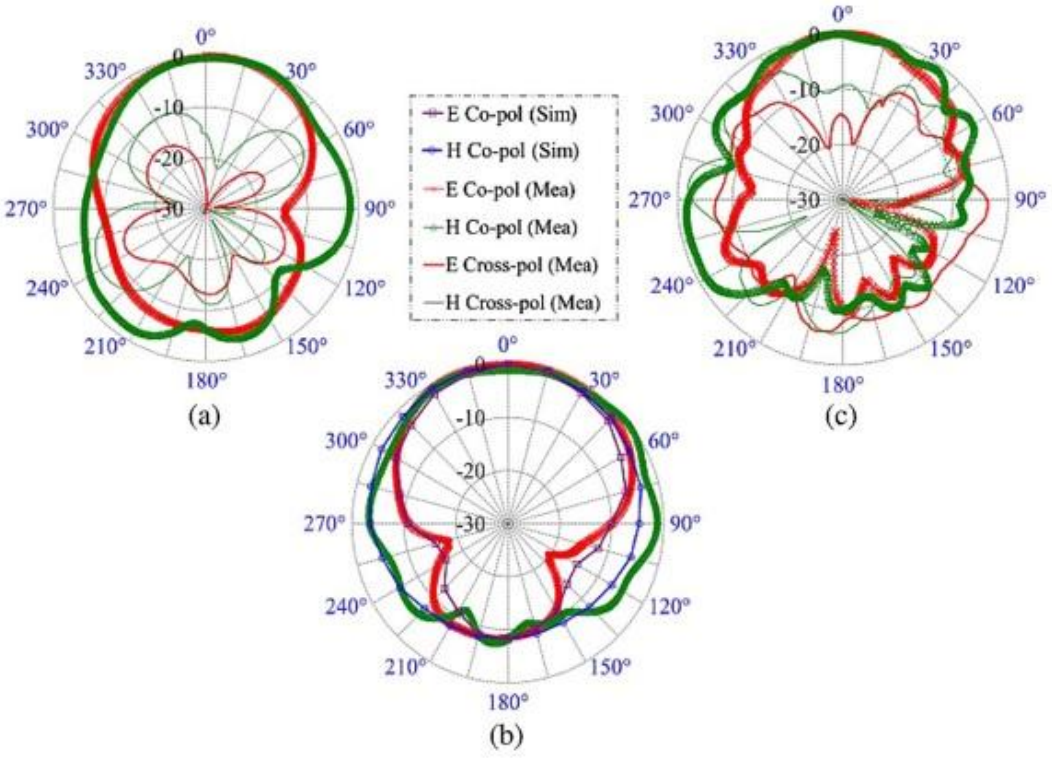

Fig. 3.48 Measured and simulated E-(XZ) and H-(YZ) plane far-field radiation patterns of the prototyped antenna in (a) 1.15, (b) 1.95 and (e) 3.25 GHz.

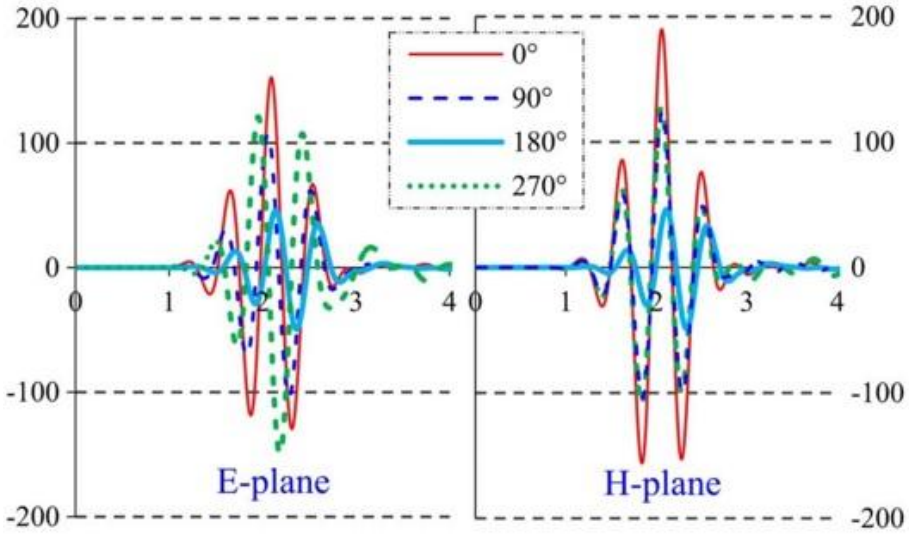

Fig. 3.49 Simulated received near-field time-domain pulses radiated by the antenna in different angles in E-(XZ) and H-(YZ) planes. Vertical axis represents field strength (mV/m) and horizontal axis indicates time (ns).

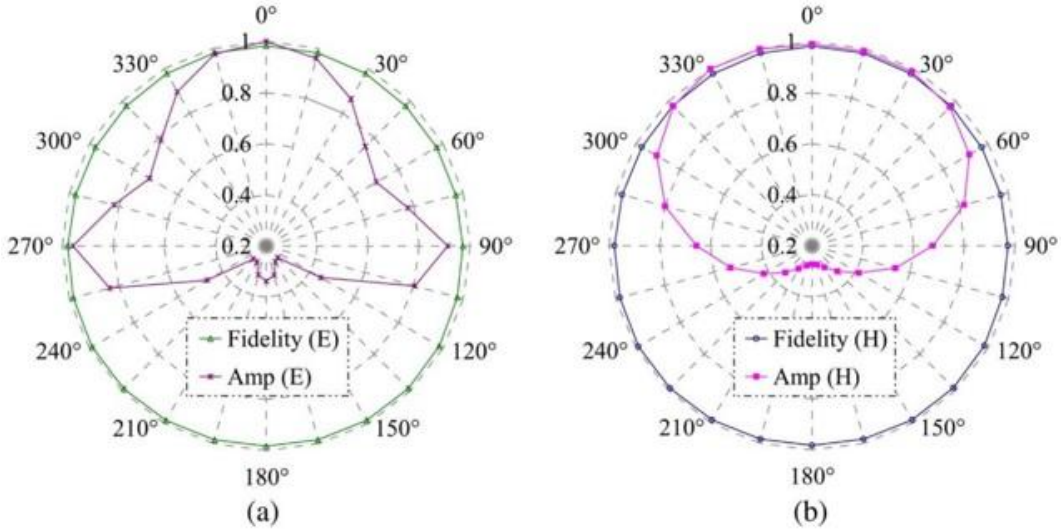

Fig. 3.50 Simulated fidelity factors and time-domain near-field radiation patterns of the proposed antenna in (a) E-(XZ), and (b) H-(YZ) plane.

3.9.2 Frequency-domain characterization

The designed antenna is prototyped (inset of Fig. 3.47) and its performance is examined for verification. Fig. 3.47 exhibits the simulated and measured reflection coefficient of the prototyped antenna in different frequencies. The plotted simulated and measured graphs fairly track each other well with negligible discrepancies. The reflection coefficient of the prototype is below -10 dB over

102.2% fractional bandwidth (1.1-3.4 GHz). In comparison with our recent design [130], the proposed antenna has less than 50% of the size with more than 30% additional fractional bandwidth.

The measured and simulated gain along Z-direction ($\theta = 0^{\circ}$, $\varphi = 0^{\circ}$) is also demonstrated in Fig. 3.47. The gain curve of the proposed antenna starts from small values compared to the measurements of higher frequencies. This is obviously due to the electrically small size of the antenna at the lower frequencies. However, the Z-directed gain is found to be stable over the rest of the operating band.

The radiation characteristics of the antenna are tested in an anechoic chamber. The measured E-(XZ) and H-(YZ) plane radiation patterns of the prototype in 1.15, 1.95 and 3.25 GHz are illustrated in Fig. 3.48. This exhibits that the simulation and measurement patterns matches quite well with each other. The antenna radiates in a directional manner with stable radiation patterns along the boresight direction, which is normal to the antenna orientation ($\theta = 0^{\circ}$, $\varphi = 0^{\circ}$). Also, the polarization purity of the antenna along the desired direction (Z-axis) is less than -15 dB in the lower frequencies which tends to increase in the higher end. This can be attributed to the excitation of higher order current modes which are significant along Y-direction. These Y-directed currents contribute to the cross-polarization of the antenna in higher frequencies. Nevertheless, the cross-polarization level is found to be better than -10 dB over the band of operation. It is noted that the H-plane has wider 3 dB beam-width along the direction of radiation compared to the E-plane. This can be explained by the effect of the vertical copper walls, which reduce the side radiations in E-plane, but in H-plane these copper walls are absent. Hence, the antenna tends to radiate in a wider manner in H-plane. However, this is not an issue for the desired application since the designed brain injury diagnostic system is intended to operate in E-plane. The antenna attains an average front to back ratio (FBR) of 9 dB along Z-axis. It is noted that FBR is large in the higher frequencies and comparatively goes down in the lower end. This is reasonable as the antenna itself is electrically small at the lower frequencies.

Despite properly designing the feeding structure of the antenna to transform the unbalanced feeder to the balanced antenna, the aforementioned measurements were done with and without ferrite beads covering the coaxial feeder to make sure of the feeder's design. We noticed that the effect on the antenna's performance is negligible.

3.9.3 Time-domain characterization

Since the antenna in the head imaging system operates in the far- and near-field regions, its performance should be examined at both of them. The aforementioned results are all related to the performance in the far field region. Thus, this section, which mainly looks at the time-domain performance of the antenna, is dedicated to the near field. The finite-difference time-domain based

electromagnetic tool CST Microwave Studio is used for this characterization utilizing the CST default Gaussian pulse signal in the simulation.

The level of pulse distortions can be examined by calculating the fidelity factors of the radiated pulses in various directions. For the radiated electric field intensity E_{rad} and the template waveform of E_t, the fidelity factor at a specific direction is defined as,

$$F(\varphi,\theta) = m \quad \frac{\int_{-\infty}^{+\infty} E_r \quad (t,\varphi,\theta) E_t(t-\iota,\varphi,\theta) d}{\sqrt{\int_{-\infty}^{+\infty} |E_r \quad (t,\varphi,\theta)|^2 d \quad \int_{-\infty}^{+\infty} |E_t(t,\varphi,\theta)|^2 d}} \tag{3.11}$$

Here, the excitation pulse is taken as the template waveform [126]. The fidelity factor, *F*, which indicates the level of distortion introduced by the antenna, computes the maximum amount of cross correlation between the two pulses where only the patterns are analyzed. An *F* value close to unity indicates similarity between the excited and received signals. However, the magnitudes of the two pulses are not considered in fidelity factor calculation. Therefore, it is also important to compare the amplitudes of the radiated time-domain pulses around the proposed unidirectional antenna.

To investigate the fidelity factors and time-domain amplitude responses around the antenna, co-polarized electric field (E_x) probes are positioned around the antenna at angular differences of 15˚ apart from each other. Both E and H-planes are considered in this analysis. The probes are placed at distances of 45 *mm* from the center of the antenna in E-plane and at 35 *mm* from the center of the antenna in H-plane. The reason for assuming the slightly higher spans for the probes of E-plane than those of H-plane is due to the antenna length along X-axis, while it was intended that the probes are as close as possible and do not touch the surface of the antenna. However, in both cases the probes are located in the near-field region of the antenna. Hence, the results in fact characterize the near-field time-domain responses of the antenna. Fig. 3.49 exhibits the time-domain responses received by several probes surrounding the antenna in both E and H-planes.

The computed fidelity factors of the proposed antenna in both E and H-planes are shown in Fig. 3.50. It is seen that the antenna radiates almost distortionless time-domain pulses in an omnidirectional manner. High fidelity factors of more than 0.95 are observed in both planes, which indicate that the antenna provide stable radiation patterns across the band of interest [126]. The time-domain directionality patterns in free-space environment are also demonstrated in Fig. 3.50. The calculated front-to-back ratio of the received time-domain electrical signal's amplitude reaches about 3.5:1 along Z-direction in both planes.

It is seen that the time-domain directivity decreases rapidly in E-plane with the change in angles starting from the Z-axis compared to that of H-plane. Since the antennas of wideband systems are mainly designed to radiate and receive electric fields, rapid reduction of radiation beam in E-plane is highly desirable in directional wideband antennas [119, 126]. However, Fig. 3.50 indicates that the antenna radiates strongly along ± X axis because the probes are closer to the antenna surface in these positions. In practical cases, the antennas are placed vertically in front of the human head with equal distances.

3.10 Radiation Patterns Improvement of Half-cut Antennas

The miniaturizing technique based on magnetic symmetry has been proposed to attain a halved version of a three-dimensional folded antenna. However, the direction of the main-beam shifts from the boresight direction due to this modification. Similar beam-shifts are also observed for omni-directional antennas [81, 131]. Typically, the excitation points of the full sized antennas are located around the center of the structure. As a result, the antennas are directly fed through their centreline. As the antenna is halved, its feeding line is located at one side of the structure resulting in tilted-beam radiation patterns.

This section describes how the existing side-feeding technique of a symmetrical antenna can be applied to cross-feed a half-cut antenna in order to correct the radiation performance. The direct and cross-feeding techniques are compared in details by means of current distributions, impedance matching and near-field performance and the mechanism of cross-feeding technique is demonstrated. The prototyped half-cut slot-loaded folded dipole antenna maintains its main-beam radiation at the boresight direction in both near- and far-fields. The antenna is applied in an automated head imaging system and the reconstructed results demonstrate suitability of the wideband directional antenna for such applications.

3.10.1 Antenna Geometry, Challenges and Design Considerations

The schematic diagrams of the half-cut antenna are illustrated in Fig. 3.51. The antenna is designed on two low loss Rogers 3003 substrate slabs with permittivity ε_r = 3.0, loss tangent $t\delta$ = 0.003 and thickness h = 1.52 *mm*. The top slab is printed double-sided and the antenna is fed at the top layer with a 50Ω microstrip line. The bottom slab is printed on one side and connected to the first and second layer of the top slab from two opposite sides along X-axis using two 0.2 *mm* thick copper walls.

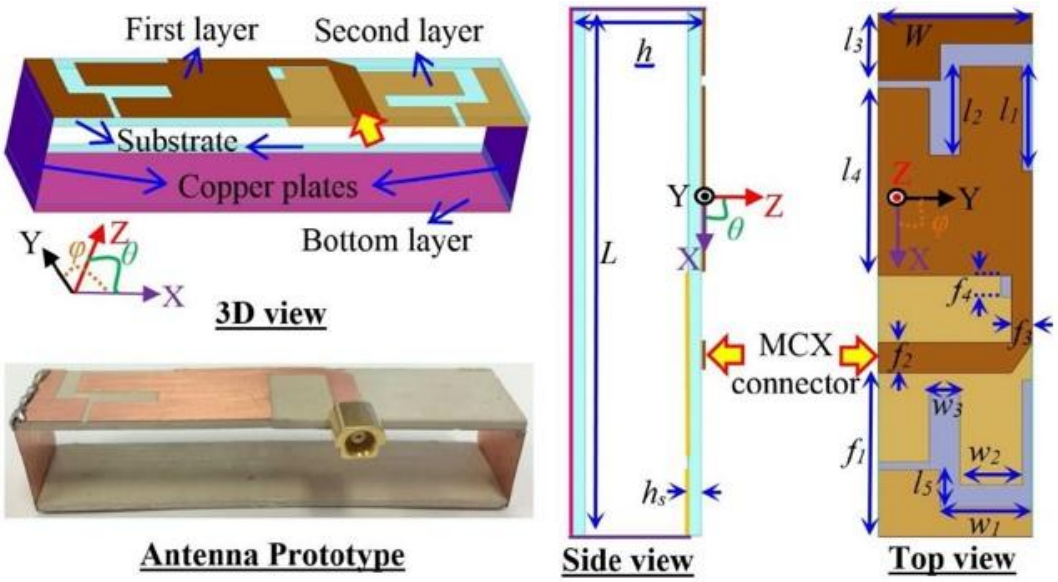

Fig. 3.51 The schematic diagrams of the proposed cross-fed antenna with a photo of the fabricated prototype.

The antenna is adopted from the conventional slot-loaded folded dipole antenna [58]. It is consequently halved using the modified halving and feeding technique based on the theory of magnetic symmetry of the radiating structure [35, 131]. However, it is found that most of the full-sized antennas are centre-fed [35, 81, 131]. As a result, the half-cut antennas become side-fed after miniaturization. The existing side-feeding technique [58] which is utilized to simplify the center excitation mechanism, turns the half-cut antenna into cross-fed with the potential to correct the radiation beam. To understand the underlying mechanism, both types of feeding techniques need to be analyzed.

It is seen from Fig. 3.52(a) that the direct feeding from one side of the antenna causes an increased surface current density at that side. Consequently, most of the radiation comes from that end of the antenna, prompting the radiation patterns to incline along that side. Although radiation patterns of both E- and H-planes are effected, it is noted that the inclination can be observed vividly from the H-plane radiation perspective. Fig. 3.52(b) demonstrates the inclination of the radiation pattern by around 15˚ from the boresight when fed using the conventional feeding method [35]. In full-sized antenna, the currents of the feeding line are not significant, as the currents are distributed over a big surface. However, it can be seen from Fig. 3.52(a) that the cross-feeding technique in the proposed half-sized antenna, increases the current distribution at the opposite part of the excitation end. As a result, the tilted radiation beam due to the one-sided excitation current, reported for halved antennas [35, 81, 131], is balanced, as can be seen from the Fig. 3.52(b). In addition to the adjustment of the radiation patterns, the cross-feeding technique reduces the input resistance and increases the

capacitive reactance by reducing the feeding line distance and meandering process, respectively (Fig. 3.53(a)). Eventually, the impedance matching of the antenna is enhanced and the highest operating frequency of the antenna is increased from 2.6 GHz to 3.0 GHz. The simulated optimized design provides 93% total fractional bandwidth covering 1.1-3.0 GHz (Fig. 3.53(b)), which is the band used for microwave head imaging as a compromise between the required signal penetration in the head and image resolution.

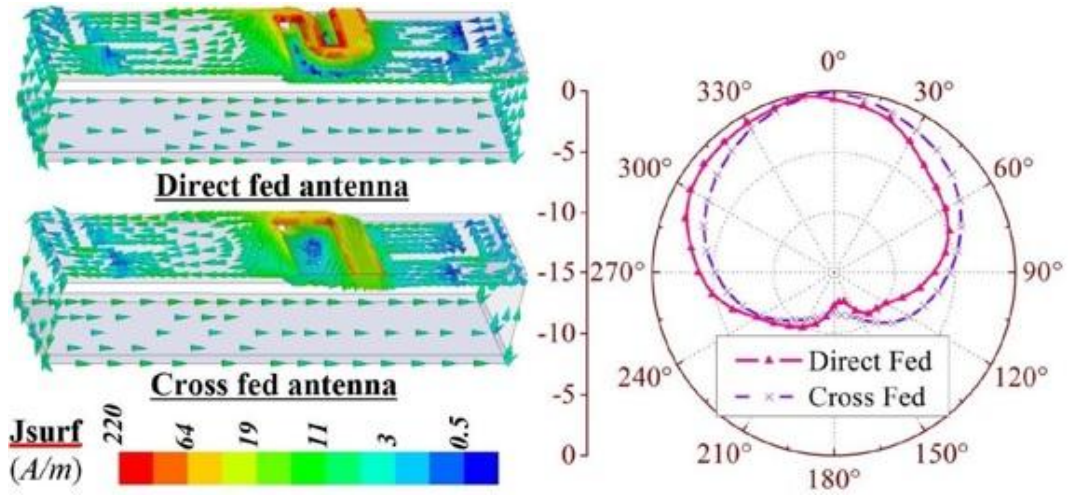

(a) (b)

Fig. 3.52 (a) Surface current distributions comparisons between the direct-fed and cross-fed proposed antenna. (b) H-plane radiation comparisons of the antennas at 1.2 GHz.

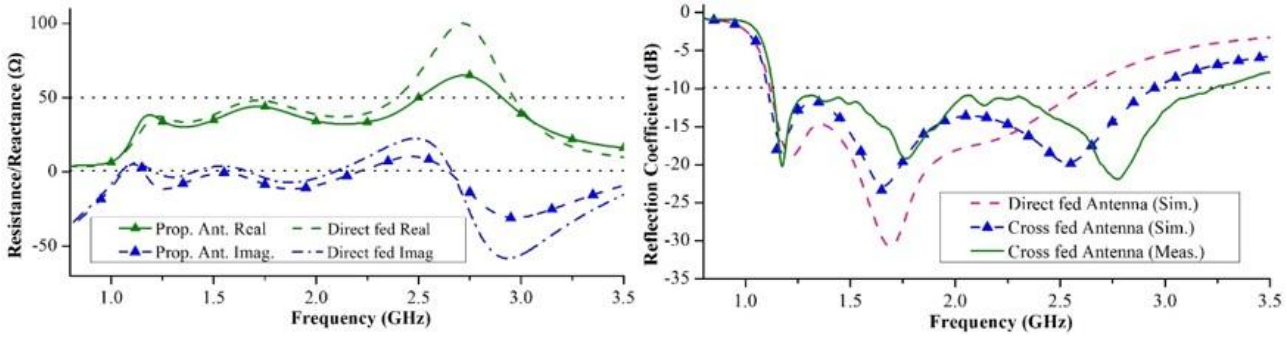

(a) (b)

Fig. 3.53 The Measured radiation characteristics of the cross-fed antenna: (a) Near-field radiation patterns of the antenna in E- and H-planes. (b) Far-field radiation patterns of the antenna in E- and H-planes.

The operating principle of the proposed halved antenna remains the same as the conventional slot-loaded antenna [58]. It relies on the compact loop mode for the first resonance and folded dipole

mode for the concurrent resonances. Nevertheless, the unidirectional radiation of the antenna is dependent on the high concentration of surface currents on the top slab and reflection from the bottom slab. The optimum design dimensions of the proposed antenna are (in *mm*): L= 70, W= 15, h= 15, l_1= 14, l_2= 12, l_3= 9, l_4= 25, l_5= 5, w_1= 9, w_2= 6, w_3= 3, f_1= 22, f_2= 4, f_3= 2, f_4= 3.

3.10.2 Antenna Performance

The proposed antenna is prototyped and the performance is verified through measurements. As seen from Fig. 3(b), the measured reflection coefficient closely matches the simulated one. The prototyped antenna covers a wide bandwidth of 2.1 GHz (1.1-3.2 GHz) which is equivalently 97% fractional bandwidth with respect to the centre frequency of 2.15 GHz. There are some discrepancies between the simulated and measured results due to the fabrication process of the prototype.

The radiation patterns of the antenna in both the near- and far-fields are measured in an anechoic chamber. Since the antenna in head imaging systems is placed in close proximity to the human head, its near-field radiation performance is important and thus measured by using a near-field wideband probe. The measured near-field performance (shown in Fig. 3.54(a)) shows that the antenna transmits in a unidirectional manner with more than 10 dB front-to-back ratio, which ensures less noise from the unintended backward direction and increases the dynamic range of the scattered signal received from the targeted front direction. As a result, the antenna promises less artefacts incurred by noise. Again, due to the high permittivity of the human head, the antenna might also need to operate in the far field [35]. For this reason, the far-field radiation patterns of the antenna are measured (shown in Fig. 3.54(b)). An average gain of around 3 dBi is found over the operating band along the boresight direction. The cross-polarization of the antenna is less than -10 dB along the +ve Z-direction. Moreover, extended simulations reveal that the antenna attains an average radiation efficiency of 85%. The antenna also provides unidirectional radiation in the far field. Most importantly, the prototype shows that both near- and far-field radiation patterns are quasi-symmetrical and the main-beam is consistently along the intended Z-direction.

In order to demonstrate the outcome of the cross feeding technique, the E-field distributions at 1.6 and 2.6 GHz on the planes normal and parallel to antenna alignment are exhibited in Fig. 3.55. The field intensities of direct fed and cross-fed antennas in both planes are comparable to each other. From the centre of the antennas in XZ-plane, the field distributions of both antennas look similar; however, the cross section distributions (XY-plane) of the same field at 25 *mm* away from the top of the antenna's surface reveals that the main-beam of the direct-fed antenna is slightly tilted to the right. That title is corrected by the cross feeding technique.

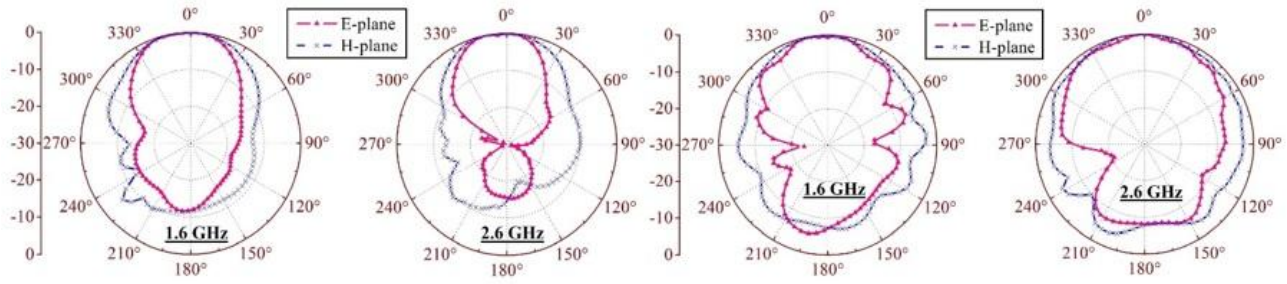

(a) (b)

Fig. 3.54 The Measured radiation characteristics of the cross-fed antenna: (a) Near-field radiation patterns of the antenna in E- and H-planes. (b) Far-field radiation patterns of the antenna in E- and H-planes.

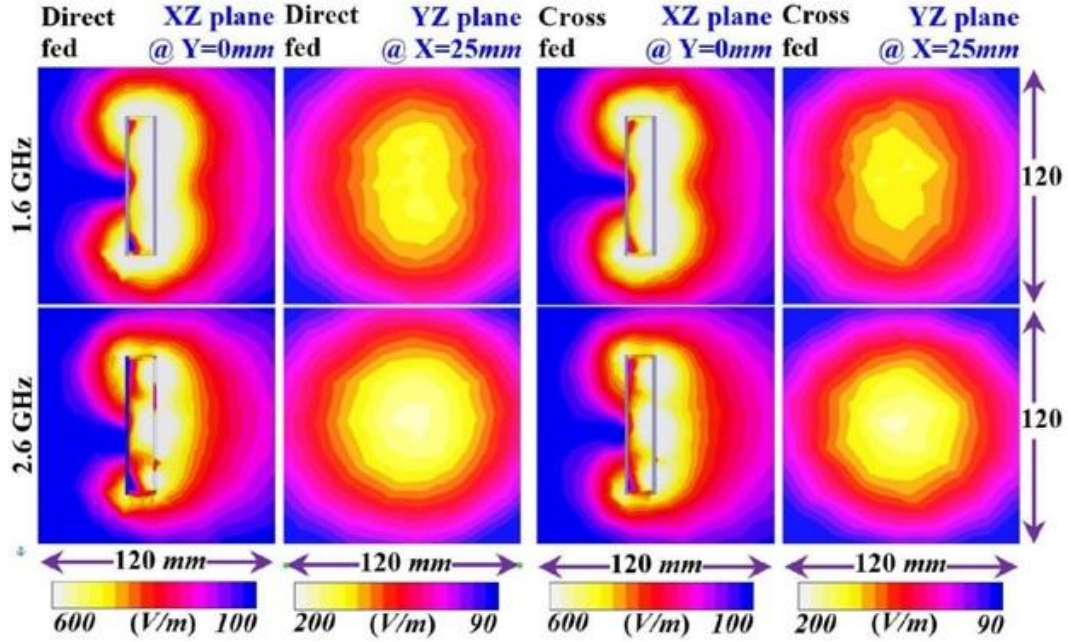

Fig. 3.55 Simulated E-field distributions of the antennas in XZ and YZ planes, while the antennas are centered at the origin of the co-ordinate system.

3.10.3 Compactness of the Proposed Antenna

The overall size of the proposed antenna is $0.25\times0.06\times0.06\ \lambda_0^3$, where λ_0 is the wavelength at the lowest operating frequency (1.1 GHz). Dimensions and bandwidths of previously reported wideband directional antennas are compared with the prototyped antenna. As illustrated in Table 3-IX, the proposed design requires at least 50% less space and provides comparable amount of fractional bandwidth (FBW) when compared to the previously reported compact unidirectional antennas [35, 58, 98].

Table 3-IX: Comparisons with the Reported Antennas

Parameters	[98]	[35]	[81]	[131]	[132]	[58]	This Work
Length (λ_0)	0.46	0.46	0.55	0.48	0.33	0.25	0.25
Width (λ_0)	0.43	0.43	0.27	0.39	0.12	0.12	0.06
Height (λ_0)	0.19	0.19	0.18	0.06	0.07	0.06	0.06
Reflector	*N*	*N*	*N*	*N*	*N*	*N*	*N*
FBW (%)	153	153	128	33	77	102	97

* λ_0 = the lowest operating wavelength

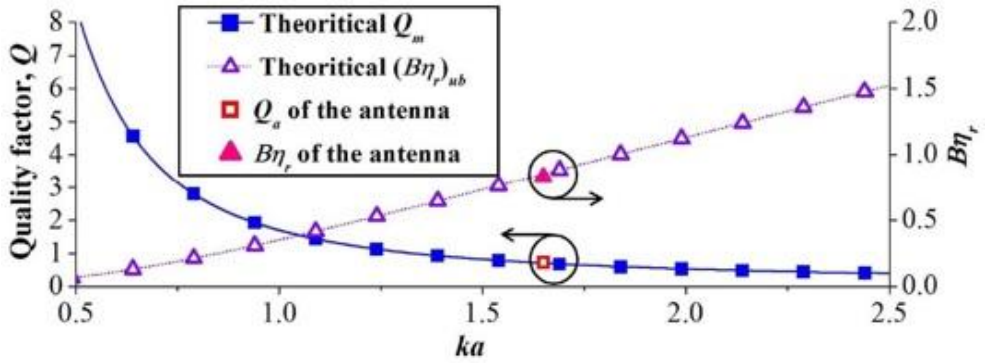

Fig. 3.56 Theoretical Q_m and $(B\eta_r)_u$ limits of antennas against size expressed in terms of k , and the calculated Q_a and $B\eta_r$ values of the designed antenna.

From the concept of fundamental limits of antennas, we can determine how optimum the antenna is toward achieving best performance considering its physical size, which is defined by k (wavenumber, $k = 2\pi/\lambda_c$, λ_c = wavelength at center frequency and a = minimum radius of the antenna's circumscribing sphere) [132]. At the center frequency 2.15 GHz, the corresponding k of the proposed antenna is 1.65. The minimum quality factor, Q_m and upper bound of bandwidth-efficiency product $(B\eta_r)_u$ can be calculated by [132],

$$Q_m = \eta_r \left[\frac{1}{k} + \frac{1}{(k)^3}\right] a \qquad (B\eta_r)_u = \frac{1}{\sqrt{2}}\left[\frac{1}{k} + \frac{1}{(k)^3}\right]^{-1} \tag{3.12}$$

Fig. 3.56 depicts the resulting Q_m and $(B\eta_r)_u$ curves for an antenna with radiation efficiency, η_r = 85% and different values of k . It is noted that when k =1.65, achievable limits of an antenna are Q_m = 0.70 and $(B\eta_r)_u$ = 0.86. Nevertheless, the quality factor, Q_a of the designed antenna is estimated as [133],

$$Q_a = \frac{1}{B}\left(\frac{s-1}{\sqrt{s}}\right) \qquad (3.13)$$

Considering the maximum allowable voltage standing wave ratio, s = 2, the proposed antenna yields Q_a = 0.73 and $B\eta_r$ = 0.83. As plotted in Fig. 3.56, these resultant values are very close to the attainable limit of antennas of such size and operating frequencies. This indicates the optimum design of the antenna.

When compared to another optimum antenna [64] (k = 1.48, Q_a = 1.24, Q_m = 1.18), it is noted that the prototyped design presents much wider bandwidth with smaller volume.

A compact wideband antenna for microwave head imaging has been introduced. The beam-tilting limitation of half-cut folded dipole antenna is fixed by using the side-feeding method, which turns the half-cut antenna to cross-fed. The operating principle of the cross-feeding technique is analysed and shown to have superior performance compared with the direct-fed technique. The measured near- and far-field radiation patterns illustrate the efficacy of the antenna. The analysis of the fundamental limit of antennas demonstrates that the proposed antenna is close to attainable performance limit considering the utilized volume and frequencies.

3.11 Compact Slot-loaded Antennas with Low Impulse Distortion

Wideband antennas often employ slots and thin strips to achieve a relatively compact size. Consequently, high impulse distortion occurs, as different parts radiate different frequency components and the antenna's phase center changes rapidly over the band [122]. For medical imaging, antennas with low distortion and directional radiation patterns in the time domain in both of the near- and far-fields are highly demanded. However, in most reported contributions about time-domain characterizations of antennas, only the far-field radiation performance is analyzed [134].

The objective of the research reported in this section, is to design antennas that meets the aforementioned requirements for head imaging. The proposed antennas have compact three-dimensional structures, which are based on slot-loaded folded dipoles. The antennas' frequency and time domain performances are verified in both of the near- and far-fields to assure its applicability in head imaging system. The low level of impulse distortion is verified by high fidelity factors of the received transient responses.

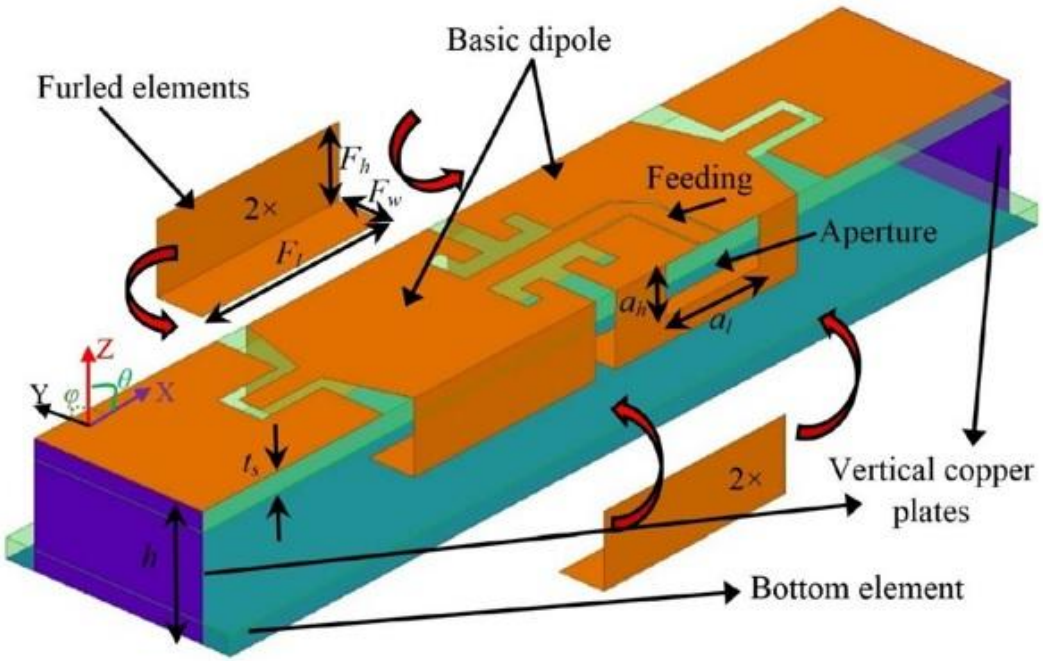

(a)

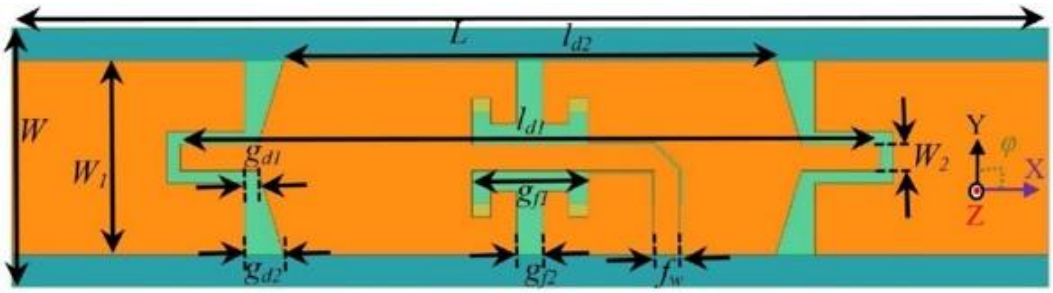

(b)

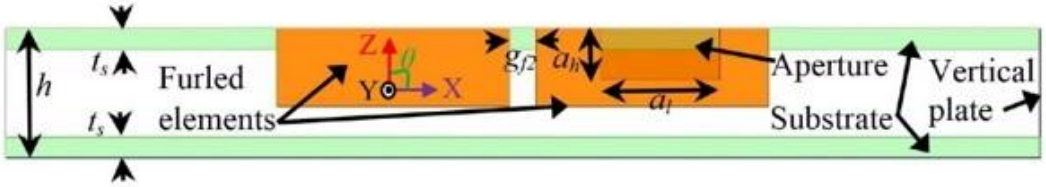

(c)

Fig. 3.57 Schematic diagrams of the three-dimensional antenna, (a) perspective view, (b) top view, and (c) side view.

3.11.1 Design of Multi-folded Slot-loaded Antenna

The geometry of the compact unidirectional antenna is illustrated in Fig. 3.57. The antenna includes two printed dielectric blocks, two copper side-walls and four furled copper plates. The top and bottom layers of the antenna are printed on low-cost dielectric substrate, FR4 with relative permittivity ε_r = 4.5, loss tangent of $t\delta$ = 0.025 and thickness t_s = 1.6 *mm*. Two vertical copper-plates connect the

top and bottom layers along the width of the antenna. The antenna is fed at the center of the top layer by using a 50 Ω coplanar waveguide (CPW) with line width of f_w = 2 *mm* and gap of f_g = 0.2 *mm* gap from the ground. The CPW line is terminated with a 50 Ω SMA connector. The top layer of the antenna is loaded with two U-shaped slots, which separates the basic dipole (see Fig. 3.57(a)) from the folded structure. This loaded-slot induces capacitive coupling and decreases the inductive impedance of the structure, assisting the antenna to attain good impedance matching with 50 Ω reference system [65]. Four L-shaped furled copper plates with height F_h = 6 *mm*, width F_w = 4 *mm*, and length F_l = 18 *mm* are connected to the basic dipole. An aperture of height a_h = 4 *mm* and length a_l = 18 *mm* is cut from the furled copper plate close to feeding, in order to avoid shorting with the SMA connector. The furled copper plates increase the effective electrical length of the basic dipole and significantly widen the operating band of the antenna. The directional radiation mechanism of the antenna is attributed to the presence of stronger currents on the top layer and reflections from the slightly extended bottom layer [64]. The design of the antenna is verified initially using the electromagnetic simulator HFSS. Dimensions of the antenna (in *mm*): W = 20, L = 80, h = 10, t_s = 1.6, W_1 = 15, W_2 = 2, l_{d1} = 54, l_{d2} = 38, g_{d1} = 1, g_{d2} = 3, g_{f1} = 9, g_{f2} = 2, f_w = 2, a_h = 2, a_l = 7.2, F_h = 6, F_w = 4, F_l = 18.

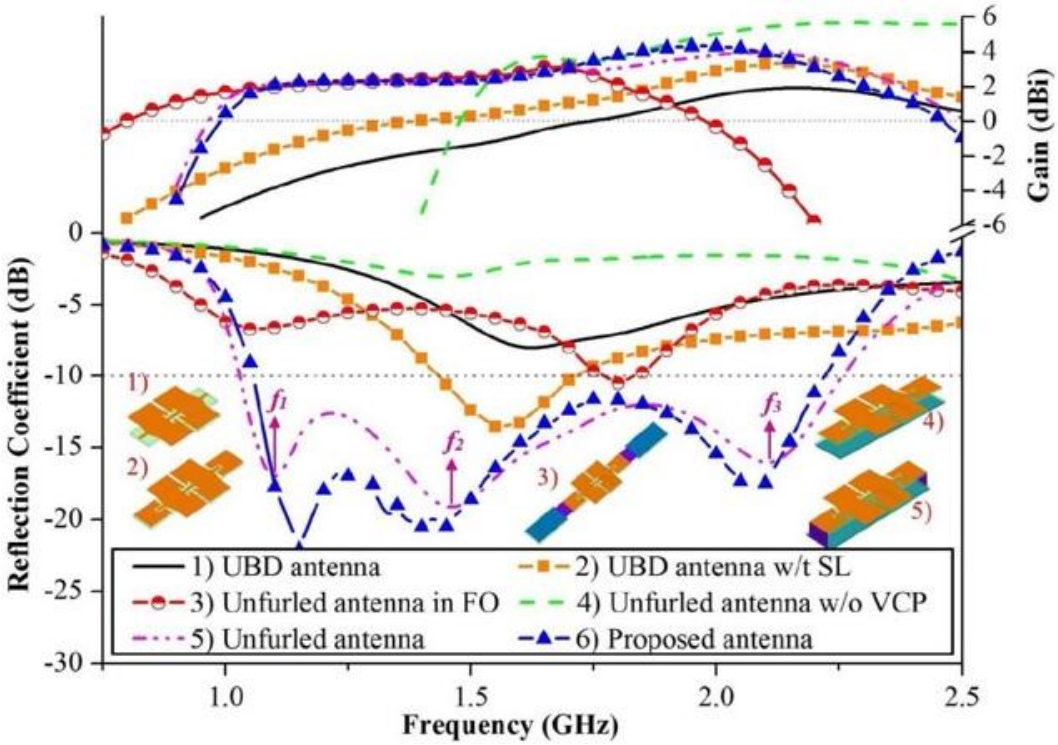

Fig. 3.58 Effects on the reflection coefficients and Z-directed gain of the proposed antenna in various orientations with and without different parts.

The effect of various parts of the antenna structure on the scattering parameter and radiation characteristics is exhibited in Fig. 3.58. Without the folded structure, the unfurled basic dipole (UBD) element (antenna-1) attains a resonance at 1.6 GHz. The addition of the slot-loaded (SL) capacitive coupling to the basic dipole (antenna-2) significantly improves impedance matching. In the flat orientation (FO), the proposed folded dipole antenna (antenna-3) generates a lower resonance at 1.1 GHz, which is due to the longer conducting path, created by the dipole mode in FO. Although these structures create promising resonances, they display omnidirectional radiation patterns. It is observed that without vertical copper plates (VCP), the unfurled antenna produces unidirectional radiation patterns with higher gain. However, with this structure, the antenna (antenna-4) becomes narrow-band with poor impedance matching. Thus, connecting the top and bottom layers with VW is crucial in achieving a wide impedance matching and directional gain as seen in antenna-5. Nevertheless, furling marginally shrinks the operating bandwidth. In extended simulations, it is noted that the optimum furling positions (F_h and F_l) are crucial for proper impedance matching of the antenna. The slight change in the proposed antenna's gain after furling can be attributed to the reduction in the effective radiating area at the top layer.

The resonating frequencies of the folded dipole with unfurled sides can be approximated by [64]:

$$f_1 = {}^{c}/_{2\{(2L - 2W_r - l_d + 10/g_d)\sqrt{\varepsilon_e} + 2h\}} \quad (3.14)$$

$$f_2 = {}^{c}/_{2\{((L + l_{d2})/2 + W_2 - 10 \square g_{d2} + 2 \square g_{f2})\sqrt{\varepsilon_e} + W_t - W_1\}} \quad (3.15)$$

$$f_3 = {}^{c}/_{2\{((L + l_d)/2 + W_1 - 10 \square g_{d1} + 2 \square g_{f1})\sqrt{\varepsilon_e} + W_t - W_1\}} \quad (3.16)$$

where f_1, f_2 and f_3 are the sequential resonances (Fig. 3.58), c is the speed of light, the width difference between the bottom and top layer, $W_r = W - W_1$, average length of basic dipole, $l_d = 0.5(l_{d1} + l_{d2})$, average length of the loaded-slot, $g_d = 0.5(g_{d1} + g_{d2})$, total width of the basic dipole antenna, $W_t = W_1 + 2(F_h + F_w)$. ε_e is the effective permittivity of the proposed antenna and ε_e can be estimated by,

$$\varepsilon_e = \left[1 + \frac{t_S}{h_a}\left\{a - b \ln\frac{W_1}{h_a}\right\}\left(\frac{1}{\sqrt{\varepsilon_r}} - 1\right)\right]^{-2} \quad (3.17)$$

which is adopted from the suspended-substrate microstrip lines [125] where $a = (0.8621 - 0.1251 \ln \frac{t_s}{h_a})^4$, $b = (0.4986 - 0.1397 \ln \frac{t_s}{h_a})^4$, t_s =total substrate thickness= $2t_s$ (see Fig. 3.58(c)) and h_a= height of the air-gap between the lower and upper substrates= $h - t_s$.

The overall size of the proposed antenna is 80×20×10 mm^3, which is equivalent to 0.29×0.08×0.04 λ_0^3, where λ_0 is the wavelength at the lowest operating frequency (1.1 GHz). Compared to the previously reported compact, directional antennas, the proposed antenna is at least 30% more compact in both of the volume [35, 64, 66, 98, 128] and profile [65], which makes it suitable to form a compact array for head imaging.

3.11.1.1 Frequency domain Results

The compact three-dimensional antenna is prototyped and its performance is characterized in both of the frequency and time domains. Since the antenna is aimed to operate in the near and far field regions for head imaging, the characterization is done in both of these regions.

The reflection coefficient and gain of the antenna is measured and compared to the simulated ones. From Fig. 3.59, it is observed that the prototyped antenna operates below -10 dB reflection coefficient from 1.1-2.2 GHz which is equivalent to 67% fractional bandwidth at 1.65 GHz. A good agreement between the simulated and measured plots is observed. The gain of the antenna along Z-direction (θ = 0˚, φ = 0˚) is also measured and a slight discrepancy is found between the simulated and measured values. It is observed that owing to the comparatively electrically smaller size of the antenna at lower frequencies, the gain at the low end of the operating band is relatively low. However, the gain rises gradually with increasing frequencies and the highest gain of 4.6 dBi is achieved at 2.04 GHz. The antenna exhibits an average gain of 3.15 dBi over the band of operation. The results in Fig. 3.59 (a) show that antenna's simulated directivity is very close to the simulated gain, indicating high radiation efficiency. Using the well-known relation between those two parameters, it is possible to verify that the antenna attains more than 90% radiation efficiency over the operating band.

Fig. 3.59(b) demonstrates the measured E- and H-plane radiation patterns of the antenna at 1.2, 1.5, 1.8 and 2.05 GHz. It is noted that the antenna emits in a unidirectional manner along the Z-axis (θ = 0˚, φ = 0˚). H-plane radiation patterns of the antenna exhibit consistently wider beam-widths along the boresight direction than those of E-plane. No side-lobes in the radiation patterns are observed indicating the absence of higher modes of current distribution that, if present, creates current nulls on the top radiating element owing to the compact electrical size of the antenna. Similar patterns are also found in simulations, but not plotted for sake of brevity. More 10 dB cross-polarization level is

observed along the Z-axis in both E- and H-planes which assures high polarization purity along the intended direction radiation.

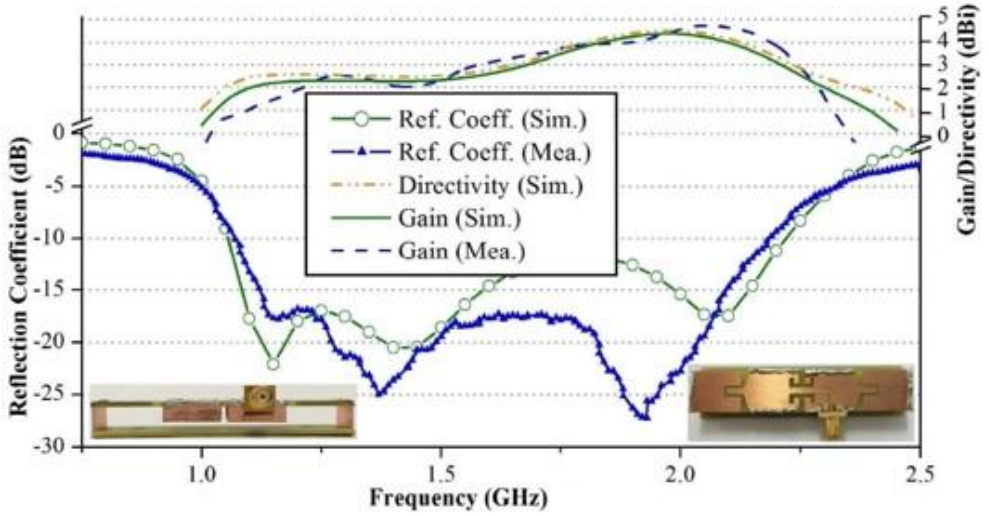

(a)

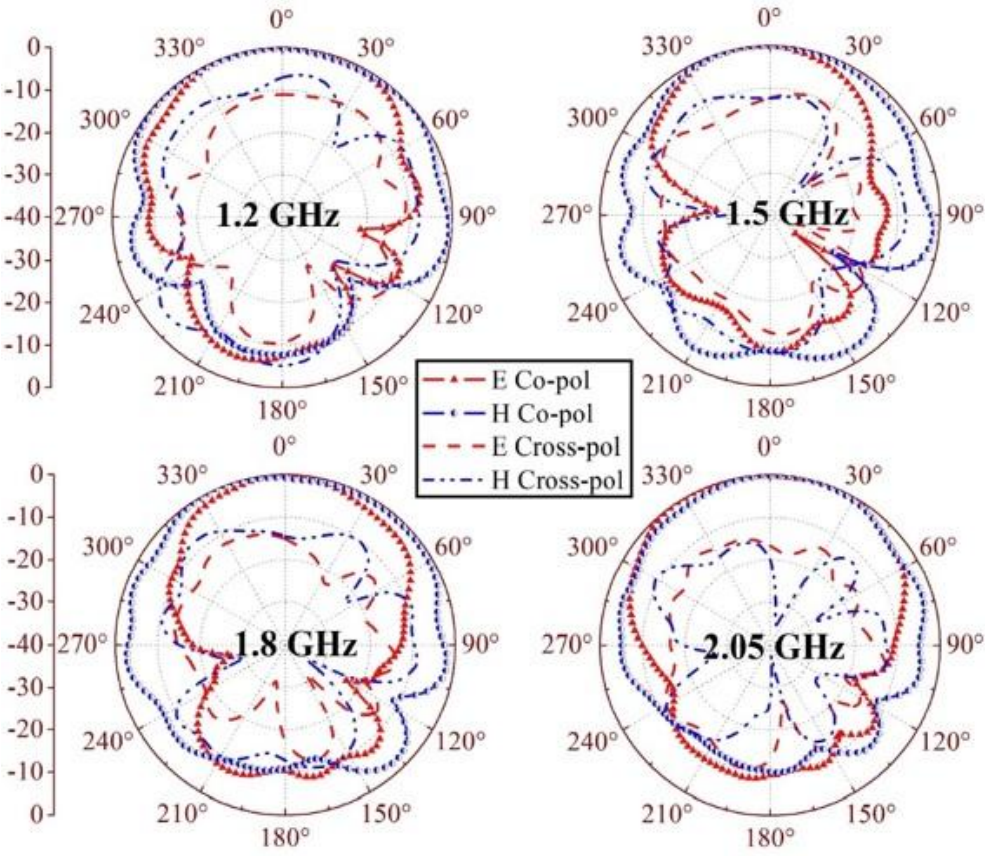

(b)

Fig. 3.59 (a) Input reflection coefficient and Z-directed ($\theta = 0^{\circ}$, $\varphi = 0^{\circ}$) gain with inset depicting the prototype. (b) Measured Co- and cross-polarized radiation patterns of E-(XZ) and H-(YZ) planes at 1.2, 1.5, 1.8 and 2.05 GHz.

3.11.1.2 Time domain Results & Discussions

Since the antenna operates in both of the far and near fields in head imaging, the near field characterization is necessary to complete its performance evaluation. To reduce the mutual coupling and increase the measured E-field accuracy, an E field probe based measurement setup is adopted for the near field radiation pattern measurement of E- and H-planes. The measurement setup is illustrated in Fig. 3.60(a). An Aaronia E near field, calibrated from DC to 9 GHz, is utilized to measure the E-field in a circular manner, which is achieved by rotating the mounted platform of the designed antenna under test using an in-house built step-motor controller (SMC). A vector network analyzer (R&S ZVA 24) captures the E-field from the probe placed at 10 cm away from the antenna. High quality coaxial cables and adequate calibration are utilized to reduce the losses. An amplifier can be optionally used to enhance the received field strength, especially at the high end frequencies that are vulnerable to high attenuation. The VNA and motor controller are interfaced with and controlled by a personal computer (PC).

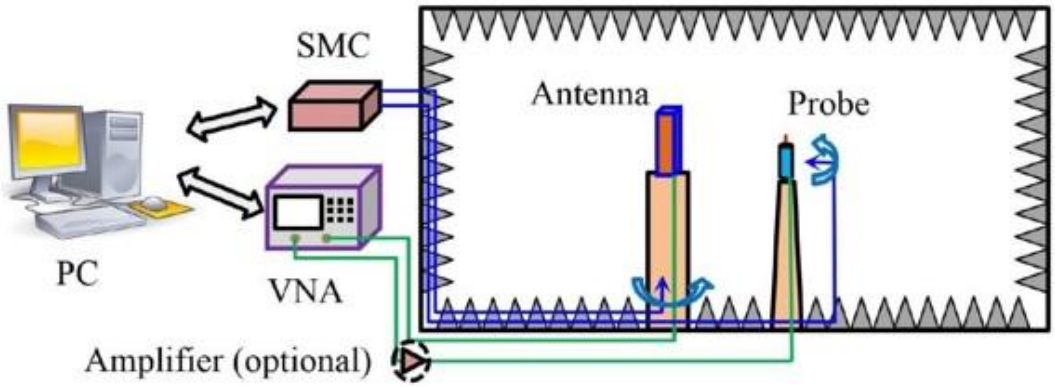

(a)

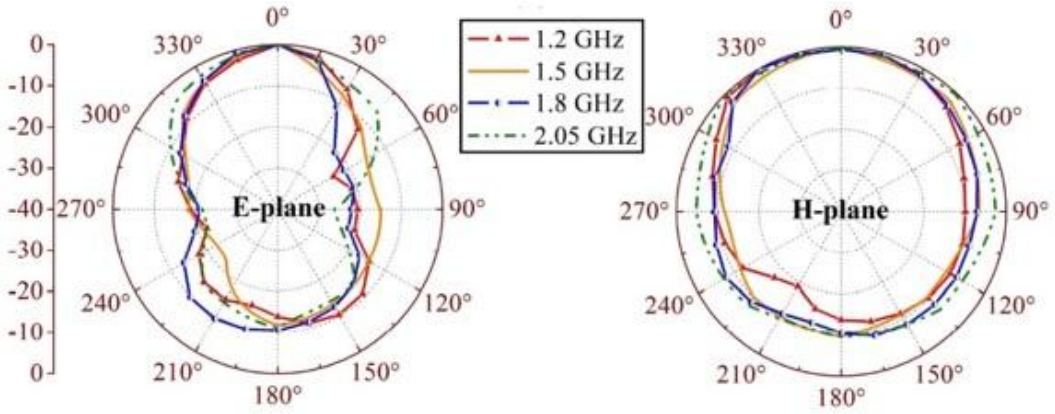

(b)

Fig. 3.60 (a) Near-field radiation pattern measurement system in an anechoic chamber and (b) measured near-field radiation patterns of the E-(XZ) and H-(YZ) planes at different frequencies.

The measured normalized E- and H-plane near field radiation patterns at 1.2, 1.5, 1.8 and 2.05 GHz are shown in Fig. 3.60(b). Both E- and H-plane near field radiation patterns are stable over the operating band. Although symmetrical radiation patterns are attained in the far field, a slight deviation from symmetry along the Z-axis is noted in the near field radiation patterns. That deviation can be attributed to the increased effect of the SMA connector in the near field. High polarization suppression is also observed from the cross-polarization measurements (not shown for brevity). However, more importantly, the antenna demonstrates unidirectional radiation patterns along the Z-direction in the near field. A front to back ratio of more than 10 dB is observed in the E- and H-plane measured near field radiation patterns.

As the antenna is slot-loaded and folded, it might suffer from high distortion [122, 134]. Hence, the time domain characterization is of great importance to evaluate the pulse-shaping feature of the prototyped antenna and level of distortion generated by the antenna across the utilized band. Although the time domain characterization using time domain measurements (transmitting and receiving ultra-short pulses) is faster, the characterization is performed by post-processing frequency domain measurements to time domain owing to the advantageous high dynamic range of frequency domain measurements [124].

To measure the received pulse in the far-field, the prototyped antenna is placed on the rotating platform of the anechoic chamber [121, 123]. A linear polarized horn antenna with known characteristics is utilized as the receiving antenna. The system is calibrated, and using a vector network analyzer, complex transmission coefficient or transfer function ($S_2\ (\omega)$) of the antenna is measured. The transmission coefficients are calculated in different angles of E- ($\varphi = 0^{\circ}$) and H- ($\varphi = 90^{\circ}$) plane with an angular resolution of $\Delta\theta = 15^{\circ}$.

For the post-processing, a time domain modulated Gaussian pulse covering the operating band is generated as the antenna's excitation waveform, which is shown as inset of Fig. 3.61(a). A fast Fourier transformation (FFT) of the input pulse is multiplied with the transfer function of the antenna. Taking the inverse Fourier transformation (IFFT) of the resultant signal yields the complex function, while its real part is taken as the intended transient response of the antenna [122].

Owing to the imperfect pulse-shaping filtering capability of the antenna and the channel, the transient response of the antenna gets distorted and dispersed compared to the input pulse. The level of distortion in the time domain pulse generated by the antenna can be quantified by calculating fidelity factor, $F(\theta, \varphi)$ which can be expressed as [58],

$$F(\theta,\varphi) = \max_{\tau} \int_{-\infty}^{+\infty} U_n(t) R_n(t-\tau,\theta,\varphi) d \qquad (3.18)$$

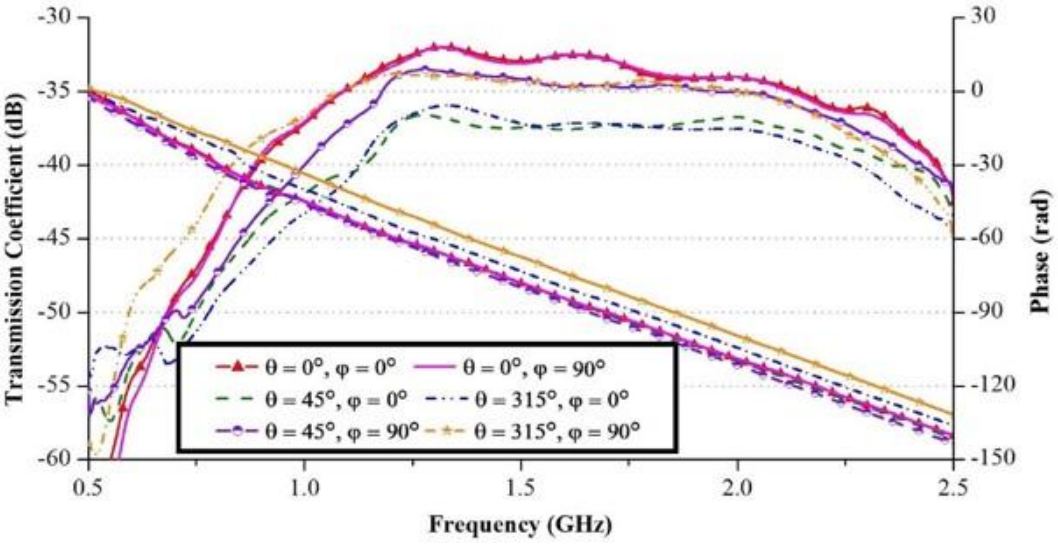

(a)

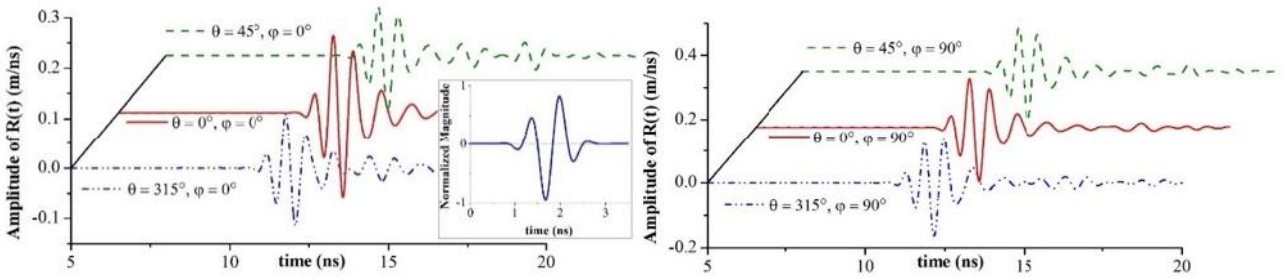

(b) (c)

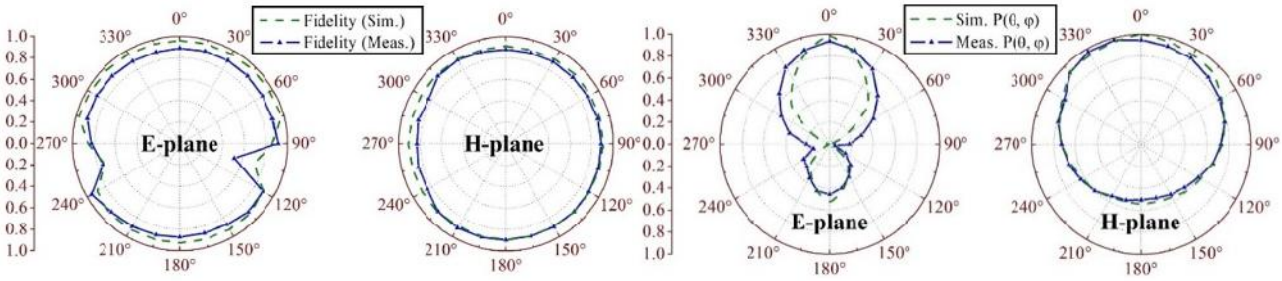

(d) (e)

Fig. 3.61 (a) Magnitude and phase of received transmission coefficient at different angles. Measured far-field transient responses of (b) E- and (c) H-planes with inset illustrating the input short pulse. Quantitative analysis of the transient responses in far-field: (d) fidelity factor and (e) combined $P(\theta, \varphi)$ patterns in E- and H-planes.

where $U_n(t) = \frac{U(t)}{\sqrt{\int_{-\infty}^{+\infty}|U(t)|^2 d}}$ is the normalized input signal, and $R_n(t-\tau,\theta,\varphi) = \frac{R(t-\tau,\theta,\varphi)}{\sqrt{\int_{-\infty}^{+\infty}|R(t,\theta,\varphi)|^2 d}}$ is the normalized transient response of the antenna. Minimum distortion between the input and received

signals is attained when $F(\theta, \varphi)$ is maximum. The fidelity factor of the antenna only conveys signal correlations in different directions and ignores amplitudes due to normalization. To accumulate these two characterizations of the transient response, a combined matrix $P(\theta, \varphi)$ is defined as [123],

$$P(\theta, \varphi) = \frac{P \quad _R(\theta,\varphi)F(\theta,\varphi)}{\mathrm{m}_{\theta} \ (P \quad _R(\theta,\varphi)F(\theta,\varphi))} \tag{3.19}$$

Here, the peak values of individual received signal are normalized on that plane (φ constant) for comparative realization of the radiation capability. Values of $P(\theta, \varphi)$ close to unity indicate higher power transmission capability with low distortion in the time domain.

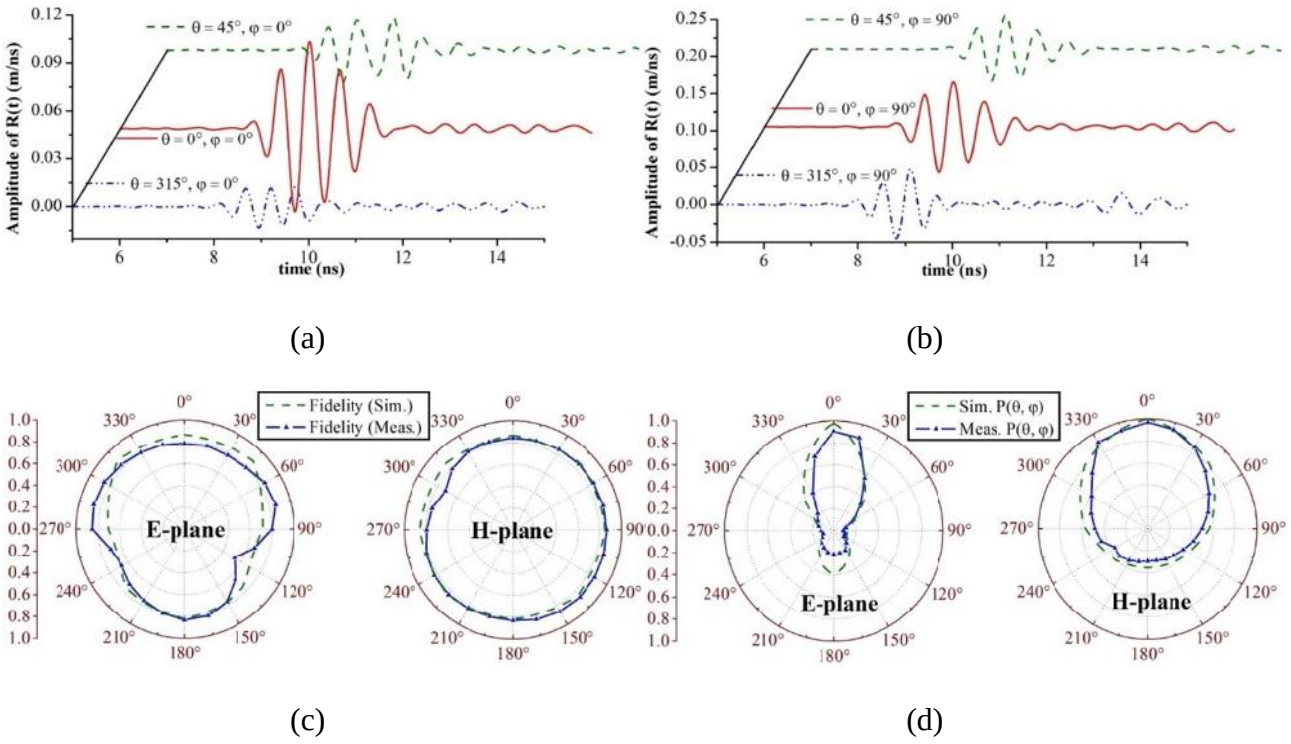

Fig. 3.62 Measured near-field transient responses of the prototyped antenna at various angles of (b) E- and (c) H-plane. Simulated and measured quantitative analysis comparisons of the near-field transient responses of the antenna: (d) fidelity factor and (e) combined $P(\theta, \varphi)$ patterns in E- and H-planes.

Fig. 3.61(a) illustrates the magnitude and phase of the measured transmission coefficients (S_2) in different directions. It is noted that the magnitude of S_2 is higher along the boresight direction. A linear phase, which assures constant time delay in the time domain, is observed. The received transient responses of the antenna in the far field are depicted in Fig. 3.61(b, c). The amplitude of the received pulses decays as the angles deviate from the boresight direction. The measured time domain

results are also compared with the simulated ones by using FDTD based electromagnetic software CST Microwave Studio. The measured time domain pulses closely match the simulated results. However, for the sake of illustration simplicity, they are not presented here. The measured and simulated fidelity factor inspection (Fig. 3.61(d)) shows that the antenna generates almost omnidirectional dipole-like $F(\theta, \varphi)$ patterns in both of the E- and H-planes. More than 85% fidelity factors is observed along the Z-direction. Finally, the combined matrix $P(\theta, \varphi)$ patterns of E- and H-planes are presented in Fig. 3.61(e). It is noted that in the far field, the main beam of the antenna is directed along Z-axis. The half power beamwidth of H-plane is wider than that of E-plane. A front to back ratio of 2.7:1 is observed along the main beam.

The time domain characterization of the antenna is also performed in the near field. An E-field probe is utilized to collect the data. The received time domain signals shown in Fig. 3.62(a, b) demonstrates low level of ringing generated by the antenna. The magnitudes of the received signals tend to gradually reduce with increasing angles from the Z-axis. The measured signals are similar to the simulated results. The measured and simulated fidelity factor patterns are compared and displayed in Fig. 3.62(c). Owing to the near-field radiation mechanism, the omnidirectional dipole-like nature of the $F(\theta, \varphi)$ patterns noted for the far-field is changed in the near-field and the antenna radiates less distortedly (fidelity factor > 80%) along the front direction. Slight deviation of the simulated and measured $F(\theta, \varphi)$ is attributed to the fabrication limitations and the effect the connector. The combined $P(\theta, \varphi)$ patterns of E- and H-planes (Fig. 3.62(d)) represent the directional transient responses emitted from the antenna. A front to back ratio of approximately 4:1 is found along the Z-direction.

3.11.2 Design and development of Optimized Slot-loaded Compact Antenna

For unidirectional operation, the typical patch type antennas require large ground plane that increases the weight of the array and unsuitable for the current application [96, 100, 135]. The presented antenna of the previous section meet all the requirements, but still able to allocate a limited number of elements in the array owing to its wider bottom layer which contributes to mutual-coupling between elements and affects the impedance matching due to the position of the neighbouring antennas and consequently results degraded imaging performance. Reducing the width of the sensing antenna is one of the ways to increase the number of elements in the array, however, this procedure significantly affects impedance matching performance of the antenna, which ultimately makes it narrow/multi-band [136]. The proposed antenna demonstrates an effective way of miniaturization which enable the system to house 16 elements with low mutual coupling effects.

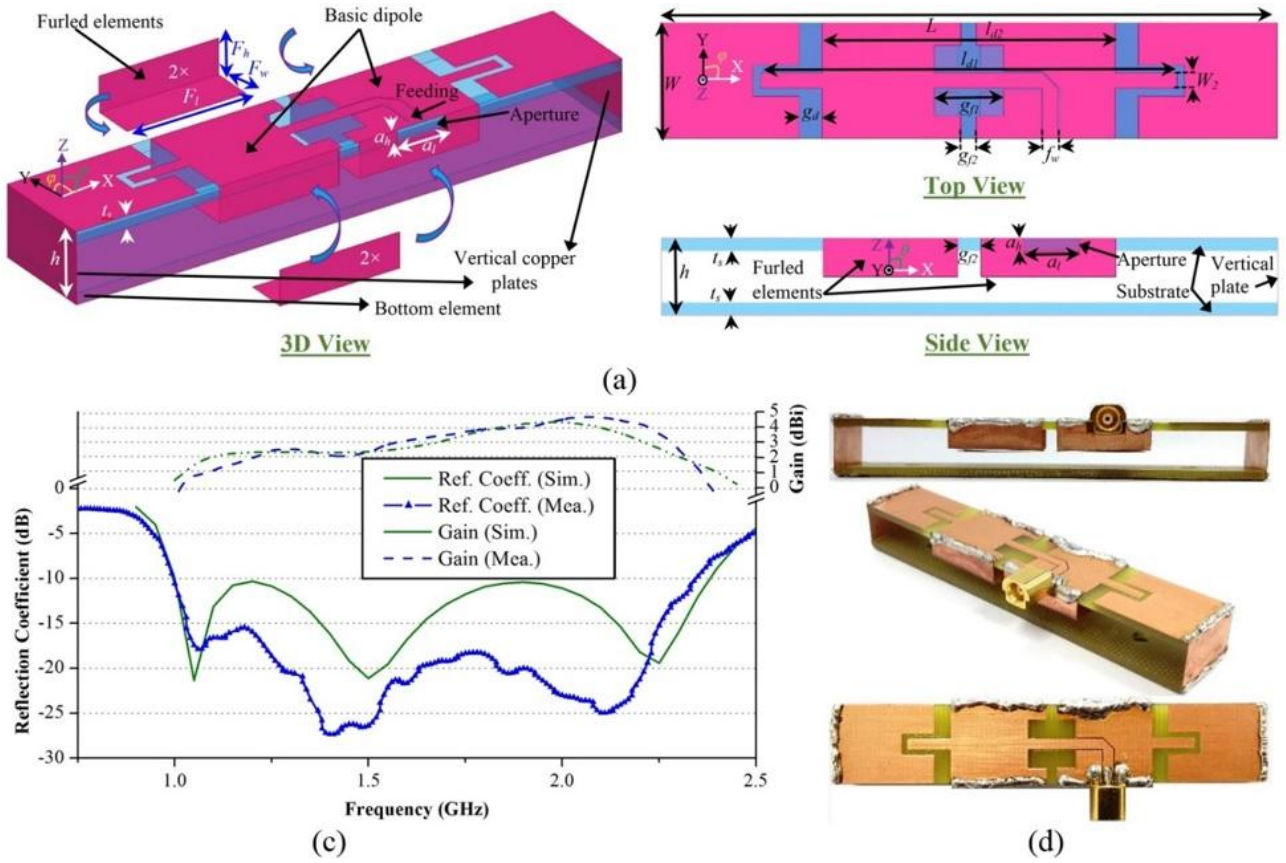

Fig. 3.63 (a) Schematic diagrams of the designed antenna showing the 3D, top and side views and indicating the detailed dimensions of different parts. (b) Comparison between the measured and simulated reflection coefficient and gain versus frequency performance of the antenna over a wideband. Very low deviation in measurement from the simulated results is observed. (c) Different perspectives of the prototyped antenna illustrating the multiple soldering connections required for fabrication.

Fig. 3.63(a) illustrates the geometry of the proposed compact antenna. The antenna is printed on two-slabs of low-cost glass-reinforced epoxy substrate with dielectric constant, ε_r = 4.4, loss tangent, $tan\delta$ = 0.0245 and thickness, t_s = 1.6 *mm*. The top and bottom slabs are connected with two vertical copper plates at the opposite sides along X-axis, creating a ring-like structure. The proposed antenna is based on a typical slot-loaded folded dipole structure presented in Section 3.7. The top side contains the basic dipole structure and the rest of the ring-like structure acts as a slot-loaded parasitic element. Four L-shaped copper plates are connected with the flares of the basic dipole, converting the sides of the antenna furled into its own structure. This furling technique effectively reduces the width of the folded dipole antenna and helps in increasing the number of elements in the array. As the arms are furled inside the antenna, their dimensions are optimized to attain less intra-coupling effects with the top and bottom layers. It is noted that increasing or decreasing the height of the furled arm will

encounter intra-coupling which worsens the impedance matching of the antenna. The optimized antenna is prototyped and measured.

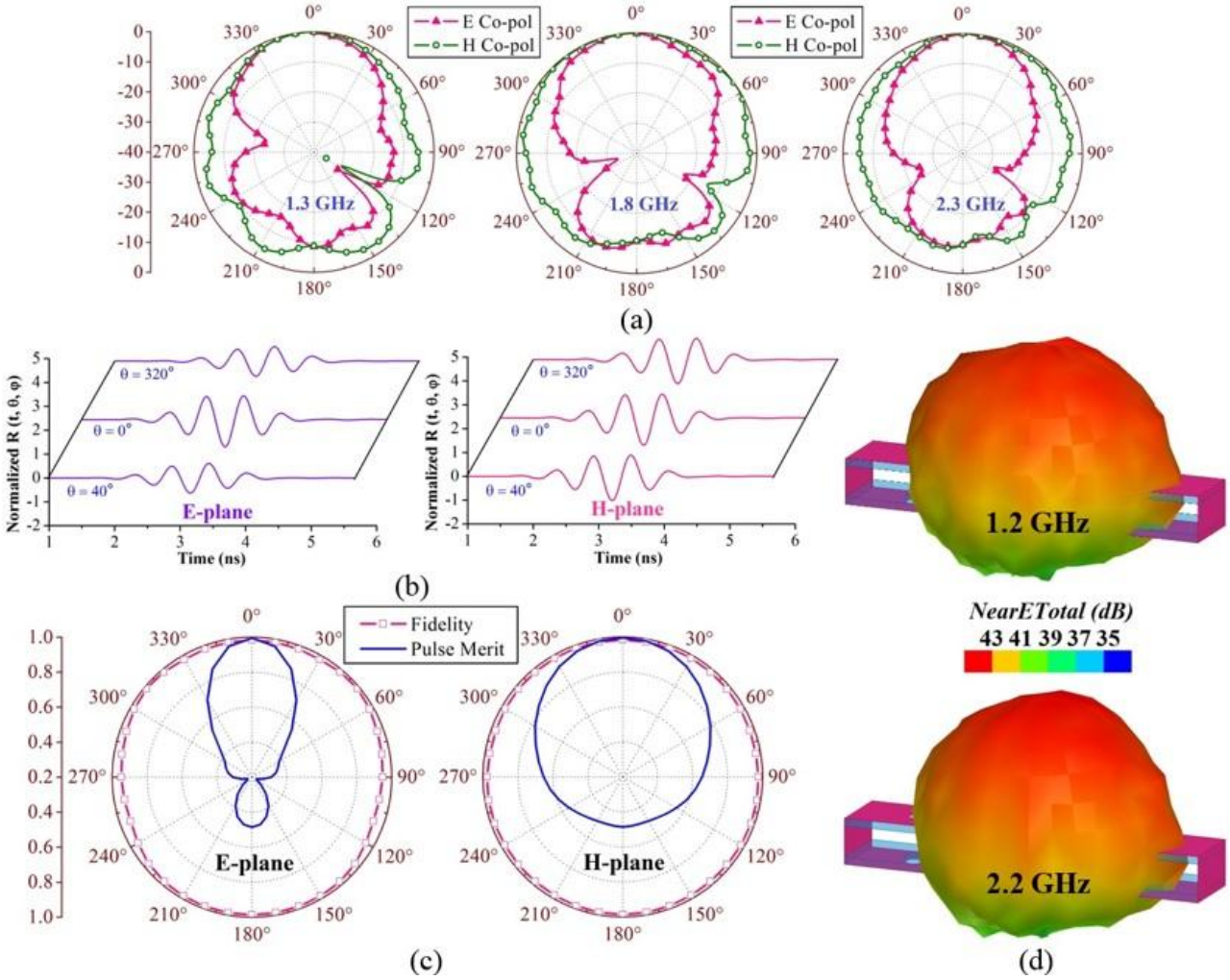

Fig. 3.64 (a) Measured radiation patterns of the prototyped antenna at 1.3, 1.8 and 2.3 GHz in both E- and H-planes. (b) Simulated 3D radiation patterns of the antenna at 1.2 and 2.2 GHz. (c) The time-domain signals received by the probes placed around the antenna in different angles on both E- and H-planes. (d) The fidelity and pulse merit factor patterns of the wideband antenna in E- and H-planes resulted from the transient analysis.

It is noted from Fig. 3.63(b) that the prototype operates over the band from 1-2.4 GHz, which is approximately 83% fraction bandwidth with respect to the center frequency of 1.7 GHz. This wide bandwidth is resulted by the accumulation of three different resonances. Different lengths of the antenna dimensions mostly define the resonating frequencies. The antenna length L primarily determine the first resonance, while the second resonance is regulated by the longer extent, l_{d1} of basic dipole and the third resonance is mainly created by the smaller extent, l_{d2} of basic dipole. Extended current distribution analysis indicate that the antenna operates in loop mode in the lowest resonance and in folded-dipole mode in the subsequent modes. Different dimensions of mentioned in

the schematic diagram are (in *mm*) : L = 80, W = 10, h = 10, l_{d1} = 54, l_{d2} = 38, W_2 = 2, a_h = 2, a_l = 7.2, F_h = 5, F_w = 6, F_l = 17.5, g_{f1} = 9, g_{f2} = 3, g_d = 3, f_w = 2. The overall dimension of the antenna is 10×10×80 mm^3 , which is equivalent to 0.033×0.033×0.27 λ_0, where λ_0 is the wavelength at lowest operating frequency (1 GHz). As demonstrated in Table 3-X, the proposed antenna is very low profile and has smaller width when compared to the recently reported literature.

Table 3-X: Comparison between wideband antennas

Antennas	Fractional bandwidth with respect to center frequency (%)	Relative antenna dimensions (Compared to lower frequency wavelength)			Additional ground plane?
		Length	Width	Height	
[66]	77	0.33	0.25	0.07	No
[115]	83	0.66	0.17	0.08	Yes
[117]	128	0.57	0.29	0.19	No
[65]	109	0.26	0.11	0.05	No
[128]	100	0.27	0.2	0.07	No
[64]	57	0.24	0.1	0.05	No
[35]	63	0.29	0.12	0.06	No
This Work	83	0.27	0.033	0.033	No

The radiation performance of the antenna is also measured. It can be noted from Fig. 3.63(b) that the antenna attained an average gain of around 3 dBi over the operating band. The gain performance is lower in lower frequencies, which is due to the electrically small dimensions of the antenna in those frequencies compared to the higher frequencies. The radiation patterns of the antenna is measured in anechoic chamber and reported in Fig. 3.64(a). It is seen that the antenna radiates with directional radiation patterns in both E- and H-planes having an average front to back ratio of 9 dB along the direction of radiation (+ve Z-axis). The simulated 3D near-field radiation patterns of 1.2 and 2.2 GHz are also presented in Fig. 3.64(d), where unidirectional radiations is also observed, which assures the compatibility of the antenna in head imaging system. Again as the imaging system is based on the time-domain algorithm, the transient characteristics of the antenna is also analysed in the near-field region, 10 cm away from the antenna surface. The received time-domain signals (Fig. 3.64(b)) illustrate that the antenna transmits visually similar wideband transient signals with gradually reduced amplitudes from $\theta = 0^\circ$ in both E- and H-planes of. In order to quantify the transient pulses received from the antenna the fidelity factors and pulse merit factors of the received signals are calculated.

From Fig. 3.64(c), it is seen that the time-domain signals radiated by the antenna has more than 90% pulse fidelities compared to the input signal at the feeding point. This translates that the antenna is highly efficient in transmitting wideband pulses. The pulse merit factor patterns which indicate the total time-domain pulse radiation of the antenna [137], demonstrate that the antenna is also unidirectional for transient signals in both E- and H-planes and suitable for systems relying on time-domain based imaging algorithms.

3.12 Conclusions

This chapter discussed the requirements of the antenna elements for microwave head imaging systems and several antennas are presented for the applications. Both omni-directional and directional antennas are proposed. An antenna miniaturization technique utilizing the plane of symmetry and based on image theory is presented which can be generalized for antennas having both microstrip and co-planar waveguide feeding methods. The operating and radiation mechanism of the miniaturization technique is explained with the help of the characterization mode analysis. A compact omni-directional antenna based on the plane of symmetry is also introduced afterwards. Furthermore, a folded antenna having directional performance in wide operating frequencies is presented. The plane of symmetry is also applied on it and it is seen that even if the antenna takes half the volume of the previous one, it does not compromise the penetration capability, which is attained by the lowest operating frequency and achieves directional radiation patterns over the wide operating band. A near-field time-domain characterization is proposed and it is seen that the directional antennas are more suitable for current application where the antennas mostly operates in near-field. Hence, concentration is given in designing directional antennas for the head imaging systems. A slot-loaded dipole antenna is proposed as more compact solution for directional and wideband operation. It is seen that by different types of feeding and optimization objectives, e.g. antenna profile, operating bandwidth etc. of and this type of antenna has the potential to satisfy the antenna requirements of practical head imaging systems. Afterwards, a cross-feeding technique is presented to be an effective way for correcting the beam-tilting limitation of half-cut antennas. Finally, multi-folding techniques are introduced to reduce the sizes of wideband directional antennas. The design procedures of all antennas are elaborated with supporting theory behind them. The antennas are prototyped and performances are verified by both frequency and time-domain analysis for both near and far-field radiations. The imaging performance of these antennas are discussed in Chapter 6 and 7.

Chapter 4 - Realistic Human Head Phantom

This chapter firstly introduces the motivation of a realistic human head phantom by depicting the limitations of existing validation scenarios and the differences between them and the practical situations. Different phantom types are presented and their advantages along with their limitations are discussed. The features and functions of different ingredients typically used in phantom fabrications are also illustrated. Finally, the fabrication process of a 3D human head phantom is discussed in details which is targeted to be applied in head imaging systems.

4.1 Motivation of Using Realistic Human Phantoms

Quantitative and explicit validation of the performance and safety of microwave systems and devices that have electromagnetic interaction with the human body are critical factors of the technological development process. Although a numerical model of the system environment can be ideally simulated, it cannot reflect the realistic environment which is vulnerable to various electrical, mechanical and environmental interferences. Hence, the presence of human body is the best measurement environment for these systems. However, newly designed devices/systems that rely on the human body-electromagnetic fields interactions require multiple tests/measurements under a controlled environment. That environment is needed to validate the performance at all the possible scenarios of operation, and make sure of the safety of those devices and systems. For example, a breast imaging system is needed to be evaluated by detecting tumors in multiple locations and it is unthinkable to do that on a real patient; hence breast phantoms are demanded in order to obtain optimum system design and algorithms before moving to human clinical trials. Moreover, some experiments, such as specific absorption rate (SAR) and hyperthermia cannot be done on human beings due to the need to monitor variation of power intensity and temperature inside tissues. Employing live human participants for testing devices exposes the entire test procedure to several inherent uncertainties, such as respiratory movement, cardiovascular vibration and variable skin humidity in addition, of course, to the safety concern of the new devices. Also, application of the devices and systems on human subjects or human-related materials is a serious ethical issue where the researchers must receive an ethical clearance from proper authorities, and it can be difficult to reasonably estimate and investigate the level of risks from various scientific, physical and psychological aspects beforehand. Thus, the utilization of artificial tissue emulating (ATE) phantoms is much beneficiary for the testing purpose of a device or system.

Emulating a human organ or tissue with an exact substitute requires an accurate artificial phantom that is expected to have several features: anatomically realistic, dielectric precision across the band of interest and long lifetime. The anatomic distribution of various tissue layers in the phantom has to

be accurate to analyse the real scenario. This is especially important if the application is heavily dependent on the constitution of the body part, like microwave head imaging applications. The electrical properties of the phantoms are essential to mimic the real situation. The properties of the ATE materials are compared with those of actual tissues over the band of interest. Lifetime of the phantom is particularly important for the repeatability of experiments and continuation of research. The shape and tissue distribution as well as the dielectric properties of the appropriate phantom has to be stable over a sufficiently long time.

Despite the heterogeneous anatomic tissue distribution of human body, the electrical properties (permittivity, ε_r and conductivity, σ) of various tissues of the human body are vastly different according to their types. The properties also vary in wide range with respect to operating frequencies. Several researchers have systematically measured the properties for various tissues of the body [138-142]. Table 4-I lists the range of values of the electrical properties (dielectric constant, or relative permittivity, and conductivity) of fourteen different main tissues of the human body for the frequency range of 500 MHz to 10 GHz as extracted from [140, 141]. It is noted that since various studies are not taken from the same samples or subject and as the dielectric properties of some tissues vary from individual to another and with age, the values presented in [138-143] are slightly different from each other with a reasonable tolerance level [143]. However, it needs to be acknowledged that whilst various human ATE materials and body phantoms have been designed and reported by idealizing different sources, they in fact represent human tissues in different scenarios [144, 145].

Table 4-I: Electrical properties of different main tissues of the human body across the band 500 MHz to 10 GHz.

Tissues	**Muscle**	**Blood**	**Fat**	**Nerve**	**Grey Matter**	**White Matter**	**Lung Inflated**
ε_r	56.5-42.8	63.3-45.1	5.54-4.6	34.5-23.8	56-38.1	41-28.4	23.2-16.2
σ(S/m)	0.8-10.6	1.38-13.1	0.04-0.6	0.5-6.03	0.8-10.3	0.47-7.3	0.4-4.21
Tissues	**Dura**	**CSF**	**Bone**	**Heart**	**Tongue**	**Vitreous Humour**	**Dry Skin**
ε_r	46-33	70.1-52.4	5.6-4.6	64-42	57-41.5	69-58	45-31.3
σ(S/m)	0.9-8.6	2.3-15.4	0.03-0.6	1.02-11.8	0.8-11.1	1.54-15.1	0.73-8

There are very few experiments announced in the literature claiming microwave imaging on realistic human head. The reported experiments involve over-simplified systems and head phantoms [55, 146-

148]. These studies utilized head phantoms with simplified structures where the heterogeneity and dispersive properties of complicated head structure is neglected as well as the contrast of electrical properties between the normal head tissue and hemorrhagic target is overestimated for the sake of the detection. Although some recent innovations described head phantoms with dispersive electrical properties, still they lack the details of human brain constructions [21]. It can be inferred that wrong head phantom can lead to incorrect decision regarding the brain injury. Hence there is a pressing need of realistic human which extensively imitates real human head. Such human phantom will play an important role to implement various test techniques and imaging algorithms; besides, it will be useful to realize a successful pre-clinical head imaging test bed.

4.2 Phantom Material Types – Advantages and Limitations

ATE materials can be classified in various types from different perspectives. Depending on the electrical properties, they can be of low-water-content and high-water-content ATE materials [138, 149]. While that classification gives a useful information on the suitability of a certain ATE type to emulate a specific tissue, it does not provide any opinion on the benefits of using a specific type of ATE material over other types. In order to analyse the pros and cons of different types, the ATE materials are divided into four kinds according to their physical appearance.

4.2.1 Liquid ATE Materials

Tissues with high water content, such as muscle and main brain parts, exhibit high electrical properties. One way to closely mimic those tissues is to use water, which is usually utilized in ATE materials as the main source of high permittivity, as the basis of liquid mixtures. The main advantage of liquid ATE materials is the easy preparation by mixing different components according to an appropriate recipe. The preparation procedure of several liquid ATE materials is discussed in [150]. Fig. 4.1 illustrates the generalized flow chart for the fabrication of a muscle equivalent ATE material. A gentle heating is applied at the early fabrication stages to warm up the solution and enable creating the required solutions faster, although a keen observation to the temperature has to be maintained to reduce the evaporation of water caused by the heat.

To fabricate ATE materials of low permittivity, like fat and bone, a low percentage of water is used in the recipe. Several oil-in-water emulsions are reported in the literature for low-water-content ATE materials [150]. Another technique is to mix salted water with various nonionic surfactants (e.g. Triton X-100) [151].

The ATE liquid mixtures have some inherent disadvantages. It is difficult to maintain consistency of the material properties, as the materials tend to dehydrate, which drastically alters the relative

permittivity and conductivity. Moreover, the mold growth might spoil the material by changing its electrical properties.

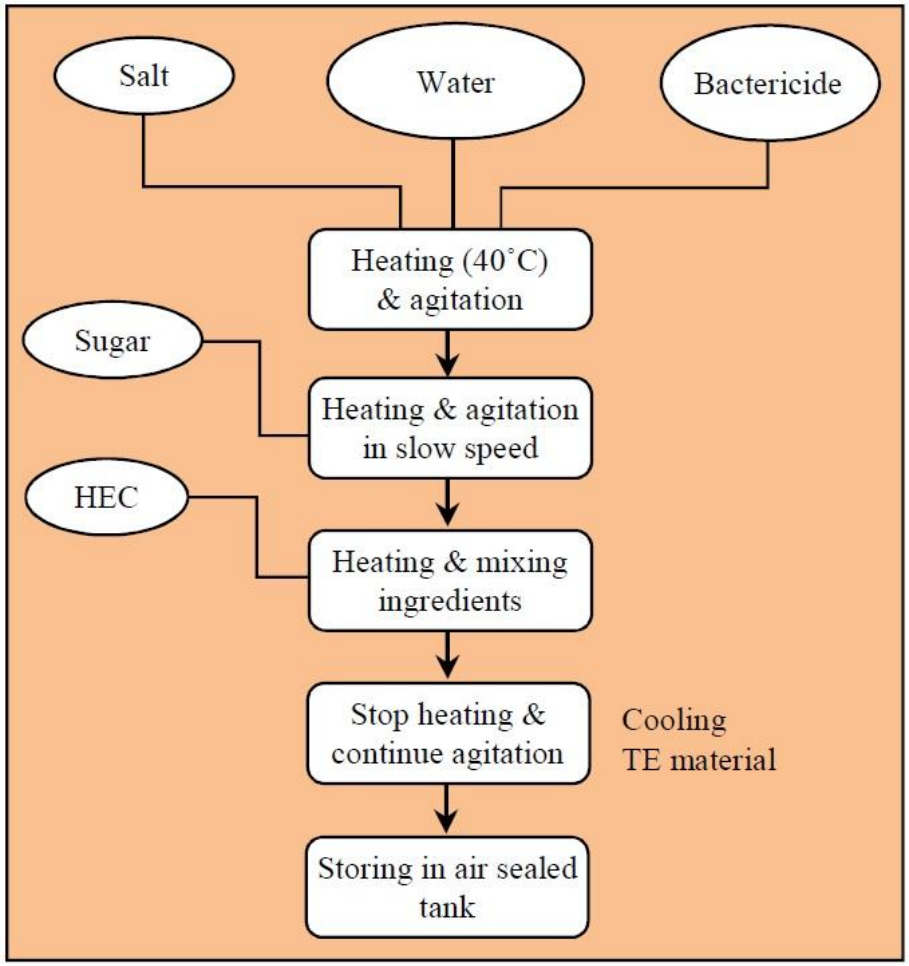

Fig. 4.1 An outline of liquid muscle ATE material fabrication.

The moist materials are kept in shape using defining containers. Thus, a difficulty is imposed by the container at the time of emulating invasive or in vivo tests, such as implantable radio frequency components. The direct estimation of SAR on the phantom surface is also difficult to attain. In microwave imaging, for example, if the containers are not built from a material of suitable electrical properties, they are more likely to produce high scattering, which may jeopardize the validity of the experiments.

The components used to build liquid-based ATE materials are not usually dissolvable. Thus, to attain the desired electrical properties, the solution should be stirred properly until it becomes homogeneous. However, the used components in the solution tend to get separated forcing stirring the solution again; although early separation of the components exhibits minor changes in the electrical properties [152].

4.2.2 Gel ATE Materials

Gel or semi-liquid ATE materials are more solid of course than liquid materials, but cannot hold its figure independently without a container or shell. These types of mixtures overcome the component separation problem of the liquids and sustain homogeneity over a long period. The fabrication procedure of these ATE materials are also straight-forward. A flow diagram of gel type muscle material as mentioned in [153] is depicted in Fig. 4.2. It is seen that the mixing is controlled using various rotation speeds as the mixture gradually becomes thicker. At the end of the procedure, the ATE material turns into a gel type substance, which is then poured into a phantom container.

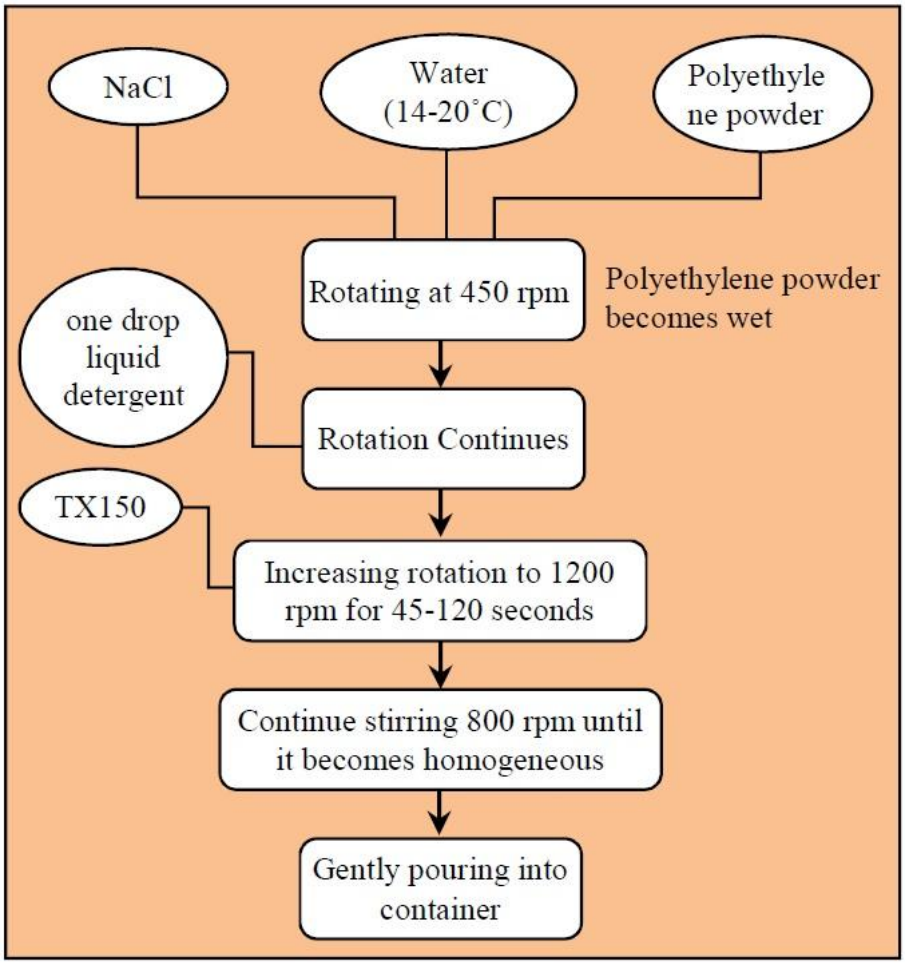

Fig. 4.2 An outline of gel type muscle ATE material fabrication.

Along with the advantage of the gel ATE materials, they demonstrate the rest of the weaknesses of liquid ATE materials. Besides, there are some other issues. This type of ATE material take some time to form as gel's most undesirable feature is its variable setting time, which may extend to 1 day [153]. This variation may not be a serious problem to many applications, but it could disrupt the rapid phantom prototyping procedure and validation of the intended system.

As the ATE material is thick and prepared by continuous rotation, this type of material tends to trap air bubble during the fabrication. Hence, slow and consistent rotations should be applied at the end of the process to avoid the bubble formation.

4.2.3 Semi-solid or Jelly ATE Materials

Semi-solid or jelly ATE materials are capable to conform to any shape independently. This castable attribute of these materials is particularly beneficial to emulate the realistic situation of soft tissues, where the tissue layers have a particular form and pattern. Moreover, no osmosis is seen to be occurred between adjacent layers when multiple types of semi-solid ATE materials are placed one after another. As a result, the electrical properties are found to be stable in the investigations [154]. This feature allows the phantoms to be constructed in a multi-layered fashion, which reflects the anatomical structure of the human body reasonably well. The castable and non-diffusive natures are primarily because of the addition of right proportion of gelatin, agar or dough to ATE materials which also assist in adjusting the electrical properties of the final material. The fabrication process involves weighing the ingredients separately, heating of water by accordingly adding various components in different temperatures and finally mixing the preservative elements before cooling down to room temperature for storing or experimental purpose. A generalized graphical diagram of the fabrication procedure of semi-solid ATE materials is illustrated in Fig. 4.3 following the procedure explained in [155].

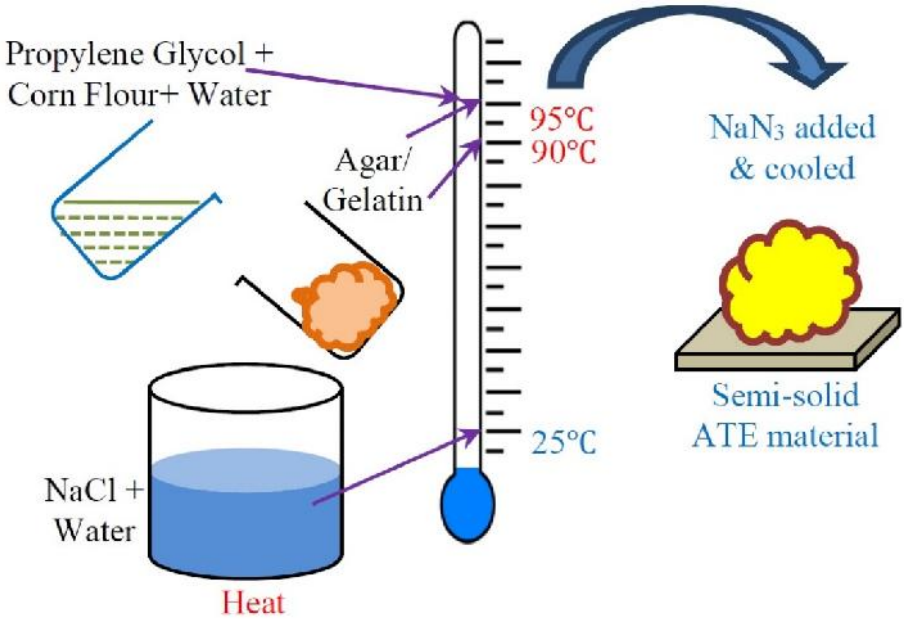

Fig. 4.3 A generalized diagram of gel type brain ATE material fabrication.

The semi-solid ATE materials are relatively low-cost and are able to mimic human tissues over a wide frequency band. However, they also have some limitations. Although this type of material is useful in medical imaging purposes, experiments which require invasive measurements (e.g. SAR measurements, implantable devices, hyperthermia etc.) become complicated with this tissue type as altering measurement position results in deformation of ATE layers.

Unlike the liquid and gel ATE materials, semi-solid materials are usually neither reusable nor dielectrically adjustable. For example, the electrical properties of liquid and gel materials can be altered by adding water or oil components. Consequently, the electrical properties can be adjusted. Following this procedure, the liquid and gel ATE materials can be used to build phantoms of different parts of the body (e.g. head, arm, leg etc.). This feature is usually not present in the semi-solid ATE materials. Nonetheless, the materials also tend to dehydrate and it is hard to preserve the materials over a long period of time [151, 155].

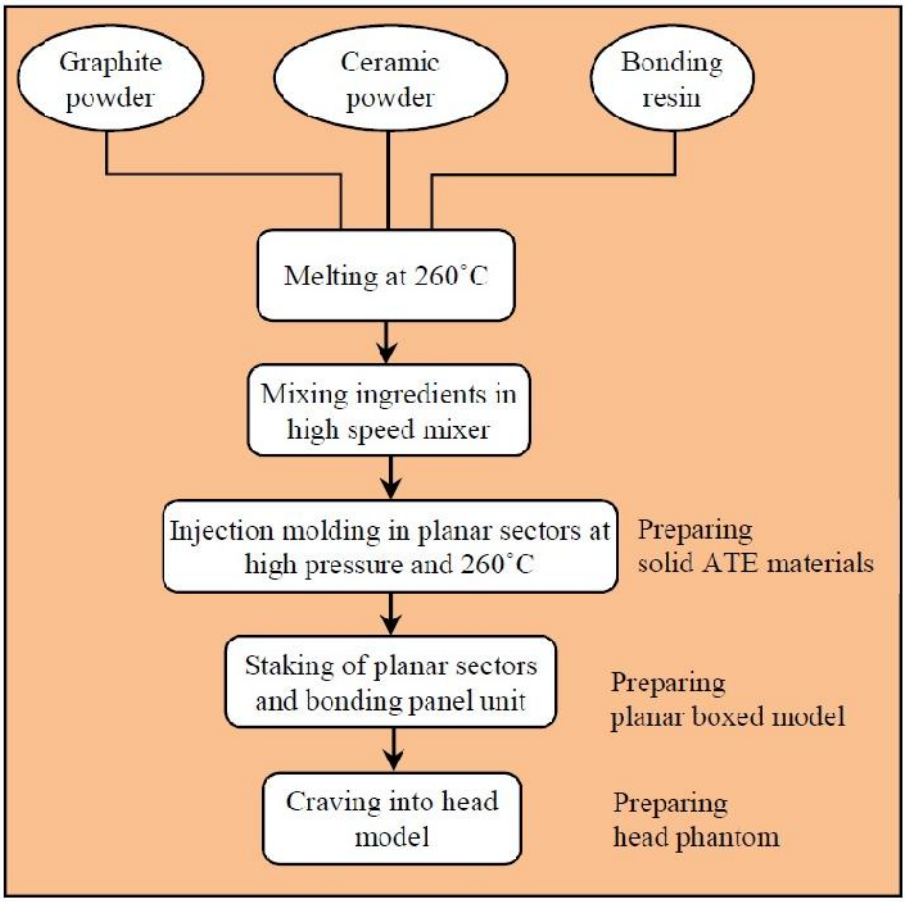

Fig. 4.4 A generalized flow chart of solid ATE materials for head phantom fabrication.

4.2.4 Solid ATE Materials

Since solid ATE materials are not water-based, they overcome the hydration drawbacks of the liquid, gel and semi-solid ATE materials. For this reason, they are called dry ATE materials [156]. Those materials are built primarily from ceramic powders, which are available in wide varieties with a wide permittivity range [156]. Nonetheless, the ceramic materials are of low loss, which represents a challenge to building lossy materials to emulate the actual conductivity of many human tissues. However, the composition of ceramic powders with various conductivity enhancing materials provide the flexibility of separately controlling the permittivity and conductivity values of the solid ATE materials [157].

An outline of the solid phantom fabrication as mentioned in [158] is shown in Fig. 4.4. To fabricate solid materials special production equipment is required due to the need for high temperature for material blending and high pressure is required for injection molding purpose. The specialized ceramic materials and instrumentations make the whole fabrication procedure more expensive than the rest of the ATE materials. Moreover, specialized adhesive materials are used with the ceramic powder for removing the air gaps between adjacent ceramic pieces. Those adhesive inclusions are difficult to use and make the ATE phantoms difficult to cut or reshape. In order to overcome this problem, soft and dry ATE materials are introduced utilizing silicone rubber with carbon fiber [159] or carbon nanotubes [160], which can be used to develop lightweight solid ATE materials whose specific density is less than 1. Whilst experiments that require invasive measurements can be problematic with the solid ATE materials, this type of ATE material can sustain over a long period of time without changing its shape. Moreover, a temperature dependency of the dielectric properties is observed, which may be beneficiary for some applications, like hyperthermia.

4.3 Human Head Phantoms

The head is one of the most complicated structures of the human body. Mimicking the human head is a challenging task as the head includes a lot of different tissues with complex distribution. To simplify the situation and ease the fabrication process, many researchers have utilized homogeneous ATE material, which equivalently represents the overall dielectric properties of the real head. In the narrow frequency arena, homogeneous liquid head phantoms are mostly prepared from sugar-water-salt based solutions with various preservatives [140, 161, 162] or using readymade commercial liquids as ATE materials [163-165]. Along with sugar-water-salt based solutions, a mixture of propylene glycol and deionized water has shown broadband performance in homogeneous liquid phantoms [166]. The dielectric properties of brain equivalent materials in those phantoms are calculated by averaging the properties of gray and white matter tissues [162, 166]. The container of

the liquid is made from low permittivity polyster or Polyvinyl chloride (PVC) materials. It is found that lumping of polymerizing materials during the fabrication procedure of liquid ATE materials can be resolved using water-soluble hydroxyetheylcellulose (HEC). This viscosity increasing agent also enhances the bacteria resistance of the solution and increases the lifetime of the phantom.

Gel head phantoms are basically agar based in both narrowband [167] and wideband [168]; although polymer based substances are also utilized to attain intended properties for narrowband application [169]. Semi-solid head phantoms are more common in broadband applications. These phantoms are built from several homogeneous ATE materials which are then utilized to fabricate heterogeneous/layered semi-solid phantoms [20, 58, 145, 155, 170]. The phantoms are mostly agar based to maintain the phantom's shape. Several gelling agents, like TX-151 is used in several phantoms to increase the viscosity of the materials [145, 170, 171].

There are very few solid head phantoms reported in the literature. Fig. 11(a) depicts a photograph of the solid head phantom reported in [156]. The comparatively more sophisticated fabrication procedure and expensive materials of solid phantoms than the other ATE counterparts might be the underlying reason. The solid head phantoms are mainly designed for narrowband applications [139, 156, 157]. However, a broadband solid ATE material is reported for broadband application in the ultra-high frequency (UHF) band [172]. In terms of accuracy of the tissue distribution, most of the phantoms are anthropomorphic. Several multilayer stylized human head phantoms with realistic ATE materials are also found in the literature (Fig. 11(b)). Recently, several studies reported three-dimensional (3D) printed head phantoms with semi-solid homogeneous and multi-layer realistic tissue compositions [58, 155]. Fig. 11(c) illustrates the three-dimensional 3D printing selective laser sintering (SLS) process. However, filling up the intracranial portion with semi-solid materials and 3D fabricated molds is a challenging task especially as the human head has a complex structure. Details of the fabrication process and layer are demonstrated by using a photographic sequence in Fig. 12.

It is noted that most of the reported ATE materials are proposed for specific applications. Analyzing them reveals the suitability of various phantoms/materials in verification of different systems or devices. The study of SAR measurements and hyperthermia technique verification are largely performed using homogeneous liquid and gel head phantoms. Solid head phantoms are also used for SAR measurements, especially where there is a flexibility of thermographic measurements [139, 156, 157, 172]. Otherwise, wearable communication systems mostly use solid head phantoms. Homogeneous gel and heterogeneous semi-solid ATE phantoms are popular in implantable device experiments. On the other hand, microwave imaging systems are validated using homogeneous gel and heterogeneous semi-solid head phantoms.

It is found that exterior of most of the liquid phantoms are constructed from low-loss plastic or polyester type materials. Although the shelf lifetime of the phantoms is one of the important issues in the fabrication strategy, descriptions are found to be insufficient for most of the reported works. An easily developable liquid tissue has been reported to attain over one year long lifetime [150]. Some gel type ATE materials have shown dielectric consistency over 40 days [168]. However, most of the semi-solid ATE materials are highly vulnerable to dehydration due to their lower water content, they limit the safe testing time and have comparatively short lifetime. Some semi-solid ATE materials have demonstrated reasonable changes (2-5%) over 4 weeks [20, 21, 130]. The fabricated head phantoms are summarized in Table 4-II.

Table 4-II: Summary of the reported head phantoms

Ref.	**Freq.**	**T or P**	**Type of tissue/ phantom**	**Included tissues**	**Head phantom structure /shape**	**Application**
[169]	13.6, 27, 40.7, 2450 MHz	T	G, HO	Muscle, fat, skin, brain	-	Hyperthermia
[161]	0.9 GHz	P	L, HO	Tissue-equivalent liquid	ANM	SAR
[162]	0.9 GHz	P	L, ML	Bone, skin, muscle, brain (average of grey and white matter), eye	ANM /realistic	SAR
[173]	0.9 GHz	P	L, HO	Human brain equivalent liquid	Stylized	Antenna performance analysis
[139, 156, 158]	900 MHz, 1.5 GHz	P	S, HO	Average head equivalent	ANM	SAR
[165]	0.9, 1.8 GHz	P	L, HO	Head simulation liquid	ANM	SAR

[163]	0.9, 1.8, 1.9, 2 GHz	P	L, HO	Human tissue equivalent	ANM	SAR
[174]	2.4 GHz	P	L, HO	Human brain simulant	ANM	Hyperthermia
[167]	2.45 GHz	P	G, HE	Bone/fat, muscle, grey matter, white matter, blood	CT scan based realistic shaped	Microwave tomography
[171]	3.4 GHz	T	SS, HE	Neonate brain tissue	Modelled	Microwave radiometry
[175]	1M-10 GHz	P	S, ML	Grey matter, fat, muscle	Layered, spherical	SAR measurement
[150]	0.1 - 1 GHz	T	L, HO	Bone (cast, liquid), brain, and muscle	-	Hyperthermia
[170]	0.2-3 GHz	P	SS, ML	Brain, skull	Cubic, spheric	SAR
[168]	0.3-2.5 GHz	P	G, HO	Muscle, brain	Cubic	Hyperthermia
[58, 155]	0.5-4 GHz	P	SS, HE	Head exterior, grey matter, white matter, dura, CSF, eye, cerebellum, spinal cord, blood	MRI devolved realistic	Head imaging, SAR
[172]	835-925 MHz	T	S, HO	Muscle, brain, skull	-	Electromagnetic dosimetry
[20, 130]	1-4 GHz	P	SS, HE	Hair (normal/dyed), scalp, skull, CSF, grey (dead/alive), white (dead/alive), blood	ANM	Microwave brain imaging
[166]	1.1-1.6 GHz	P	L, HO	Scalp, skull, brain	ANM	Radiometric monitoring
[145]	2-5 GHz	P	SS, ML	Skin, bone, dura, grey matter, and white matter	Stylized	Implantable electronics
[176]	3-6 GHz	T	SS, HO	Head tissue equivalent	Box shaped	SAR

* T = Tissue, P = Phantom, HO = Homogeneous, HE = Heterogeneous, ML = Multilayered; L = Liquid, G = Gel, SS = Semi-solid, S = Solid; ANM = Anthropomorphic;

4.4 Features and Functions of Different Phantom Ingredients

The ATE materials described in the previous section can be applied to build multiple types of phantoms. For example, the muscle can be found in all over the body, thus the muscle tissue mimicking materials described for head is also applicable in fabricating phantoms for other body parts. The ingredient composition of an ATE material defines its physical characteristics and dielectric properties. Altering the composition of the utilized ingredients wisely can be used to control the dielectric properties over a wide range which can be very useful in realizing other types of human tissues [151]. Moreover, the physical and mechanical characteristics can be altered by introducing some new ingredients or decreasing some existing ones. For these reasons, a proper understanding of the reasons behind applying different materials is very important for researchers working on phantom design. From the numerous materials used for the fabrication purpose of the various ATE materials and phantoms discussed above, the features and functions of the vital materials that define the material characteristics are listed in Table 4-III.

Table 4-III: Features and functions of the main ingredients reported for phantom fabrication procedures

Name	**Features**	**Functions/Benefits**
Water	Main solvent or constituent of ATE material	Primarily contributes to frequency dispersive high ε_r
Sodium chloride (NaCl)	Crystallized salt	Increases imaginary part of ε_r and ionic σ, while slightly decreases real part of ε_r; however, NaCl has no influence above 25 GHz.
Sucrose (Sugar)	White, crystalline, odorless powder	Used to significantly tune down relative ε_r, while also slightly increases σ
TWEEN	Nonionic, viscous liquid detergent material	Emulsifying agent for stable oil-in-water emulsions
Triton X-100	Viscous nonionic surfactant fluid.	Used as emulsifier in ATE liquids; reduce ε_r
TX-150 (super stuff)	Water-soluble powder	Thickener, and to increase viscosity and homogeneity
Sodium azide (NaN_3)	White powder, however toxic	Generally, used as a preservative; also to linearly increase σ in water solution

Ceramic powder (Ba, Ca)(Ti, Sn)O)	Can be pulverized into powders with particle size of 30 µm.	To increase ε_r of the ATE materials
Graphite (carbon) powder	A semiconductive material that presents electrical properties when covered with bonding resin (e.g. Poly Vinylidene Fluoride (PVDF))	To increase σ of the ATE materials
Hydroxyetheyl cellulose (HEC)	A nonionic water-soluble polymerizing agent (gelling agent)	Increases viscosity of water based compounds
Agar, Gelatin	Both are gelatinous substances; agar is yellowish white powder and gelatin is colorless	As gelling agent to hold artificial tissues to its shape and tune the dielectric properties
Oil (Paraffin, grape seed oil, Kerosene, safflower oil, etc)	A hydrophobic viscous liquid	To fabricate low-water-content ATE materials
Carbon fibre, aluminium powder	μm thick fibers of carbon, powdered aluminium	Enables refinement of the process in different semi-solid ATE materials
Silicone (not to be confused with Silicon (Si))	A heat-resistant, rubber-like synthetic polymer	Provides a matrix to hold the active ingredient; carries required amount of carbon in solid ATE materials and cure to the right consistency; silicone emulsion is utilized to control ε_r.
Acrylamide (C_3H_5NO)	Reacts with water to form polyacrylamide	Used in polymerization reaction, lowers ε_r and slightly increases σ, increases mechanical strength, slightly impairs transparency.
Bactericide, preservative	Several substances that resists the growth of bacteria	To prevent decomposition of ATE materials by microbial growth to enhance shelf lifetime
TX151	modified polysaccharide with propyl-paraben preservative	As a gelling agent, also functions to prevent thermal convection currents, mimics tissue texture and increases stickiness
Polyvinyl chloride (PVC)	White polymer powder	For exponentially decreasing σ and linearly decreasing ε_r

4.5 Fabrication of 3D Printed Realistic Head Phantom

Recent developments of three-dimensional (3D) printer have reshaped the small-scale manufacturing process of complex prototypes. 3D printing of phantoms has recently been incepted in semi-heterogeneous breast phantom fabrication [18]. In this section, a new breed of realistic head phantom is constructed using MRI-derived model with the help of 3D printing facility and bio-mimicking materials for the experimental validation purpose of wideband microwave imaging test bed. Selective laser sintering (SLS) 3D printing material is used to print the exterior of the head phantom, while the interior void portion (brain) is filled with tissue emulating mixture-materials that are given proper anatomical shape by using respective 3D printed molds. The phantom is fabricated in different individual parts which are finally united into a whole head. The fabricated 3D printed realistic human head phantom is prescribed to be used in the experimental validation of various microwave imaging platforms prior to the clinical trials to ensure the effectiveness of the medical diagnosis.

Table 4-IV: Summarized recipe of the ingredients to form various tissue types (Per 100 grams)

Ingredients / Tissues	**Water (%)**	**Corn Flour (%)**	**Gelatine (%)**	**Agar (%)**	**Sodium-azide (%)**	**Propylene Glycol (%)**	**NaCl Salt (%)**
Dura	72.38	24.13	0.00	0.97	0.36	1.93	0.24
CSF	83.75	2.03	0.00	11.24	0.37	1.49	1.12
Blood	81.97	2.73	0.00	12.75	0.36	0.91	1.28
Grey	80.65	16.59	0.00	1.04	0.35	0.92	0.46
White	70.67	26.86	1.41	0.00	0.35	0.71	0.00
Cerebellum	76.53	19.13	0.00	1.53	0.38	2.04	0.38
Spinal Cord	65.36	32.68	0.65	0.00	0.33	0.98	0.00
Eye	75.62	4.72	14.52	3.02	0.30	0.60	1.21

The construction procedure of the realistic head phantom can be divided into two main consequent steps.

4.5.1 Modelling and printing of the molds

To accomplish the anatomically realistic structure of the head, a 3D voxel model of the human head is derived from 2D MRI images at 1 *mm* interval of a patient by following the modeling process explained in [18, 177] in MATLAB. The layers of fat, skin, muscular parts and skull are united to construct the exterior of the phantom. The air holes of the nose and ear are cleared to maintain the realistic situation. The brain part is subdivided into Dura, CSF, gray matter, white matter, cerebellum and spinal cord portions. As the internal parts are intended to develop using tissue-mimicking materials with the help of 3D printed molds, separate volumetric binary models are created for every subdivision. The volumetric models are then hollowed to 2 mm thin structure and halved for the ease of molding process. Several pointers are added to the molds to maintain the accurate positioning from the adjacent layers in both distances and heights.

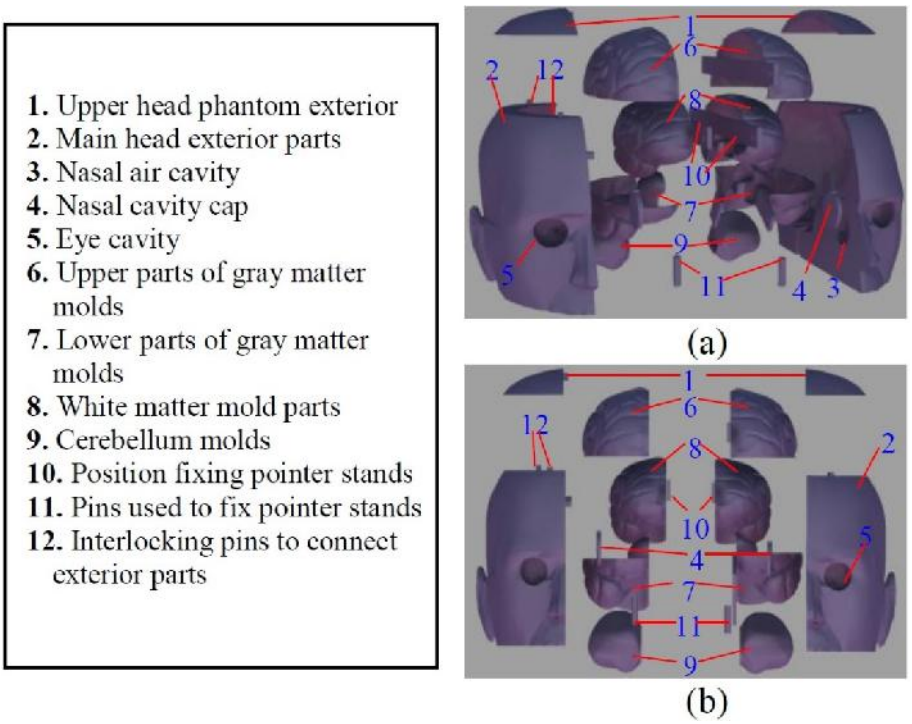

Fig. 4.5 Exploded view of the phantom parts modelled for the 3D printer from (a) perspective angle and (b) front side.

To meet the resolution constraint of the 3D printer, the volumetric models were re-meshed and smoothed, although this process brushes off some tiny pores present in the structures. The exterior is constructed in four parts; some interlocking pins and holes are added in these four parts of the exterior that allows assembling of the phantom into one firm piece and easy access to the internal brain parts that will allow the researcher to change the position of the target. Finally, all the different parts are exported as separate STL files, as desired by the 3D printer. The exploded view of the phantom parts

is depicted in Fig. 4.5. The 3D printing facility (DTM Sinterstation, 3D Systems Inc.) of the University of Queensland supported the fabrication process. The printer has a layer thickness of 0.1 mm and spatial resolution of 0.5 mm. The printing process of all the parts took around 16 hours. SLS powder is used in the 3D fabrication. The permittivity of the used powder is found to be around 6 and the conductivity is around 0.5 S/m over the bandwidth of 0.5 - 4 GHz. Basically high powered laser is used to melt down the powder for 3D printing; as a result, the construction of the 3D parts are very firm, which is required for the reusability of the phantom.

4.5.2 Tissue fabrication and phantom formation

The cavity of the head-skull is filled with brain-tissue equivalent materials by using their respective molds. Different compositions of gelatin, water, agar, corn flour, propylene glycol, sodium azide and sodium chloride (NaCl) are used to manufacture low-cost tissue emulating materials like gray matter, white matter, blood, Dura, CSF, cerebellum, spinal cord and eyes. The recipe of producing different mixtures for respective tissues is summarized in Table 4-IV. The general procedure followed at the time of material fabrication is as follows:

1. In a small beaker, Propylene Glycol is added with one-third of the water quantity at room temperature and the corn flour is added with the mixture by stirring gradually in small portions to make it thick viscous syrup.
2. In another beaker, the gelatin and/or agar is added with the rest of the water quantity and heated gradually to 90 and/or 95 □. The NaCl salt is then added to the mixture. The heating is continued for 3-4 minutes until the gelatin and agar is melted and the mixture becomes a thick. Bubble formation is observed in the heating process, however, the less bubbles are observed as the mixture turns into thick. Big bubbles appear at the end of this stage.
3. The viscous syrup from stage 1 is added with that of stage 2 while the burner is kept running as well as the stirring process until the whole mixture becomes nearly semi-solid.
4. The heating is stopped and the mixture is allowed to cool down to 40-50 □. At this stage, sodium azide is added to the mixture. The mixture forms into a semi-solid material.

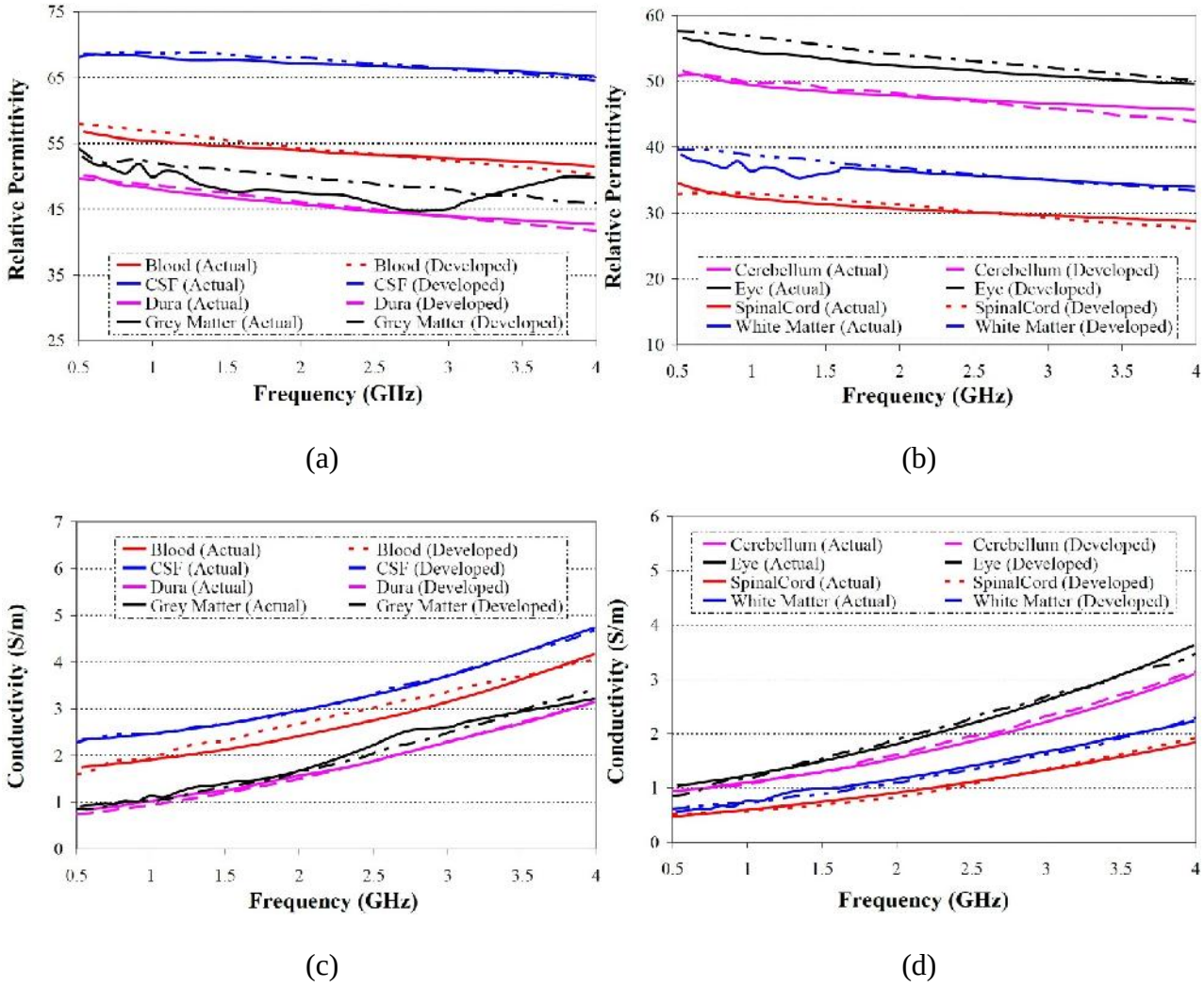

Fig. 4.6 (a, b) Relative permittivity and (c, d) conductivity comparisons of actual and developed head tissues.

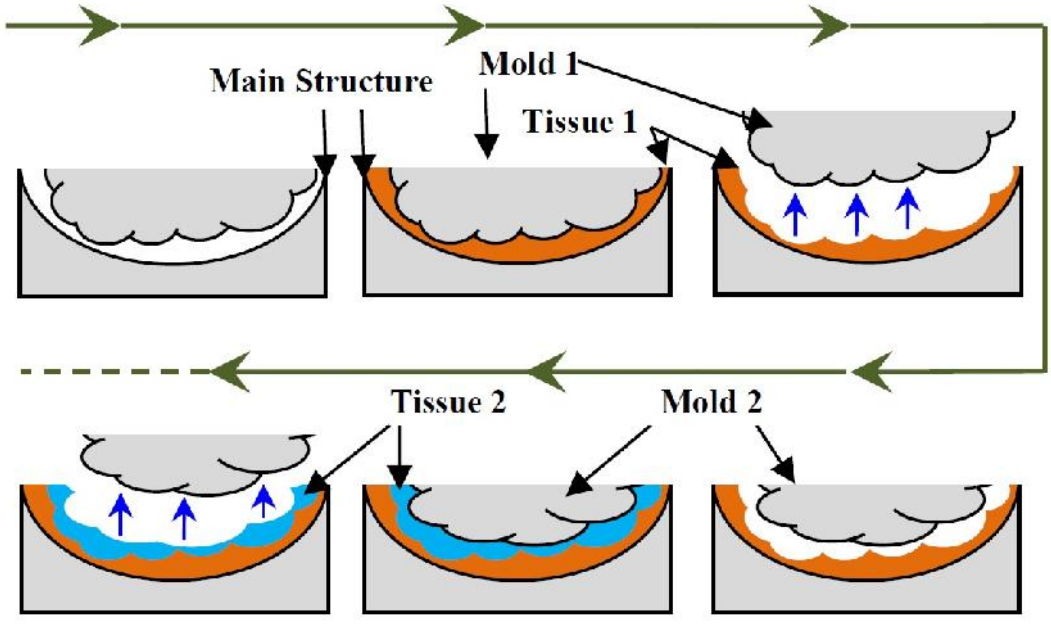

Fig. 4.7 The process of phantom development using various 3D printed molding structures.

After fabricating the tissue-equivalent materials, a dielectric probe HP85070 is used with the help of a network analyzer in order to measure their respective properties at room temperature. The measurement is done over the frequency band of 0.5-4 GHz. Comparisons between the actual electrical properties from [141] and the developed tissue-mimicking materials are demonstrated in Fig. 4.6. Reasonable similarities are observed between them. It was observed that out of the shown band, the material properties tend to exhibit decreased values compared to the actual electrical properties of the respective tissues.

To make sure of the stability of the materials, measurements are done again after 2 weeks and less than 5% deviation from the previous measurement is noted. One of the reasons behind this phenomenon is the evaporation of water from the tissue equivalent materials. As water has high permittivity, reduction of water from the materials results in reduction of dielectric constants and conductivity. However, the evaporation might also happen while the samples are preserved below freezing point by a process named sublimation, where ice directly turns to vapor. Keeping the tissues in a less aired package or bag reduces the evaporation processes. Nevertheless, the evaporation is a continuous process as the phantom has to be used at room temperature. For the developed phantom, it was observed that the electrical properties decrease by around 10%–15% after several months and then tend to reach stable values.

In the final fabrication step, the warm mixture is put inside the skull-cavity and given proper shape by using the 3D printed molds. A couple of steps of the molding process are exhibited in Fig. 4.7. It is noted that only the external surfaces of the molds are used for the internal structure fabrication. After finishing all the brain –tissue layers, the phantom is formed in one piece by using the locking pins. Afterwards the eye-cavity is filled with the emulating materials and preserved in a controlled temperature environment. It is worth to mention that, a wig can be used to emulate the condition of the hair [178].

In the composition mentioned in Table 4-IV, water is used as the main material or source of permittivity, as it exhibits high dielectric values over a wideband. Corn flour, gelatin and ager are used to control the relative permittivity of the mixtures. These substances also help in the semi-solid formation of the final tissues. The corn flour helps to increase the viscosity of the mixtures, so that the bonds between the different layers of the tissues do not get apart from each other. Propylene glycol is added as a humectant and stabilizing agent. It also lowers the freezing temperature of the developed tissues, which is helpful for the preservation purpose. NaCl is primarily responsible to control the conductivity of the mixtures. Nevertheless, no mold growth is observed in the phantom or samples which can be attributed to the use of sodium azide as preservative. The whole phantom development procedure is exhibited in Fig. 4.8 by means of the photographs taken from different fabrication steps.

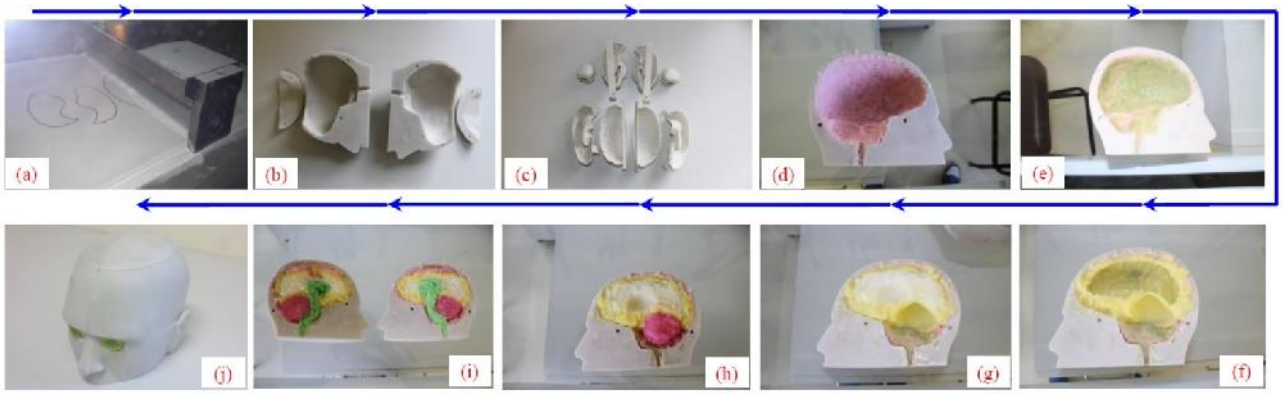

Fig. 4.8 Photographs from different steps of the phantom fabrication (clockwise): (a) 3D printing process, (b, c) various 3D fabricated parts; head phantom after filling up (d) Dura layer, (e) CSF, (f) grey matter, (g) white matter, (h) cerebellum; (i) the halves of the fabricated phantom, (j) the whole head phantom.

Some cautions have to be taken into consideration when following the aforementioned procedure. Proper, fast heating and temperature controlling equipment and probes have to be chosen for the ease of fabrication. Magnetic stirrer might be used for stirring purpose. The size of the beaker should be chosen according to the amount of the intended tissue equivalent material. The used water must be distilled. The conductivity of the mixture might increase if tap water is used.

An MRI-derived, 3D printed realistic head phantom has been reported. The main structure of the phantom contains the exterior part of the human head excluding the brain. This part is 3D printed by using an SLS material whose properties are chosen such that it represents the electrical properties of the exterior tissues. Brain tissue-emulating mixtures are developed from low cost materials and are characterized over a wide bandwidth of 0.5 -4 GHz. By utilizing the 3D printed internal molds, the skull cavity are filled with tissue equivalent mixtures layered one upon another, while the tissue abnormality like hemorrhagic or ischemic targets can be inserted by putting mimicking objects inside the brain. The different parts of the exterior can be locked to unite all the parts to one firm structure. The anatomically realistic heterogeneous head phantom can be used for the experimental validation of microwave head imaging systems which will lead to the clinical trials of the final medical diagnostic system.

4.6 Conclusion

In this chapter, the developments of realistic human head phantoms are described. Firstly, the motivation behind developing realistic human phantoms are presented with examples of applications.

The types of artificial phantom materials are classified into four types and the advantages and limitations of different types are elaborated. The previously reported artificial human head phantoms are tabulated in order to understand the utilizations of narrow- and wideband head phantoms in various applications. The features and functions of different phantom ingredients are also outlined. Finally, the development process of a 3D printed realistic human head phantom is described with the ingredient recipe and step by step depiction of the fabrication procedure with a comparison with the actual tissues and measured electrical properties ATE materials. The imaging results from wideband microwave imaging systems utilizing this fabricated realistic human head phantom is presented in Chapter 5 and 6.

Chapter 5 - Developments of Single Antenna Based Head Imaging Systems

This chapter presents the developments of single antennas based head imaging systems for brain injury detections. Firstly, a numerical verification process of a preliminary head imaging system by means of electromagnetic simulation of realistic brain injuries is described, which is followed by the experimental investigations using two simplified head phantoms. The results attained from both simulation and experiment are promising. However, as there are numerous directional and omni-directional antennas reported in the literature, there is no conclusive evidence in the literature to conclude the superiority of one type over another. Hence, the comparative imaging performance of directional and omni-directional antennas for head imaging system is also presented with relative quantitative analyses between the reconstructed images. A model of portable head imaging system is introduced with the verification on a realistic human head phantom. It is seen that the imaging performance of the portable head imaging system can be significantly improved by using a back-projection algorithm with a model of effective head permittivity. The efficacy of the system along with the imaging algorithm is verified in both simulations and experiments by using realistic numerical head models and 3D printed head phantoms. Nevertheless, results from a pilot human test is also presented. Later, a compact head imaging system with automated scanning capabilities is presented. Imaging improvements are also discussed when the surface waves are considered in reconstructing the image. Last but not least, a detection and differentiation system of brain injury types in brain stroke scenario is presented and numerically verified by using spherical and elliptical cylindrical stroke targets inside human head.

5.1 Simulation of the realistic head phantoms and image reconstruction

Wideband microwave imaging (WMI) is a good candidate for head imaging systems because of its non-invasive, non-ionizing and cost-effective features. However, realistic 3-D head phantoms are rare in software simulation environment to test the imaging and detection techniques. Mainly simplified head phantoms were used in the reported literature [20, 21]. Some of them used 2-D MRI slice to investigate the stroke scenario in mathematical model [52]. However, the construction of a realistic head phantom is one of the serious issues that the diagnostic system faces to get initial detection results using designed antennas and image algorithms in simulation environment.

This section describes a WMI system that is portable and of low cost. A realistic 3-D human head phantom is generated to accurately simulate the stroke circumstances. Unlike most of the reported

manuscripts [20, 21, 52], both hemorrhagic and ischemic strokes are considered as brain injury scenarios. The system effectively identifies and locates the position of the strokes.

A wideband antenna described in Section 3.4 is utilized in this realistic simulation. The antenna supports a wide bandwidth of 1.35 GHz covering from 1.17 to 2.52 GHz, which is equivalent to 73% fractional bandwidth with 1.85 GHz center frequency. A stable gain of around 5 dBi is attained with a front to back ratio of 10 dB along the direction of radiation (+ve Z-axis).

5.1.1 Generation of Realistic Human Head Phantom

Anatomically realistic numerical brain phantom is built using MRI images. This phantom considers the frequency dispersive properties of the biological tissues of a real human head. To that end, a fourth-order Debye model is derived and included in the numerical model over the band from 0.5 to 2.5 GHz, which is widely used in microwave-based head imaging as a reasonable compromise between penetration and resolution. The model is created using a combination of MATLAB and CST Microwave Studio from MRI slices of a real patient. The head phantom is comprised of a three-dimensional grid of 256 × 256 × 128 cubic voxels where the size of each voxel is 1.1 *mm* × 1.1 *mm* × 1.1 *mm*.

In order to obtain the best estimation of the Debye parameters compared with measured data from [140, 141], the measured properties of the head tissues at the available few discrete frequencies over the spectrum of 0.5 - 2.5 GHz are interpolated to get a larger number of discrete values and more accurate representation of the dispersive characteristics. The new data set are fitted to a fourth-order Debye model represented by the following formula.

$$£_r'(w) = £_\infty + \sum_{i=1}^{4} \frac{\Delta £_i}{1 + jw^2{}_i} + \frac{\pm_s}{jw£_0} \qquad (5.1)$$

The complex relative permittivity $\varepsilon_r'(w)$ as a function of angular frequency is composed of frequency dependent permittivity $\varepsilon(w)$ and conductivity $\sigma(w)$. It is expressed in terms of Debye model of five terms in addition to a conductivity term in which σ_s is the static value. ε_0 denotes the permittivity of free space; ε_∞ is the permittivity at infinite frequency; ε_S is the static permittivity, $\Delta\varepsilon_i = \varepsilon_S - \varepsilon_\infty$.

As an example of the fitted model, Fig. 5.1 depicts the electrical properties of the one of the main head tissues (white matter) based on the derived fourth-order Debye. A comparison in the same figure indicates that the derived model accurately emulates the measured properties across the band of interest.

The data set generated by Debye model is then imported into CST microwave studio. Thus, the CST model not only demonstrates physical structure of realistic human model but also its electromagnetic properties.

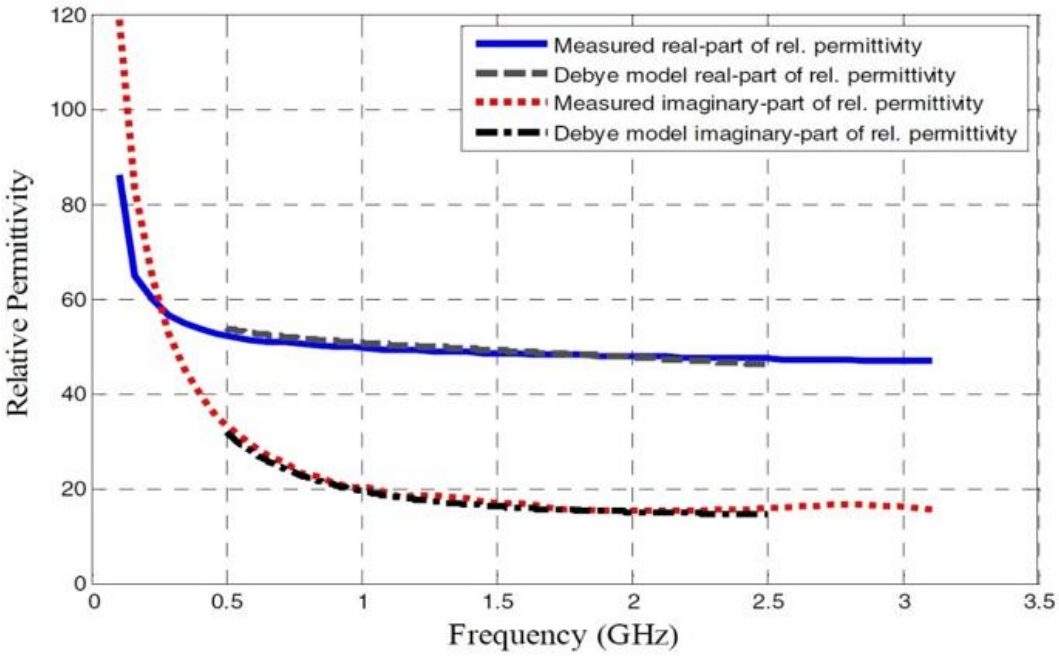

Fig. 5.1 Comparison between measured and Debey model permittivities of white matter.

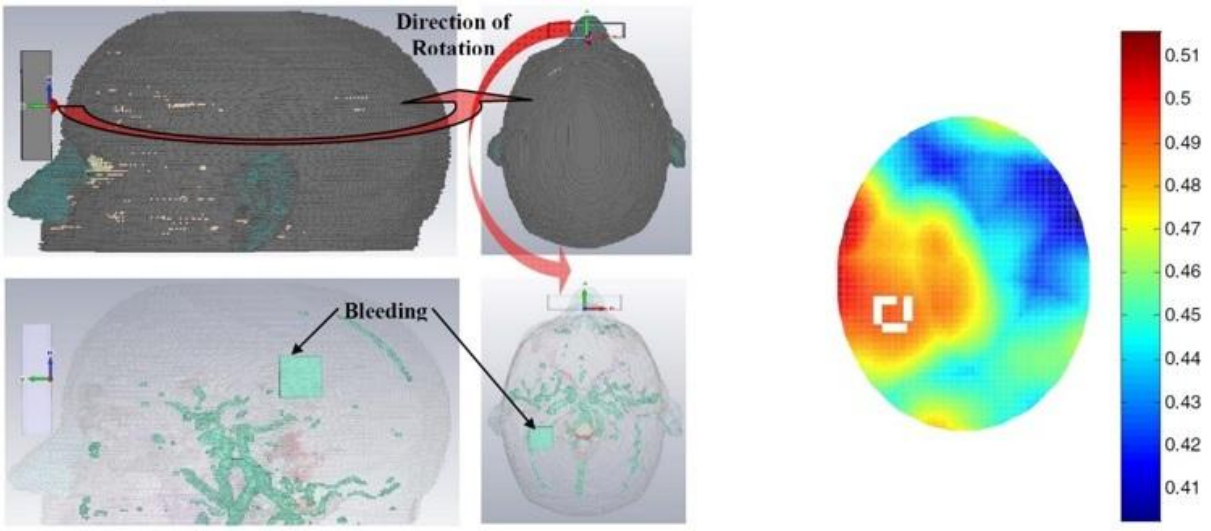

(a) (b)

Fig. 5.2 (a) Simulation setup of the diagnostic system with cubical hemorrhagic stroke and first antenna position, (b) reconstructed image of the human head model; while the white dashed square represents the bleeding position.

5.1.2 Investigation of Brain Injury Detection

Two types of brain injuries are analyzed in this section: hemorrhagic and ischemic stroke conditions. The simulation environments and their imaging results are described below.

To simulate the hemorrhagic stroke, a cubic object with 20 *mm* arm length is inserted inside the realistic head phantom (shown in Fig. 5.2 (a)). Since this type of stroke is caused by bleeding, the electrical properties of blood are assumed for the target. In order to investigate the hemorrhagic stroke, the wideband antenna was placed at 0° angle in front of the head model. A Gaussian pulse covering a bandwidth from 1.1 to 2.6 GHz is emitted from the antenna and the scattered time domain signals are received by the same antenna. The process is repeated in 16 different positions with an angle of 360°/16° = 22.5° apart from each other. The direction of antenna rotation is shown in Fig. 5.2 (a). Fermat's principle was used to determine the path of travel of the emitted signal from the antenna. As there is no matching liquid used in this experiment, high reflected signal is presumed from the exterior of the head phantom. The common background signals are then cancelled out from the received signal. Finally the image was constructed using the monostatic confocal imaging approach adopted from [21], and modified for the current technique. Fig. 5.2 (b) exhibits the reconstructed image for hemorrhagic stroke. The white square marked on the image represents the position of the bleeding. It is seen that the image can locate the approximate position of the stroke affected cells.

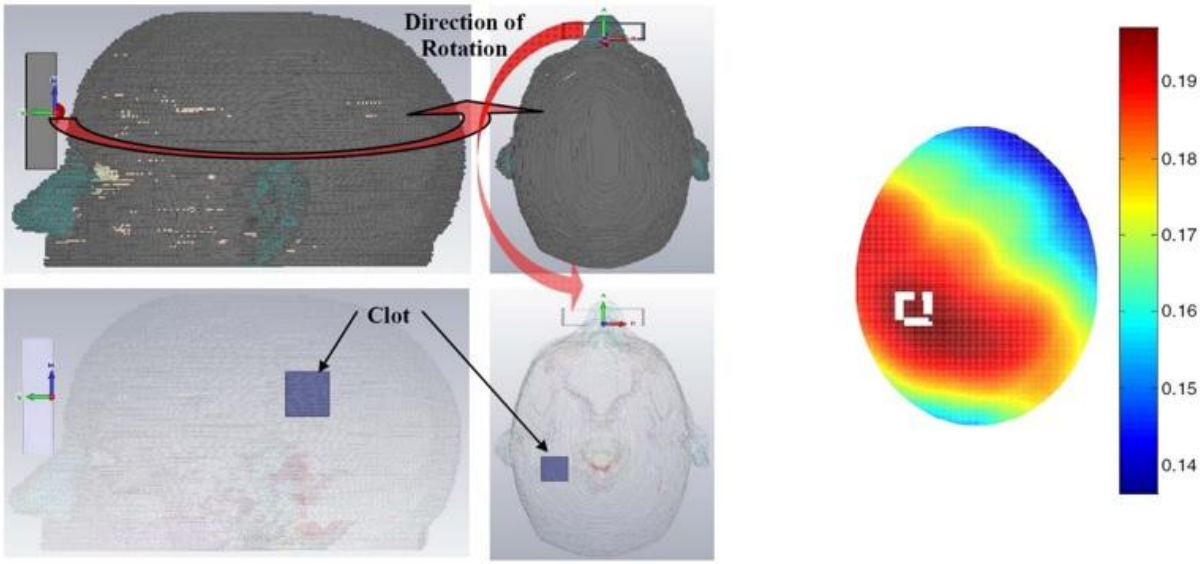

(a) (b)

Fig. 5.3 (a) Test setup of the diagnostic system with cubical ischemic stroke and the first antenna position, (b) reconstructed image of the human head model; while the white dashed square represents the clot position.

In case of ischemic stroke simulation, the target is placed in the same spot and filled with the properties of clot (permittivity and conductivity of 30 and 0.5 S/m respectively [20, 21]). As shown in Fig. 5.3 (a), same experimental setup discussed in the previous section is followed here. The back scattered signal is received in 16 points using a single antenna. The constructed image is shown in Figure 5.3 (b). It is seen that the algorithm effectively detects the location of the stroke, although it assumes a bit larger size than the original. This can be attributed to the basic assumption made by the algorithm that the propagating medium is homogeneous, which lead to some error in deciding the correct path of the travelling wave. Moreover, the electrical properties of the clot are closer to the white matter, which makes the detection system more challenging.

A compact microwave imaging system employing only one antenna that rotates around the head has been described. A realistic 3-D human head model is developed to simulate accurately the conditions of both hemorrhagic and ischemic conditions of brain injury. Monostatic radar approach is utilized to receive the backscattered signals at 16 equiangular positions around the head model. Finally, the confocal imaging technique accumulates the information obtained from the antenna and used to reveal the position of the bleeding and clot inside the head phantom. It is seen that the system is able to detect and locate the position of the different strokes.

5.2 Experiment on Simplified Head Models

This section describes an initial experimental system and the resultant imaging results of a head imaging system where simplified head models are used. As depicted in Fig. 5.4(a), a compact diagnosis system is designed to detect brain stroke inside human head. The antenna, described in Section 3.3, is applied in the system to test the position of bleeding due to hemorrhagic targets. The head phantom is placed at the center of the imaging system. Mono static radar technique is utilized to collect the scattered signals. In this approach, only one antenna is used to transmit and receive time domain signal at 32 antenna positions hemi-elliptically placed around the head phantom. The data acquisition is done by using R&S ZVA24 VNA at the time of experiment, yet this will be replaced by a microwave transceiver in the final prototype.

For the sake of investigation, the head phantom is accordingly rotated clockwise by an angle of 360° / 32° = 11.25° to acquire all the antenna positions' data, which can be alternatively replicated by using a small stepper motor to control the antenna position around the head. As the antenna is designed to be light weight, very small mechanical force will be required. The use of a single antenna also eliminates the consideration of mutual coupling among the array elements, making the processing less complex.

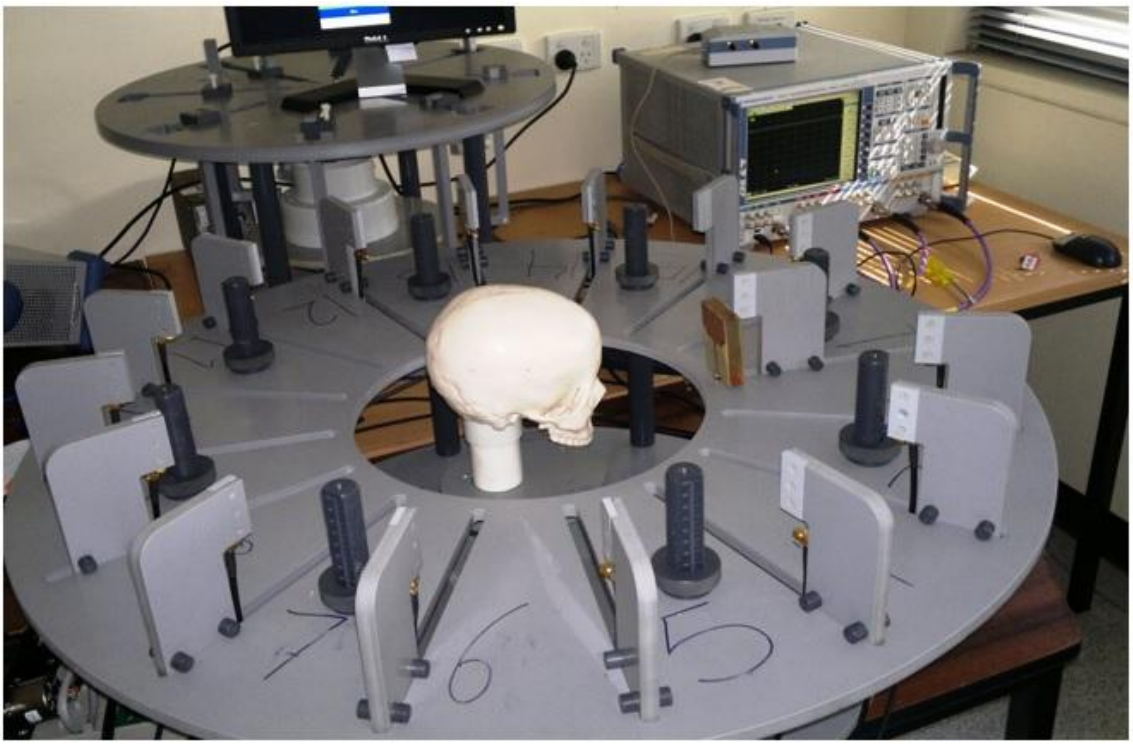

Fig. 5.4 The brain injury diagnosis system used for the investigation

Two experimental imaging are performed by using this experimental setup. These are described in the following portion. First experiment describes the imaging result received as the antenna is applied on a simplified SAM head phantom, while a sophisticated head phantom imaging is explained in the latter investigation.

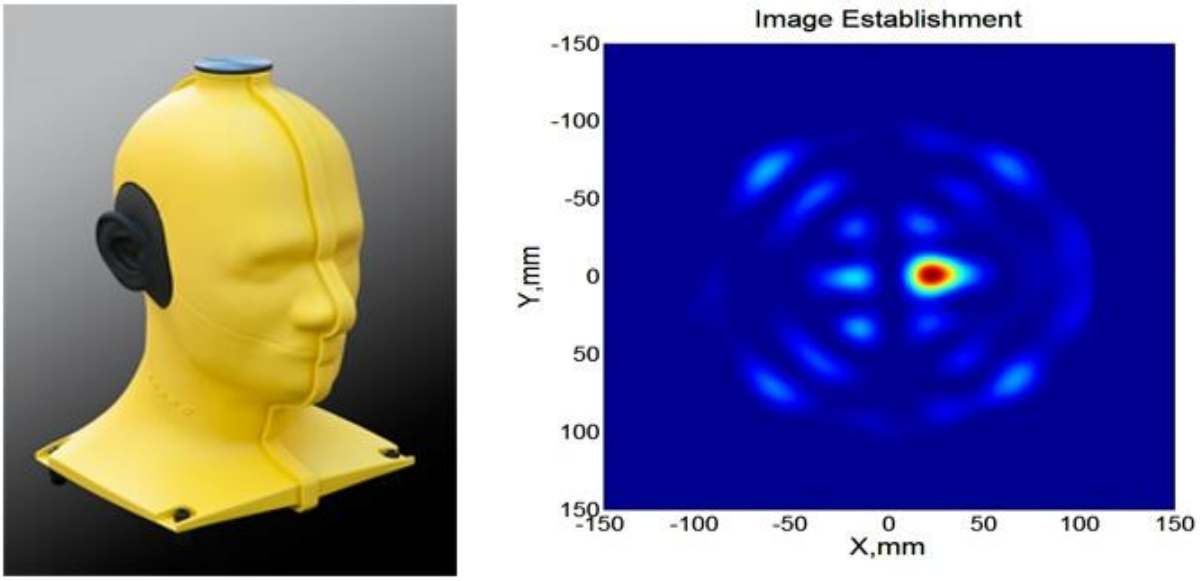

(a) (b)

Fig. 5.5 (a) Tested SAM head phantom utilized for the experiment, (b) constructed image exhibiting the position and size of the stroke.

A light-weight SAM head model with homogeneous high dielectric substance mimicking the average electrical properties of human head is used in this experiment. A metal ball with 7 mm diameter is used as a target and inserted inside the SAM head phantom. The antenna is used to radiate a time-domain pulse with a bandwidth of 1.2-2.8 GHz and the scattered signals are received by the antenna. The procedure is repeated in total 32 positions surrounding the head phantom and the scattered signals are processed from these 32 points. A wideband confocal imaging algorithm is used in this regard. Fig. 5.5(b) shows the reconstructed image. It can be realized that the stroke target can be identified perfectly in high contrast with the surroundings.

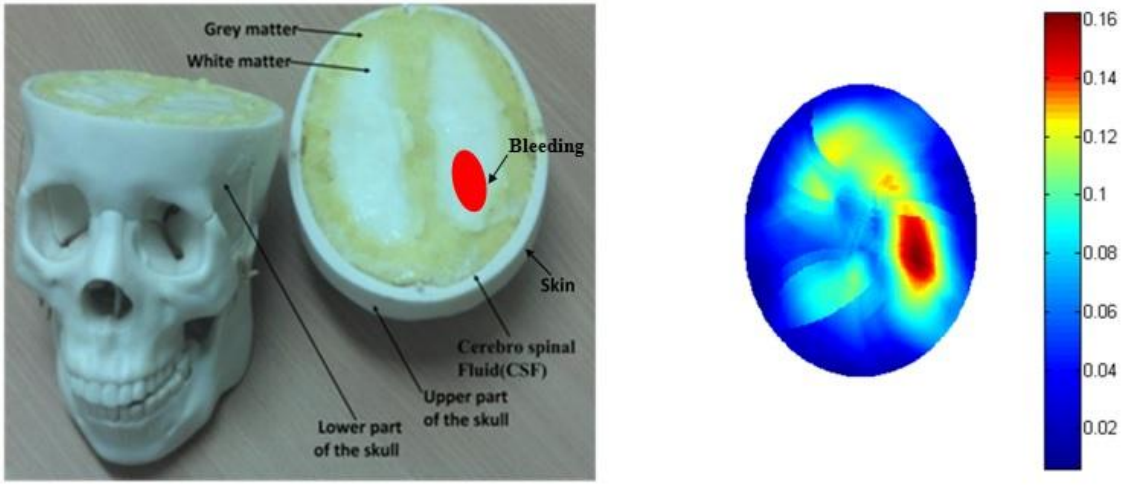

(a) (b)

Fig. 5.6 (a) Head phantom used for the stroke diagnosis, (b) constructed image maping the position and shape of the hemorrhagic brain injury.

A head phantom containing a target caused by hemorrhagic stroke was fabricated with various chemical materials that emulate the frequency dependent electrical properties of real brain tissues [178]. The properties of the fabricated head phantom matched well with the electrical properties of the real tissues reported in [140]. The properties of blood are assumed for the target, as hemorrhagic stroke is caused by bleeding. The head phantom is demonstrated in Fig. 5.6(a). The bleeding area is an elliptical shaped cylinder with radii of 1.5 and 1 cm, and height of 1 cm. A mono static radar system that uses data from 32 antenna positions hemi-elliptical placed around the head phantom is used to construct the image shown in Fig. 5.6(b). Details of the imaging technique can be found in [21]. It can be seen from the image that the antenna is capable to detect the exact position of the bleeding.

5.3 Imaging Performance Comparison of Directional and Omni-directional Antennas

Researchers have proposed numerous wideband antennas with directional or omnidirectional radiations to meet the requirements of microwave based head imaging systems. This section aims to study the effect of directionality on image quality of those systems. For a fair comparison, both types of antennas are designed to cover the same band. Their near-field radiation patterns and pulse performances in free space and inside a realistic head model are examined. Nevertheless, experimental validations are performed to investigate the effect of wideband antenna's directionality in near-field head imaging systems.

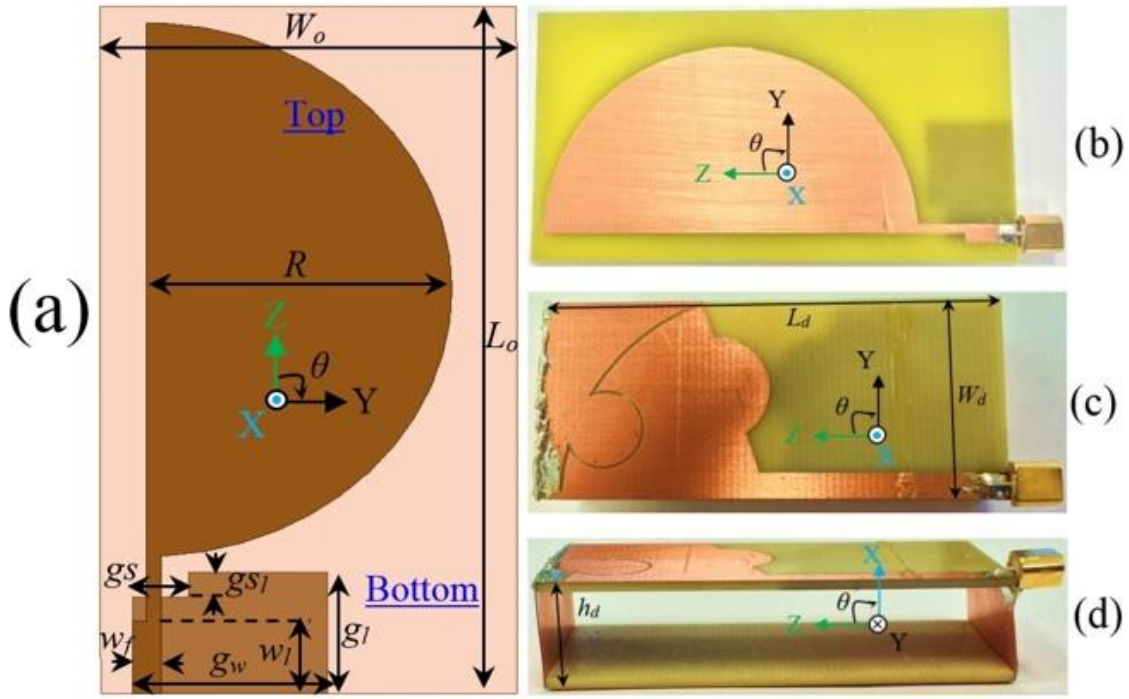

Fig. 5.7 Schematic diagram of the omnidirectional antenna with dimensions (in *mm*) of: R = 32, W_o = 45, L_o = 80, w_f = 3, w_l = 9, g_l = 15, g_w = 21, gs_l = 3, gs_w = 6. Photographs of the fabricated prototypes: (b) top view of the omni-directional antenna, (c, d) top and side views of the directional antenna with dimensions (in *mm*) of: L_d = 70, W_d = 45, h_d = 15.

5.3.1 The utilized antennas

A compact directional wideband antenna that has been introduced in Section 3.5 is considered as the directional sample. The antenna is built using the low-cost GML 1032 substrate with permittivity, ε_r=3.2 and loss tangent, $\tan\delta$ =0.002, is adapted for this study. The antenna covers the band 1.25-2.4 GHz, which is equivalent to 63% fractional bandwidth with respect to the central frequency of 1.83 GHz. The antenna exhibits an average gain of 3.5 dBi along the direction of radiation (X-

direction). The overall size of the antenna is $0.29\lambda_0 \times 0.12\lambda_0 \times 0.06\lambda_0$, where λ_0 is the free space wavelength at 1.25 GHz.

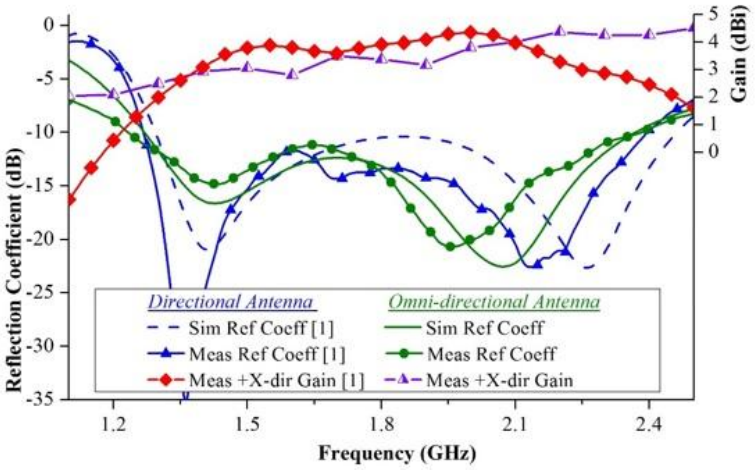

(a)

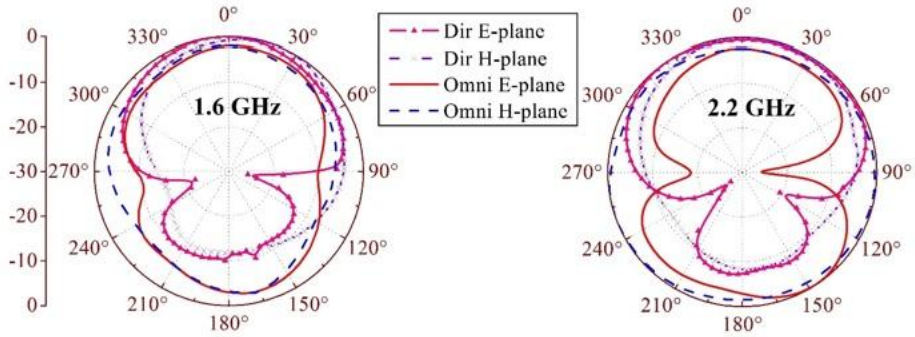

(b)

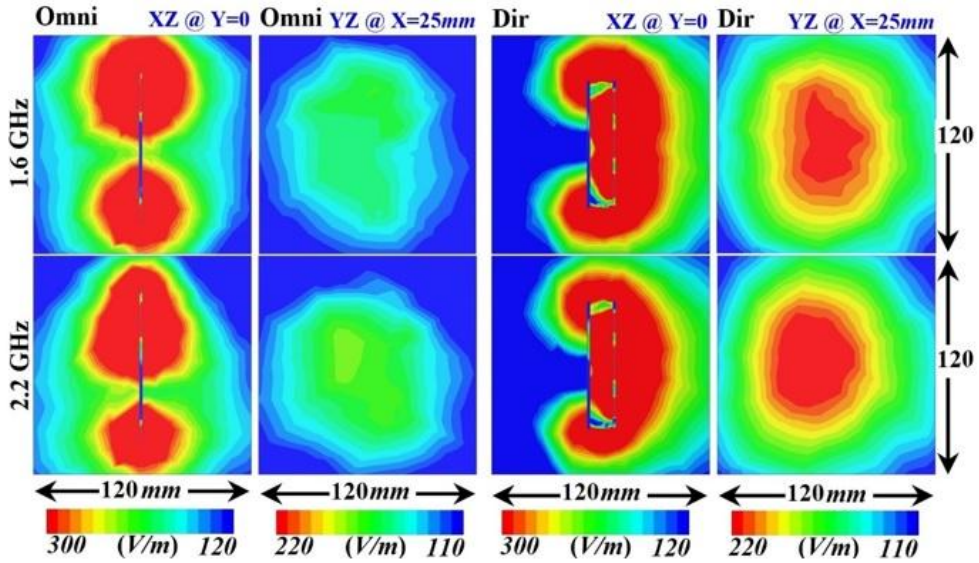

(c)

Fig. 5.8 (a) Measured and simulated reflection coefficient and gain performance of the directional and omnidirectional antennas. (b) Measured normalized near-field radiation patterns of the antennas at 1.6 and 2.2 GHz. (c) Simulated E-field distributions of the antennas in XZ and YZ planes, while the antennas are centered at the origin of the co-ordinate system.

A wideband monopole antenna with omnidirectional radiation is designed relying on a similar principle and presented in Section 3.2 is considered for comparison. To reduce discrepancies between the utilized omni- and direction-al antennas, the omnidirectional antenna is designed to operate over the same band (1.25-2.4 GHz) with an average gain of 3.5 dBi along X-direction. The antenna is printed on FR4 substrate (ε_r=4.5, $\tan\delta$ =0.02) and occupies a space of $0.32\lambda_0 \times 0.19\lambda_0 \times 0.006\lambda_0$. The geometries and photographs of the antennas are illustrated in Fig. 5.7. The reflection coefficients and X-directional gains of the antennas are presented in Fig. 5.8(a). The directional antenna exhibits smoother gain patterns than the omnidirectional antenna because of its less fluctuating current distributions over the operating band. Consequently, the phase center of the directional antenna is almost constant, while the omnidirectional antenna suffers from the rapid change of phase centers over the operating band. However, owing to the high permittivity of the human head and compact size of the antenna, E-fields propagate inside the head beyond the near-field region and into far field [35]. Therefore, while the near-field characterization is generally the deciding factor in microwave medical imaging, both near- and far-field characterizations are needed for antenna selection in head imaging.

Fig. 5.8(b) shows the near field radiation patterns measured at 10 cm distance from the antennas in both E-(XZ) and H-(XY) planes at 1.6 and 2.2 GHz. The patterns are normalized to the maximum values. Along with high front-to-back ratio, the directional antenna exhibits 1-2 dB higher near-field radiation performances than the omnidirectional antenna. Nevertheless, for the directional antenna, the beamwidth is found to be wider at higher frequencies because of the radiation mechanism in the near-field region.

As shown in Fig. 5.8(c), at lower frequencies, the monopole antenna starts radiating with two equally strong E-field concentrations along the feeder. With the increase in the frequency, most of the E-field is concentrated on half circular patch region, resulting in a slightly narrow, unstable radiation pattern [17, 131]. On the other hand, E-field distributions on the directional antenna are uniform on the front-side, resulting in a stronger near-field radiation compared to that of the omnidirectional antenna (YZ-plane distributions). Moreover, the E-fields are relatively stable over the band, making the beam relatively wider than the monopole antenna at higher frequencies. Nevertheless, unlike electrically large or dielectrically loaded antennas, electrically small size of the directional antenna constricts the achievable collimated beam and directivity [179, 180].

5.3.2 Near-field pulse analysis

Since the antennas are intended to operate from a close proximity to human head, near-field pulse quality analysis of the transmitted pulses is useful to examine the efficacy of the antennas. To that end, individual antennas are vertically placed in CST MWS software in free space. An array of co-polarized (Z-directed) E-field probes is positioned with a linear 5 *mm* interval in both front and backward directions in order to monitor the radiated time-domain electric fields. The antennas are fed with a Gaussian pulse covering the band 1.25-2.4 GHz (Fig. 5.9(a)). Owing to the pulse-shaping characteristics of wideband antennas, the pulses transmitted from the antennas are different from the input pulse. The pulses received by the probes also vary depending on the channel characteristics, especially in near-field, where the antennas radiate in a different manner from the far-field region. For that region, the analyses are performed both with and without the presence of a head model.

5.3.2.1 Pulse Analysis without Head Model

Fig. 5.9(a) shows the input and received signals in free space at various distances from the surfaces of the antennas. The quality of the received pulses can be quantified by calculating fidelity factors [58]. It is seen from Fig. 5.9(b) that the fidelity factor of the directional antenna is higher than the omnidirectional antenna. Nevertheless, in both cases, more than 90% fidelity factors are observed indicating the reception of low-distorted wideband pulses in free space. While for omnidirectional antenna almost the same pulse fidelities are found in both the forward and backward direction, in case of directional antenna the front directional pulses exhibit slightly less distortion than those of the backward direction.

However, fidelity factor calculation excludes the effect of signal strengths at different probes. To that end, the amplitudes of the received pulses are analyzed by normalizing with respect to the maximum pulse amplitude from both antennas as depicted in Fig. 5.9(c). The omnidirectional antenna demonstrates very small time-domain amplitude variations along the forward and backward directions. On the other hand, the directional antenna exhibits more than 10 dB front-to-back ratio at any point in the near-field region. Along +ve X-direction, the pulse strength of the directional antenna is more than 5 dB stronger than those of the omnidirectional antenna, while along –ve X-direction, the omnidirectional antenna emits much strongly than the directional one. The increased front-directional signal strength of the directional antenna is expected to create stronger scattering signals from injury target inside the head.

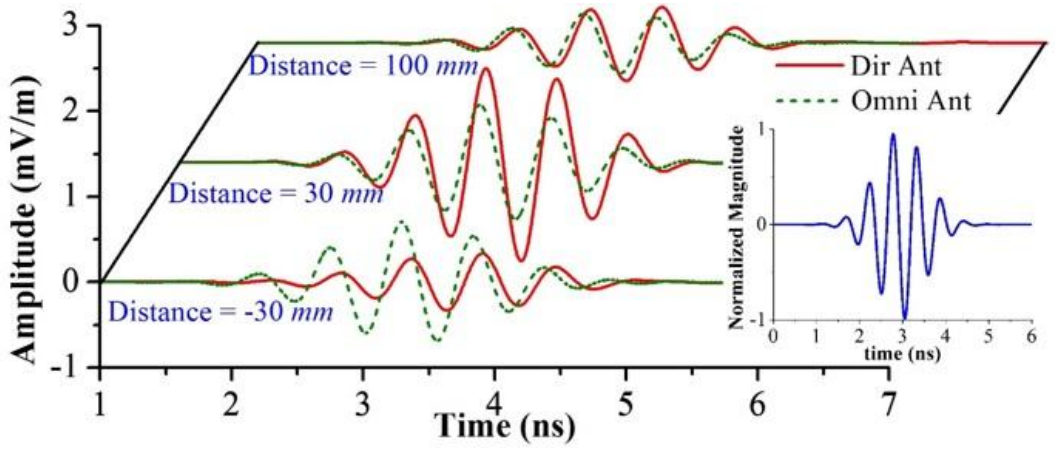

(a)

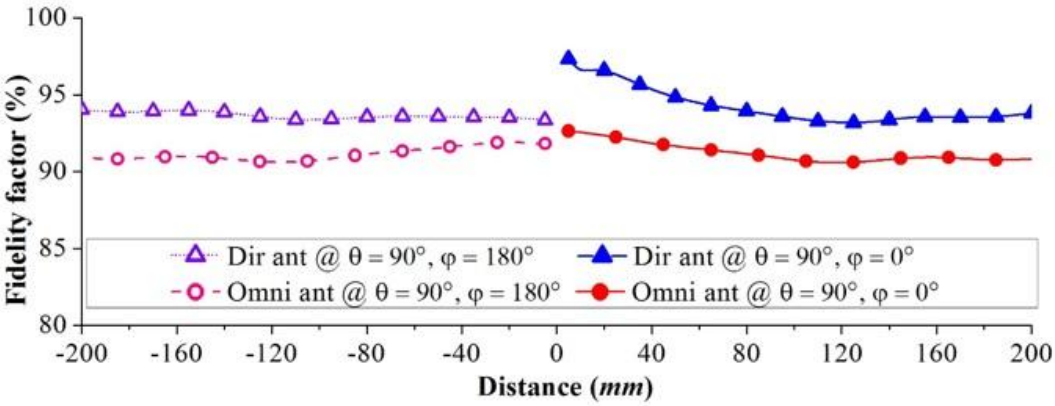

(b)

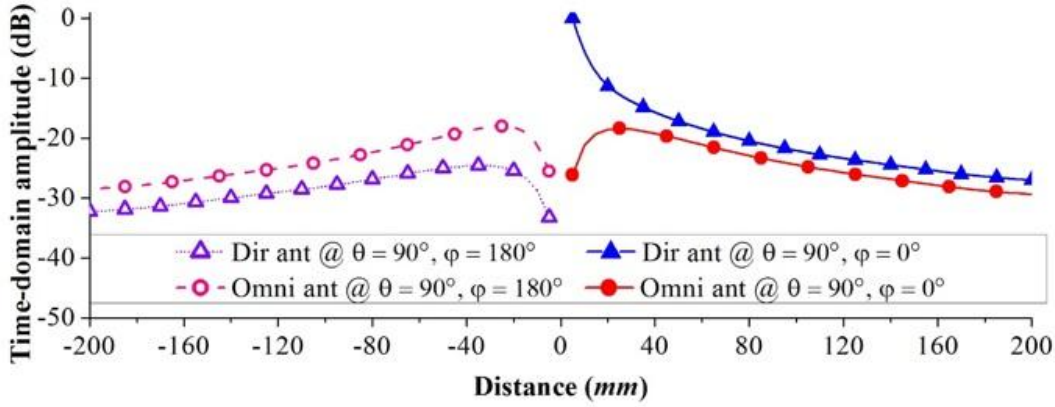

(c)

Fig. 5.9 (a) Received E-field impulse responses of the antennas in free space at different distances along ±X-direction with input pulse at inset. Distance = 0 *mm* states the antenna position. Results of the pulse analysis of the received pulses along ±X-direction: (b) fidelity factor and (c) peak impulse response.

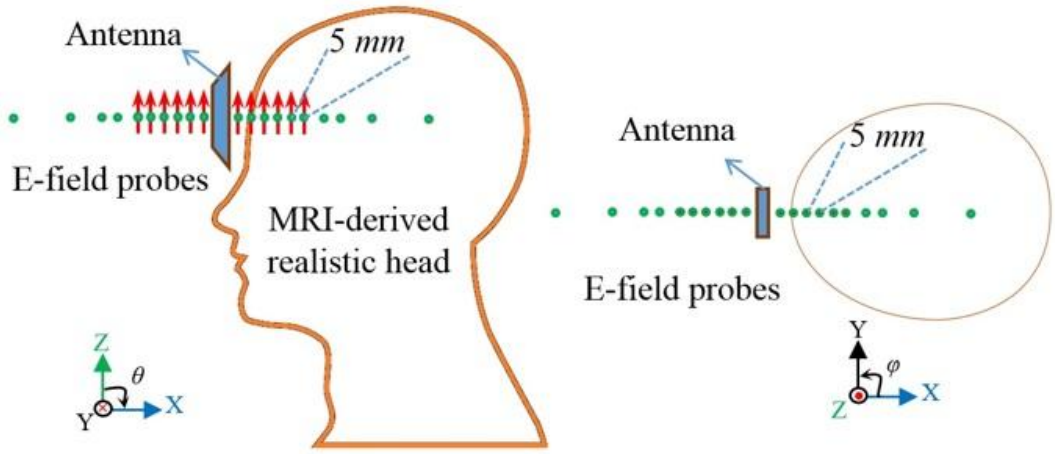

(a)

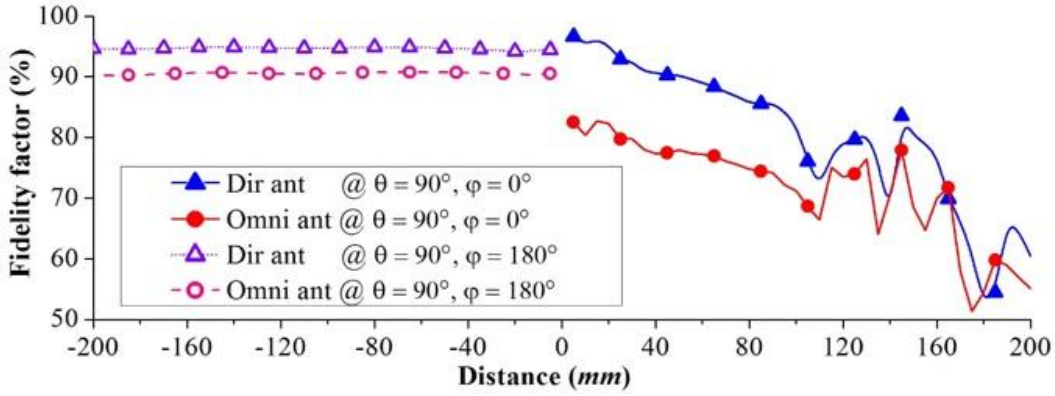

(b)

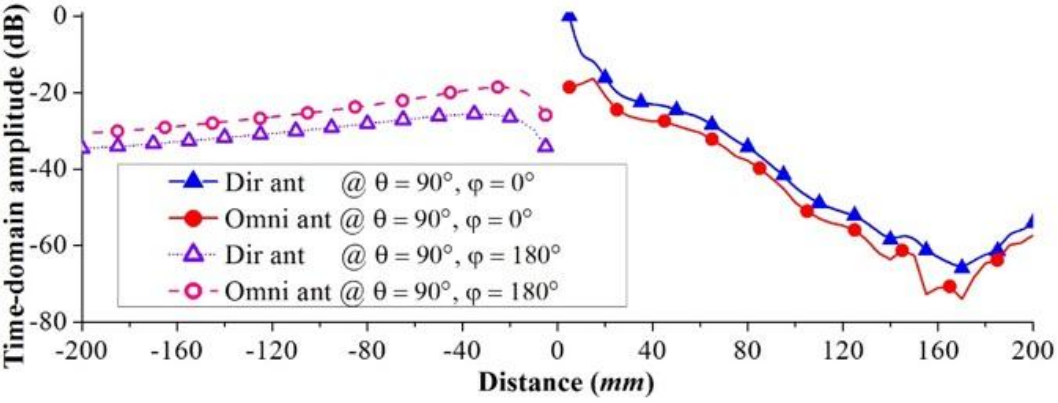

(c)

Fig. 5.10 (a) Simulated E-field probe setup while antennas are placed in front of the realistic head model. Distance= 0 *mm* being antenna position. Results from the quality analysis of transient responses of the antennas along ±X-direction in presence of head model: (b) fidelity factor and (c) peak impulse response.

5.3.2.2 Pulse Analysis in Presence of Head Model

In close proximity of the human head, the antenna characteristics are expected to be changed. To study that effect, the antennas are placed 10 *mm* away from an MRI-derived realistic human head model with 1.1×1.1×1.1 mm^3 voxel resolution as shown in Fig. 5.10(a). The model includes 17 different head tissues which are assigned with their relevant frequency dispersive dielectric properties. The antennas are excited with the previously utilized wideband pulse and the received E-field pulses from the probe array, including probes inside the head, are analyzed (Figs. 5.10(b, c)). It is noted that for both antennas, the pulse distortion along +ve X-direction increases and the transient signal strength drops dramatically, while impinging on the lossy head model. However, signals received at the backward direction are less susceptible to the change and remain almost unchanged. In the first half section of the head model, the directional antenna yields around 20% higher fidelity factors (Fig. 5.10(b)) and 4 dB stronger signals (Fig. 5.10(c)) than the omnidirectional antenna.

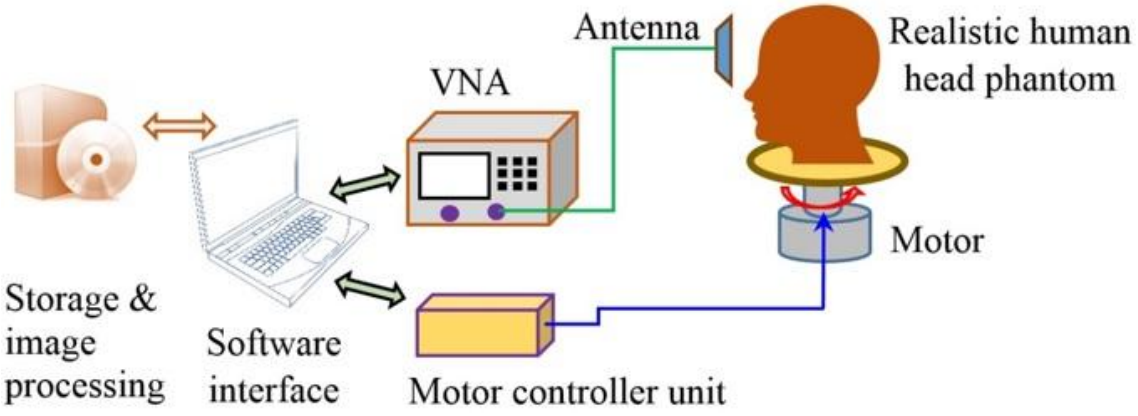

Fig. 5.11 Experimental setup of the head imaging system.

Rapid fluctuations on fidelity curves are also noted mostly as the signal crosses the center of the head model. This is caused by the accumulated signals which occur as the leakage signals traveling through alternate routes within the head add up with the weaker direct traveling signal. It is also noted that due to this multipath interferences, the signal loss seems to be less at the other half of the head, while in fact the loss of the direct travelling signal continues to the end of the model. This multipath interferences can be opted out by calculating the shortest path as described in [58]. Nevertheless, the higher front-directional transient signal strength inside the head model and lower backward-directional signals of the directional antenna results in low environmental noise and higher dynamic range which is one of the critical factors that defines reconstructed image quality.

5.3.3 Head Imaging Performance

5.3.3.1 Experimental Setup

Fig. 5.11 illustrates the experimental setup of a monostatic head imaging system. It consists of an antenna mounting and phantom rotation platform. The antenna is connected to a vector network analyzer (VNA), which collects the scattered data at different angular positions around a head phantom. The anatomically realistic head phantom (described in Chapter 4) with dispersive electrical properties of actual head tissues including dura, CSF, gray matter, white matter etc. is utilized in this system. A hemorrhagic target of 2×2×1 cm^3 volume is placed inside the head phantom to emulate the intracranial brain injury. The phantom is mounted on the rotating platform. A motor-controller is utilized to synchronize the motor rotation and data acquisition. The collected data over the band of operation (1.25-2.4 GHz) is stored and sent for time-domain post-processing and image reconstruction. A delay-and-sum based confocal algorithm is utilized for image generation [58].

5.3.3.2 Results and Discussions

Fig. 5.12 shows the imaging results from the head imaging system using the directional and omnidirectional antennas. Reconstructed images with 40 data samples (360˚/40 = 9˚ angular differences) around the head phantom shows that both antennas are capable to detect the position of the intracranial brain injury. However, visual inspection can determine that the directional antenna is more efficient in detecting the target positions with less artifacts.

A qualitative analysis of the generated images is demonstrated in Table 5-I. It is noted that the average signal to clutter ratio, Q of the reconstructed image using directional antenna is more than 3 dB higher than that of omnidirectional antenna. Again, the maximum signal to clutter ratio, M, and the target accuracy indicator, δ, are enhanced in case of the directional antenna. In an extended measurement, 100 data samples are collected around the head phantom. The resulted images (Figs. 5.12(c, d)) show clearer located targets using both antennas. Qualitative analysis of Table 5-I illustrates that due to sample increments, the average signal to clutter ratio, Q of the reconstructed image using the omnidirectional antenna is improved by 1 dB, while for the directional antenna, Q is improved by 2 dB. The other matrices (M and δ) have also improved resulting an easier and more accurate brain injury localization.

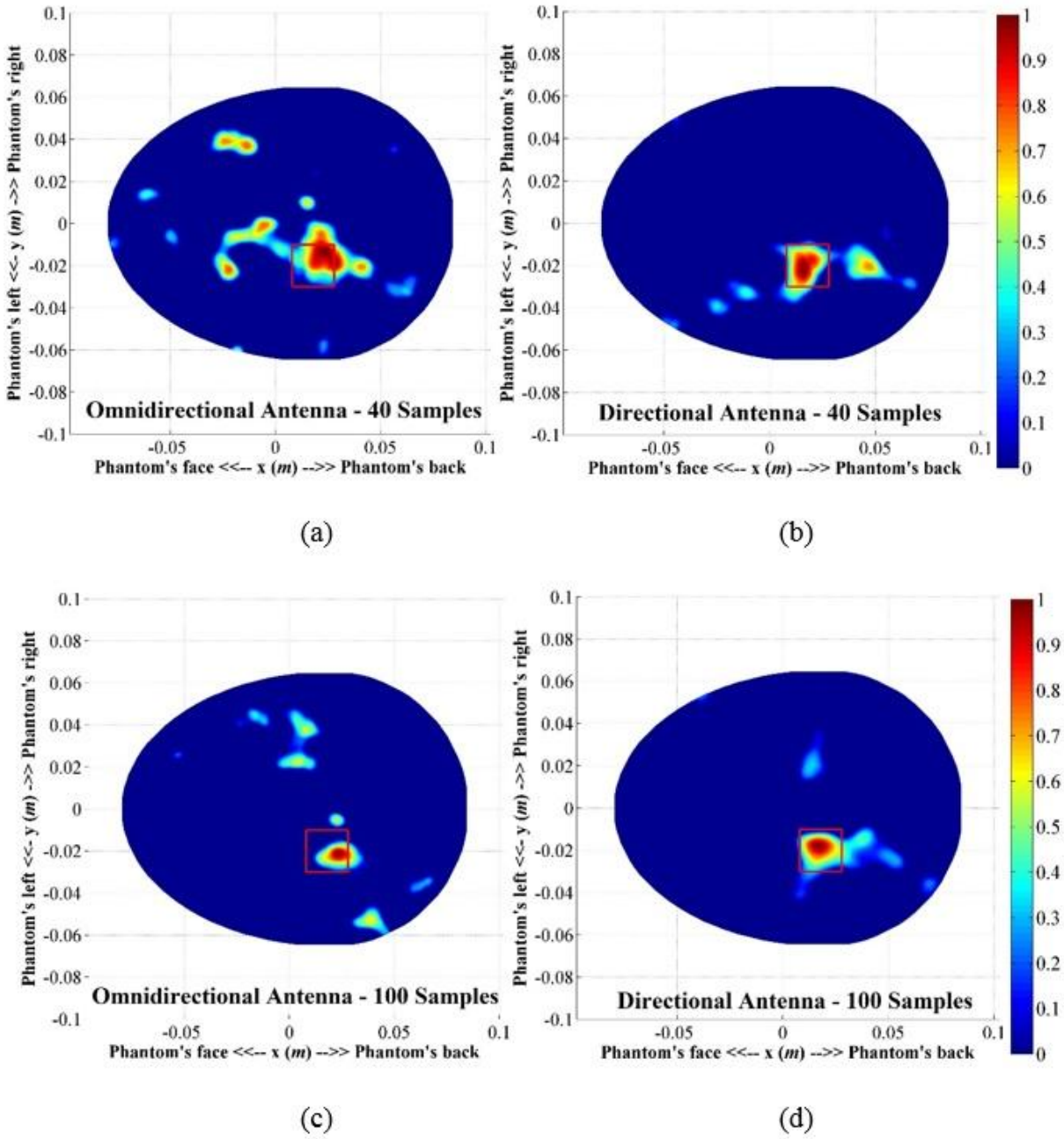

Fig. 5.12 (a, b) Reconstructed images from the imaging system with 40 data samples using omnidirectional and directional antennas respectively. (c, d) Reconstructed images from the imaging system with 100 data samples.

Since the quality of the reconstructed image relies on the quality of acquired scattering data by the antennas, the improvement in reconstructed images of the directional antenna compared to the omnidirectional antenna can be attributed to the improved received scattered signals. Because of the stable phase center and stronger near-field radiation, the directional antenna provides stronger impulse peaks with low distortion. Again, near-field radiation patterns demonstrate that the unidirectional antenna has wider beamwidth which assists it to cover wider angular region in front of

it. Impulse characterization indicate that owing to the higher dynamic range of the directional antenna, it reacts negligibly for the environmental movements and interfering signals operating at the same band coming from the exterior of the imaged region. For these reasons, images reconstructed using directional antenna suffer less from noise and consequently result low artifacts with focused target. From the instrumentation viewpoint, as the front and back sides of the antennas react individually upon the change of environment of that side (i.e., placement of the head), both antennas are useful for head imaging in a controlled environment. But, due to the stronger backward radiation, omnidirectional antenna requires larger controlled environment to reduce multipath affects [181]. However, it is recognized that for both antennas, vertical scanning or 3D array is needed for 3D localization of a target. If a 3D array is used, an array of directional antennas will outperform omnidirectional-based array due to the lower mutual interactions between neighboring elements.

Table 5-I: Quantitative analysis of the images

Images (Ant. - Samples)	$Q = 1 \left(\frac{\overline{I(p)}}{\overline{I(q)}}\right)$ **(dB)**	$M = \frac{m \ [I(p)]}{m \ [I(q)]}$ **(Ratio)**	$\delta = \|p - c\|$ **(*mm*)**
Omni - 40	11.5	1.03	9.2
Dir - 40	14.7	1.31	2.9
Omni – 100	12.6	1.30	5.7
Dir - 100	17.0	1.99	2.5

* p is the set of points inside the target region and q is the set outside the target region. $I()$ indicates intensity of a particular set of points. p represents the position of maximum intensity [58].

The effect of directionality of wideband antennas on image quality of microwave head imaging has been investigated. To that end, directional and omnidirectional antennas covering the same band (1.25-2.4 GHz) and average boresight gain (3.5 dBi) are designed, prototyped and measured. The investigation demonstrates that, inside human head, the directional antenna provides better impulse performance with lower distortion than the omnidirectional antenna. The low pulse transmission in the backward direction provides higher dynamic range to the directional antenna. This is validated by experimental head imaging results. Directional antenna detects highly focused hemorrhagic targets inside a realistic head model using less number of data samples, which indicates superiority of directional antennas for such systems.

5.4 Portable Head Imaging System and Experiments on Realistic Head Model

In order to detect brain injuries, an integrated imaging system utilizes a prototyped wideband unidirectional antenna, built and tested for system integration. The system employs a custom-made microwave transceiver and an adjustable scanning platform to collect the backscattered signal from the imaging object. The compact wideband antenna, with directional radiation patterns, presented in Section 3.9 is adopted in the data acquisition system. One antenna is used in the system and thus the data is captured in many positions with the same antenna around the head using the virtual array concept. For signal processing and image reconstruction, the system uses a back-projection (delay-and-sum) technique, which requires the antenna to scan the head from various positions along a semi-circular trace that align with the border of the head.

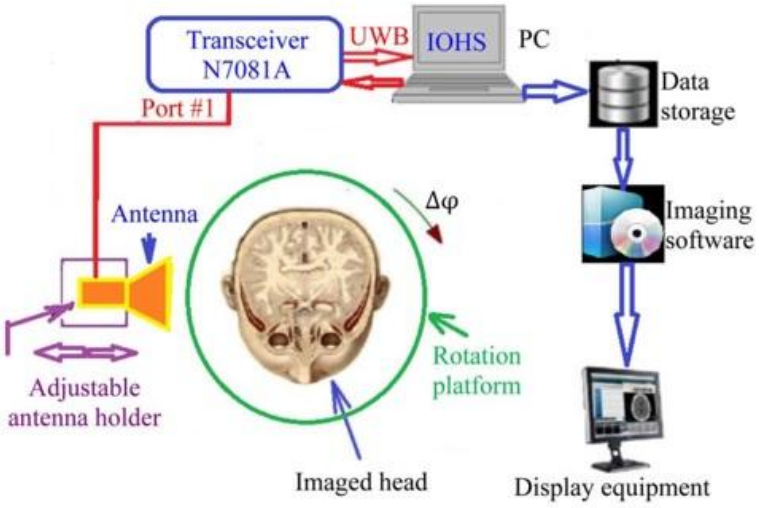

(a)

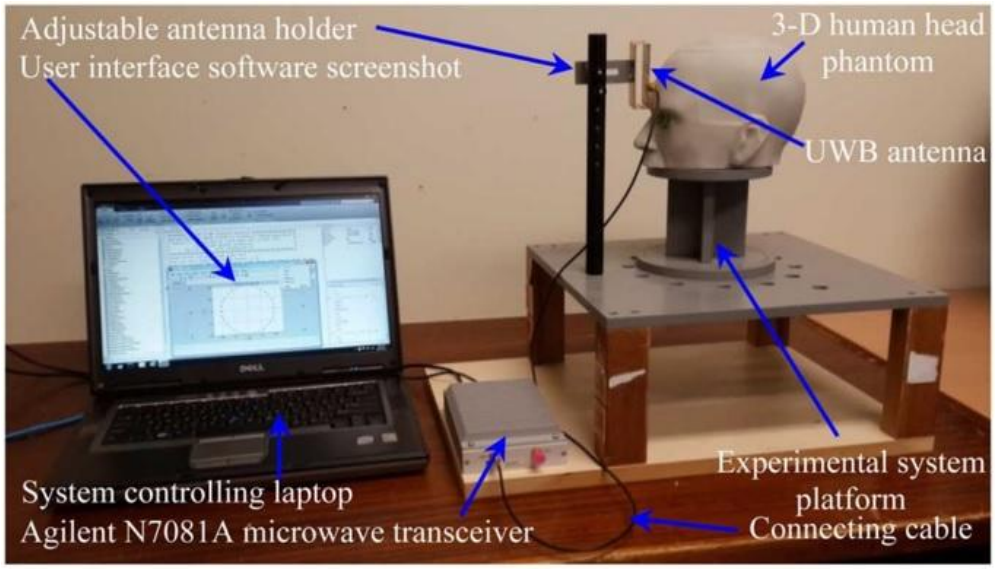

(b)

Fig. 5.13 (a) Diagram of the head imaging system, and (b) experimental setup.

The architecture of the system hardware is shown in Fig. 5.13. It employs an adjustable antenna holder to fix the antenna and move it into the desired distance from the imaged object. A manual horizontal rotation platform is used to fix the imaged head and change its orientations for different scanning angles. The system uses a portable custom-made microwave transceiver from Agilent Tech (N7081A) to send/receive pulses with pre-defined frequency components. For this application, the transceiver operates in a monostatic mode and its pre-defined pulses occupy the band from f_L to f_H. The received signals are then converted by the same transceiver to digital data and stored in a laptop for post-processing by using an in-home operation system (IHOS). The design and operational details of each system unit are described in the following sections.

5.4.1 Data Acquisition Infrastructure

The data acquisition system utilizes portable transceiver from Agilent Tech (N7081A) which is controlled by the IHOS. N7081A is a high-speed, small, low-cost and modular wideband transceiver device. It can operate over the wide bandwidth of 0.1 MHz to 4 GHz and offers an update rate of around 100 frames per second for signal acquisition. This portable transceiver provides a maximum dynamic range of 80 dB and can be controlled via USB or LAN connections by a computing tool.

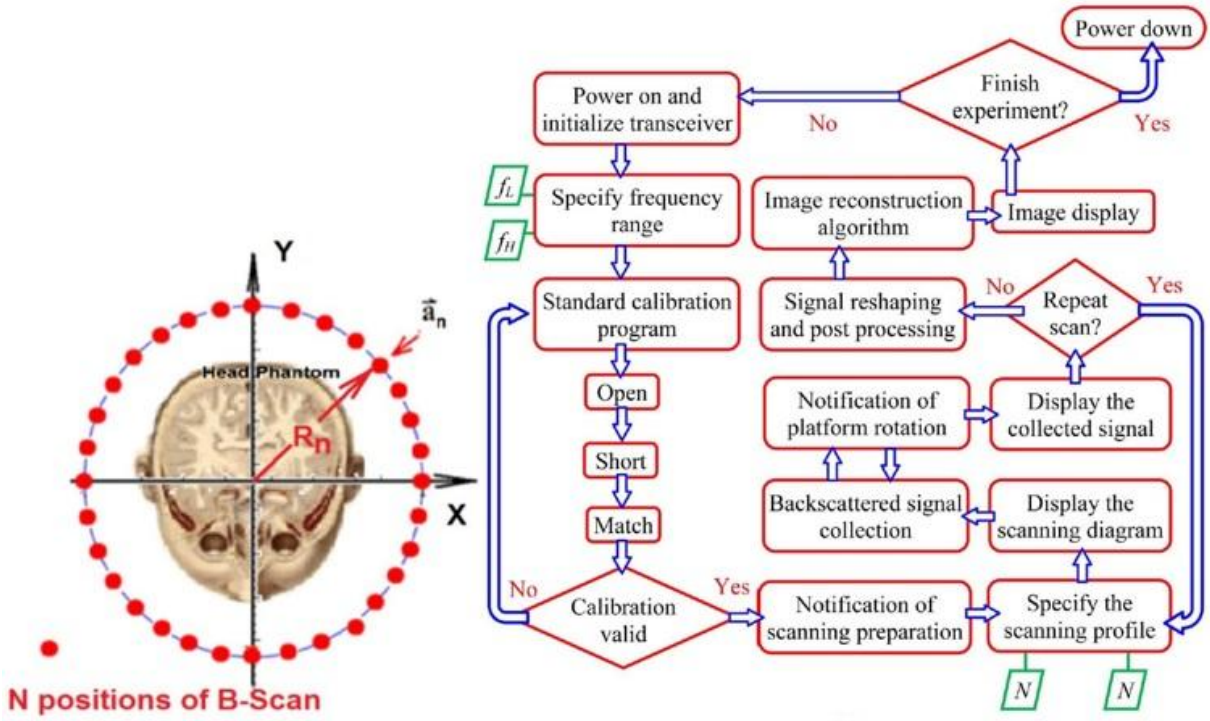

(a) (b)

Fig. 5.14 (a) B-scan positions, and (b) graphic description of In-home Operation System (IHOS).

The backscattered signals from the head phantom are captured during a two-stage scan: 1) The A-scan (the fast scan), which collects *M* reflection coefficients ($\boldsymbol{\Gamma} \in \mathbb{C}$) from individual scan position by performing an electronic sweeping in the pre-defined frequency domain, and 2) the B-scan (the slow scan), which repeats the process of the A-scan on *N* various antenna positions around the head. Assuming the origin of the coordination system is at the center of the head (Fig. 5.14(a)), the B-scan positions, which are distributed on a semi-circular trace on X-Y plane, are located at $\overrightarrow{a_n}$.

$$\overrightarrow{a_n} = \begin{pmatrix} R_n \cos \Phi_n \\ R_n \sin \Phi_n \end{pmatrix}; \; where \quad \Phi_n = \frac{2\pi(n-1)}{N}; n = 1,2, \dots, N. \tag{5.2}$$

The collected data by the two-stage scan generates a two-dimensional signal $\boldsymbol{\Gamma}(\Phi_n, f_m)$ expressed in the following format, which is required by the image reconstruction algorithm.

$$[\boldsymbol{\Gamma}(\Phi_n, f_m)] = \begin{pmatrix} \boldsymbol{\Gamma}(\Phi_1, f_1) & \cdots & \boldsymbol{\Gamma}(\Phi_N, f_1) \\ \vdots & \ddots & \vdots \\ \boldsymbol{\Gamma}(\Phi_1, f_M) & \cdots & \boldsymbol{\Gamma}(\Phi_N, f_M) \end{pmatrix} \tag{5.3}$$

$$f_m = f_L + (m-1)(f_H - f_L)/(M-1) \tag{5.4}$$

where f_L and f_H are the range of the used frequency in the A-scan, m is the index number represent M frequency sampling points, n is an index number representing the sequence of the B-scan at $\overrightarrow{a_n}$.

A back-projection image reconstruction algorithm is used to interpret those stored digital signals and sends the computed two-dimensional image matrix to the display equipment. Within the whole hardware infrastructure, all the modules are controlled and synchronized by a laptop equipped with the IHOS. The description of the in-home operation system, which is coded in MATLAB environment, is illustrated by the flow-chat in Fig. 5.14(b). Its main function is to manage the whole detection process over three scopes: 1) initializing the microwave transceiver and specifying the frequency band of the transmitted pulse, level of transmitted power, dynamic range and sampling density of the frequency-domain data, 2) controlling the pre-test calibration procedure and synchronizing the data acquisition with semi-circular scanning procedure, 3) illustrating the scanning angles (Φ_n) to the end users for manual platform rotation, and 4) image reconstruction and display.

5.4.2 Imaging Algorithm

Using the portable microwave transceiver with both A-scan and B-scan, the reflection coefficients, $\boldsymbol{\Gamma}(\varphi_n, f_m)$ are captured in M = 359 discrete frequency domain data points over the operating band of 1.1-3.4 GHz from N = 32 different angular positions ($\Delta\varphi$ = 360°/32 = 11.25°) around the head phantom. To apply an imaging algorithm, the collected vector data set are reshaped in the following matrix:

$$[\boldsymbol{\Gamma}] = \begin{pmatrix} \boldsymbol{\Gamma}(\Phi_1, f_1) & \cdots & \boldsymbol{\Gamma}(\Phi_N, f_1) \\ \vdots & \ddots & \vdots \\ \boldsymbol{\Gamma}(\Phi_1, f_M) & \cdots & \boldsymbol{\Gamma}(\Phi_N, f_M) \end{pmatrix}_{M\times N} \qquad (5.5)$$

Due to the heterogeneous nature of the fabricated phantom, the received time-domain signal endures reflections from various dielectric transitions which exist along the propagation path. At the time of data acquisition, the distance between the antenna and head phantom is maintained at 15 *mm*. Hence, it is assumed that the adjacent antennas will face almost similar reflections and thus the common background reflections are cancelled out by constructing difference signals from adjacent antenna data set. Therefore, a difference matrix $[\Delta\boldsymbol{\Gamma}]$ is generated by subtracting the shifted matrix $[\boldsymbol{\Gamma}]^{s}$.

$$[\Delta\boldsymbol{\Gamma}] = [\boldsymbol{\Gamma}] - [\boldsymbol{\Gamma}]^{shi} \qquad (5.6)$$

$$[\boldsymbol{\Gamma}]^{shi} = \begin{pmatrix} \boldsymbol{\Gamma}(\Phi_N, f_1) & \boldsymbol{\Gamma}(\Phi_1, f_1) & \cdots & \boldsymbol{\Gamma}(\Phi_{N-1}, f_1) \\ \vdots & \ddots & \ddots & \vdots \\ \boldsymbol{\Gamma}(\Phi_N, f_M) & \boldsymbol{\Gamma}(\Phi_1, f_M) & \cdots & \boldsymbol{\Gamma}(\Phi_{N-1}, f_M) \end{pmatrix}_{M\times N} \qquad (5.7)$$

Since the investigation in this system is done in the time domain, the next step is to perform the inverse Discrete Fourier transform to convert the difference matrix $[\Delta\boldsymbol{\Gamma}]$ from frequency domain to time domain for each source antenna. The transferred data set $\boldsymbol{\gamma}(\Phi_n, t_{m'})$, which represents M'=2000 time-domain sampling points, can be obtained by multiplying the difference matrix with the transform matrix $\exp[\boldsymbol{D}_{M'\times M}]$.

$$[\boldsymbol{\gamma}]_{M'\times N} = \exp\{[\boldsymbol{D}_{M'\times M}]\} \times [\Delta\boldsymbol{\Gamma}]$$

$$= \begin{pmatrix} \boldsymbol{\gamma}(\Phi_1, t_1) & \cdots & \boldsymbol{\gamma}(\Phi_N, t_1) \\ \square & \ddots & \square \\ \boldsymbol{\gamma}(\Phi_1, t_{M'}) & \cdots & \boldsymbol{\gamma}(\Phi_N, t_{M'}) \end{pmatrix}_{M' \times N} \quad (5.8)$$

Where

$$[\boldsymbol{D}_{M' \times M}] = \begin{pmatrix} 2\pi j f_1 t_1 & \cdots & 2\pi j f_M t_1 \\ \square & \ddots & \square \\ 2\pi j f_1 t_{M'} & \cdots & 2\pi j f_M t_{M'} \end{pmatrix}_{M' \times M} \quad (5.9)$$

In order to map the time-domain signal onto a 2D imaging space, a square area including the cross-section of the imaged body is divided into P × Q cells, each cell is of 0.5 × 0.5 mm^2 centered at $\overrightarrow{r_{p,q}}$ =(x_p, y_q). The propagation model shown in Fig. 5.15 is used to estimate the wave propagation time $\tau_n(\overrightarrow{r_{p,q}})$ from the antenna's phase center $\overrightarrow{a_n}$ to a hypothetical point $\overrightarrow{r_{p,q}}$ in the imaged area. The region Ω represents the head phantom with average relative permittivity ε_h = 42, while the antennas located outside the phantom ($\bar{\Omega}$) are surrounded by free space. The wave travelling from the antenna position $\overrightarrow{a_n}$ to the hypothetical point $\overrightarrow{r_{p,q}}$ passes a point $\vec{\xi}$ on the border of Ω ($\vec{\xi} \in \partial\Omega$) [20, 21]. According to Fermat's principle, it should be the minimum value of $\tau(\cdot)$ with all possible $\vec{\xi} \in \partial$. Thus the propagation time is:

$$\tau_n(\overrightarrow{r_{p,q}}) = \tau_o + \tau_{ti}$$
$$= \min_{\vec{\xi} \in \partial} \left\{ \frac{\left\| \overrightarrow{A_t} - \vec{\xi} \right\|}{c} + \frac{\left\| \vec{\xi} - \overrightarrow{r_{p,q}} \right\| \sqrt{\varepsilon_{he}}}{c} \right\} \quad (5.10)$$

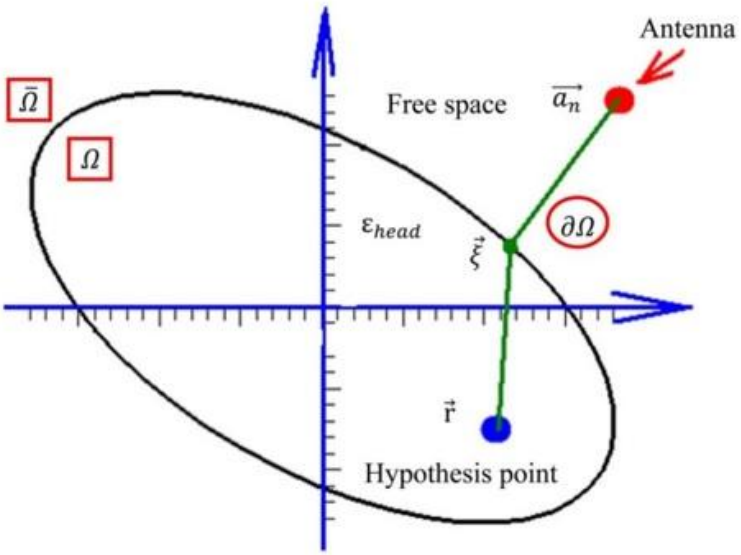

Fig. 5.15 Wave propagation modal for time delay estimation.

After knowing the propagation time from each antenna to the hypothetical point, the final step is to use a back-projection (time delay-and-sum) technique to correlate the time-domain data onto the imaging region. This technique makes a hypothesis that the reflective object is located at a certain point and the constructed signals ($\boldsymbol{\gamma}(\Phi_n, t_m)$) from all the antennas are added to that originating point. In case the hypothesis is affirmative, the signals coherently add to form a large summation. Contrariwise, a hypothetical error will result in incoherent addition of the difference signals and the outcome will be a small summed value. The intensity of the correlation value on each hypothetical point is expressed by $I(x_p, y_q)$.

$$I(x_p, y_q) = I(\vec{r}) = \sum_{n=1}^{N} \left| \boldsymbol{\gamma}\left(\Phi_n, 2\tau_n(\overrightarrow{r_{p,q}})\right) \right| \quad (5.11)$$

The matrix of intensity value is illustrated via a colored image, thus substantial scatters can be easily identified from the depicted image.

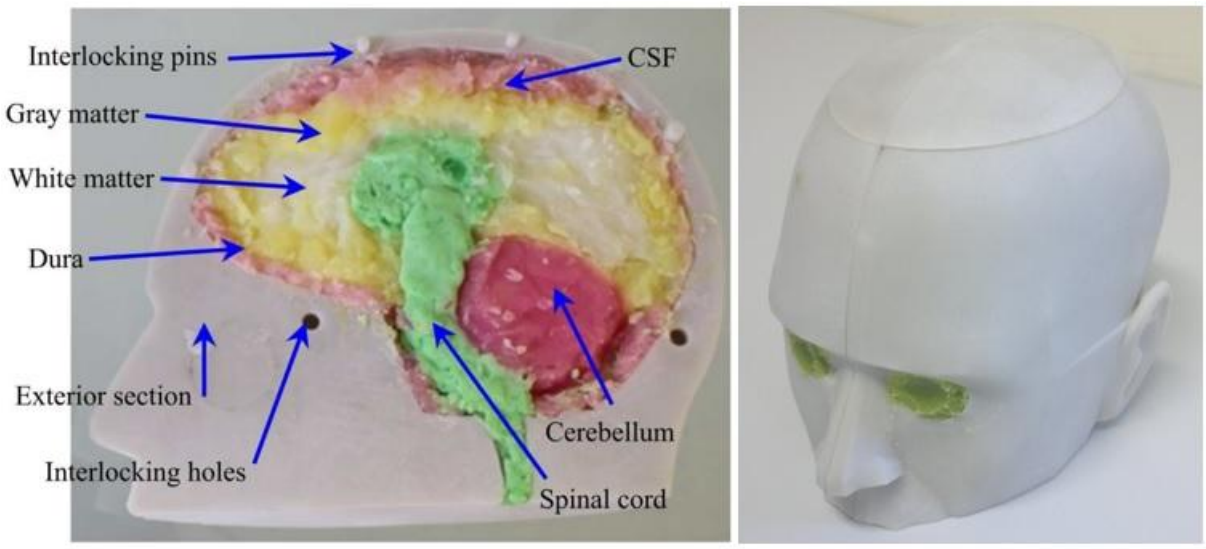

(a) (b)

Fig. 5.16 Photographs of (a) one of the fabricated halves of the head phantom and (b) the finished realistic 3D human head phantom.

5.4.3 Imaging Results and Discussions

The performance of the designed head imaging system and the imaging algorithm in detecting a brain injury is investigated. The constructed realistic human head phantom is employed in the evaluation process of the head imaging system. Photographs of the head phantom are depicted in Fig. 5.16. For the validation purpose, two different sized rectangular blocks of hemorrhagic phantom targets, imitating the electrical properties of actual bleeding [140, 141] is prepared and inserted in the head

phantom. The big target is of 2 × 2 × 0.5 cm^3 and small target is of 1 × 2 × 0.5 cm^3. Two different scenarios of deep and shallow placements of the target inside head are considered in each case.

The initiation procedure of the microwave transceiver is activated and the calibration process is completed over the band of interest (1.1 - 3.4 GHz). The first two steps of the calibration process include the regular short and open loads. However, at the final stage of calibration, the terminal is matched with the antenna itself instead of using a 50Ω match load [182]. This procedure is important for the imaging purpose of the system as it reduces the reflections at the air-antenna interface. Afterwards, the antenna is placed in front of the realistic head phantom and the complex reflection coefficient data is collected. Since the algorithm is based on the monostatic radar approach, only one antenna is used in the system. By utilizing the experimental system platform (Fig. 513(b)), the S-parameter data is captured at 32 uniformly distributed positions around the head phantom. This data set is imported in the imaging algorithm and the 2D image is generated in less than 30 seconds.

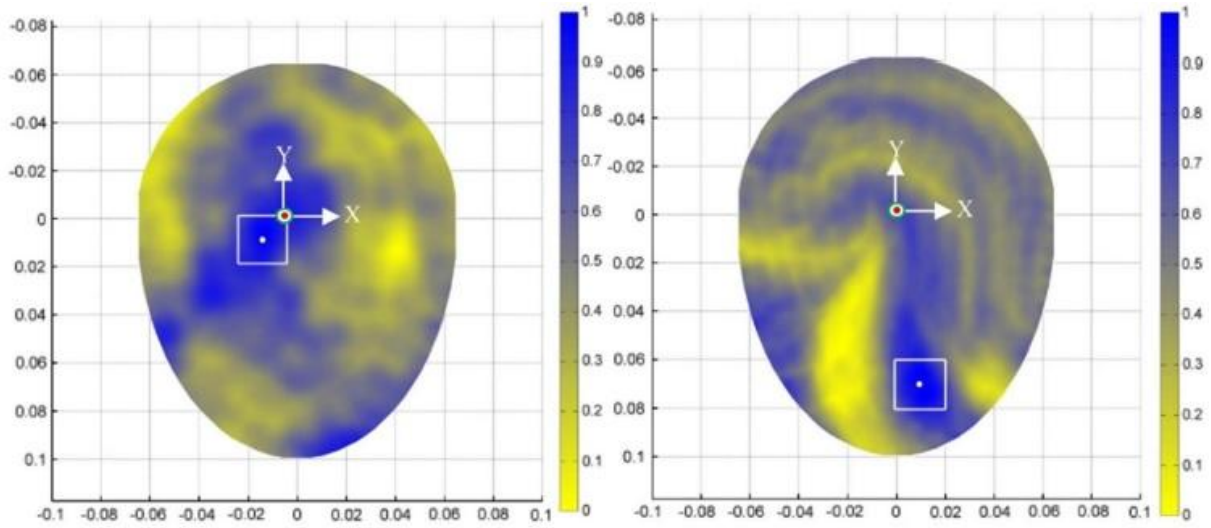

(a) (b)

Fig. 5.17 The measured reconstructed image using 32 antenna positions around a head phantom with a big traumatic brain injury in (a) deep and (b) shallow location, indicated by the rectangular blocks (2 × 2 × 0.5 cm^3).

Figs. 5.17 and 5.18 exhibit the reconstructed images which are generated using a standard laptop within 8-10 seconds after storing the scattered signals. Fig. 5.17 illustrates the images for big rectangular targets (2 × 2 × 0.5 cm^3) placed in deep and shallow locations accordingly centered at (−1 cm, −1 cm) and (1 cm, −7 cm) from the center. Again, reconstructed images for small rectangular targets (1 × 2 × 0.5 cm^3) placed in deep and shallow locations individually centered at

(−1.6 cm, −0.5 cm) and (−1.5 cm, 5 cm) from the center are shown in Fig. 5.18. Here, the cross-sectional images of the head phantom is observed in the form of a heat-map where blue color represents intense scattering parts and yellow color states the absence of scatterers at that part of the head phantom. It is apparent that the positions of the brain injuries have high intensity of distributed energy compared to the remaining healthy tissue regions.

The theoretical estimation of the constructed image resolution using the utilized antenna can be calculated by $\delta = c/2B\sqrt{\varepsilon_{he}}$. Here, c is the speed of light in free space, B is the antenna bandwidth and ε_{he} is the average permittivity of the head. In our system, the theoretical resolution of the reconstructed images is approximately 1 cm, which is enough to detect traumatic brain injuries. Nevertheless, the image quality is improved by utilizing the unidirectional antenna that reduces interferences from the backward direction and gathers more signals from the imaged head. The imaging experiments are done by exciting the antenna with 0 dBm power level which poses insignificant radiation effect on the human body [35].

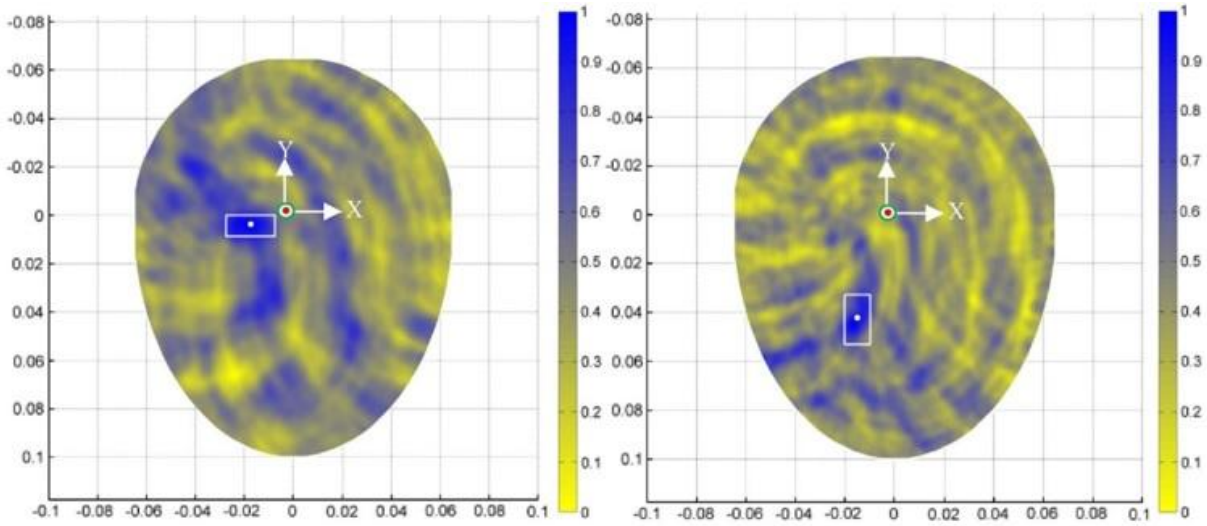

(a) (b)

Fig. 5.18 The measured reconstructed image using 32 antenna positions around a head phantom with a small traumatic brain injury in (a) deep and (b) shallow location, indicated by the rectangular blocks ($1 \times 2 \times 0.5$ cm^3).

To investigate the effectiveness of the reconstructed images from the head imaging system, two quantitative functions defined in [21] are also computed. The first function compares the maximum magnitude of the targeted region, $\boldsymbol{\mathcal{T}}$ with the maximum magnitude of the whole head image, $\boldsymbol{\mathcal{H}}$. This comparative function, γ can be mathematically denoted as,

$$\gamma = \frac{m \quad [I(\boldsymbol{p})]}{m \quad [I(\boldsymbol{q})]} \quad \begin{matrix} \forall \boldsymbol{p} \in \mathcal{T} \\ \forall \boldsymbol{q} \in \mathcal{H} \end{matrix} \qquad (5.12)$$

Here, γ in fact validates the acceptance of the resultant image. If the algorithm can exactly identify the actual position of the injured hemorrhagic portion, computed γ becomes 1. In case of wrong image, the comparative function γ will be less than 1. Since, the strongest scatterers are located inside the targeted regions, the values of γ of all the images (both Fig. 5.17 and 5.18) are found to be 1.

The contrast of the image, Q is defined as the average intensity of the bleeding region, $\mathcal{T}$ over the average intensity of the rest of the head region. Mathematically as,

$$Q = \frac{\overline{I(\boldsymbol{p})}}{\overline{I(\boldsymbol{q})}} \quad \begin{matrix} \forall \boldsymbol{p} \in \mathcal{T} \\ \forall \boldsymbol{q} \in \mathcal{H} \,\&\, \boldsymbol{q} \notin \mathcal{T} \end{matrix} \qquad (5.13)$$

To easily identify the actual hemorrhagic target a high value of Q is desirable. For the reconstructed images depicted in Fig. 5.17 and 5.18, minimum value of Q is found to be 1.78, which is higher than the reported values [21] despite using realistic head phantom in this work.

The summary of the system performances in terms of the two functions are listed in Table 5-II. This table indicates that the images produced by the proposed detection system can reasonably identify and locate the position of both small and large brain injuries. The values for the parameter **Q** indicate that detecting a shallow injury is easier (**Q** is higher) than deep injuries. Also, the detection of large bleeding is obviously easier than small injuries. In case of a healthy head, the accumulated spectrum magnitude is much lower than the bleeding induced injury as the normal blood arteries are of much smaller size than the bleeding regions. Thus, the chance of false positive detections is very slim, but this has to be verified in pre-clinical tests.

Table 5-II Performance of the system with different injuries

Image (Fig. No.)	**γ**	**Q**
5.17(a)	*1*	*1.78*
5.17(b)	*1*	*1.88*
5.18(a)	*1*	*1.79*
5.18(b)	*1*	*1.82*

A portable microwave system for the real-time diagnosis of brain injuries has been presented. The main units of the system are a three-dimensional antenna, compact microwave transceiver and computing tool that includes the pre- and post-processing and image reconstruction algorithms. Since the antenna is a critical part of any microwave imaging system, a compact and low profile antenna is designed for this application. The developed antenna, which uses a folded structure, covers the band 1.1-3.4 GHz (102.2% fractional bandwidth) with directional radiation patterns (9 dBi average front-to-back ratio) and high polarization purity.

The operating principles of the system have been described with appropriate flow charts and diagrams. To test the system, a realistic human head phantom is fabricated using a three-dimensional printer. Finally, a set of data is collected from 32 positions around the head phantom which emulates an early stage brain injury case, and then processed using a back-projection technique. The quantitative metrics calculated from the resultant image demonstrate the feasibility of the system for the early detection of traumatic brain injuries.

5.5 Improvement of Back-projection Algorithm with Model of Effective Head Permittivity

This section reports a portable microwave head imaging system, which is simple to employ and consists of an imaging platform, a compactly designed wideband antenna (described in Section 3.8), a microwave transceiver and a data storing and processing unit. An improved delay-and-sum (DAS) algorithm relying on the derived permittivity model is then employed for reconstructing an image of the head interior with enhanced detection accuracy.

The architecture of the experimental head imaging system is illustrated in Fig. 5.19. The system primarily consists of a compact antenna to transmit and receive wideband signals, a microwave transceiver for signal generation and data acquisition and a personal computer for signal processing and image formation. A head imaging platform is designed to evaluate the system’s performance on detecting ICH using a realistic head phantom. During image, the head phantom is placed at the rotatable platform and scanned using the wideband antenna, which is mounted on an adjustable antenna holder.

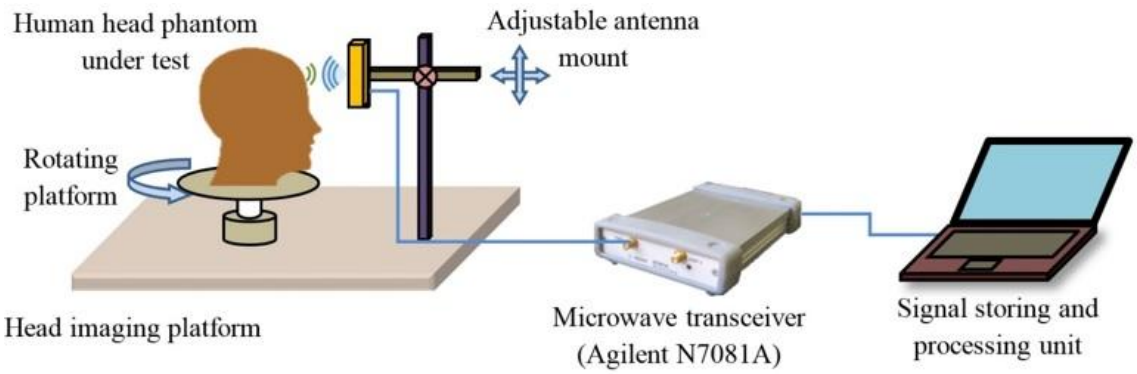

Fig. 5.19 Schematic representation of the wideband microwave head imaging system.

5.5.1 Data acquisition system

The data acquisition system includes a compact microwave transceiver and an antenna. An Agilent N7081A microwave transceiver is utilized for generating the transmitted microwave signals towards the imaged head via the antenna and collecting backscattered signals with a maximum dynamic range of 80 dB. The utilized wideband antenna is introduced in Section 3.8. The antenna has 109% fractional bandwidth covering the band 0.75-2.55 GHz, which provides a reasonable compromise between the required signal penetration inside the head and acceptable image resolution. The antenna is compact and has low profile ($0.26 \times 0.11 \times 0.05\ \lambda_0^3$, λ_0 = wavelength at 0.75 GHz) with 3.5 dBi gain and 9 dB front-to-back-ratio (FBR) along the boresight direction. Considering the high (around 45) average dielectric constant for the human head over the used band, the far-field region originates approximately from 30 *mm* (2.55 GHz) to 95 *mm* (0.75 GHz) away from the point of penetration [183]. Therefore, near field characterization is equally important for the intended head imaging application. The analysis is performed using electromagnetic simulation tools considering +ve Z-axis as the desired direction of antenna's radiation. In near field, the antenna emits directionally with low distortion. Analysing all the near and far-field radiation patterns, it can be concluded that the unidirectional radiation of the antenna (phase center) starts from the center point of top layer over the operating band, enabling to scan a representative 2D layer [19] of the human head that is located at the centerline of the antenna.

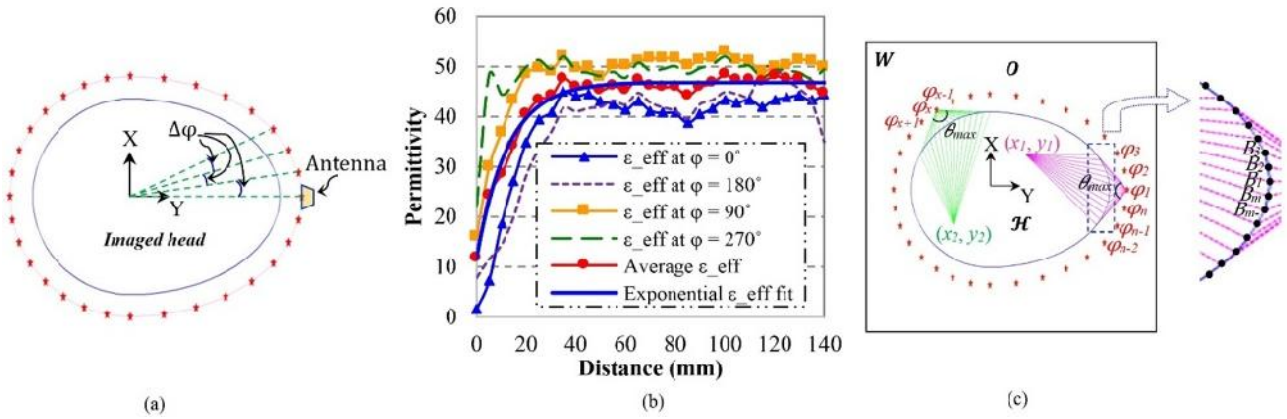

Fig. 5.20 (a) Illustration of Equiangular and equidistant scanning system. Readings that are taken from the same distance and equal angular position faces similar reflection from the skin-air interface; hence, it is easier to cancel the strong background reflection in order to obtain the scattering signal from the actual target. (b) The effective permittivity data attained from realistic human head model simulations by calculating the delay time of the signal arrival. The effective permittivity values of the head sides (φ = 90˚ and 270˚) are slightly higher than those of the front and back (φ = 0˚ and 180˚) due to the presence of the heterogeneously thick high permittivity muscle (55-52.6 across the band 0.75-2.55 GHz) layer along the sides of the head. (c) Path selection of algorithm's procedure from a particular antenna position to an arbitrary point inside the head.

5.5.2 Signal processing and imaging algorithm

As depicted in Fig. 5.19, the data acquisition system utilizes an equiangular and equidistant scanning approach. The transceiver sends, via the antenna, a frequency-domain signal with *M=284* samples covering the band 0.75-2.55 GHz. The transceiver measures via the same antenna (monostatic approach) the complex frequency–domain reflection coefficient, $\boldsymbol{\Gamma}(\varphi_n, f_m)$ where m = 1, 2, ….., M. Here, n represents the different angular positions of the antenna, which extends from 1 to N, while the adjacent antenna's positions have angular differences of $\Delta\varphi = 360°/N$. The inverse discrete Fourier transformation is performed to convert the reflection coefficient, $\boldsymbol{\Gamma}(\varphi_n, f_m)$ from frequency domain to time domain for each source antenna.

$$\boldsymbol{S}(\varphi_n, t_k) = \exp\{[\boldsymbol{D}_{k\times m}]\} \times \boldsymbol{\Gamma}(\varphi_n, f_m) = \begin{bmatrix} S(\Phi_1, t_1) & \cdots & S(\Phi_N, t_1) \\ \vdots & \ddots & \vdots \\ S(\Phi_1, t_m) & \cdots & S(\Phi_N, t_k) \end{bmatrix} \tag{5.14}$$

where $\boldsymbol{\Gamma}(\varphi_n, f_m) = \begin{bmatrix} \Gamma(\varphi_1, f_1) & \cdots & \Gamma(\varphi_N, f_1) \\ \vdots & \ddots & \vdots \\ \Gamma(\varphi_1, f_M) & \cdots & \Gamma(\varphi_N, f_M) \end{bmatrix}$ where $f_m = f_l + (m-1)(f_h - f_l)/(M-1)$

$$\text{and} \quad [\boldsymbol{D}_{k\times m}] = \begin{bmatrix} \mathrm{j}\omega_1 t_1 & \cdots & \mathrm{j}\omega_m t_1 \\ \square & \ddots & \square \\ \mathrm{j}\omega_1 t_m & \cdots & \mathrm{j}\omega_m t_k \end{bmatrix} \tag{5.15}$$

where ω_m is the angular velocity at the individual frequency points; *c* is the speed of light in free space; *k* represents the equidistant points starting from the antenna's phase center to the distance where the amplitude of time-domain signal is close to zero. Eqn. (5.14) considers the positive distances from the point of excitation located in free space.

The transmitted signals are confronted by substantial amount of reflections from the air-skin interface. To extract the useful scattered signals from the internal tissues of the head, it is assumed that as the antennas are positioned in close proximity to each other, the adjacent positioned equidistant antennas face similar reflections from the air-skin interface. Hence, the scattered signals are computed by

$$\boldsymbol{U}(\varphi_n, t_k) = \boldsymbol{S}(\varphi_n, t_k) - w \quad a \quad \left(\boldsymbol{S}(\varphi_{n+1}, t_k) + \boldsymbol{S}(\varphi_{n-1}, t_k)\right) \tag{5.16}$$

$$\boldsymbol{U}(\varphi_N, t_k) = \boldsymbol{S}(\varphi_N, t_k) - w \quad a \quad \left(\boldsymbol{S}(\varphi_1, t_k) + \boldsymbol{S}(\varphi_{N-1}, t_k)\right) \tag{5.17}$$

The adjacent average subtraction takes the advantages of both adjacent [184] and average [185] subtractions. In this case, Woody average (average with first alignment of individual signal) is utilized which is also proven to be effective for biomedical and imaging applications [186].

The variation of the antenna gain over the wide bandwidth is compensated by normalizing the amplitude of the scattered signals by

$$\boldsymbol{U^N}\ (\varphi_n, t_k) = \boldsymbol{U}(\varphi_n, t_k) \Big/ \max(|\boldsymbol{U}(\varphi_n, t_k)|) \tag{5.18}$$

The imaging area of 300 × 300 mm^2 is segmented into P×Q cells, having fine resolutions of 0.5×0.5 mm^2, which are defined by their center points at (x_p, y_q). The head outline is defined by a boundary vector, $\boldsymbol{B_i}$ where $i = 1, 2, ..., I$, located at the skin-air interface in the Euclidean space. The propagation path from the antenna to a hypothetical point inside the head consists of: *1)* a route in free space $\boldsymbol{O}$ from the emitting source to the skin layer and *2)* path inside the head $\boldsymbol{\mathcal{H}}$ extending from the skin layer to the investigated point. According to Fermat's principle, the wave propagates along the shortest possible electrical path $\boldsymbol{D}$ and thus the propagation time index $\boldsymbol{\tau}$ can be calculated as,

$$\boldsymbol{\tau}(x_p, y_q) = \tau_a + {}^{m}\left(\boldsymbol{D}(x_p, y_q)\right)/_{C} \tag{5.19}$$

where τ_a is the antenna delay, defined as the time required to emit electromagnetic radiation from the antenna exterior from the inception of the signal at the feeding port; ***D*** is defined by,

$$\boldsymbol{D}(x_p, y_q) = \|\boldsymbol{\varphi}_n - \boldsymbol{B}_i\| - \sqrt{\varepsilon_e}\,\|\boldsymbol{B}_i - \boldsymbol{p}\| \quad \text{where } \boldsymbol{p} \in \boldsymbol{\mathcal{H}} \tag{5.20}$$

Here ε_e is the effective head permittivity which is a constant number in the previously utilized algorithms [16, 21, 58]. A model for the effective dielectric constant as a function of signal's point of entry and imaged location within the head is utilized in the proposed algorithm.

In order to get a realistic effective permittivity map of the human head interior, a simulation model is created in CST Microwave studio. The MRI based realistic human head model is imported and assigned with the actual dielectric properties of individual head tissues. The radiating antenna is placed in front of the point of entry of the human head, which is theoretically at the transition of air and skin layer. Electromagnetic field probes are inserted in different distances into the head model and the antenna is excited with the frequency band of 0.75-2.55 GHz and run in time-domain solver. The received signals are analysed and the difference between the times of signal arrival, Δt_a is calculated for every field probe inside the head from the reference entry point field probe. The effective permittivity from the point of entry is calculated as, $\varepsilon_e = \left({}^{c\Delta t_a}/_{d}\right)^2$, where d is the distance from the entry point to the particular investigation point and c is the speed of light in free space. The acquired data received from the simulation model is presented in Fig. 5.20(a).

When a signal enters into head, it has to interact with an irregularly thin high permittivity skin (50-44 across the band 0.75-2.55 GHz) layer and then penetrates through thick fat and skull layers having low permittivity. Afterwards, the signal goes through very high permittivity CSF (69-66.2 across the band 0.75-2.55 GHz) and Dura (44-41.9 across the band 0.75-2.55 GHz) tissues, and gradually passes through grey and white matters. The models found in the literature reporting the binary liquid mixture law conclude that the value of the effective permittivity of a mixture of two materials inclines toward the liquid with higher volume. If the volume of higher permittivity liquid is more than the volume of lower one, the resultant permittivity value falls near to the higher permittivity value [151]. In order to extend this phenomenon to the heterogeneous human head, a realistic simulation model with a

MRI-derived healthy human head is analysed in CST Microwave Studio environment over the band 0.75-2.55 GHz.

Fig. 5.20(b) exhibits the effective permittivity graphs of the healthy human head from various φ angles. The effective permittivity is calculated by analysing the differential time of signal arrival from the point of entry. It is seen that the effective permittivity starts from a small value at the point of entry due to the thick low permittivity layers, gradually increases as the signal interacts with thick permittivity values, and subsequently reaches a maximum effective permittivity value and remains around that value for the rest of the propagation distance. The effective permittivity of an arbitrary point inside the head is different for various points of entry of the signal and related to the distance of that arbitrary point from the skin. To have a unified propagation model, the values are averaged and the result is expressed using a distance based function for a particular point of entry of the head,

$$\boldsymbol{\varepsilon_{e\ \ ,i}} = \varepsilon_m \ \ (1 - \alpha e^{-\beta\ /a}) \tag{5.21}$$

Here d is the distance of the investigation point, a is the normal distance from the signal entry point to the center of the head, ε_m is the maximum permittivity, and α and β are constants. For the band of 0.75-2.55 GHz, the effective permittivity values from the realistic simulation environment suggests values of ε_m = 46.8, α =0.75 and β =6.4.

In mono-static radar approach, the transmitted signal travels to and scattered from the arbitrary point; thus, the required total time from the antenna is twice of the propagation time

$$\boldsymbol{\tau_{t\ \ \ l}}(x_p, y_q) = 2\boldsymbol{\tau}(x_p, y_q) \tag{5.22}$$

To reduce the computation complexity, it is realized that the points located on the skin ($\boldsymbol{B_i}$) receive a direct wave from the antennas through free space and that consequently results in a minimum propagation path. Hence, the line of sight points of each antenna ($\boldsymbol{B_{i,n}}$) are traced out by calculating the tangent points of the $\mathcal{H}$ area and the points between them (Fig. 5.20(c)). The tangent points can be calculated by finding the maximum angle, θ_{max} centered at the antenna location. Thus, (6) can be written as,

$$\boldsymbol{D}(x_p, y_q) = \left\|\boldsymbol{\varphi}_n - \boldsymbol{B}_{i,n}\right\| - \sqrt{\boldsymbol{\varepsilon_{ef\ \ ,i}}}\left\|\boldsymbol{B}_{i,n} - \boldsymbol{p}\right\| \tag{5.23}$$

Utilizing (5), (8) and (9), the total time, $\boldsymbol{\tau}_{t_i}\ \ (x_p, y_q)$ is calculated for every (x_p, y_q) points of $\boldsymbol{\mathcal{H}}$ region.

The delay-and-sum back-projection algorithm is employed for the image reconstruction. According to this algorithm, it is assumed that the normalized scattered signals, $\boldsymbol{U^N}\ \ (\varphi_n, t_k)$ are originated from a given point $\boldsymbol{p} \in \boldsymbol{\mathcal{H}}$ and a coherent summation of the signals originating from surrounding antenna is computed.

$$\boldsymbol{I}_i\ \ (x_p, y_q) = \left|\sum_{n=1}^{N} \int_0^{\infty} \boldsymbol{\tau}_{t_i}\ \ (x_p, y_q) \boldsymbol{U^N}\ \ (\varphi_n, t_k) dt_k\right| \tag{5.24}$$

If this hypothetical scattering point is correct, the coherent summation of all the antenna responses results in a large value. Wrong assumption gives a small value; this contribution can be considered as noise. A continuous colour image is produced by plotting the computed $\boldsymbol{I}_i\ \ (x_p, y_q)$ function for each point on the segmented 2D cross-sectional scanned plan of the head phantom. High intensity (usually normalized, thus highest intensity is 1) of colours indicates positions of significant scatterers (hemorrhage) inside the head.

5.5.3 Performance evaluation in simulation environment

In order to validate the head imaging system along with the utilized signal and image processing algorithm, a set of full-wave simulations are performed in the presence of a 3D human head model. Figs. 5.21(a, b) depict the realistic 3D head model and the direction of scanning. The electromagnetic simulation tool CST Microwave Studio is utilized in this regard. To mimic the realistic scenario in the simulation environment, a 3D human head model is created in MATLAB environment using high-resolution magnetic resonance imaging (MRI) scans of a real patient. The model comprises 128 transverse slices and consists a three-dimensional grid of 256 × 256 × 128 cubical voxel elements while the voxels have dimensions of 1.1 × 1.1 × 1.1 mm^3. Using MATLAB, a small amount of hemorrhage (bleeding) of 20 × 20 × 20 mm^3 is inserted into the model to emulate the hemorrhagic target scenario. The bleeding is positioned in the intended investigation area. The model is imported in CST Microwave Studio and each tissue types are assigned with respective frequency dispersive electrical properties of actual human tissues [140, 141]. The hemorrhagic voxel elements are defined according to the properties of blood. The antenna element is placed 15 mm away from the 3D human head model and a set to simulations are carried out over the frequency band of 0.75-2.55 GHz using the equiangular and equidistant scanning approach. A parabolic scanning profile is selected by using

intersections of the $N = 32$ number of vertices of the parabola in $\Delta\varphi = 11.25° \ (= 360°/N)$ angular differences. The indices ($\boldsymbol{S}_{n}, \boldsymbol{S}_{n}$) of the parabolic scanning profile can be defined as:

$$\boldsymbol{S}_{n} = \cos\varphi_n \sqrt{r_a^2 \cos^2\varphi_n + r_b^2 \sin^2\varphi_n} \tag{5.25}$$

$$\boldsymbol{S}_{n} = \sin\varphi_n \sqrt{r_a^2 \cos^2\varphi_n + r_b^2 \sin^2\varphi_n} \tag{5.26}$$

where r_a and r_b are radii of the parabolic path and $\varphi_n = 360°(n-1)/N$, N is the total number of scanning positions. Simulation time required for each antenna position is 7-8 minutes using a computer with 3.4 GHz processing speed and 8 GB RAM in a 64-bit operating system. Results from the simulation model are demonstrated in Fig. 5.21(c).

A signal-to-noise ratio (SNR) of 30 dB, which is usual in real-life environment, is selected for the simulation. Fig. 5.21(c) shows the reflection coefficient results of the antenna in different positions. It is seen that the antenna reacts differently according to the material (tissue type and thickness) placed in front of it. The received signals are translated into images of the head interior using the aforementioned approach. The treated signals in different stages of the data processing pipeline is also demonstrated in Figs. 5.21(d-f). Figs. 5.21(g-l) depict a comparative illustration of the reconstructed images using both the existing [16, 20, 21, 58], and the proposed algorithm. It is noted that with existing algorithm, the reconstructed images significantly vary with the assumed effective permittivity values. However, the proposed algorithm is more accurate in reconstructing the target location inside the head interior.

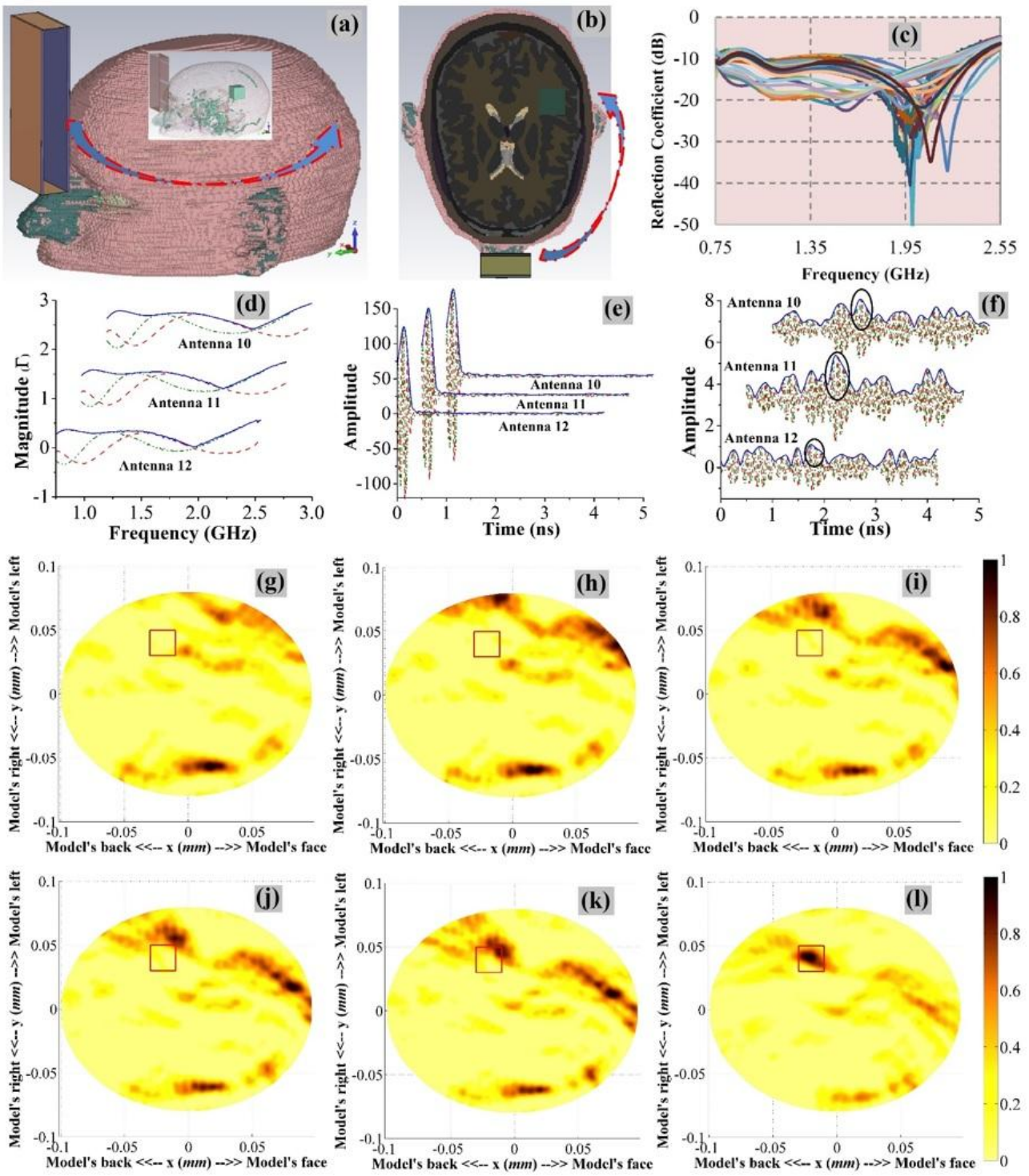

Fig. 5.21 (a) Perspective view of the 3D head model with an inset showing the target location, and (b) top view of the simulation environment. (c) The raw data received by the antenna in different positions. (d-f) Various signals from closest antennas 10, 11 and 12 in the processing pipeline. (g-l) The images are reconstructed using the existing algorithm with fixed effective permittivity of (g) ε_e = 30, (h) ε_e = 35, (i) ε_e = 40, (j) ε_e = 45, (k) ε_e = 50, and (l) proposed model of effective permittivity.

5.5.3.1 Analysis of the simulated results

The efficacy of the compact head imaging system and proposed algorithm is analysed comparing the image quality with the images obtained from the existing fixed average permittivity based imaging algorithm [16, 20, 21, 58]. Several quantitative matrices are investigated as defined in the previous section.

Considering images from simulation environment, qualitative and quantitative matrix analyses of pre-known hemorrhagic location and size reveal that the existing algorithm using fixed ε_e fails to identify the location of the target. While a sense of target localization is noted in case of ε_e = 50, another substantial artifact exists in the frontal area which results low signal to maximum clutter and contrast ratios with wrong detection. Details of the quantitative matrices are listed in Table 5-III. On the other hand, the proposed algorithm distinctly identifies the position of hemorrhagic target. The resultant image of Fig. 5.21(l) presents higher amplitude ratio of γ = 1.39 and contrast of Q = 5.83. The image demonstrates very low deviation of δ = 0.71 *mm* from the center of hemorrhagic position to the highest amplitude. Based on the quantitative matrices, it is noted that the proposed algorithm is more accurate in reconstructing the target location inside the head interior.

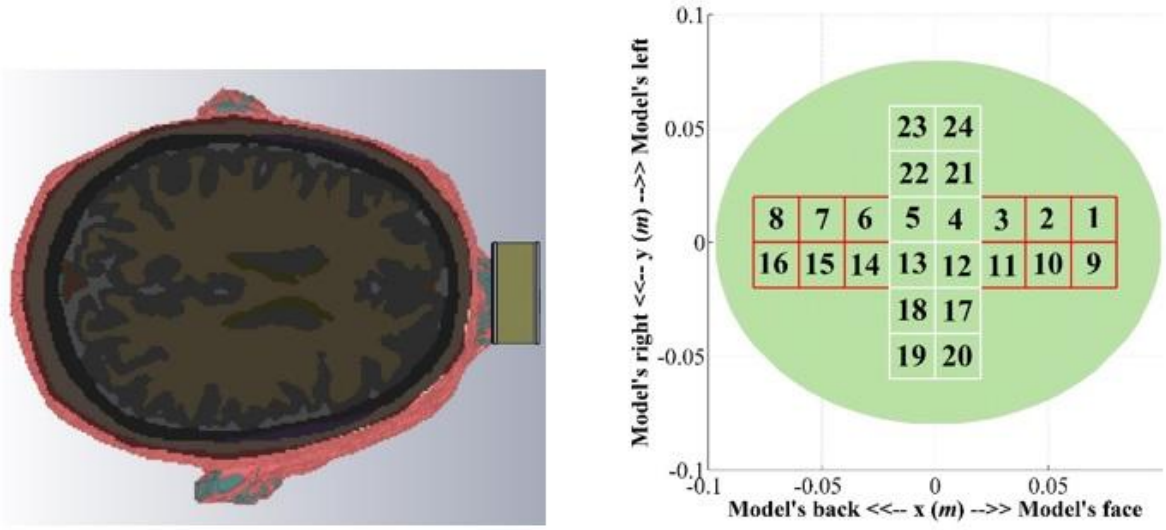

(a) (b)

Fig. 5.22 Illustration of the cross section of (a) healthy human head model and (b) ICH target positions.

5.5.3.2 Map of reconstruction accuracy

To systematically validate the potential of the system, a map of its image reconstruction accuracy is generated through systematically choosing 24 positions along the horizontal X and Y axes of the imaged layer. The details of the ICH target positions are described in Fig. 5.22. The results of the

reconstructed images using the proposed modified back-projection and existing algorithms of every position are illustrated in Fig. 5.23. It is noted that for every location, the signal to maximum clutter function, γ is more than 1 indicating the ability of the algorithm to detect the ICH targets effectively. However, the detection sensitivity is different from one location to another.

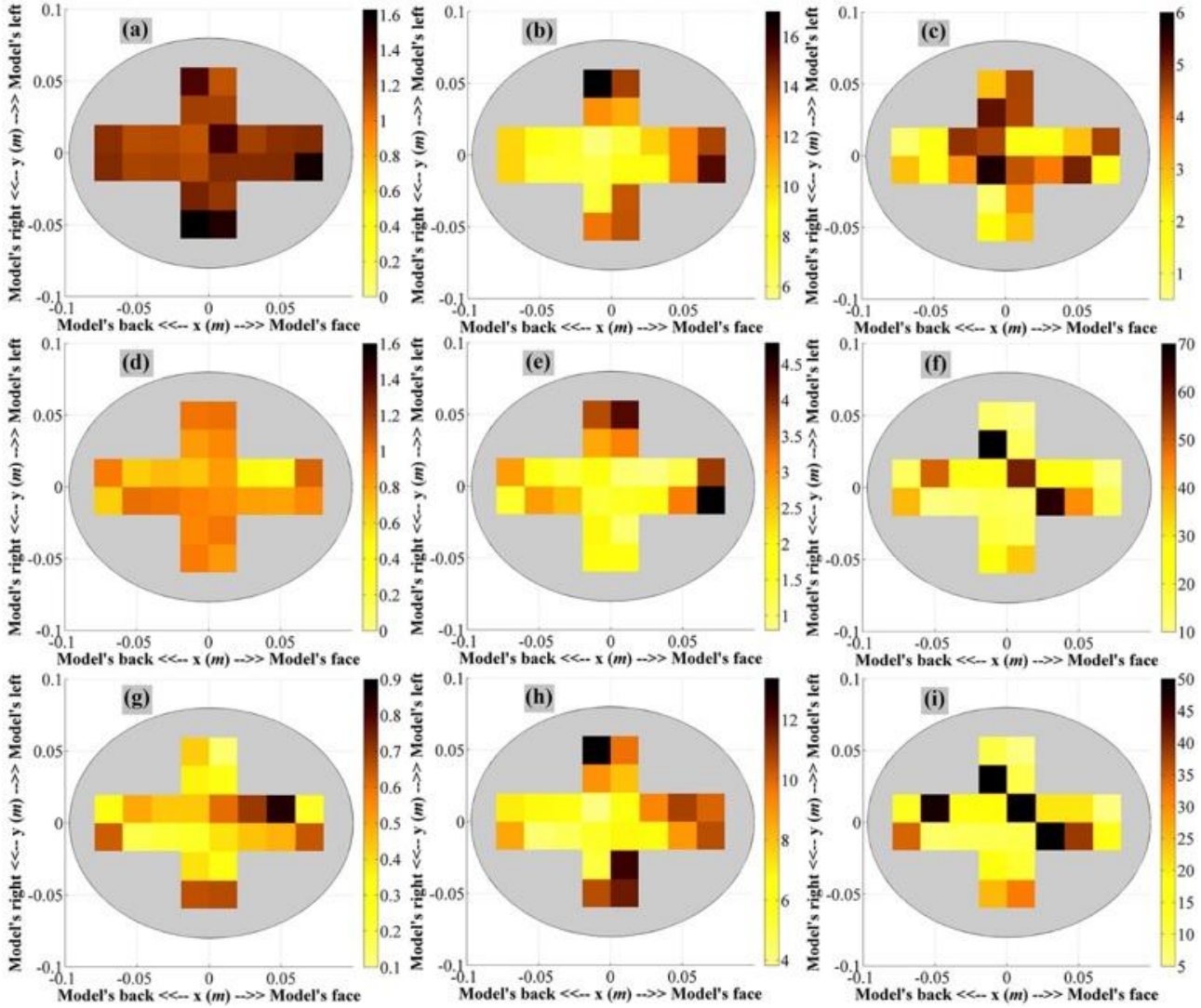

Fig. 5.23 The map different quantitative matrices demonstrating the reconstruction accuracy of the realistic human head model using the introduced back-projection algorithm.

Figs. 5.23(d-f) presents the map different quantitative matrices ((d) the map of signal to maximum clutter function, γ; (e) the map of average signal to clutter ratio function, Q. (f) the distance between the true central location of the target, δ) demonstrating the reconstruction accuracy of the realistic human head model using the existing back-projection algorithm relying on constant effective head permittivity of ε_e = 45. Finally, quantitative comparisons between the existing and proposed algorithms are presented in Figs. 5.23(g-i). The differential map of the head model's cross section demonstrating the improvement of image reconstruction when the proposed modified back-projection

algorithm is compared to the existing one. (g) The map of differential signal to maximum clutter ratios defined as, $\gamma_d = \gamma_p \; _{po} - \gamma_e$. (h) The differential map of average signal to clutter ratio functions defined as, $Q_d = Q_p - Q_e$. (i) Difference map of the distances between true central location of the targets defined as, $\delta_d = \delta_e - \delta_p$. This differential map demonstrates significant quantitative improvements in the detection capability of the proposed algorithm.

5.5.4 Experimental validation of the head imaging system

After the performance evaluation in the simulation environment, the head imaging system is tested experimentally. A realistic human head phantom is constructed for the validation purpose. The phantom is fabricated by emulating the electrical properties of various tissues of human head, such as gray matter, white matter, Dura, cerebellum, CSF, and so on. The exterior structure (skin, fat, muscular parts and skull) and the interior moulds of the head phantom are built in 3D printer [155]. The exterior is utilized to hold the internal brain parts which are fabricated with tissue emulating materials. Additionally, skin emulating viscous liquid is also utilized to include the effects of the skin [178].

The experimental flow chart of the data collection and storing process is illustrated in Fig. 5.24. Following the sequences, the scanned reflection coefficient signals, from which the backscattered signals are extracted, are stored in a matrix $\boldsymbol{\Gamma}(\varphi_n, f_m)$ for post processing.

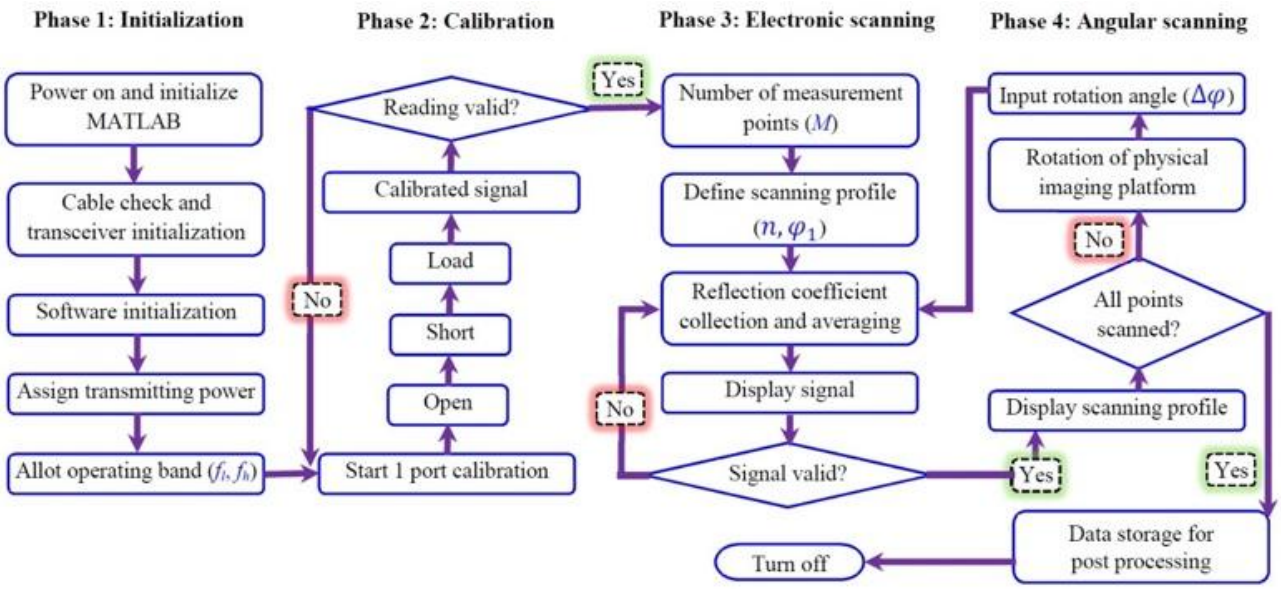

Fig. 5.24 The step-by-step flow diagram of the data collection and storage process using a customized controlling software system which creates interfaces between the utilized devices and computer.

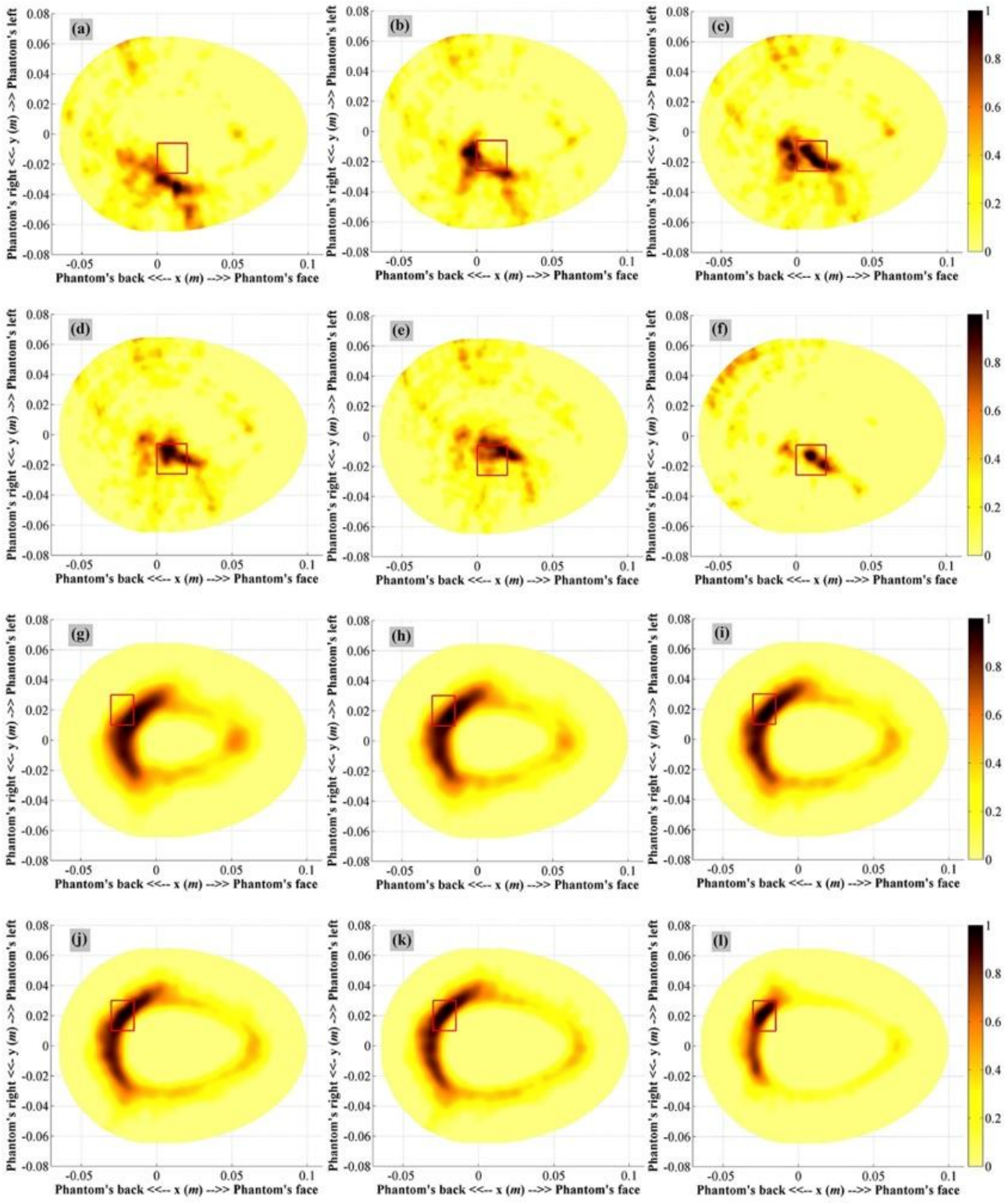

Fig. 5.25 Head imaging results of target-1 (big) in deep location and target-2 (small) in mid location, respectively, using different algorithms: fixed average permittivity based algorithm with (a, g) ε_e = 30, (b, h) ε_e = 35, (c, i) ε_e = 40, (d, j) ε_e = 45, (e, k) ε_e = 50, and (f, l) algorithm relying on model of variable effective permittivity.

The data collection process (Fig. 5.24) is done in four main stages: 1) initialization, 2) calibration, 3) frequency scanning and 4) angular scanning. As the MATLAB environment is initialized in the computer, the data acquisition devices and controlling software are started along with a check of the connections. Then, a transmitting power of 0 dBm and lowest (f_l = 0.75 GHz) and highest (f_h = 2.55 GHz) frequencies of the operating band of the system are defined. Afterwards, one port calibration process is commenced where the microwave transceiver, Agilent N7081A is calibrated with the help of standard open, short and matching load technique. Then, the number of measurement points, *M* and equidistant-equiangular scanning profile are defined in the software interface. The reflection coefficient is collected from where the backscattered signal can be extracted. The data are checked for any abnormality, like rapid impulsive change caused from interferences. After this, the scanning profile is checked and in case there are more positions to scan, the imaging platform is rotated by $\Delta\varphi$ angle. The angular input is provided in the controlling software and a combination of frequency and angular scanning is performed until readings from *N* scanning positions are gathered.

Validation of the system and algorithm of both target-1 and -2 (ICH) in different locations are performed. The collected data is utilized to reconstruct images of the head interior. The resultant images from the proposed algorithm is then compared with the images received by using the traditional method with fixed effective permittivity based algorithm. A range of fixed average permittivity from ε_e = 30 to ε_e = 50 are assumed for the whole head to observe the variations of the resultant images. It is seen from Fig. 5.25 that the proposed algorithm provides better reconstructed image for both deep and shallow targets.

The results confirm the effectiveness of the proposed model for the effective permittivity in head imaging. In case of target-1, the fixed effective permittivity based algorithm illustrates several artifacts, which can be corrected by utilizing the proposed algorithm. As seen in Table 5-III, the maximum intensity ratio, γ and average intensity ratio Q of the proposed algorithm is higher than the reported algorithm of [16, 20]. The calculated accuracy indicator, δ considers the maximum intensity point closer to the center of the target region which indicates higher accuracy of the target recognition. Although in case of ε_e = 45, the γ value is comparable to that of the proposed algorithm, the other values are relatively low, demonstrating the image quality enhancement using proposed algorithm. For the small target, the proposed algorithm results in improved values of the calculatedγ, Q and δ parameters. It indicates that as the target goes closer to the skin the scattering signals from the target becomes stronger and hence, the algorithm is able to reconstruct the target with increased accuracy in comparison to the previously developed algorithms.

Table 5-III: Quantitative metrics indicating the reconstructed image quality

Effective Permittivity	Simulation model (Figs. 5.21(g-l))			Large, deep (Figs. 5.25(a-f))			Small, mid (Figs. 5.25(g-l))		
	γ	Q	δ (mm)	γ	Q	δ (mm)	γ	Q	δ (mm)
with ε_{avg} = 30	0.37	0.26	103.53	0.75	1.35	19.81	0.99	3.98	9.7
with ε_{avg} = 35	0.24	0.11	104.37	0.91	3.94	15.7	1.03	5.11	6.02
with ε_{avg} = 40	0.28	0.34	109.08	1.07	6.5	4.3	1.02	5.8	3.64
with ε_{avg} = 45	0.71	0.97	103.96	1.12	6.62	5.15	1.04	6.11	**1.11**
with ε_{avg} = 50	0.87	2.63	99.11	0.99	5.6	11.42	1.05	5.92	3.64
Proposed model (SNR = 30 dB)	**1.39**	**5.83**	**0.71**	**1.17**	**9.9**	**3.54**	**1.25**	**11.4**	2.06
SNR = 20 dB	1.34	5.74	1.58	1.2	9.8	3.9	1.16	11.4	2.7
SNR = 10 dB	1.26	5.34	0.71	1.1	7.1	5.1	1.08	11	4.6
SNR = 5 dB	0.99	4.71	118	0.86	1.8	53.2	0.77	3.8	59

5.5.5 Effect of Noise

The effects of noise on the proposed head imaging system and its reconstructed images are also investigated. The SNR values of the simulated and measured images are gradually decreased from 30 dB to 10 dB. Figs. 5.26(a-c) show the simulation and measured results when the SNR = 20 dB, whereas Figs. 5.26(d-f) report the reconstruction at SNR = 10 dB. The quantitative results of the reconstructed images are listed in Table 5-III. Nevertheless, maps of the quantitative analyzes of the image reconstruction are also plotted in Figs. 5.26(g-o) for the gradual SNR reduction. As expected, a substantial diminution of image quality is noted for a significant reduction in the SNR.

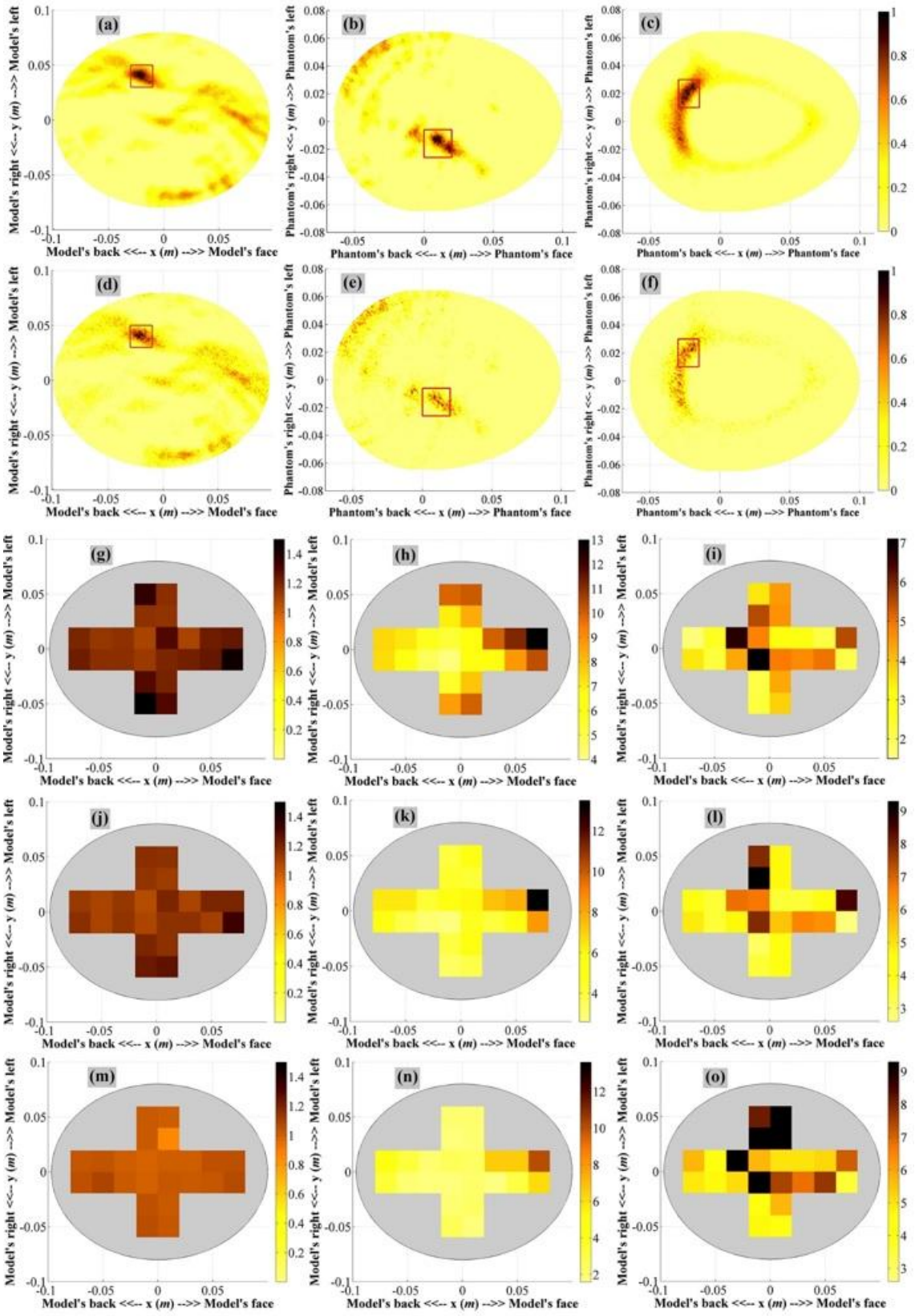

Fig. 5.26 (a-c) The simulated (a) and measured (b, c) reconstructed images at SNR = 20 dB. (d-f) The simulated (d) and measured (e, f) reconstructed images at SNR = 10 dB. The maps of the quantitative investigations, namely γ, Q and δ accordingly, demonstrating the reconstruction accuracy at (g-i) SNR = 20 dB. (j-l) SNR = 10 dB, and (m-o) SNR = 5 dB.

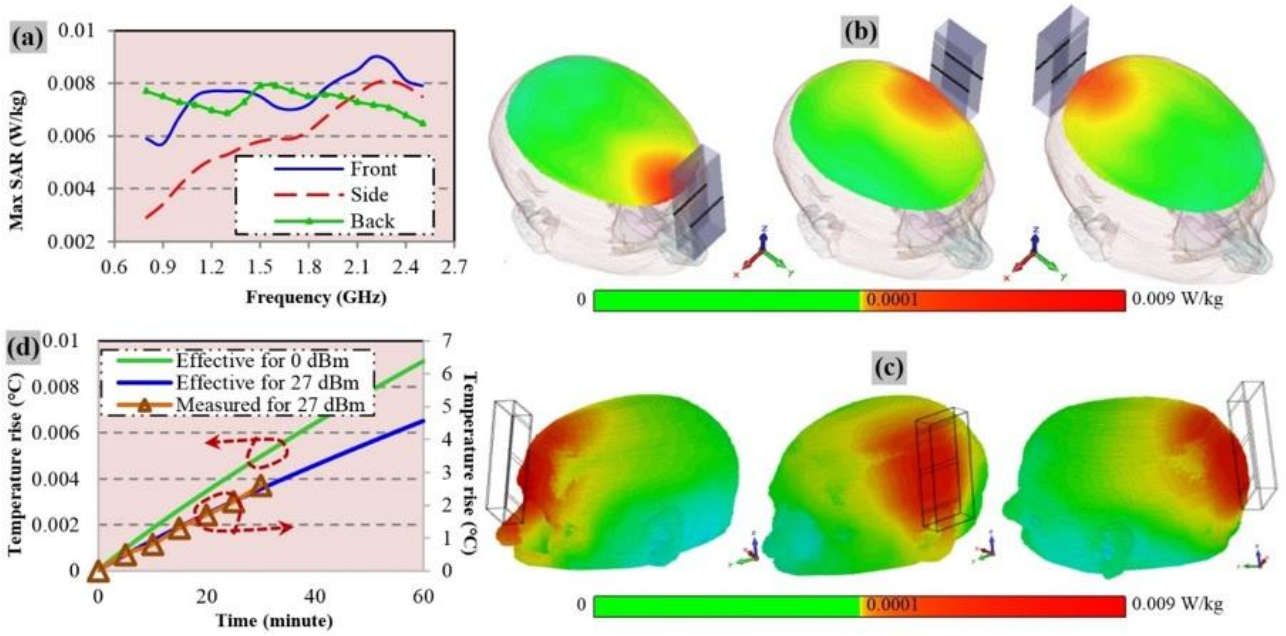

Fig. 5.27 (a) The calculated maximum SAR over the functional bandwidth for antennas operating from various directions. (b) Cross-sectional view and (c) perspective view of the realistic human head model while the antenna is operating at 0.8 GHz and 2.4 GHz. (d) Simulated and measured effective skin surface temperature rise due to the electromagnetic emission from the antenna.

5.5.6 Safety considerations of the system

The radiation safety of the patient while applying the presented detection and monitoring device is also investigated. Since the system works in mono-static manner, only one antenna is active at any particular time even if an array of antennas is used for fast data acquisition. Each of the antennas transmits 0 dBm or 1 mW power toward the head and receives the backscattered signals. The specific absorption rate (SAR) of the head is calculated by using CST simulation tool. An MRI-scan based in-house built human head phantom is utilized for this purpose where the frequency dispersive electrical properties of the actual tissues are employed [44]. The head model and the SAR results are presented in Fig. 5.27(a, b). It is observed that the SAR values are well below the IEEE safety limit of 2 W/kg [187]. The mid-cross section illustration of the head model while the system operates at 0.8 GHz (Fig. 5.27(c)) reveals the gradual dissipation of the emitted signal. Again, Fig. 5.27(d) presents the system at 2.4 GHz and it is noted that most of the power loss is located at the skin layer of the human head especially at the nearest point from the middle of the antenna.

Since the system might be active over a long time for continuous monitoring of the patient, the thermal effect of the electromagnetic signals is also a matter of interest along with SAR verification. The effect on skin is particularly important as skin absorbs most of the emitted power and heating from

the system might cause skin burns or discomfort to the patient. The rise of temperature at the skin from the emitted power of an antenna can be calculated by [188],

$$T_s \quad (f) = C_1\sqrt{t} - C_2\left(1 - e^{t/\tau}e \quad \left(\sqrt{t/\tau}\right)\right) \tag{5.27}$$

$$\text{where } C_1 = \frac{2I_0T}{\sqrt{\pi}}, C_2 = \frac{I_0TS_d}{k} \text{ and } \tau = \frac{4}{\pi}\left(\frac{C_1}{C_2}\right)^2 \tag{5.28}$$

Here, $e \quad (x)$ is the complementary error function and coefficient of surface transmission of skin is, $T = 1 - |r_1|^2$, while reflection coefficient of skin/air interface is expressed as, $r_1 = (\sqrt{\varepsilon} - \sqrt{\varepsilon_0})/(\sqrt{\varepsilon} + \sqrt{\varepsilon_0})$. Here complex permittivity of the skin, ε is dependent on the operating frequency, f and absolute relative permittivity of air, $\varepsilon_0 = 1$. Thermal inertia of skin, $k\rho = 1.7 \times 10^6$ $W^2s/m^4°C^2$ and thermal conductivity of skin, $k = 0.3$ $Wm^{-1}°K^{-1}$. The thermal time constant τ is defined as the time needed for thermal wave to diffuse skin depth ($= S_d$) equivalent distance.

The effective temperature rise of the skin at a particular time can be calculated by,

$$T_e \quad (f) = \frac{1}{M}\int_{f_l}^{f_h} T_s \quad (f)\, d \tag{5.29}$$

With the transmitted power of the antennas, at 15 *mm* distance, the incident power density on the skin is calculated as 1.24 W/m^2 or 0.124 mW/cm^2, which is less than the radiation safety limit [188] of 1 mW/cm^2. Since the scanning approach of head imaging system operates by sweeping from lower frequencies to higher ones (0.75 to 2.55 GHz) for an individual reading, all frequencies do not operate at the same specific moment. The effective rises in the temperature of skin at particular times are calculated and presented in Fig. 5.27(d). From the governing eqns. (5.27-5.29), it is noted that the skin temperature is highly sensitive to the operating frequencies and the higher frequencies increase skin temperature much quickly than the lower ones. This is due to the increase of skin's conductivity at higher frequencies that reduces the skin depth (penetration depth) of the skin tissues resulting in the accumulation of thermal energy due to electromagnetic losses around the skin surface. As the temperature rise is comparatively low for the used thermal camera, the measurement is performed by using higher transmission power of 27 dBm (= 0.5 W) for the sake of validation. It is seen that the measured skin temperature rise for 27 dBm matches the calculated results, which validates the previous calculated temperature rise for 0 dBm, indicating the safety of the head imaging system.

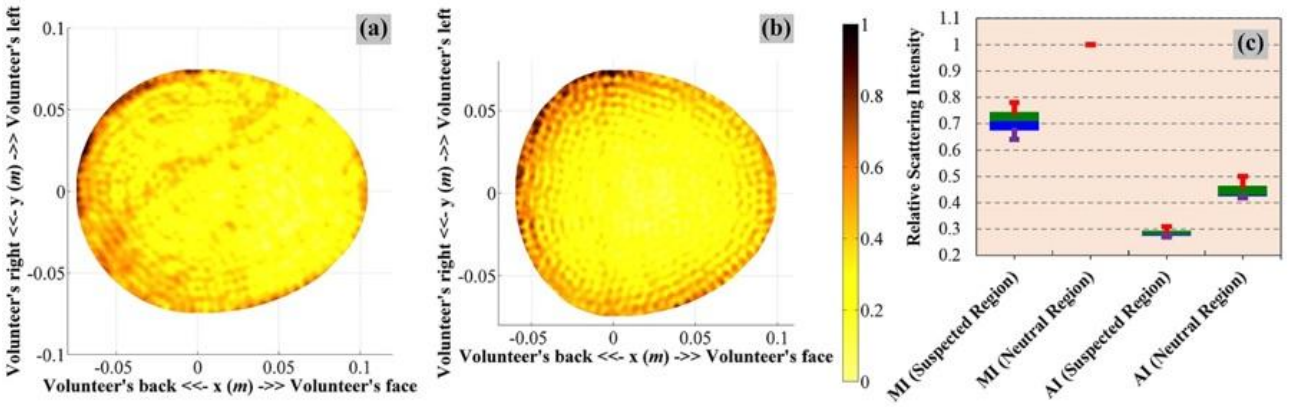

Fig. 5.28 (a, b) Examples of the reconstructed images of healthy volunteers using a prototype of the head imaging system. (c) The statistics of the maximum and average scattering intensities of the neutral and suspected regions of the volunteers. The green and blue boxes represent the 75th and 25th percentiles respectively and the transitional line between them presents the median. The red and violet lines accordingly states the maximum and minimum magnitudes. MI = Maximum intensity, AI = Average intensity. The MI of neutral region in all regions is one, as the images are normalized with respect to the highest intensity and it falls in the neutral region.

5.5.7 Pilot human tests of the system prototype

A prototype of the head imaging system is utilized to analyse the images that can be obtained from healthy volunteers with different head shapes and sizes. Samples of the reconstructed images of the volunteers depicted in Fig. 5.28(a, b) illustrates that in any healthy volunteer's head the most significant scatterers are located along the skin layer. This scenario demonstrates that in healthy volunteers the skin exhibits the strongest scattering compared to the other brain parts. The interior of the head does not pose any substantial scattering; hence, the images are free from false positive responses. Since ICH does not occur in the skin or skull region [2, 189], the skin and skull tissues (which are about 10 *mm* thick) can be considered as a neutral region, whereas the rest head interior as the suspected region. To that end, the images of healthy volunteers are statistically analysed (Fig. 5.28(c)). It is found that the median of maximum and average intensities of the neutral region are around 1.4 and 1.5 times higher than those of the suspected region.

Although all images are normalized with respect to the maximum intensity of that individual image, extended observations indicate that while the un-normalized maximum magnitude due to hemorrhagic target in the simulated (Fig. 5.21) and experimented (Fig. 5.25) phantoms with hemorrhagic is in the scale of 10, the experimental images (Figs. 5.28(a, b)) from the human subjects exhibit highest intensity of around 1. Thus, it is anticipated that in the presence of ICH, the scattering

from the neutral region is going to be negligible compared to that of bleeding and there might be a possibility of imaging threshold. However, further investigation of healthy and unhealthy subjects is required to finalize the conception of the imaging threshold.

5.5.8 Discussions

A simple and effective head imaging system operating from 0.75-2.55 GHz is introduced in this section. A data acquisition system, including a compact microwave transceiver and a low-profile UWB antenna, is utilized to collect the backscattered signals. The near-field characteristics of the antenna are analysed to verify suitability for system application and the antenna is found to be unidirectional with low distortion radiation performance compared to the previously reported compact antennas [190]. Furthermore, the point–of-entry dependent permittivity based delay-and-sum algorithm is introduced in this section which has demonstrated its potential by providing enhanced image quality and accuracy compared to the previously developed fixed effective permittivity based algorithm. The efficacy of the head imaging system is firstly verified on a 3D human head model with a hemorrhagic target in simulation environment. It is noted that the target's response (Figs. 5.21(d-f)) is masked in the background and the modified processing algorithm is able to uncover the scattered signal from the target. Reconstructed images from simulation data reveals that the fixed permittivity based algorithm shows a lot of artifacts and fails to detect the actual position of the hemorrhage Figs. 5.21(g-k), while the proposed algorithm is able to detect its actual location Fig. 5.21(i).

In the first simulated model (Fig. 5.21), the ICH hemorrhagic target is positioned along the edge of gray matter tissue. It is found that the system can detect ICH with low contrast which can be explained as follows. The wave impedance that combines both dielectric properties (permittivity (ε_r) and conductivity (σ)) for the operating frequencies can be calculated by, $Z_m = \left|\sqrt{j\omega\mu_0/(\sigma + j\omega\varepsilon_0\varepsilon_r)}\right|$, where ω is the angular velocity, μ_0 is absolute permeability and ε_0 is absolute permittivity. Z_m of blood ranges from 44.8 to 49.9 Ω over the same operating band; whereas for gray matter, it is 48.9 to 52.5 Ω. This gives a wave impedance contrast of 9.2 to 5.2 % between the hemorrhagic target and the background (gray matter) across the band from 0.75 GHz to 2.55 GHz. However, deep targets with white matter background have contrast ratio of around 27.5 to 23.6 % over the band. This higher contrast assists in ICH detection. However, in deep locations, owing to the increase of penetration losses, the average signal to clutter ratio function, Q decreases with an increase of localization error, δ. This effect can be realized from the maps of the image reconstruction accuracy Figs. 5.26(a-c).

The head imaging system is practically validated on a 3D printed human head phantom having frequency dispersive electrical properties by using the prototyped data acquisition system (SNR = 30 dB) and the controlling software. Signals are measured for both target-1 ($2 \times 2 \times 0.5$ cm^3) and target-2 ($1.5 \times 2 \times 0.5$ cm^3) hemorrhagic targets in different locations with high and low contrast ratios respectively. The measured signals are post processed and images are reconstructed using both algorithms. The quantitative analysis discloses that the proposed algorithm demonstrates better image quality with clear and easily distinguishable bleeding location. However, due to the penetration losses mentioned before, the shallowly located targets are easier to detect (Table 5-III). These resultant matrices of the proposed algorithm are comparatively higher with much accurate detection capacity than those of the existing algorithm and even the reported values [20, 21].

A comparison between simulation and measurement with similar setup can be performed. In this case, reconstructed images presented in Fig. 5.25(f) and Fig. 5.26 (position 13, see Fig. 5.22) are considered, where ICH target is located at the centre of the frontal right quarter of the head with 2×2 cm^3 cross section. Quantitative analyses reveal that with SNR=30 dB, the reconstructed image from simulation attains better detection and localization than that of measurement. For simulation, the values of the matrices are γ=1.3, Q=10 and δ=0.7 *mm*, while from measurement the values are γ=1.17, Q=9.9 and δ=3.54 *mm* respectively. The similarity in values illustrates the efficiency of image reconstruction. However, the realistic head phantom in the measurements is smaller than the simulated head model, which is acceptable as different patients will have different head shapes and sizes. It is realized that with a bigger head model, the detection and localization ICH target with same contrast and position will tend to degrade as concluded from discussions pertaining Figs. 5.23(a-c).

The gradual SNR reduction from 30 dB to 5 dB as a result of increased noise demonstrates (Fig. 5.26) the gradual reduction in image quality, yet the shallower ICH targets show higher quantitative matrices than the deeper ones. Nevertheless, the differential quantitative studies from one SNR to another indicate that shallow ICH targets are also more sensitive to change in SNR than the deep ones. Quantitative investigations of both simulations and measurements reveal that if SNR < 10 dB, the system heavily sacrifices the image quality and mostly unable to detect or falsely detect ICH targets. However, real-life environment usually provide SNR of more than 10 dB.

The system has the potential to be operated for continuous quasi- real time monitoring purposes of head injured patients. For this reason, the safety issues of the head imaging system including the radiation and temperature safety are checked to avoid any operational danger. The SAR values of the system are found to be much lower than the IEEE safety limit ensuring the electromagnetic safety of the system. The temperature rise at the skin layer is also computed for 60 minutes of realistic frequency swiping operation over the frequency band. It is observed from Fig. 5.27(d) that the

temperature rise is not significant even after the continuous operation of the head imaging system for 60 minutes. However, it is found that for the utilized level of power, the temperature rise is very small. Temperature rise is also verified for 27 dBm transmission power through measurement, which proves the effectiveness of the calculated estimations.

The sources of the simulated and measured phantoms are different. Hence, although the simulated and measured antennas in free space show the same performance, the experimental results are not exactly the same as the simulation when the antennas are placed in front of the phantoms. However, appropriate reconstruction of the ICH target reflects the effectiveness of measurements.

A system prototype is developed to perform a pilot human test on two healthy volunteers. A significant scattering from the skin is noted from Figs. 5.28(a, b). This is attributed to the residual scattering response of the skin after the adjacent average subtraction. This residual scattering from the skin can also be seen from the $\boldsymbol{U}(\varphi_n)$ signal of Fig. 5.21(f). Due to slight variation of skin thickness between adjacent positions, it can be seen that residual skin scattering present in $\boldsymbol{U}(\varphi_n, t_k)$. However, they are not dominant for the scenario where there is an ICH target. For this reason, even though the simulated model and the emulated measured phantom have skin response, it is not significant when compared to that of ICH target. But these skin reflections plays vital roles at times when there is no ICH inside the patient, as seen for healthy volunteers. In healthy head, no significant target coherently adds up like ICH target and hence the skin becomes the significant scatterer.

The head imaging system can successfully detect targets of volume 2c2×2 cm^3 in simulation and 2×2×0.5 cm^3 in one of the measurements. In another measurement, the system is able to detect an even smaller target of 1.5×2×0.5 cm^3. At early stages, the suspected ICH patients exhibits ICH targets with a median of 17 cm^3 [191] or in the scale of centimetres [189]. Therefore, the detectable amount by the system is more than adequate for the early stage ICH detection. Because of the reduced computational complexity, the image reconstruction with proposed algorithm takes 7-10 seconds, which is less than the time required by existing algorithms [20, 21]. Other reported low-cost and portable imaging technologies (e.g., EIT [27], MIT [28], MIS [29], PSSMI [30]) demonstrate advantages in either simulations or on simple phantoms without much realistic demonstration. Nevertheless, tomography based imaging system requires more data acquisition and long computation time [192]. However, at this point of research, pilot human tests are limited to healthy volunteers. Hence, although the tests illustrate the absence of false positive results, more measurements of healthy and unhealthy subjects are required for a successful preclinical system.

The system is compact and light weight (less than 1 kilograms including the data acquisition system) which can be applied as a portable system. Although data acquisition process takes 3-4 minutes it can be made less than 30 seconds by using an array of antennas. The future works involve implementation

of the array of antennas in a compact package. Thus, the future generation of portable head imaging system can consequently be sent for preclinical trials to detect head injuries.

5.6 Compact Imaging System with Automated Scanning Capabilities and Imaging Improvements by Considering Surface Waves

The head imaging system described in the previous section utilized a semi-automatic scanning system, which is susceptible to movement error owing to the considerably longer scanning time. This section reports the design and implementation of a non-invasive automated head imaging system for brain injury detection based on wideband microwave imaging technology. The automated, portable mono-static scanning based system is described in detail. An ultra-wideband antenna is designed and prototyped for sensing the scattering fields from an ICH affected human head model. An image theory-supported magnetic symmetry line concept and a cross-feeding technique are applied on a previously reported symmetrical antenna [58] to minimize the space requirements as well as to fix the well-known beam-tilting problem. In order to understand the underlying physics of the head imaging system, head models of different sizes, with different ICH targets in varied locations and excitations are numerically studied. A sophisticated image reconstruction algorithm considering the nature of signal propagation in the complex near-field region is presented. The algorithm takes the surface wave propagation around the head phantom into account and calculates the minimum scattering path on the basis of a permittivity model. The head imaging system is tested on a realistic human head phantom containing frequency dispersive emulated head tissues with MRI-derived anatomical distributions. A stepper motor with a controller unit and a compact microwave transceiver is utilized for fast data acquisition. The reconstructed images demonstrate that the head imaging system with the image processing algorithm is capable to detect and locate the position of ICH brain injuries of various sizes in different depths inside the head phantom. The images are analysed qualitatively and quantitatively using standard metrics, and the results are discussed from different statistical perspectives.

5.6.1 Head Imaging System

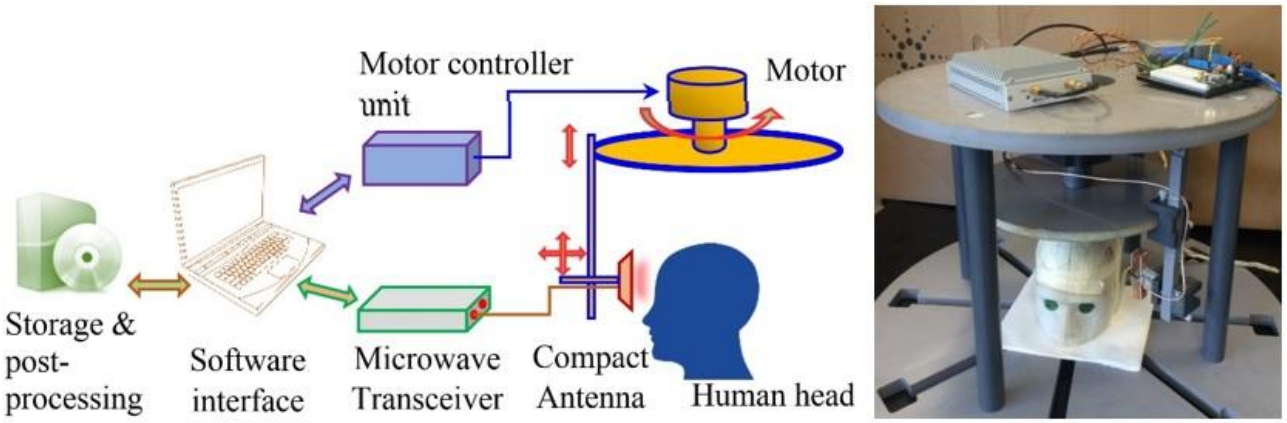

(a) (b)

Fig. 5.29 The proposed microwave head imaging system.

The proposed head imaging system is demonstrated in Fig. 5.29. The system can scan the human head by sending low-level electromagnetic fields at microwave frequencies towards the head and measuring the reflected fields from the brain. The system consists of a custom made head imaging platform, a compact wideband antenna, a compact microwave transceiver, a motor controller unit, a software interface, and a storage and post-processing algorithm. The head imaging platform, which is flexible to different head sizes and orientations as per the requirements, holds the DC stepper motor (MYCOM 5-phase DC motor) and other movable system hardware parts. A motor controller unit (MYCOM INS500-120 motor driver) is utilized for controlling the stepper motor, by which the scattered fields are collected from around the head. A compact antenna with wideband operation and directional radiation is designed and prototyped. One sensing antenna is applied in the system to mono-statically transmit and receive electromagnetic signals. The details of the antenna are described later. The antenna is mounted on an adjustable mount. A compact microwave transceiver (model-N7081A) from Keysight, USA is employed for data acquisition. The transceiver is low-cost and light weight with wideband (100 kHz-5 GHz) operating capacity up to a dynamic range of 105 dB. Unlike traditional vector network analysers, which are bulky and expensive, this transceiver enables portability and mass application of the head imaging system. A software interface is designed to control and synchronize the motor controller and microwave transceiver via LAN and USB connections, respectively. The scattering data is recorded and post-processed using a delay-and-sum based signal processing algorithm.

The organization of the rest of this section is as following: the details of the design procedure and characteristics of the wideband antenna is described. Then, the penetration and scattering mechanism

of the head scanning system is discussed in order to understand the scattering of ICH targets inside human head in various situations. The radiation safety of the system is checked to ensure that the radiation is below the standard safety limit. Afterwards, the signal processing algorithm is explained in detail followed by the experimental validation procedure and the reconstructed images. The resultant images are quantitatively analysed from multiple perspectives. Finally, the concluding remarks are discussed focussing on the overall performance and advantages of the proposed head imaging system.

5.6.2 Penetration and Scattering Characteristics of Head Model

To investigate the radiation characteristics and overall operation of the mono-static imaging system, full wave electromagnetic simulations are performed using CST Microwave Studio, which is a finite-difference time-domain (FDTD) based solver. The antenna is excited using a discrete port representing the SMA-microstrip feeding transition used in practice. An anatomically realistic 3D numerical head model, based on MRI scans of a real patient, is imported for the numerical analysis [193]. The phantom contains 256 × 256 × 128 voxel cubes with each voxel having dimensions of 1.1 × 1.1 × 1.1 mm^3. To represent the realistic scenario, each of the seventeen segmented tissues of the 3D phantom are individually assigned with actual measured electrical properties [141]. In the simulations, these broadband dispersive properties can be accurately fitted [44] by the following 4th-pole Debye model:

$$\varepsilon_c(\omega) = \varepsilon_\infty + \sum_{i=1}^{4} \frac{\Delta\varepsilon_i}{1 + j\omega\tau_i} + \frac{\sigma_s}{j\omega\varepsilon_0} \qquad (5.30)$$

Here ε_c is complex relative permittivity as a function of angular frequency (ω). The permittivity of free-space (ε_0), relative permittivity at infinity (ε_∞), ith relaxation time (τ_i), magnitude of ith dispersion ($\Delta\varepsilon_i$) and static conductivity (σ_s) vary depending on the tissue type within the head. The field distributions in and out of the phantom are analyzed in both time- and frequency domains.

5.6.2.1 Time-domain analysis and effect of head size

To analyse the variation of time-domain E-field in the phantom, two arrays of co-polarized E-field probes are placed along the forward and backward directions of the antenna through the mid-line of head phantom. The adjacent probes have a 5 *mm* gap between each other. Figs. 5.30(a, b) depicts the simulation setup of the numerical study. In order to examine the effects of head size on transient response, a scenario with 25% smaller head phantom (Phantom-B) is also simulated in addition to the original healthy phantom (Phantom-A). The time-domain E-field signals at different probes are measured and their position (d) dependent transient amplitudes, *T* and fidelity factors, *FF* are calculated using the following equations [137],

$$T(d) = 10l\mathrm{o}_{\ 1}\left(\frac{P \quad |E_d(t)|}{m_{\ d} \quad (P \quad |E_d(t)|)}\right) \tag{5.31}$$

$$F\ \ (d) = m \quad \frac{\int_{-\infty}^{+\infty} E_d(t)E_t(t-\tau)d}{\sqrt{\int_{-\infty}^{+\infty}|E_d(t)|^2 d \ \ \int_{-\infty}^{+\infty}|E_t(t)|^2 d}} \tag{5.32}$$

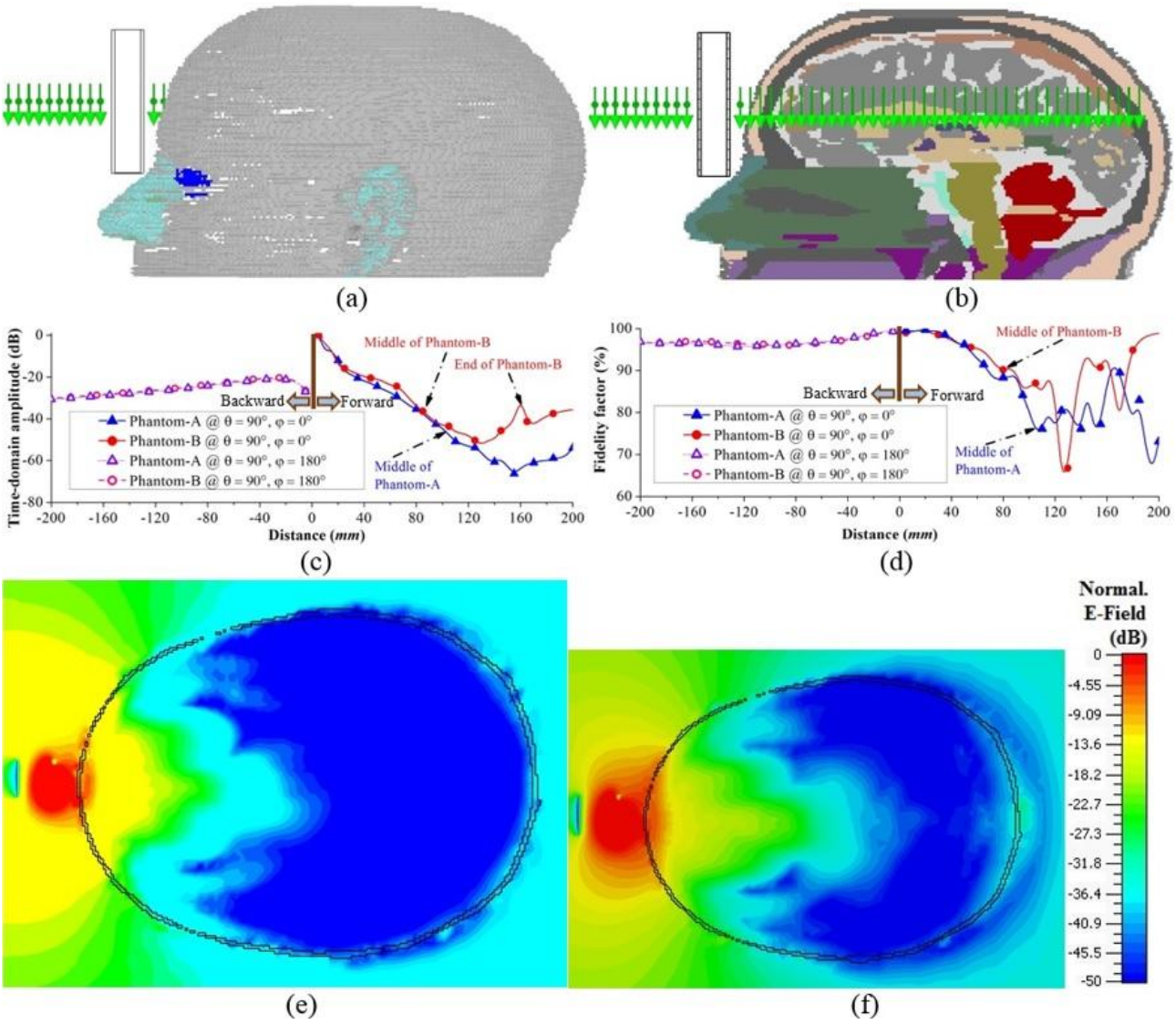

Fig. 5.30 Time-domain analysis of the antenna in presence of different head phantoms. (a) The lateral view of the simulation setup. (b) Midsagittal plane cross-section at the middle of the head phantom showing the positions of E-field probes. (c) The normalized time-domain amplitudes and (d) fidelity factors of the various transient signals at different distances inside and outside the phantoms. Horizontal cross-sections of (e) Phantom-A and (f) Phantom-B, showing the transient E-field distributions normalized to individual maximum.

where $E_d(t)$ is the transient E-field response received by probes in various distances and the template waveform is the generated transient input pulse of choice expressed as:

$$E_t(t) = -s\ n(2\pi f_c t)\, e.\quad (-2\pi t^2/t_w{}^2) \qquad (5.33)$$

Here, $f_c = (f_h + f_l)/2$ is the central frequency, f_l and f_h are the lowest and highest operating frequencies, respectively. The Gaussian pulse width (t_w) is employed so that the pulse spectrum covers the whole operating bandwidth of the antenna in the frequency domain.

Figs. 5.30(c, d) show the transient analysis results at various distances inside and outside of the head phantom. Position zero indicates the position of the antenna. It is seen that in close proximity of the antenna, the fields in the front direction are 20 dB stronger than those of the backward direction due to the high FBR of the antenna in the near-field. Moreover, high fidelity factors of around 98% are attained along the front side, which ensures the transmission of distortionless impulses. These characteristics enable the antenna to collect more information from the desired forward side.

In both phantoms (Phantom-A and B) the attenuation slope of the peak E-field amplitude varies as the pulse crosses different tissue types at different distances. Although minor, the field at a depth of 20 to 30 mm in phantom-B is seen to be smaller than Phantom-A. This is because in Phantom-B the wave at that distance enters into CSF, Dura and gray matter which have high dielectic properties, while in Phantom-A at that distance, the wave passes fat and skull layers with low electrical properties. As shown in Figs. 5.30(c, d), values of $T(d)$ and $F\ \ (d)$ at the middle of Phantom-A are respectively, -44.47 dB and 80.41%, while, for Phantom-B, the values are -36.38 and 90.49%, respectively. An 8.09 dB enhancement in transient amplitudes and 10.08% improvement in fidelity factors are attained by 25% reduction of the head size. This conclusion is significant because it reveals how the detection capability, which is related to the signal attenuation inside the head, of a mono-static head imaging system varies from one head to another. It is expected that the size and tissue distribution of the head vary from one patient to another.

The normalized transient field distributions inside the head phantoms at the mid-cross section of the antenna are illustrated in Figs. 5.30(e, f). Owing to its smaller size, higher transient E-field distributions are observed in Phantom-B as compared to Phantom-A. However, in the smaller phantom-B, stronger surface waves are also observed. The surface waves yields multi-path interference, which is added to the direct waves travelling through the phantom. The effect of multi-path waves can also be observed in Figs. 5.30(c, d). It is seen that the fidelity factors rapidly fluctuate after the middle of the phantoms because there is no longer a direct travelling wave, but summation of multiple waves. For the same reason, the transient amplitude attenuation slope gradually reduces

and then increases. However, the minimum path calculation can be used to mitigate this multi-path interference as described in the image processing algorithm section.

5.6.2.2 Analysis of broadband frequency-domain scattering characteristics

Although the time-domain field distributions illustrate the overall radiation scenario inside a healthy head phantom, frequency-domain characterization is also important to understand the scattering behaviour of hemorrhagic targets inside the head. The electromagnetic scattering of a target from a non-magnetic, dielectrically heterogeneous domain at a measurement location of $\boldsymbol{r}$, can be reliably modelled [194] by the following volume integral equation:

$$\Delta \boldsymbol{E}_s(\boldsymbol{r}) = \omega^2 \mu \int_{\Omega} \bar{\bar{G}}^b(\boldsymbol{r}, \boldsymbol{r}') \boldsymbol{E}^t(\boldsymbol{r}') [\varepsilon^t(\boldsymbol{r}') - \varepsilon^b(\boldsymbol{r}')] d\boldsymbol{r}' \qquad (5.34)$$

where $\Delta \boldsymbol{E}_s$ is the total scattered field representing the total observed field difference between the target environment and the background environment. Ω is the investigated region. The Green's dyadic function $\bar{\bar{G}}^b$ provides the field inside the head without the target. The relative permittivity of the target and background are denoted by ε^t and ε^b accordingly. $\boldsymbol{E}^t$ is the total incident electric field due to the source antenna in the unhealthy head environment. The 3D FDTD simulation is performed in CST environment and the total scattered field of the hemorrhagic target is sequentially post-processed by subtracting the healthy case from the ICH affected case. Various aspects of scattering of hemorrhagic targets are considered.

(i) Hemorrhagic scattering in different depths

ICH can occur at any point inside the brain parenchyma [2, 195]. Hence, it is important to understand the scattering of haemorrhage at different depths inside the head. Fig. 5.31(a) exhibits the cross sections of Phantom-A having hemorrhagic targets of 2×2×1 cm^3 in front (target-1), middle (target-2) and back (target-3) positions. While the head phantom is illuminated with the antenna from θ = 90˚ and φ = 0˚, different frequency component of the operating bandwidth yields different scattering output depending on the position of the scatterer. The peak value of the relevant co-polarized components, E_z of $\Delta \boldsymbol{E}_s$ in different frequencies are calculated and normalized to the impinging electric field on the head phantom, which is 1 V/m. As illustrated in Fig. 5.31(b), the higher frequencies in most cases suffer more losses due to the reduction of signal penetration. Again depending on the position of the targets, the maximum scattering of E_z-field varies. It is seen that the in shallow regions, both target-1 and -3 scatters more strongly than the deep target-2. However, target-1 emits stronger fields than target-2. This is because the former is closer to the excitation and scatters

the received direct travelling fields, while the latter is far from the source and mostly interacts with the surface waves rather than the direct travelling waves.

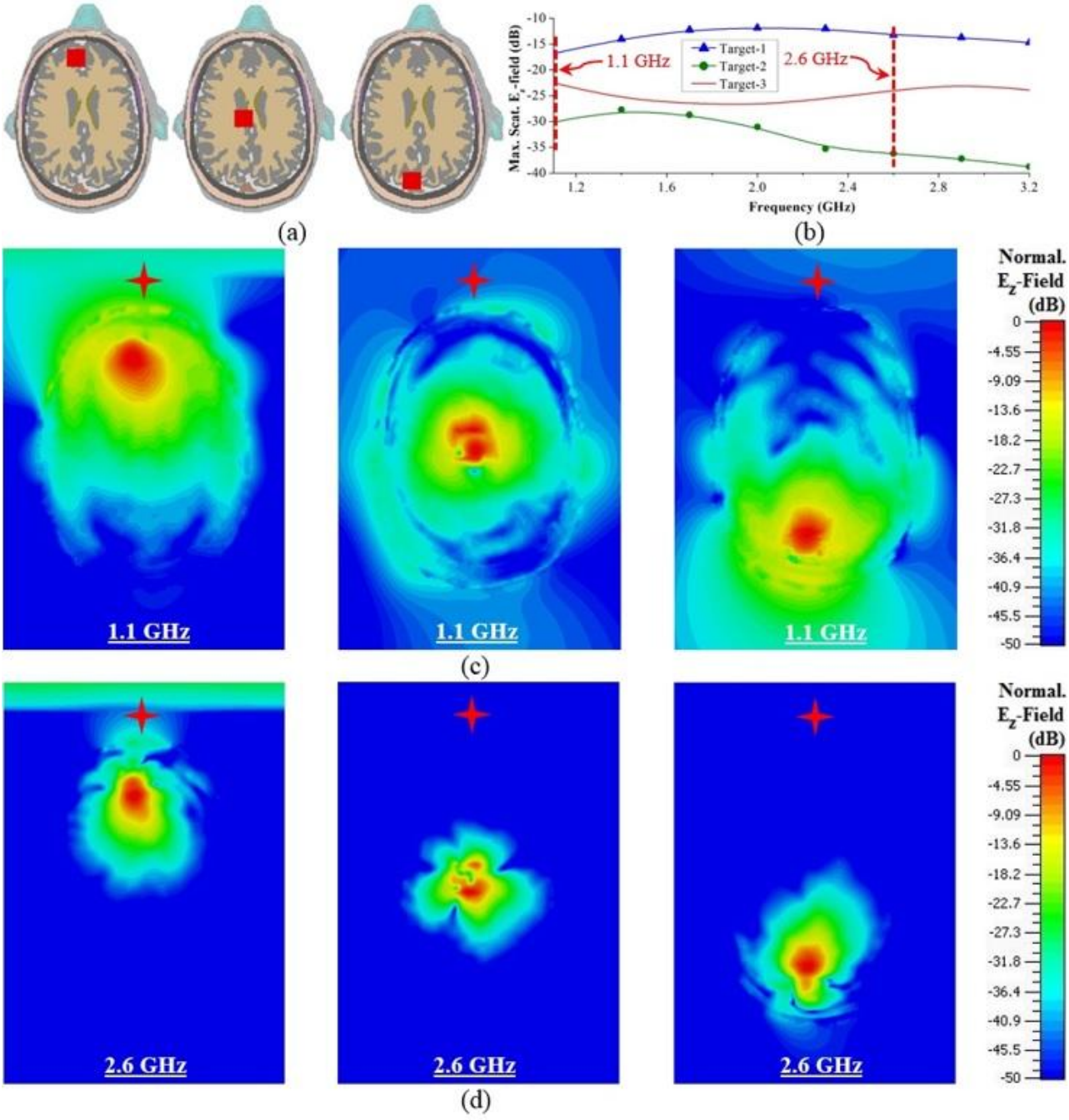

Fig. 5.31 Frequency-domain analysis of ICH affected head with different target positions. (a) Cross-sectional view of the realistic head showing the positions of the ICH targets in front (target-1), middle (target-2) and back (target-3) positions. (b) Maximum E_z-field scattered by different targets over the utilized band of operation. Horizontal cross-section illustrating the distributions of the scattered E_z-field normalized with respect to their individual maximum E_z-fields at (c) 1.1 GHz and (d) 2.6 GHz as marked in (b). Red stars indicate the positions of the antennas.

The cross-sections of the head model showing the scattered E_z-field distributions for 1.1 and 2.6 GHz are illustrated in Figs. 5.31(c, d) for the three targets. The images are normalized with respect to the maximum E_z-field of each frequency plotted in Fig. 5.31(b). It can be seen that while the source is at $\theta = 90^\circ$ and $\varphi = 0^\circ$, all three targets can scatter back to the source within -40 dB at 1.1 GHz with the help of direct scattering waves or scattering surface waves. However, at 2.6 GHz, the targets far from the antenna are unable to strongly scatter back to the antenna, especially for the deep target-2 because of the high losses related to the high frequencies. Hence, lower frequencies are more effective for target detection.

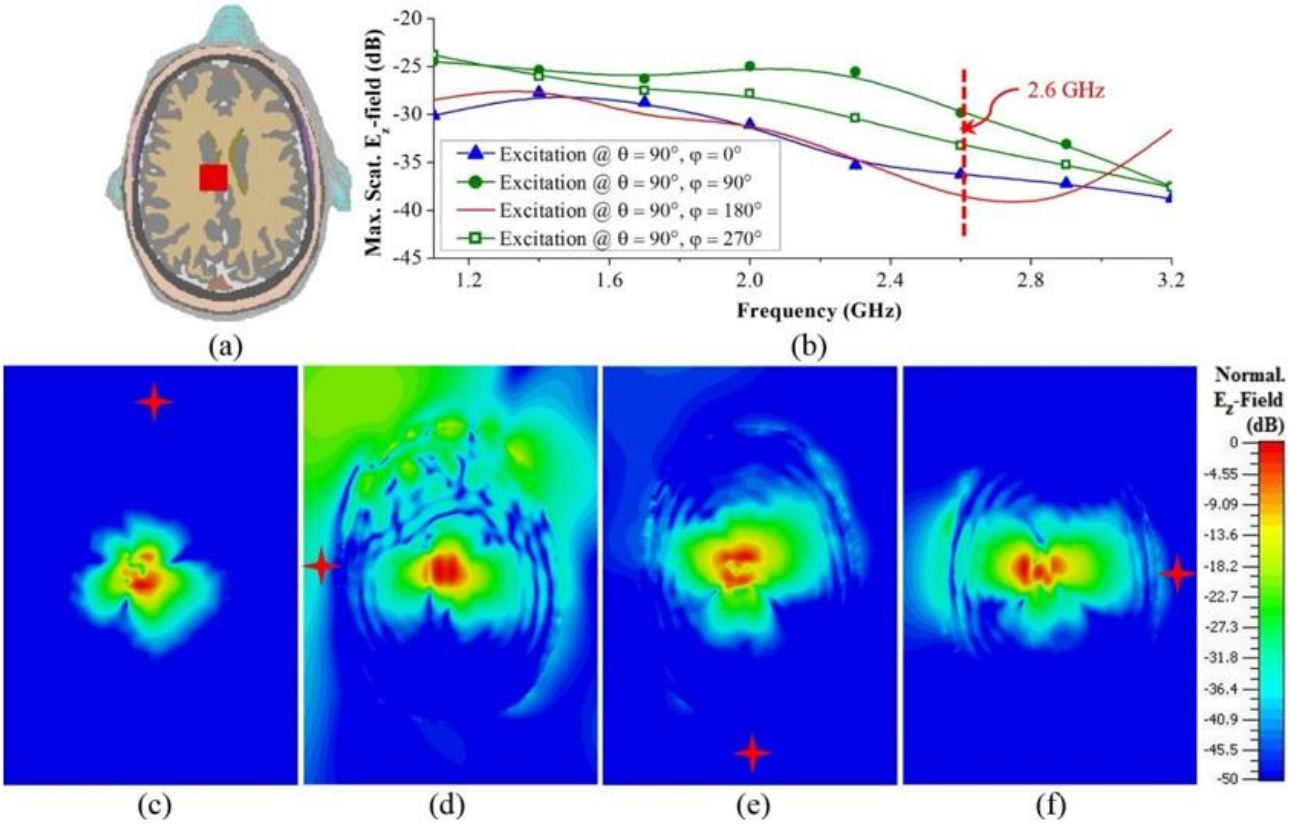

Fig. 5.32 Frequency-domain analysis of ICH affected head with deep target-2. (a) Horizontal cross-sectional view of the human head model. (b) Maximum scattered E_z-fields over the operating band when the excitations are placed in different positions around the head. (c) Cross-sectional view of the scattered E_z-field distributions at 2.6 GHz, normalized to individual maximums as indicated in (b). Red stars represents the positions of the excitations.

(ii) Hemorrhagic scattering with source at different direction

As shown in Fig. 5.31, at high frequencies, the scattered fields from deep targets are very weak and hence are difficult to detect. However, using only lower frequencies results poor resolutions. Thus,

the phantom with target-2 is illuminated from different directions and peak E_z-fields are calculated and normalized to the maximum radiated fields (Figs. 3.32(a, b)).

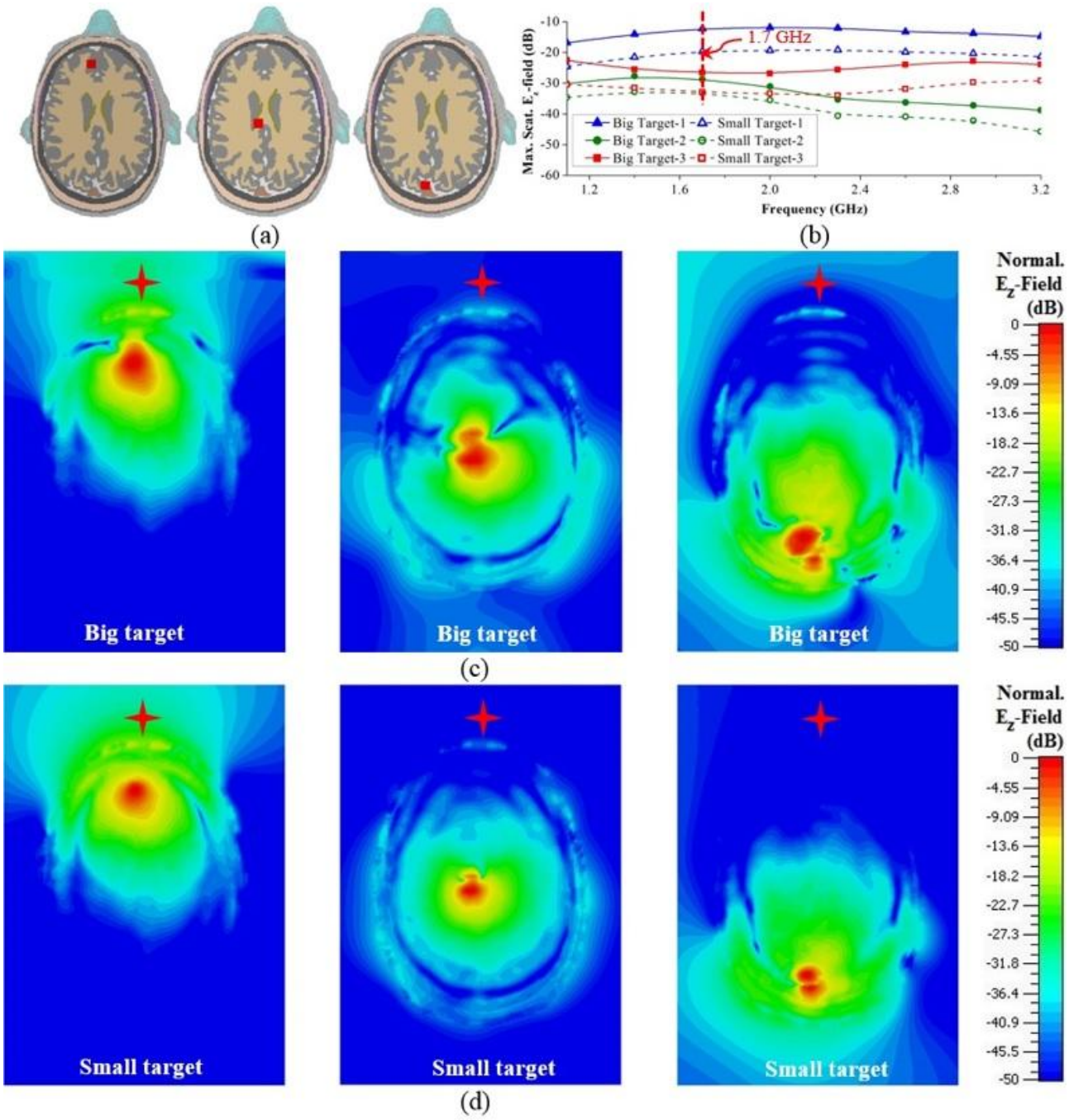

Fig. 5.33 Frequency-domain analysis of ICH affected head with different target sizes. (a) Head cross-sections depicting the positions of the small targets. (b) Comparisons between the peak E_z-fields scattered by the big and small targets over the band of operation. (c) Horizontal cross-sections showing the E_z-field distributions that are normalized with respect to the peak values pointed in (b). The locations of the excitation sources are indicated by red stars.

Since the target is at similar distance away from the front (φ = 0˚) and back (φ = 90˚) positioned antennas, the maximum scattered E_z-field values are quite comparable. But, when the antennas are places at the sides, the distance for the signal to travel to the target is smaller. Consequently, the emitted E_z-fields are also higher. However, as the left-sided (φ = 90˚) antenna is closer to the target than the right-sided (φ = 270˚) one, it scatters more. Figs. 5.32(c-f) depicts the normalized E_z-field distributions in the cross-section of the head model with different source positions at 2.6 GHz. Although the target is unable to scatter back to the source within -50 dB for excitations at φ = 0˚ and φ = 90˚, it is effective for the excitations at φ = 180˚ and φ = 270˚. Thus, at higher frequencies, even though the deep targets might not scatter strongly for longer radii of the head phantom, they are detectable for antennas facing smaller radii.

(iii) Hemorrhagic scattering of different target sizes

To analyse the effects of target size reduction, another set of simulations is performed with 1×1×1 cm^3 target at the same positions and with the same source position mentioned in Fig. 5. 31. The normalized maximum scattered E_z-field at different frequencies due to the smaller target at different positions are recorded. As seen from Fig. 5.33(b), 8-10 dB reduction in the maximum scattered E_z-fields is obtained due to the reduction of target size. The cross-sectional E_z-field distributions, normalized to the individual maximum values are demonstrated for 1.7 GHz in Figs. 5.33(c, d). It is observed that although the shallow targets are still able to send strong scattered signals, the deep target-2 suffers from low scattering. Increasing of the dynamic range of the microwave transceiver may solve this issue.

5.6.3 Radiation safety of the system

Radiation safety is a concern for the implementation of the head imaging system. To that end, the specific absorption ratio (SAR) inside the head is calculated for the mono-static imaging system. In 3D simulation environment, the MRI derived realistic head model is illuminated with the antenna from various directions. The system operates with a transmission power of 0 dBm or 1 mW. The maximum SAR values at different frequencies and for various source locations are presented in Fig. 5.34(a). It is observed that when the source is located in the front side (θ = 90˚ and φ = 0˚), the SAR values are highest compared to the other source locations. At low frequencies, SAR is the lowest and gradually increases with fluctuations. This suggests that the losses are low at low frequencies, but are frequency dependent. All the peak SAR values are lower than 2 W/kg, however, which satisfies the IEEE radiation safety limit [187] for microwave devices. The cross-sectional and perspective view

of SAR distributions at 1.8 GHz are depicted in Figs. 5.34(b, c). It is noted that the maximum SAR is located on the skin layer of the head indicating the lossiest part for the microwave signals. The SAR distributions reveal that SAR values gradually become smaller with the increased tissue depth.

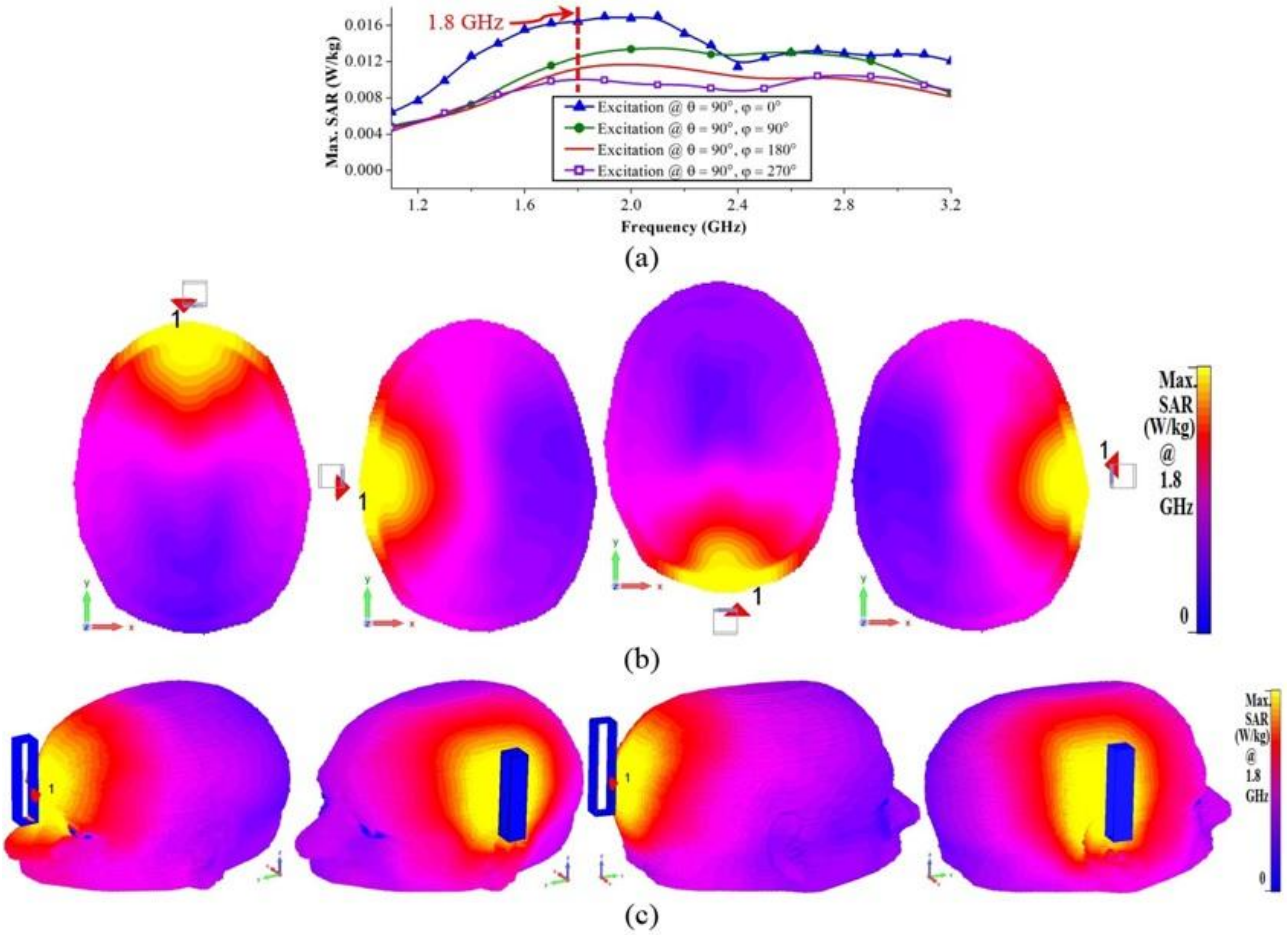

Fig. 5.34 Results from SAR calculations to analyse radiation safety of the imaging system: (a) Maximum SAR values with respect to different frequencies and different antenna positions. (b) Cross-sectional and (c) 3D-view of SAR distributions of the realistic head model with different source locations at 1.8 GHz. The colour bar represents SAR values at 1.8 GHz normalized with respect to the maximum SAR values for independent source locations as indicated in (a); yellow colour represents the highest SAR, while blue is the lowest.

5.6.4 Signal processing and imaging algorithm

The data acquisition system utilizes a circular scanning approach, symmetrical in the mid-sagittal plane (Fig. 5.35). It measures N different antennas where each angular position *n* represents a position within the range from 1 to *N*, and adjacent antenna's positions have angular differences of $\Delta\varphi = 360°/N$. A signal is sent from the compact transceiver through the antenna, which illuminates the

head. The reflected signal is measured via the same antenna thereby using a monostatic scanning approach.

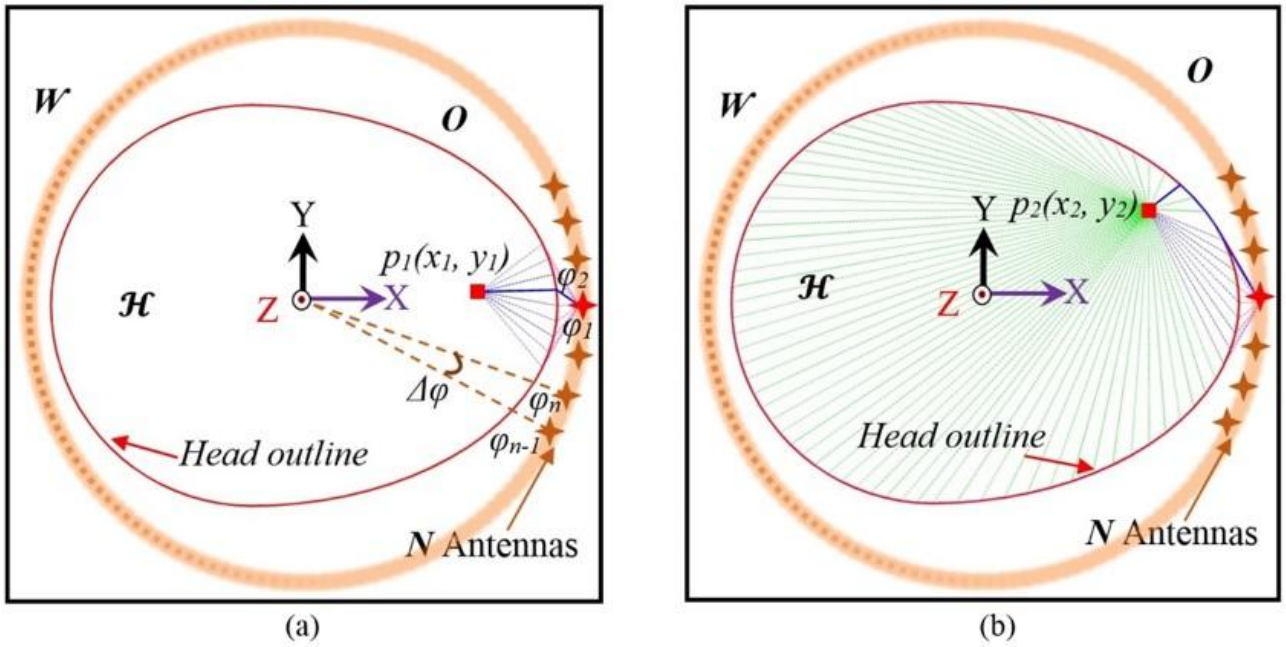

Fig. 5.35 Illustration of data acquisition from different angular locations around head and minimum path calculations for different points inside head from antenna-1 perspective.

The transceiver converts the received signals to *M=284* frequency samples covering the band 1.1-3.2 GHz. These samples are the complex frequency–domain reflection coefficient, $\boldsymbol{\Gamma}(\varphi_n, f_m)$ where *m* = 1 to *M*. and *n* = 1 to *N*. In order to apply the radar-based imaging approach, the acquired frequency domain signals ($\boldsymbol{\Gamma}(\varphi_n, f_m)$) are converted to time domain ($\boldsymbol{T}(\varphi_n, t_k)$) for each antenna through inverse discrete Fourier transformation using eqn. (5.14) and (5.15).

Signals transmitted from the antennas faces substantial reflections from the air-skin interface. It is noted that a healthy human head is largely symmetric across the mid-sagittal plane [196]. The human brain is often described as pairs of left and right-hemisphere homologues [197] and the relative symmetry is reported to be utilized as baseline for detecting tumors [198]. In order to acquire the effective scattered signals from the head interior, it is assumed that since the antenna positions are located symmetrically around the head and because of the relative symmetric distributions of the head, the antenna at symmetrical positions face similar reflections from the air-skin interface. Thus, the scattered signals from head interior are computed by subtracting the average signal of symmetrical antenna locations facing the right and left-hemispheres using the following equation

$$\boldsymbol{D}(\varphi_n, t_k) = \boldsymbol{T}(\varphi_n, t_k) - w \quad a \quad \left(\boldsymbol{T}(\varphi_n, t_k), \boldsymbol{T}(\varphi_{N+2-n}, t_k)\right) \qquad (5.35)$$

Here, the Woody average representing the average with first alignment of individual signal, is employed which is also proven to be effective for biomedical and imaging applications [47]. This condition of symmetry might fail if the target is in symmetry to all antenna locations and thus there is a possibility of false negative detection. However, it is highly unlikely situation as ICH typically occurs in either the right or left hemisphere [197].

In order to form an image, an imaging area of 0.3 × 0.3 m^2 is divided into P×Q cells, with a fine resolution of 0.5×0.5 mm^2, where cells are defined by their individual center points at (x_p, y_q) where p = 1 to P and q = 1 to Q. A boundary vector, $\boldsymbol{B_i}$, representing the skin-air interface in Euclidean space, is defined as the outline of human head. Here, $\boldsymbol{i}$ = 1 to I, states the number of considered points on head outline. Wave propagation from the phase center of the antenna to a suspected point inside the head consists: *1)* a path from the excitation point to the skin-air interface outside the head, $\boldsymbol{O}$ and *2)* a route inside the head $\boldsymbol{\mathcal{H}}$, from head outline to the suspected point. According to Fermat's principle of least time, the wave propagates along the shortest possible electrical path $L_m \quad (x_p, y_q)$ and thus the propagation time index $\boldsymbol{\tau}$ can be calculated as,

$$\boldsymbol{\tau}(x_p, y_q) = \tau_a \quad + {}^{L_m \quad (x_p, y_q)}/_{c} \qquad (5.36)$$

The time required by the antenna to radiate electromagnetic waves from the inception of the excitation is defined by antenna delay, τ_a . All possible paths for wave propagations, $\boldsymbol{L}(x_p, y_q)$ from an antenna to a point (x_p, y_q) inside the head can be defined as,

$$\boldsymbol{L}(x_p, y_q) = \|\boldsymbol{\varphi}_n - \boldsymbol{B}_i\| + \sqrt{\varepsilon_e}\,\|\boldsymbol{B}_i - \boldsymbol{p}\| \quad \text{where } \boldsymbol{p} \in \boldsymbol{\mathcal{H}} \qquad (5.37)$$

Here, the effective head permittivity, ε_e is a constant in previously utilized algorithms [58]. This assumption results in inaccurate calculations which lead to errors in image reconstruction. This is because the heterogeneous distribution of the head tissues have a diverse distribution of electrical properties and hence, using a homogeneous permittivity for all of the tissue types gives inexact computations and results in artefacts in the reconstructed images. A model for the effective dielectric constant of the human head, considering point of entry of the signal and distance of the suspect point inside the head, is implemented in the current image processing algorithm.

As the radiated signal enters into head, it has to first interact with an irregularly thin high permittivity skin layer and then it penetrates through thick fat and skull layers, which have low permittivity. Afterwards, the signal goes through very high permittivity CSF and Dura tissues, and gradually passes through grey and white matters, which have high permittivity. To that end, a realistic simulation model is studied in CST Microwave Studio environment with the previously discussed MRI-scan derived healthy human head and the effective permittivity values of the healthy human head for

different $\boldsymbol{\varphi_n}$ antenna positions are calculated over the band 1.1-3.2 GHz by analysing the differential time of signal arrival (TOSA) from the point of entry with the procedure described in [198]. It is realized from simulations and from [198] that the effective permittivity of a point inside the head is different for different entry points of the head boundary and depends on the distance of that arbitrary point from the boundary. In order to deduce a unified propagation model, the values for different point of entry are averaged and the result is expressed using a distance based function for any entry point of the head boundary as,

$$\boldsymbol{\varepsilon_{e\ \ ,i}} = \varepsilon_m\ \ (1 - \alpha e^{-\beta\ /a}) \qquad (5.38)$$

Here the distance of the arbitrary point from the boundary is represented by d, the normal distance from the signal entry point to the center of the head is a, maximum permittivity is defined by ε_m , and α and β are constants. For the band of 1.1-3.2 GHz, the effective permittivity values from the realistic simulation environment suggests values of ε_m = 41, α =0.75 and β =6.4.

In a mono-static radar approach, the transmitted signal travels to and is scattered from the arbitrary point (x_p, y_q); thus, the total propagation time is proportional to twice the distance

$$\boldsymbol{\tau_{t\ \ \ l}}(x_p, y_q) = 2\boldsymbol{\tau}(x_p, y_q) \qquad (5.39)$$

It is understood that the line of sight points ($\boldsymbol{B_{i,n}}$) receive direct signals from the antennas and the waves propagate via these points through head interior. These points are the tangent points from $\boldsymbol{\mathcal{H}}$ from individual antenna position and the points between them. The tangent points are computed by estimating the maximum angle, θ_{max} centered at antenna position from $\boldsymbol{B_{i_m\ \ ,n}}$ to $\boldsymbol{B_{i_m\ \ ,n}}$. Thus, (10) can be written as,

$$\boldsymbol{L}(x_p, y_q) = \left\|\boldsymbol{\varphi}_n - \boldsymbol{B}_{i,n}\right\| + \sqrt{\boldsymbol{\varepsilon_{ef\ \ ,i}}}\left\|\boldsymbol{B}_{i,n} - \boldsymbol{p}\right\| \qquad (5.40)$$

It is observed that (13) is effective for propagation path estimation of deep points inside the head which usually follow the line of sight paths due to minimum losses (Fig. 5.35(a)). If the target appears deep from the sensing antenna and is shallow from another angle, it is likely that strongest scattering signals will pass as travelling waves through the skin (Fig. 5.35(b)). This phenomenon is also demonstrated in Figs. 5.31, 5.33. In order to resolve this issue, the travelling wave path must be considered. Thus, the calculation of possible propagation paths can be performed as,

$$\boldsymbol{L_a}(x_p, y_q) = \left\|\boldsymbol{\varphi}_n - \boldsymbol{B}_{i_m\ \ ,n}\right\| + \sum_{a=i_m}^{(N-\Delta i)/2} \left\|\boldsymbol{B}_{i_m\ \ ,n} - \boldsymbol{B}_{i_m\ \ +a,n}\right\| + \sqrt{\boldsymbol{\varepsilon_{ef\ \ ,i}}}\left\|\boldsymbol{B}_{i_m\ \ +a,n} - \boldsymbol{p}\right\| \qquad (5.41)$$

$$L_b(x_p, y_q) = \left\|\varphi_n - B_{i_m\ ,n}\right\| + \sum_{b=i_m}^{(N-\Delta i)/2} \left\|B_{i_m\ ,n} - B_{i_m\ -a,n}\right\| + \sqrt{\varepsilon_{ef\ ,i}}\left\|B_{i_m\ -a,n} - p\right\| \quad (5.42)$$

Here, L_a and L_b are the possible paths with travelling waves in the clockwise and counter-clockwise way from the perspective of antenna and $\Delta i = i_{m\ } - i_{m\ }$. The optimal paths for each point inside the head is calculated by

$$L_{m\ }(x_p, y_q) = a \qquad [L(x_p, y_q), L_a(x_p, y_q), L_b(x_p, y_q)] \quad (5.43)$$

Finally, the total time, $\tau_{t,\ }(x_p, y_q)$ is calculated from eqn. (5.39) for all (x_p, y_q) points of $\mathcal{H}$ region.

In order to reconstruct the image of head interior a delay-and-sum (DAS) based back-projection technique is utilized. According to DAS, it is assumed that the differential scattered signals, $D(\varphi_n, t_k)$ are originated from a suspected point $p \in \mathcal{H}$ and a coherent summation of the signals originating from surrounding antenna is computed.

$$I_{1\ }(x_p, y_q) = \left|\sum_{n=1}^{N} \int_0^{\infty} \tau_{t,\ }(x_p, y_q) D(\varphi_n, t_k) dt_k\right| \quad (5.44)$$

The resultant coherent summation for all the antenna responses is large, in case of correct hypothetical scattering point. Contrariwise, if the assumption is incorrect, small value is resulted which can be classified as noise. A continuous colour image is produced by plotting the computed $I_{1\ }(x_p, y_q)$ function for each point on the segmented 2D cross-sectional scanned plan of the head phantom and the values are normalized with respect to the maximum of all resulted absolute values. High intensity of colours indicates positions of suspected significant scatterers (haemorrhage) inside the head.

5.6.5 Microwave imaging results

To validate the effectiveness of the proposed microwave imaging platform and the reconstruction algorithm, an anatomically realistic 3D human head phantom was imaged. The phantom exterior and various moulds for the different brain tissues were 3D printed. Tissue emulating materials with broadband frequency dispersive dielectric properties from 0.5-4 GHz are filled inside the phantom and skin mimicking tissue materials are also used. The details of the semi-solid head phantom fabrication and properties are mentioned in [45, 155, 178]. To emulate the ICH scenario, hemorrhagic targets with frequency dispersive electrical properties are placed inside the head phantom. The compact microwave transceiver is utilized to collect and store the wideband data from 1.1-3.2 GHz through the antennas in different angular positions around the head. The stored data is then post-processed and the images are reconstructed by using the aforementioned image processing technique. As one of the objectives of the imaging system is to realize its capacity in detecting and locating ICH targets of different sizes and positions, multiple evaluations are performed as described below.

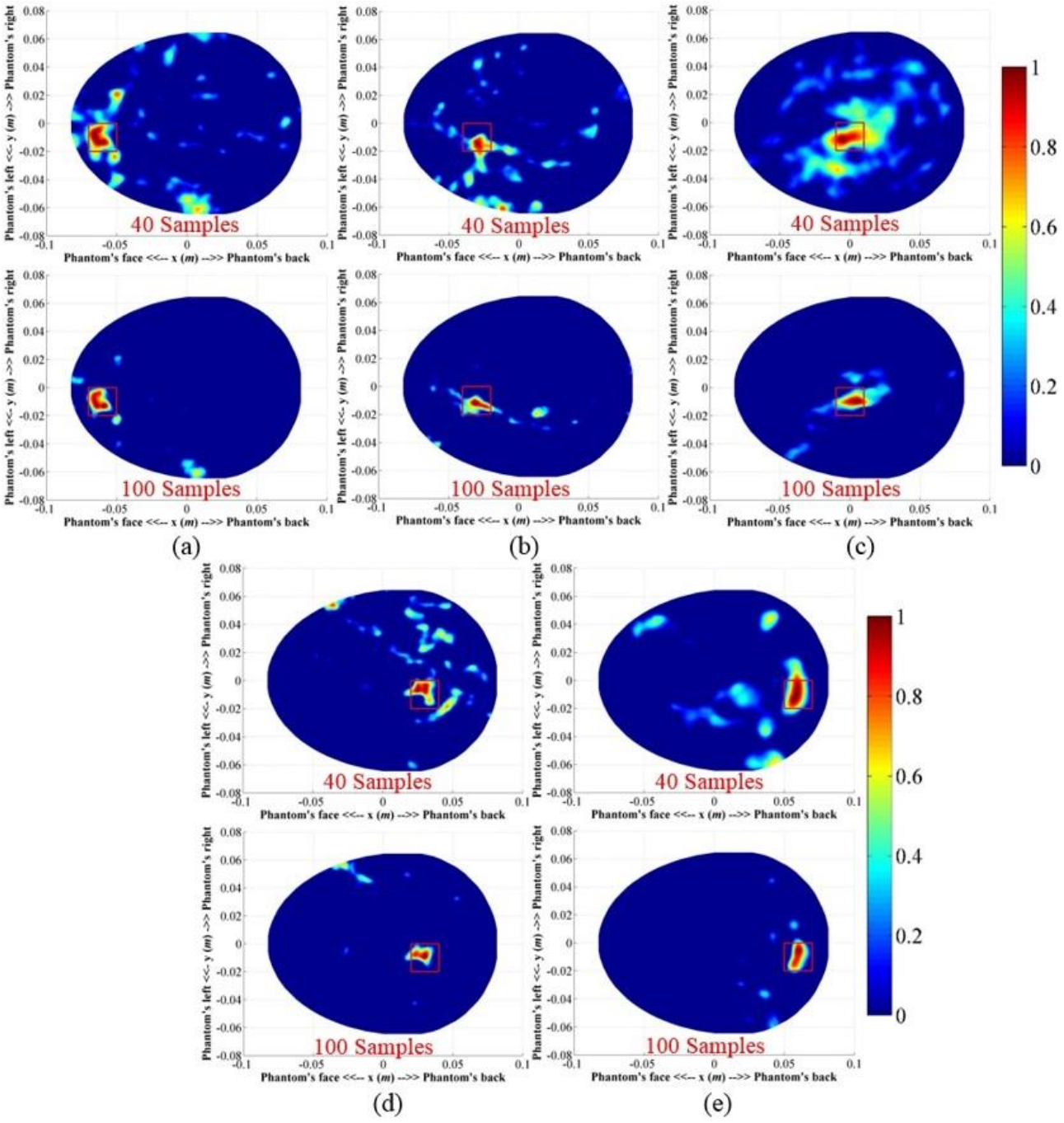

Fig. 5.36 Reconstructed images from the ICH affected head phantom with big targets in different locations and with different data samples (N = 40 and 100).

5.6.5.1 Imaging of big targets in different locations

A hemorrhagic target with a volume of 2×2×1 cm^3 was inserted into the head phantom. Position of the ICH target was varied in depths from the frontal area. Data were collected around the head phantom in two different angular samples, namely N = 40 and 100. The reconstructed images utilizing the imaging algorithm is demonstrated in Fig 5.36. It is seen that in both cases and for different locations the system is able to detect and localize the positions of the targets. A qualitative assessment

of the images indicates that when the number of angular samples is N = 40, more artefacts are visible in all positions. The increased data samples from N=40 to N=100 clearly provides better localization.

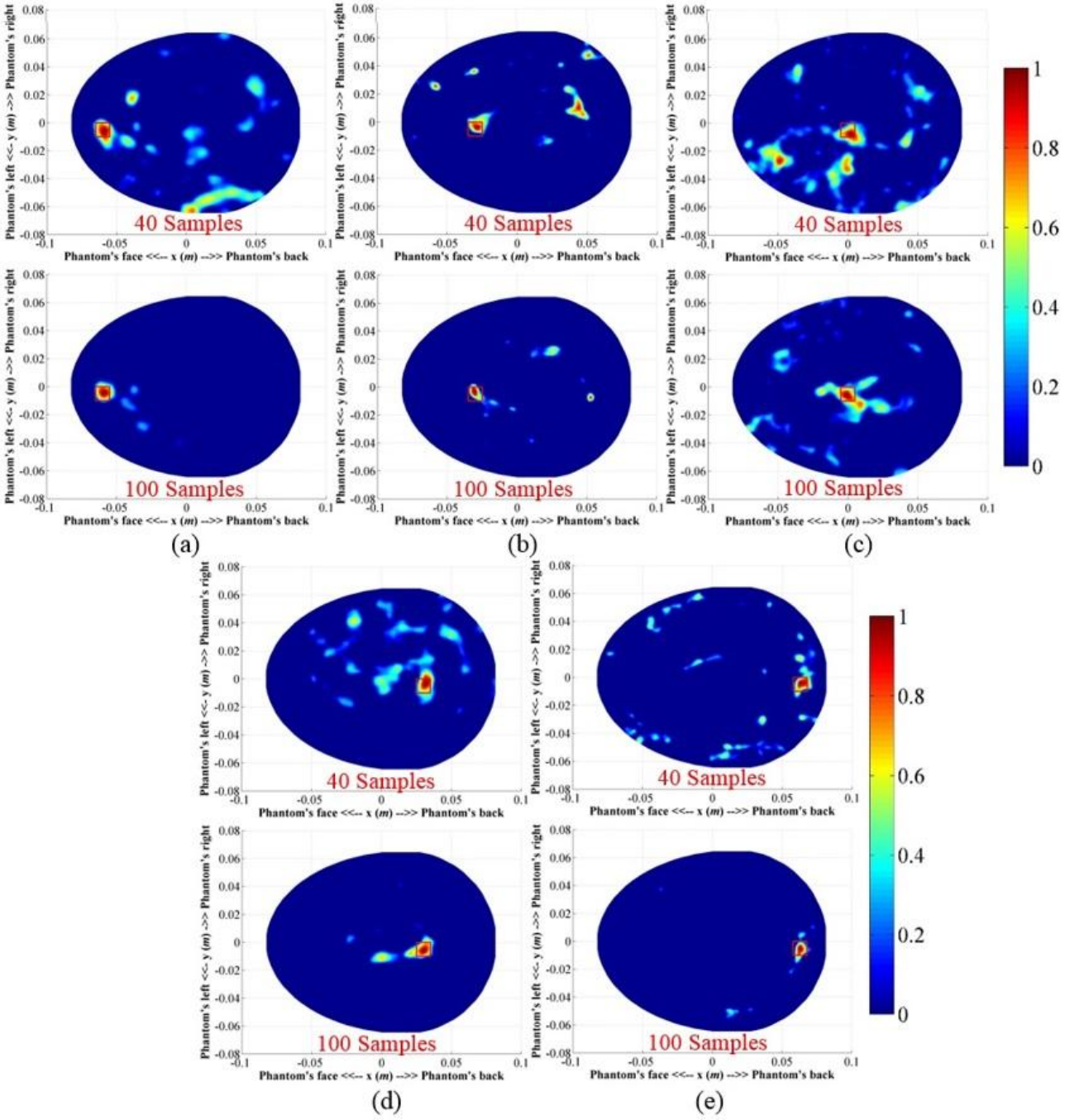

Fig. 5.37 Reconstructed images from the ICH affected head phantom with small targets in different locations and with different data samples (N = 40 and 100).

5.6.5.2 Imaging of small targets in different locations

A smaller hemorrhagic target of 1×1×1 cm^3 is placed inside the head phantom. The experiments are performed for both N = 40 and 100 angular samples. Similar to the previous section, the positions of the targets are varied from shallow to deep locations from the front to back side of the head phantom. The reconstructed images are shown in Fig 5.37. In both sample cases and different locations, the system is able to detect the strongest scattering inside the red square, which indicates the localization capability of the system. However, the visual inspection elicits that with N = 40, the resulted images contain strong artefacts compared to those of N = 100, suggesting that using a small number of antennas is not efficient in detecting small targets.

5.6.6 Quantitative analysis results

In order to investigate the effectiveness of the compact head imaging system and proposed algorithm, several quantitative metrics, as mentioned in Section 5.3, are investigated by analysing the reconstructed qualities of the reconstructed images.

Fig. 5.38 shows the results of the analysis. High values (>8 dB) of average S/C ratio, Q was attained in all cases, which represent that on average the actual target region contains stronger scattering points than the rest of the head cross section. This clearly helps in determining the position of suspected target in practice. The maximum S/C ratio, M is also important to distinctly identify the target location from other strong artefacts of the background. It is seen that all the images achieved M >1 inside the actual target region, indicating that the reconstruction algorithm is capable to attain correct localization. Fig. 5.38(c) shows that the accuracy indicator is smaller than the distances from the center to the edges of the targets. This infers the detection of maximum intensity inside the actual target region. Since the target sizes are different, the values are normalized to the maximum deviation from the center, δ_m which is half of the diagonal distance from corner-to-corner using the following equation:

$$\delta_n = \frac{\delta}{\delta_m}, \quad \delta_m = \frac{1}{2}\sqrt{{a_T}^2 + {b_T}^2} \tag{5.48}$$

Here, a_T and b_T are cross sectional dimensions of the target. The results of normalized accuracy indicator are illustrated in Fig. 5.38(d). It is noted that although in actual values it seems that accuracy of big target is much worse than the small target, the insight provided by δ_n reveals that the values are in fact comparable to each other when the sizes of the targets are considered. For both targets, high data samples provide better localization accuracy compared to those of the lower ones.

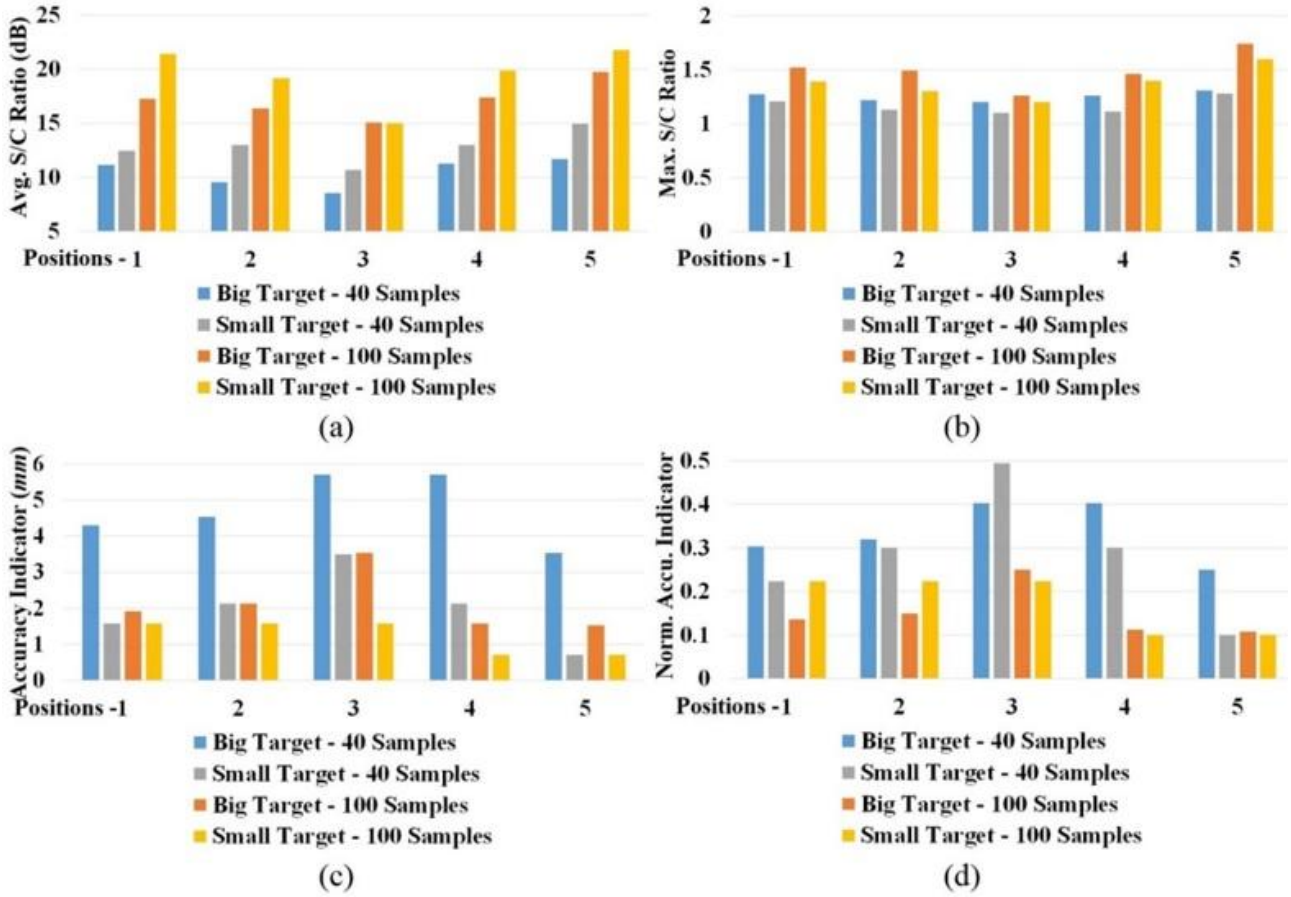

Fig. 5.38 Various quantitative analysis results of the reconstructed images with 40 and 100 data samples and at different positions. (a) Average S/C ratio, Q,(b) maximum S/C ratio, M, (c) Accuracy indicator, δ and (d) normalized accuracy indicator, δ_n are calculated by eqn. (5.45) to (5.47) accordingly.

The results show that the shallow targets provide higher S/C ratios with low accuracy deviation, while targets in the middle (position-3) yield worse metrics in all aspects. Without exception, the values gradually decrease from both front (position-1) and back (position-5) ends. This can be correlated to the quality of the scattered signals received by the antenna. As the target goes deeper into the head phantom, the scattered signals from the target have to pass through more lossy tissue. Consequently, the received scattered signals at the position of the antennas get distorted and attenuated with heavy losses. As a result, the image quality deteriorates with the increase of depth of the ICH target.

To quantify the effect of increasing data sample sizes and detection capability of smaller ICH target sizes, a statistical study was completed. The variations of relative image quality of the head with big and small ICH targets considering both cases when N = 40 and 100, are calculated using the equations:

$$Q_{r1} = \frac{(Q_{S_2} - Q_b)}{Q_{S_2}}, \quad M_{r1} = \frac{(M_{S_2} - M_b)}{M_{S_2}}, \quad \delta_{n_{r1}} = \frac{(\delta_{n_{S_2}} - \delta_{n_b})}{\delta_{n_{S_2}}} \tag{5.49}$$

Again, the relative image qualities for increasing data samples for both big and small ICH targets are computed by:

$$Q_{r2} = \frac{(Q_1 - Q_4)}{Q_1}, \quad M_{r2} = \frac{(M_1 - M_4)}{M_1}, \quad \delta_{n_{r2}} = \frac{(\delta_{n_1} - \delta_{n_4})}{\delta_{n_1}} \tag{5.50}$$

Results from (15) and (16) are shown in Fig. 5.39. The relative Q_{r1} values for both 40 and 100 samples (Fig. 5.39(a)) show positive variations indicating an improvement of average image quality. Due to the considered smaller cross-section of the small target with the same head phantom, an increase of average S/C ratio, Q, is expected. Negative relative M_{r1} values (Fig. 5.39(b)) indicate that although the targets are properly detected, the scattering of the small target is weaker than the big target. This also suggests that more artefacts are present in the reconstructed images for small ICH target. This is because scattering signals from other parts of head tissues are relatively larger in the sensing antenna than the scattering from a small target. Positive and negative fluctuations of relative accuracy indicator, $\delta_{n_{r1}}$ (Fig. 5.39(c)) conveys that no conclusive improvement or decline of target accuracy detection can be obtained when reconstructed images from big and small targets are compared. The reason behind this lies in the physics of the target's inherent scattering characteristics. A close examination of Figs. 5.31, 5.32, and 5.33 reveals that the maximum intensity of the target's scattering is not a fixed point. Although the point with maximum scattering field exists within the target region, its position vary over the operating frequency band as well as with the position of the ICH target. Nevertheless, changing the excitation source position alters the maximum scattering point for the same target and functional frequency. For these reasons, the position of maximum intensity point in the reconstructed images vary unpredictably.

When the data samples are increased from N = 40 to 100 in both big and small target cases, the relative average (Q_{r2}) (Fig. 5.38(d)) and maximum (M_{r2}) (Fig. 5.38(e)) S/C ratios show positive variations, whereas the relative accuracy indicator ($\delta_{n_{r2}}$) (Fig. 5.38(f)) exhibits negative variations. Hence, it can be concluded from this study that increasing data samples from N = 40 to 100 enhances the reconstructed images for all targets sizes and at all locations.

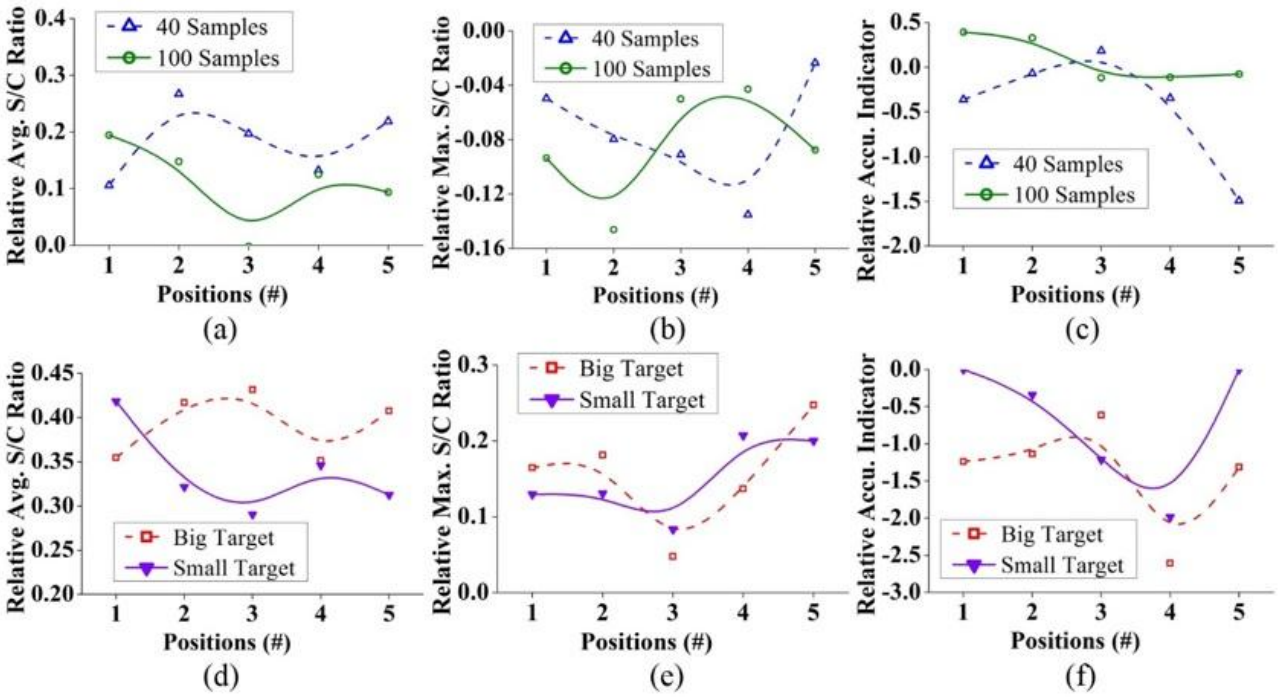

Fig. 5.39 Statistical analysis results of the quantitative metrics obtained from the reconstructed images calculated from eqn. (5.49) and (5.50) for different samples and targets.

The relative metrics are further analysed to quantify the amount of dispersion of the matrix values. Table 5-IV lists the percentage standard deviations and means of the relative metrics in different scenarios calculated with a 99% confidence level. The results indicate a mean improvement of more than 11% in Q_{r1} and reduction of around 8% in M_{r1} with percentage standard deviation (SD) of less than 7%, which represents low variations from the mean deviations. Rapid fluctuations of accuracy indicator ($\delta_{n_{r1}}$) yields negative (-41.62%) and positive (8.29%) mean values respectively for N = 40 and 100 with a huge SD, as high as approximately 58%, demonstrates the non-monotonous variations of maximum intensity points. The points of maximum intensity in the reconstructed images are always found inside the actual target region (Figs. 5.36 and 5.37), showing the efficacy of the system for both big and small targets.

On the other hand, increasing data samples from N = 40 to 100 results more than 33% and 15% improvements in Q_{r2} and M_{r2}, respectively, and more than 70% reduction of accuracy error. Although small SD of around 4% for Q_{r2} and as low as around 5% for M_{r2} are resulted from the statistical analysis, in case of $\delta_{n_{r2}}$ a high SD of around 70% is observed. The improvements of these relative mean values are higher and SD values are mostly lower in case of the big target when compared with the small target. This is because, for the relatively stronger scattering fields from the big target, the data sample increment gives better reconstructed images.

Table 5-IV: Standard deviation and mean analysis of the relative quantitative metrics

	ICH size variations		**Data sampling variations**	
Metrics	$Q_{r\ ,\ N=4}$	$Q_{r\ ,\ N=1}$	$Q_{r\ ,\ B}$	$Q_{r\ ,\ S}$
SD (%)	5.86	6.57	3.31	4.41
Mean (%)	18.43	11.17	39.24	33.78
Metrics	$M_{r\ ,\ N=4}$	$M_{r\ ,\ N=1}$	$M_{r\ ,\ B}$	$M_{r\ ,\ S}$
SD (%)	3.79	3.69	6.50	4.69
Mean (%)	-7.57	-8.4	15.55	15.02
Metrics	$\delta_{n_r\ ,\ N=4}$	$\delta_{n_r\ ,\ N=1}$	$\delta_{n_r\ ,\ B}$	$\delta_{n_r\ ,\ S}$
SD (%)	57.46	22.82	65.97	77.81
Mean (%)	-41.62	8.29	-138.3	-70.86

5.6.7 Discussion

A mono-static head imaging system relying on the wideband microwave frequencies 1.1-3.2 GHz has been presented in this section. The system utilizes a custom-designed ultra-wideband antenna as sensing element to scan the head. It is observed that the half-cut technique effectively reduces the space requirement for the sensing element, whereas the modified cross-feeding technique corrects the main beam-tilting issue. As a result, the proposed antenna is capable of radiating efficiently along the front direction. In the forward direction. Nevertheless, the compact size of the antenna confines the phase center radiation to a stable position over a wide bandwidth, which can be quantified by 98% fidelity factors [58]. These radiation features improve the detection capability of the image processing algorithm because of the basic assumption that all radiation starts from a single point, which is difficult to realize in other antennas [199].

The numerical analysis of the penetration of transient signals and the scattering of ICH targets of different sizes in diverse locations inside MRI-derived realistic head model reveals the operating mechanism of the head imaging system. In a human head model with above average size, the transient E-field signals attenuate by around 45 dB (Fig. 5.30) at the center when travelling through the longest radius (~100 *mm*). A high level of attenuation is therefore expected for deep targets. Owing to the stable phase center of the antenna, the level of impulse distortion, which is quantified by fidelity

factors, is found to be high (~ 80%) at the center. On the other hand, the scattering characteristics of ICH targets in the frequency domain demonstrates that the lower frequencies are less susceptible to the losses (Fig. 5.31) compared to the higher microwave frequencies. Shallow haemorrhages are seen to scatter the co-polarized E_z-fields strongly relative to the deep one. However, when the antenna is facing the small radius rather than the longest, it is noted that scattering signals even at high frequencies from deep target become comparatively stronger (Fig. 5.32) owing to reduced losses in this orientation. This indicates that scanning from various perspectives is vital for adequate data acquisition, especially for the deep targets. Nevertheless, it is demonstrated in Fig. 5.33 that the maximum co-polarized scattering E_z-fields from an ICH target are contingent on target's size (Fig. 5.33). Depending on the position of the target, a reduction of 8-10 dB in the maximum scattered field strength is observed when a small target ($1\times1\times1$ cm^3) is compared to a large one ($2\times2\times1$ cm^3).

A modified delay-and-summation back-projection algorithm is proposed for the signal and image post-processing from the head imaging system. The data from the imaging system is acquired in the frequency-domain and converted to the time-domain for post-processing. Data acquisition in the frequency-domain is preferred because of the beneficial high dynamic range of frequency-domain measurements [124]. As it is noted from Fig. 5.31, even though the target (target-3) is away from the antenna, it can receive signal and scatter back through surface waves. Hence, the proposed imaging algorithm includes the effect of surface waves while calculating the minimum possible paths from a specific point inside the head model to the sensing antenna. Instead of using a conventional single constant *priori* of head permittivity, distance dependent effective permittivity model which is contingent on the point of entry inside the head model is utilized.

The efficacy of the system is verified by imaging ICH targets of different sizes and in different positions inside a realistic human head phantom. The reconstructed images demonstrate that the imaging system can successfully detect and localize ICH. The quantitative analyses illustrate that when the target gets deeper inside the head, the quality of images in terms of average and maximum signal-to-clutter ratio (S/C) and accuracy indicator deteriorate for targets of any size due to relatively lower scattering signals as observed in the numerical studies (Fig. 5.31). Again, when compared between targets of different sizes located at the same positions, it is noted that the maximum S/C decreases for small targets. This result indicates that as the targets become smaller, the scattering from other parts of the brain become relatively stronger than the actual ICH scatterer. However, literatures on ICH patients report that at early stages, the median volume of ICH targets is 17 cm^3 [191] or generally in the scale of centimetres [189]. Thus, the experimental detection of both big ($2\times2\times1$ cm^3) and small ($1\times1\times1$ cm^3) targets can be considered as early goals.

The relative statistical analyses illustrates that the image quality can be significantly improved and the presence of artefacts can be debased by increasing the number of data samples (*N*) collected from around the head phantom. Statistics shows that irrespective of the size of ICH targets, when the number of samples (*N*) are increased from 40 to 100, the average and maximum S/C are enhanced by more than 33% and 15 %, respectively with SD of less than 7% for both metrics with an improvement of more than 70% in the accuracy indicator. The statistical analyses were performed with a 99% confidence level. As the image quality declines, in case of small ICH targets if non-definitive results are obtained (which can even happen in case of CT [200]) and it is only the proposed head imaging system that can be easily adjusted to produce images with higher quality while only a single antenna calibration is required. On the other hand, an adjustable array-based counterpart [20] can also be rotated using a stepper motor, it requires antenna array calibrations and can waste precious time delaying the medication of the patient. As the head shapes and sizes vary from one patient to another and in MI system sensing antennas should be placed as close as possible, the proposed single antenna system can be quickly adjusted compared to the array based system. Owing to the light weight and compact size of the proposed mono-static scanning system, it is flexible and faster to move around the head phantom in a circular scanning profile, while bulky arrays takes more space for the setup and more time to move because they are heavier.

The proposed system overcomes the strong multi-path reflection problem from the other antennas [201]. Although utilization of a single-antenna system is virtually equivalent to the array based system, the scattering contribution of the neighbouring elements might be significant in array-based systems due to the presence of surface waves around the head, even if all the remaining array elements except the active antenna are match terminated [180]. This added scattering in the array-based system increases the presence of artefacts [20], while the proposed single antenna head-imaging system is free from such artefacts in the reconstructed images. Moreover, when compared to the previously reported systems, the presented MI system is able to detect the location of targets as small as 1×1 cm^2 of cross-section in both deep and shallow locations, which was not possible in the reported systems [20, 58].

The prototyped head imaging system is compact and light weight and could be carried in an ambulance. The system does not require large computing resources, with the assistance of the fast and accurate image post-processing, reconstruction can be performed in standard portable devices. An illustration of how the imaging system could be applied in an ambulance is illustrated in Fig. 5.40. A support made from microwave frequency transparent materials can be used to support patient's head. The data acquisition time is around 1 minute for $N = 100$ data samples, and it only takes 10-12

seconds for the algorithm to generate the resultant image. Future work is planned to perform pilot human testing on healthy volunteers once safety and ethics approvals are in place.

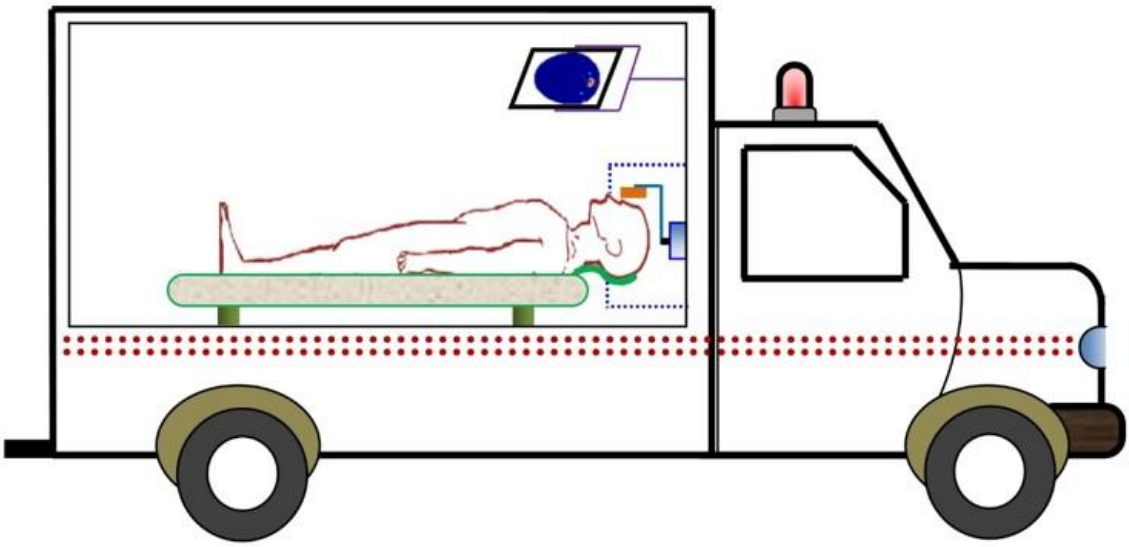

Fig. 5.40 Schematic illustration of the proposed head imaging system in an ambulance.

5.7 Conclusion

The design and developments of several single antennas based wideband microwave head imaging systems for brain injury diagnosis are introduced in this chapter. Numerical verification of a preliminary head imaging system by means of electromagnetic simulation of realistic brain injuries is performed, which is followed by the experimental investigations using two simplified head phantoms. The imaging results attained from both simulation and experiments are found promising. It is noted that in the literature, there are numerous directional and omni-directional antennas reported, but there is no conclusive evidence in the literature to conclude the superiority of one type over another. Hence, the comparative imaging performance of directional and omni-directional antennas for head imaging system is also presented with relative quantitative analyses between the reconstructed images. A model of portable head imaging system is introduced with the verification on a realistic human head phantom. It is seen that the imaging performance of the portable head imaging system can be significantly improved by using a back-projection algorithm with a model of effective head permittivity. The efficacy of the system along with the imaging algorithm is verified in both simulations and experiments by using realistic numerical head models and 3D printed head phantoms. Nevertheless, results from a pilot human test is also presented. Later, a compact head imaging system with automated scanning capabilities is presented. Imaging improvements are also

discussed when the surface waves are considered in reconstructing the image. Last but not least, a detection and differentiation system of brain injury types in brain stroke scenario is presented and numerically verified by using spherical and elliptical cylindrical stroke targets inside human head.

Chapter 6 - Developments of Array Based Portable Head Imaging System

This chapter presents the design and developments of compact array based portable head imaging systems. Firstly full wave electromagnetic simulations are performed to verify the safety of the imaging system and the imaging performances are compared between arrays using compact multi-folded 3D antenna (described in Section 3.11.1) and the imaging performances are compared with a miniaturized 3D folded antenna (reported in Section 3.5). A wideband microwave imaging system is prototyped and the prototyped system is described with detailed photographs. Numerical analyses of the head imaging system are performed in both frequency- and time-domains to examine the signal penetration and scattering performances of hemorrhagic head injuries in realistic scenarios. The experimental results from the head imaging system while applied on the realistic human head phantom are reported and the quantitative analyses are performed on the reconstructed images. The head imaging system is checked for radiation safety and employed on heathy volunteers for pilot human tests. The results from the reconstructed images are extracted and statistically analysed. Finally, the discussions on the phantom and volunteer measurements are mentioned based on the statistical comparison of the imaging results.

6.1 Full Wave Simulations of Head Imaging Platform and Results

A realistic scenario of head imaging system is emulated in the electromagnetic simulation tool CST microwave studio. A realistic human head phantom is developed from MRI slices and assigned with frequency dispersive electrical properties (permittivity and conductivity) of respective actual tissues [193]. The antenna, proposed in Section 3.11.1, is utilized to form a compact array with 16 elements around the head model (Fig. 6.1(a)). The antennas are positioned at 22.5˚ apart from each other keeping a distance of 15 *mm* from the skin of the head. However, before the detection analysis, the radiation safety of the antenna array operating at close proximity to the head is investigated.

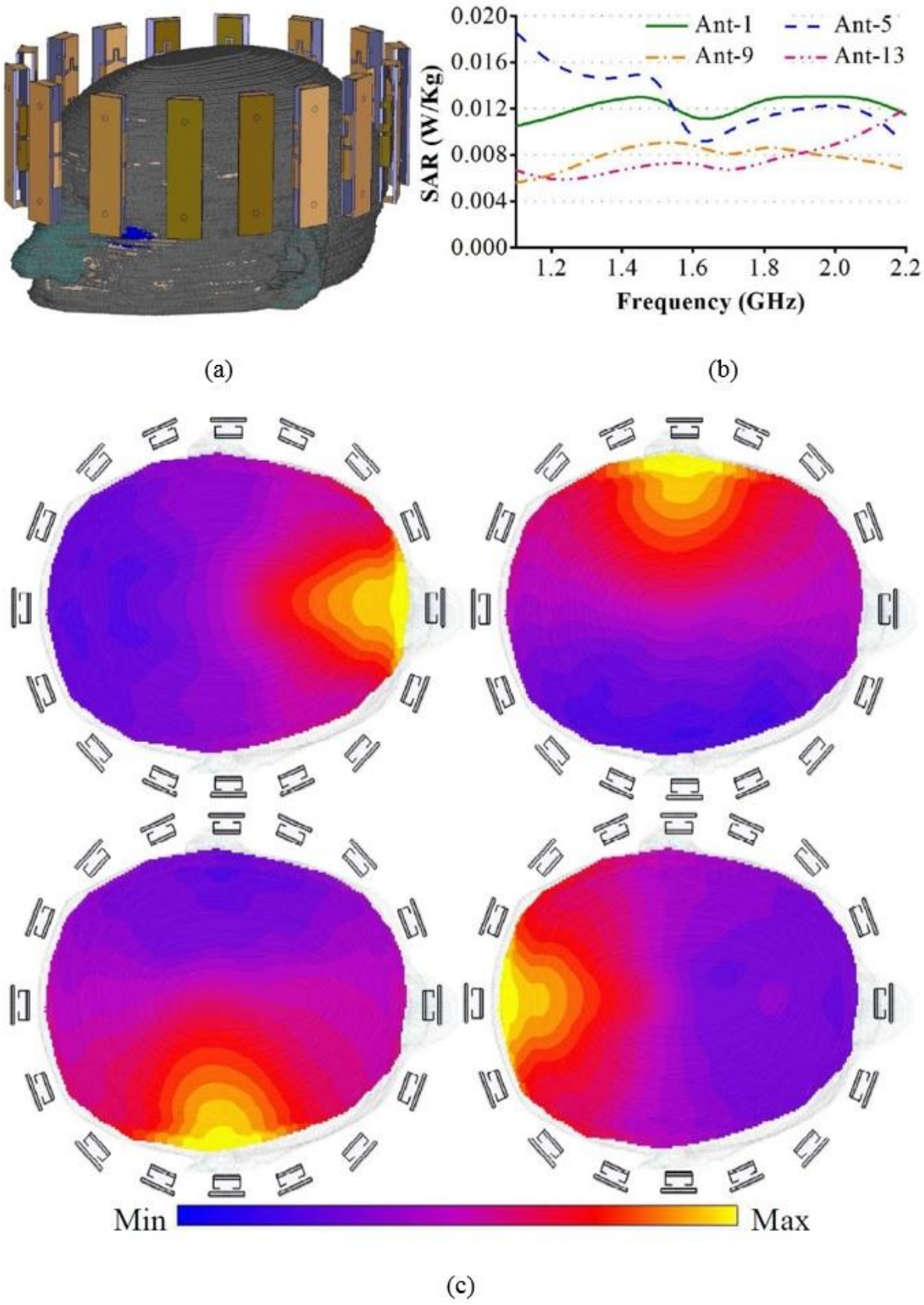

Fig. 6.1 (a) Position of the antenna elements around the head phantom. (b) Maximum calculated SAR values in the human head while operating different antennas. (c) SAR distribution inside the human head phantom when (from top left, clockwise) antenna-1, -5, -9, -13 is in operation at 1.5 GHz.

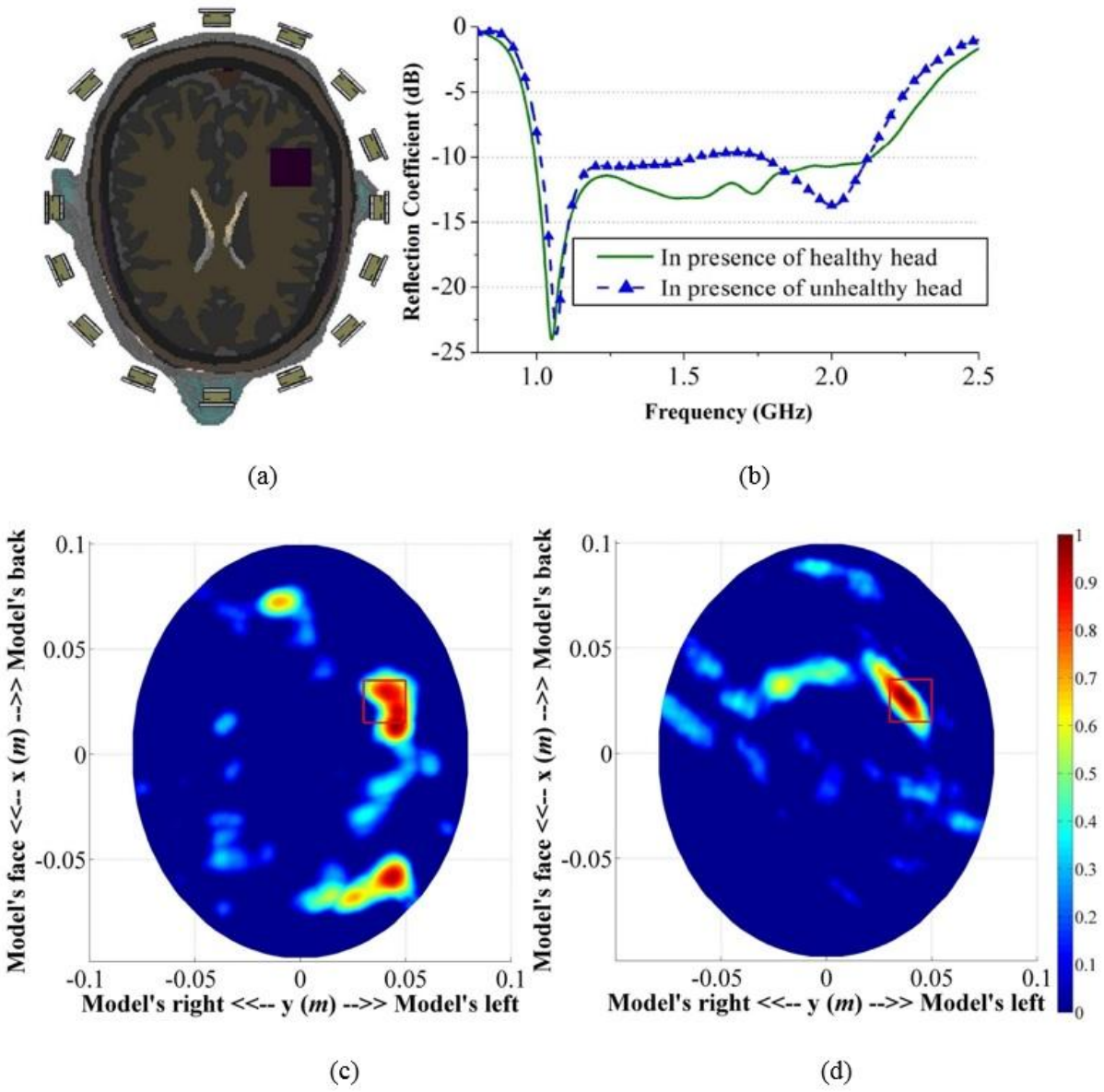

Fig. 6.2 (a) Dissected view of realistic human head, with hemorrhagic brain injury, enclosed by 16-element array. (b) Reflection coefficient of an antenna element facing a head with and without the hemorrhagic target. The reconstructed images using (c) a previously reported antenna from Section 3.5 and (d) the proposed antenna. The inserted injury is marked by a small square.

Since the system is intended for mono-static radar imaging, only one antenna is active at a certain time. A power radiation from any antenna is assumed to be 1 mW or 0 dBm. The link budget of the longest round-trip, which is from the antenna to and back from the center through longest radius of the head phantom, is numerically calculated accounting all the gains and frequency dispersive propagation losses. The estimated link budget is found to vary from 36 dB to 71 dB over the band of operation, which is less than the dynamic range of a practical compact transceiver. The 10g average SAR of the head model is also calculated for the realistic human head model and maximum SAR values for different frequencies are recorded. Fig. 6.1(b) presents the maximum SAR of the

orthogonally positioned antennas of the array, whereas Fig. 6.1(c) shows the SAR distribution inside the head model. It is noted that positions of maximum SAR are located at the exterior head tissue layers and the values are lower than 0.02 W/kg which is well below public radiation exposure limit of 1.6 W/kg [120].

A hemorrhagic (bleeding) target is inserted inside the head model in the area between grey and white matter tissues (Fig. 6.2(a)). Considering the average dielectric properties of these tissues, the contrast of the target with respect to healthy tissue is around 1.25:1 over the operating band. The reflection coefficient responses of an antenna in the presence of healthy and unhealthy heads are shown in Fig. 6.2(b), which illustrates that with the inception of bleeding, the scattered signals from the target changes the reflection coefficient. Moreover, the response in the presence of the head is different from that in free space. These changes in the response include the information needed to map the head, and detect and localize any bleeding. The antennas are excited accordingly with and without the head phantom. The calibrated data for the head phantom is extracted by subtracting the data without model from data with model. The calibrated data is processed using a delay-and-sum based image processing algorithm (reported in Section 5.4) and an image of the head's interior is reconstructed. Fig. 6.2(c, d) depicts the reconstructed images using antenna adopted from Section 3.5 and the proposed antenna of Section 3.11.1 while maintaining the same setup. It is noted that while the previous antenna detects the target in addition to false positives due to its relatively high impulse distortion, the proposed antenna is able to properly detect the position of the hemorrhagic brain injury without significant false targets. An Imaging analysis unveils that a high average target signal to clutter ratio of 11 dB, maximum target signal to clutter ratio of 1.22 is attained and localization accuracy of 1.6 *mm* is accomplished by the proposed antenna, while for previously reported antenna of Section 3.5, values are 8 dB, 0.97 and 12.75 *mm* respectively.

6.2 Hardware Architecture of Array Based Portable Head Imaging System

The architecture and different components of the proposed preclinical wideband head imaging system is illustrated in Fig. 6.3. The system primarily consists of an adjustable head imaging crown, an array of compact sensing antennas, an adjustable mounting stand, a switching system, a compact microwave transceiver and a signal post-processing and image creation unit.The different parts of the head imaging crown are fabricated using the 3D printing facility (DTM Sinterstation, 3D Systems, Inc.) of the University of Queensland, Australia and finally assembled. Acrylonitrile butadiene styrene (ABS) plastic powder, which has low dielectric constant in microwave frequencies and strong, durable finishing is chosen for the 3D printing process.

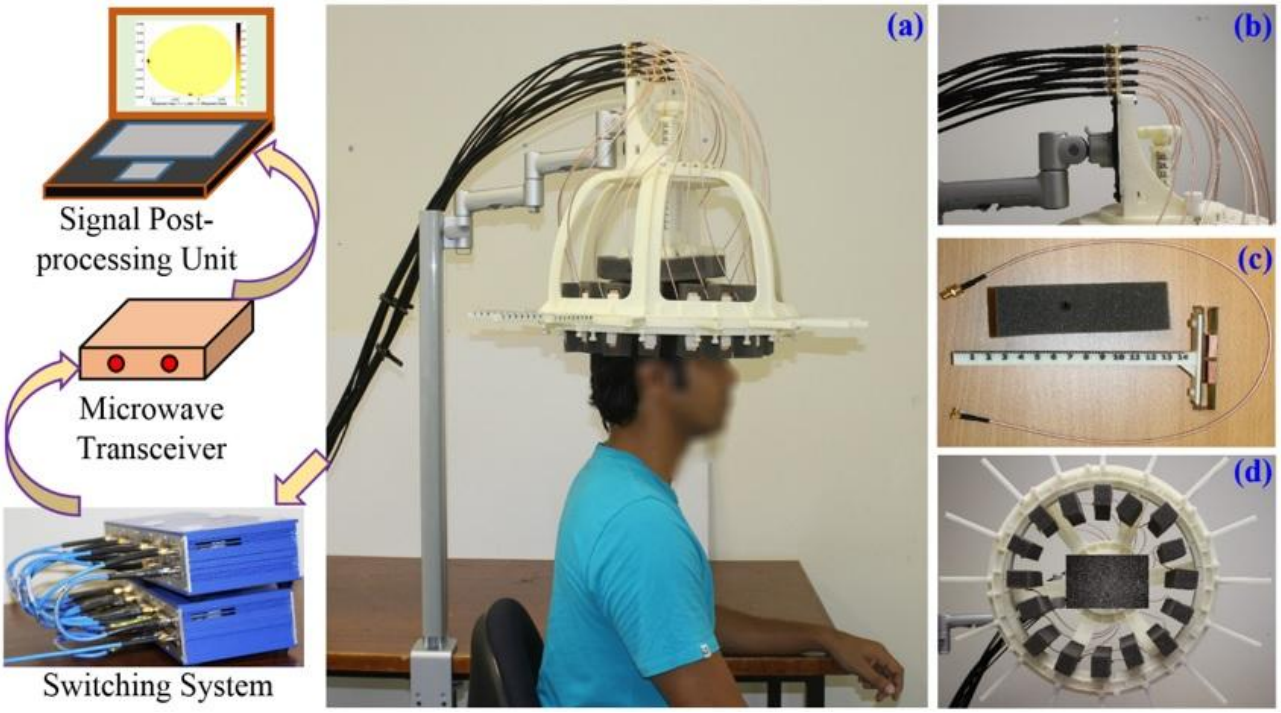

Fig. 6.3 (a) Proposed preclinical multi-level wideband microwave head imaging system with the schematic representation of the interconnections. (b) The Photograph of the 3D printed head imaging crown mount, showing the adjustable joints, height adjuster for multi-level scanning and cable holder. (c) The photograph of the scale-engraved antenna holder with the separator and utilized lightweight excitation cable. (d) Photograph of the 3D printed head imaging crown depicting the orientations of the sensing antenna holders and the top height adjusting support.

The crown is designed such that it can be mounted from the top using a suitable stand which has the flexibility of height, both vertical and horizontal angular adjustment. A low-profile, compact unidirectional antenna is designed and presented in Section 3.11.2 for the system to transmit and receive signals of wide bandwidth to and from the imaged human head. Each antenna is mounted on a 3D printed antenna mount with two nylon screws. A foam block which is transparent to the microwave signals is used as antenna separator from the head. A box having the footprint of the antenna's top portion is cut and trimmed from the foam leaving foam space of 10 *mm*, which is the constant distance between the head and antenna surface during imaging. An array of 16 antenna holders containing the compact antennas is mounted inside the crown where the arms can be extended according to the size of the head. A scale is engraved on the antenna mount in order to back-calculate the shape of the imaged head. In order to facilitate multi-level scanning of the head, a height adjuster, which touches the tip of head, and an engraved scale are used to assist in setting up appropriate height at which a slice of the head needs to be scanned. Low-loss and lightweight cables are connected to the sensing array elements and terminated at a cable holder which is also fixed with the mounting

stand to resist any twisting and turning of antennas when used. Low-loss coaxial cables further connect the cable holder to the switching system using USB-8SPDT-A18 switches. An Agilent N7081A microwave transceiver is employed to generate microwave signals v, which are transmitted through the switching system to the antenna elements in a mono-static approach. A laptop is used as a post-processing unit to process the stored signals and form an image of the head slice.

6.3 Signal penetration in the head when using multilevel Head Imaging

Analysis of the signal penetration inside the human head when using the proposed multilevel head imaging system is essential to understand the system's operation and reconstructed results. To that end, the imaging system is numerically analysed in finite difference time domain (FDTD) based electromagnetic software CST Microwave Studio (CST MWS). An MRI-scan based numerical human head model [193] is imported accordingly and different tissues are assigned with individual frequency dependent electrical properties [140, 141] (permittivity and conductivity) for the operating band using a four-pole Debye model [44]:

$$\varepsilon_c(\omega) = \varepsilon_\infty + \sum_{i=1}^{4} \frac{\Delta\varepsilon_i}{1 + j\omega\tau_i} + \frac{\sigma_s}{j\omega\varepsilon_0} \qquad (6.1)$$

Here, ε_c is the complex relative permittivity as a function of the angular frequency (ω). The permittivity of free-space (ε_0), relative permittivity at infinity (ε_∞), ith relaxation time (τ_i), magnitude of ith dispersion ($\Delta\varepsilon_i$) and static conductivity (σ_s) vary depending on the tissue type within the head. A brain injury imitating the hemorrhagic scenario of 2×2×1 cm^3 size is placed inside the numerical model, and attributed with dispersive electrical properties of blood.

The proposed multi-level head imaging system works on a mono-static technique, only one antenna in the array radiates and receives scattered fields at a certain time. The scanning system can scan multiple levels in a gradual manner by adjusting the top support system. Here, five levels (represented with L1 to L5), which requires five different vertical array scanning positions (represented by S1 to S5) where the scanned level is located at the centerline of the antennas, are considered. However, in order to understand the electromagnetic propagations inside the head and scattering mechanism of hemorrhagic target, electric fields in multiple levels are analysed for an individual scanning position. The hemorrhage is located at L3. The analyses are performed in two different sets: Firstly, three adjacent levels with 10 mm distances (L2, L3 and L4) and secondly L1, L3 and L5 (the adjacent levels with 20 mm distances among each other) are analysed to understand the relation and differences between the closely located levels.

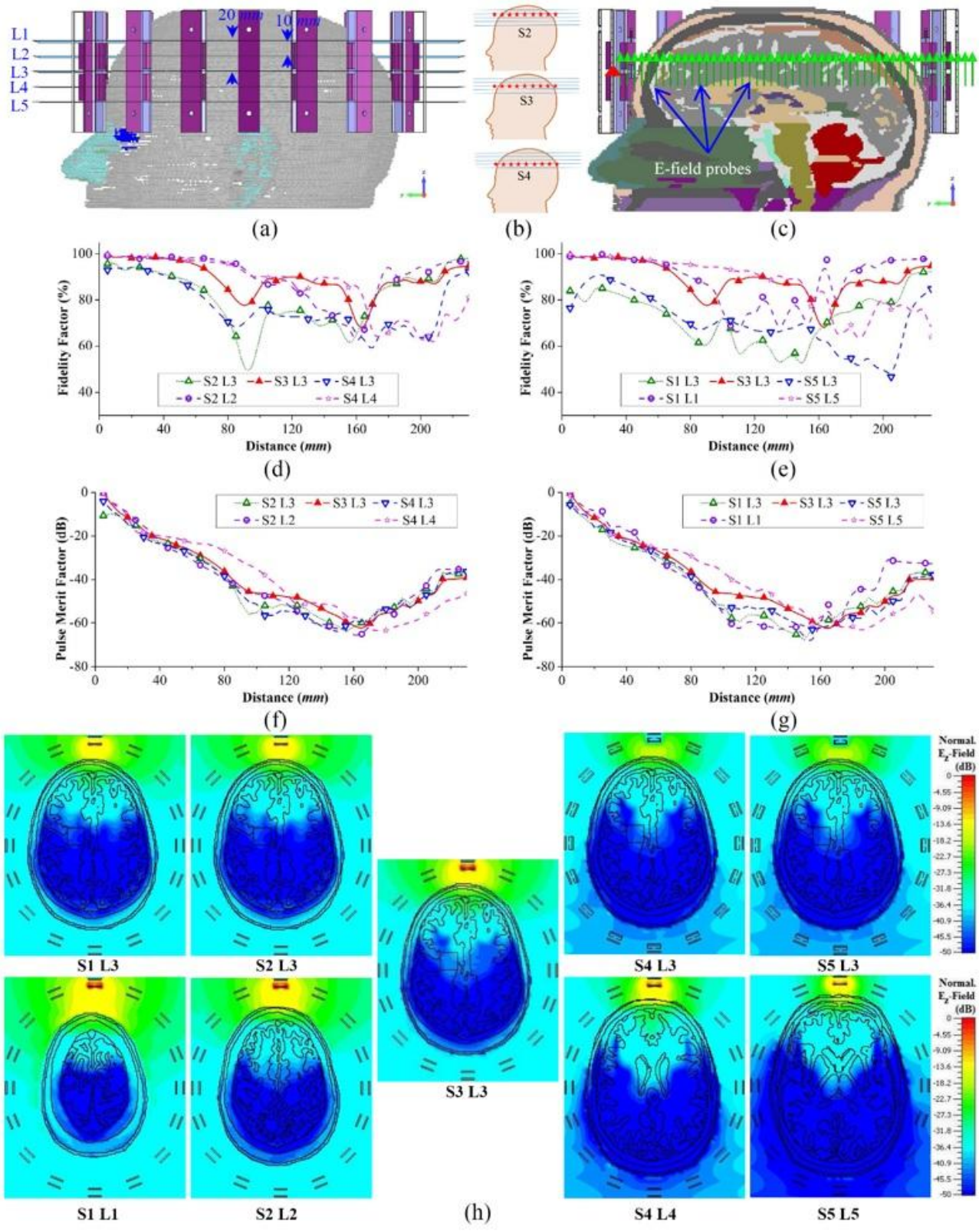

Fig. 6.4 (a) The setup environment of the numerical analysis showing different levels (L1 to L5), while the scanning array is positioned in S3. (b) The illustration of different scanning array positions. The red star marks represent the phase centres of the antennas. (c) The side view of the mid-sagittal plane cross section depicting the array of E-field probes utilized for the time-domain analysis. (d-g) The fidelity factor and pulse merit factor results of different time-domain pulses transmitted from

antenna-1 and received at different distances inside the realistic human head model. (h) The total time-domain E_z-field distributions of the horizontal cross-sections of different levels for different scanning array positions. The E_z-fields are normalized with respect to the maximum emitted E_z-field value from antenna-1 considering all scanning positions.

6.3.1 Time Domain Performance

To analyse the wave propagation inside the head, antenna-1 is excited in all 5 scanning positions (S1 to S5) with a wideband Gaussian pulse, $E_t(t) = -sin(2\pi f_c t)\, e^{(-2\pi t^2/t_w^2)}$, where f_c =1.7 GHz is the center frequency of the operating band. As the imaging system works in mono-static approach, single antenna analysis inside the array is performed. An array of E-field probes are placed in the front side of the antenna inside the head model and the received co-polarized transient E_z-fields are analyzed. The fidelity and pulse merit factors of the received transient signals are calculated for different scanning positions and at different levels. For the first set (L2, L3 and L4), it is noted that the signals received for S2 L2, S3 L3 and S4 L4 yield low distortions inside the head model and at the same time the received signals are stronger than those received at other levels, for the same excitations (S2 L3 and S4 L3). Thus, the antenna radiates most efficiently along the centreline. Nonetheless, a drastic reduction of signal quality (which is quantified by low fidelity) and signal strength is noted when the probes are not along the centreline. This scenario is vividly observed from the probe array measurements at S2 L3 and S4 L3. This is because although the distances between the probes and antenna's top surface is the same, the probes in higher/lower levels are in fact distant from the centre phase center of the antenna. Thus, the transmitted signals have to travel further from the phase center to higher/lower level probes and will thus encounter more losses and distortions. Similar observation can be concluded in case of the second set (L1, L3 and L5). However, comparing the results of S2 L3 with S1 L3 and S4 L3 with S5 L3, it can be said that increasing the observation distance results in increasing losses and pulse distortions. Again, the propagated signals at the top levels of the head suffer from less losses and distortions. This observation is also noted from the total transient E_z-field distributions inside the head model, illustrated in Fig. 6.4(h), where the top levels (S1 L1, S2 L2) are illuminated brighter than the lower levels (S4 L4, S5 L5). Again, it is noted from Fig. 6.4(h) that L3 is brightest in case of S3 scan. The implications of these observations are discussed later.

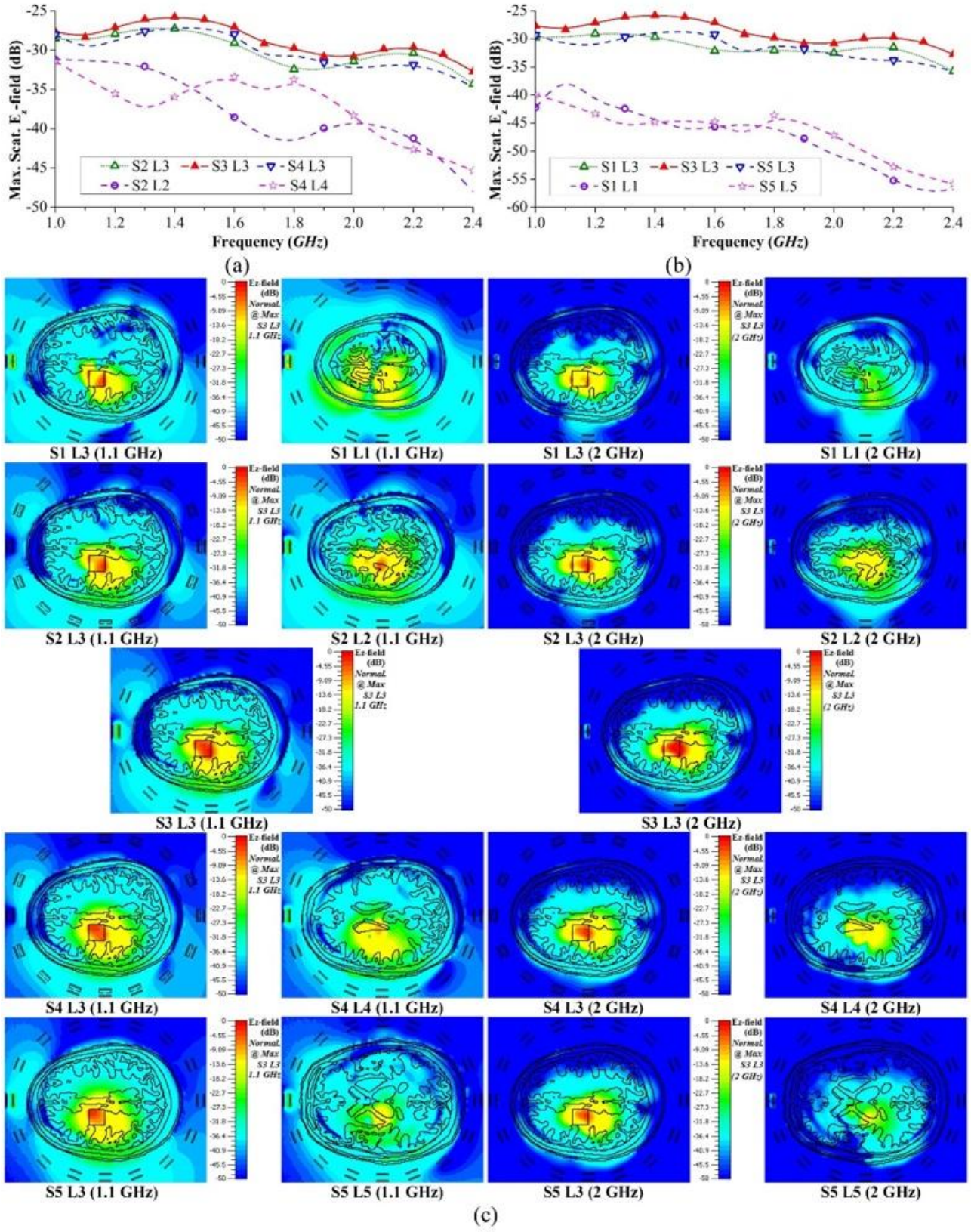

Fig. 6.5 (a) The maximum scattered E_z-field over the wide operating band at three different vertical levels with 10 *mm* separation where the ICH target is placed at the mid-level (L3) for the scanning. In the scanning array only antenna-1 is excited. (b) The scattered E_z-field for antenna-1 excitation at three different vertical levels with 20 *mm* separation where the ICH target is placed at the mid-level

(L3) for the scanning. (c) The E_z-field distributions of 2D cross-sections of different levels and for different excitations illustrating the scattered fields generated by the ICH target which is placed at L3 level.

6.3.2 Frequency Domain Performance

The frequency domain analysis of the scattering characteristics from a hemorrhagic target is necessary for understanding the working principle of the proposed mono-static multi-level head imaging system. The electromagnetic scattering of a target from a non-magnetic, dielectrically heterogeneous domain at a measurement location of $\boldsymbol{r}$, can be reliably modelled [194] by the following volume integral equation:

$$\Delta \boldsymbol{E}_S(\boldsymbol{r}) = \omega^2 \mu \int_{\Omega} \bar{\bar{G}}^b(\boldsymbol{r}, \boldsymbol{r}') \boldsymbol{E}^t(\boldsymbol{r}') [\varepsilon^t(\boldsymbol{r}') - \varepsilon^b(\boldsymbol{r}')] d\boldsymbol{r}' \qquad (6.2)$$

where $\Delta \boldsymbol{E}_S$ is the total scattered field representing the total observed field difference between the target environment and the background environment, and Ω is the investigated region. The Green's dyadic function $\bar{\bar{G}}^b$ provides the field inside the head without the target. The relative permittivity of the target and background are denoted by ε^t and ε^b accordingly. $\boldsymbol{E}^t$ is the total incident electric field due to the source antenna in the unhealthy head environment. The scattering from the previously discussed hemorrhagic target is calculated over the operating band. 3D FDTS based software CST MWS in a realistic environment is utilized for the calculations.

From the maximum scattering E_z-field results presented in Figs. 6.5(a, b), it can be seen that the scattering fields vary over the band and they tend to go lower at higher frequencies. As the conductivity of the head tissues gradually increases over the frequency band, higher frequencies face higher losses and less amount of power penetrates towards the target. On the other hand, the scattering signals from the target also gets reduced for the same reason. It is noted from Figs. 6.5(a, b) that as the array moves from one level to another, the fields received at a certain level is different in every scan. This indicates that the imaging scenario gradually changes in every scan depending on the height of the scanning level position. However, as the target is located at L3, the maximum scattering E_z-field at L3 level for any scanning position is higher than those at the top (L1, L2) or bottom (L4, L5) levels, where the fields gradually decays with increasing distance from L3. Moreover, S3 L3, where L3 is located at the centerline of the S3 scanning, the maximum E_z-field is seen to be higher than the other scanning locations (S2 L3, S1 L3, S4 L3, S5 L3). This is because the signals have to travel longer distance through the head to reach hemorrhagic target, thus suffer from higher losses.

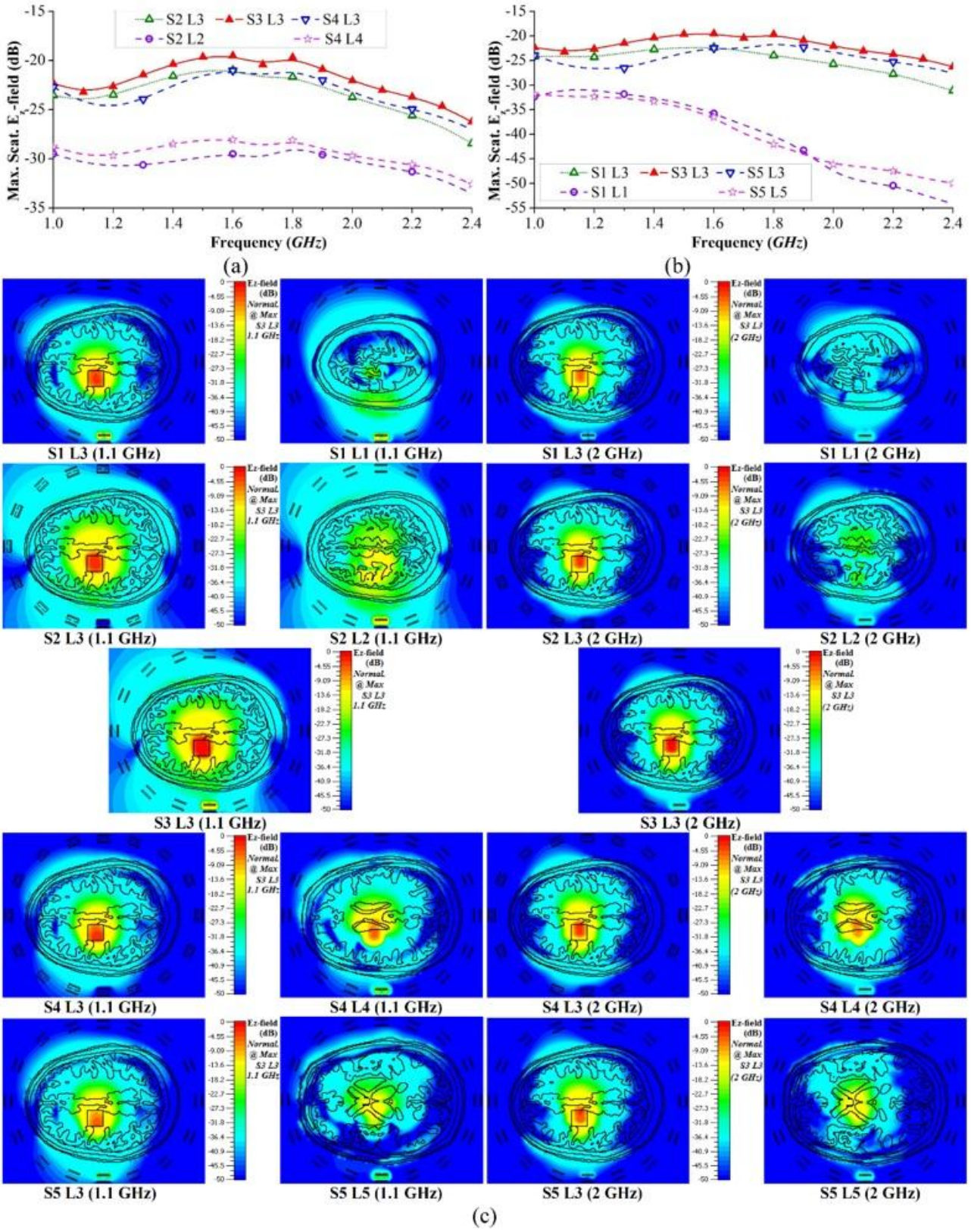

Fig. 6.6 (a) The maximum scattered E_z-field over the wide operating band at three different vertical levels with 10 *mm* separation where the ICH target is placed at the mid-level (L3) for the scanning. In the scanning array only antenna-5 is excited. (b) The scattered E_z-field for antenna-5 excitation at three different vertical levels with 20 *mm* separation where the ICH target is placed at the mid-level (L3) for the scanning. (c) The E_z-field distributions of 2D cross-sections of different levels and for

different excitations illustrating the scattered fields generated by the ICH target which is placed at L3 level.

The max. E_z-field distributions inside the head model for 1.1 and 2 GHz are illustrated Fig. 6.5(c). It can be seen that in both frequencies maximum scattering from L3 occurs at S3 scanning, as L3 is located at the middle of S3. The scattering for other scanning positions gradually becomes lower for L3 (S2 L3, S4 L3 etc.). As a result, the field distributions of their scanning levels (S2 L2, S4 L4 etc.) also demonstrate gradual decrease in scattered fields. Moreover, the scattering patterns are found different at different frequencies and also at different levels; some are collimated at one point and some are distributed over multiple points.

Extended analysis mentioned in Fig. 6.6 demonstrates that depending on the excitation, the level of scattered E_z-field also varies. It is noted that for the side excitations (antenna-5 or -13), the distance of the target from the skin layer decreases and consequently the scattered fields also increase, and thus makes the detection easier. However, the scattering patterns vary for different excitations and frequencies due to the heterogeneous head's tissue distribution, which looks different from different scanning positions for different frequencies.

6.4 Experimental Results from Realistic Phantom

To validate the detection efficacy of the multi-level compact head imaging system, multiple experiments are performed on a realistic human head phantom. Data is collected accordingly from the system and an image of the head interior is generated using an improved confocal imaging algorithm.

6.4.1 Imaging Scenarios

A realistic human head phantom, which is based on MRI-derived 3D model, is used for the validation of the multi-level head imaging system. Different parts and casts of the head phantom are 3D printed. Artificially built tissue mimicking materials are utilized to fill-up various brain tissues using the casts. The tissues are frequency dispersive over the operating band of 0.5-4 GHz. The realistic human head fabrication process and recipes of the tissue emulating materials are detailed in Chapter 4. In this work, we present four different imaging scenarios in order to investigate the performance of the imaging system. Firstly, a healthy head phantom is imaged to examine if the system is able to debar false positive detection. Subsequently, ICH targets of $2\times2\times0.5$ cm^3 in three different locations inside the head phantom are imaged to analyse the detection capability of the system. The targets are placed in shallow-right, deep-left, and deep-back positions. Targets are placed in different vertical positions

(centred at 40, 30 and 20 *mm* away from the top head level) to investigate the effects of ICH scattering in multiple levels.

6.4.2 Data Acquisition

Data acquisition of the proposed imaging system comprises both software and hardware parts in order to measure the scattering performance of the imaged head. The data acquisition is performed in five main stages: 1) system initialization and customization, 2) system calibration, 3) frequency scanning, 4) array scanning and 5) data storage. An automated data acquisition software is developed using MATLAB environment for data collection. Firstly, the controlling PC, microwave transceiver and switching network are switched on and all cable connections are checked accordingly. The positions of the antenna elements in the array are adjusted using the flexible imaging platform. The data acquisition software is initialized and the various parameters, e.g. transmitting power (P_r), operating frequencies (f_l, f_h), scanning points (M) are imported inside the software. In the calibration stage, the microwave transceiver is calibrated up to the point of antenna feeding MCX connection through the switching network. The standard calibration system including open-short-load connections is adopted. This calibration gets rid of the effects of the switching system and long connecting cables which otherwise reduce the efficiency of the system. Since the system environment remains the same for different heads imaging, the calibration file can be saved for future use. Afterwards, the frequency scanning is performed over the operating band using the data acquisition software to enable frequency scanning measurements of all 16 antenna elements in the array. The collected data is stored for post-processing.

6.4.3 Signal and Image Processing Algorithm

Data acquisition from the antennas are performed at multiple vertical levels (L) of the head phantom. In this study, L = 5 different levels at D = 10 mm separations are scanned, covering the brain portion of the head. Since the radii of the head vary from one patient to another, the positions of the antennas depend on the structure and shape of the patient's head. Typically, the human brain is double parabolic shaped and symmetrical at mid-sagittal plane of the head [196]. Each set of data for a level contains reflection coefficient measurements ($\boldsymbol{\Gamma}_n(f_m)$, n = 1 to N, m = 1 to M) from N = 16 antennas over the band of 1-2.4 GHz. In order to apply the image processing algorithm, these frequency domain signals are converted to time domain ($\boldsymbol{T}_n(t_i)$) using the inverse discrete Fourier transformation.

$$\boldsymbol{T}_n(t_i) = \mathfrak{F}^{-1}(\boldsymbol{\Gamma}_n(f_m)) \qquad (6.3)$$

$\mathfrak{F}^{-1}$ represents the M×M matrix where the (n, k)th entry is $1/Me^{j2\pi \quad /M}$, and k is the wave number.

In order to extract the scattered signals from the brain injury target, two stage calibration is utilized. The first calibration is used to trim the effects of the radiating antenna and the surround ones. In the previous single antenna based system described in Section 5.5 and 5.6, this stage is not required, because of the presence of only one antenna. Since an array of antennas is used in the system, even though only one antenna is active and others are match terminated at a certain moment, the mere presence of other antennas, especially the neighbouring antennas, scatters some signals. To get rid of these scattering signals, one set of measurement ($\boldsymbol{\Gamma}_{e\quad t}\ (f_m)$) is performed with the same setup without the presence of the imaged head and consequently converted to time domain ($\boldsymbol{T}_{e\qquad}(t_i)$). This set is subtracted from the measured data and the actual scattering from the head without the effects of scattered signals from other antennas is obtained.

$$\boldsymbol{H}_n(t_i) = \boldsymbol{T}_n(t_i) - \boldsymbol{T}_{e\qquad}(t_i) \tag{6.4}$$

The second calibration is performed to acquire the target's scattered signals ($\boldsymbol{S}_n(t_i)$) from the actual scattering signals of the head ($\boldsymbol{H}_n(t_i)$). In this case, the adjacent average subtraction technique presented in Section 5.5 and 5.6, which considers the woody average of the adjacent antenna signals ($\boldsymbol{H}_n(t_i)$), is deducted from the head scattering signals.

$$\boldsymbol{S}_n(t_i) = \boldsymbol{H}_n(t_i) - \boldsymbol{H}_{n\boldsymbol{a}\quad\boldsymbol{a}}\ (t_i) \tag{6.5}$$

A confocal imaging algorithm based on a modified delay-and-sum (DAS) technique is employed for the image reconstruction purpose. An imaging area of 0.3×0.3 m^2 is defined with a 0.5 × 0.5 mm^2 pixel resolution. The outline of the human head is calculated from the scale of the antenna mount array and is defined by the boundary vector, $\boldsymbol{B}_j$, j =1 to J, is the border circumference at the skin-air interface in Euclidean space defined by x and y coordinates. In order to estimate the optimal propagation path from the antenna to an arbitrary point ($\boldsymbol{p}$) of interest inside the head, Fermat's principle is adopted by calculating minimum propagation route from all the possible routes ($\boldsymbol{d}_j$) from the antenna ($\boldsymbol{A}_n$) at free space to the boundary vector ($\boldsymbol{B}_j$) following the propagation paths from $\boldsymbol{B}_j$ to the investigated point. b

$$\boldsymbol{D}_{\boldsymbol{i}} = \left\|\boldsymbol{A}_n - \boldsymbol{B}_j\right\| - \sqrt{\boldsymbol{\varepsilon}_{\boldsymbol{e}\quad\boldsymbol{j}}}\left\|\boldsymbol{B}_j - \boldsymbol{p}\right\| \tag{6.6}$$

Because of the highly heterogeneous distribution of the human head tissues, a point of entry based permittivity model is used which is proven to have imaging advantages compared to the traditional constant permittivity models.

$$\boldsymbol{\varepsilon}_{\boldsymbol{e}\quad\boldsymbol{j}} = \varepsilon_m\ \ (1 - \alpha e^{-\beta\ /a}) \tag{6.7}$$

Using a similar procedure presented in Section 5.5, the values for a typical human head model and the utilized antenna over the operating band of 1-2.4 GHz in a realistic simulation environment is

estimated as, ε_m = 41, α =0.7 and β =6.3. Owing to the utilized mono-static approach, the wave has to travel to and from each points; therefore, the propagation time of the optimal route is multiplied twice to determine the actual delay ($\boldsymbol{\tau}_a$) of the target's response. Finally, an image of the backscattered signals' intensity is reconstructed by calculating the coherent summation of all responses.

$$\boldsymbol{I}_i(\boldsymbol{p}) = \left|\sum_{n=1}^{N} \int_0^{\infty} \boldsymbol{\tau}_a(\boldsymbol{p}) \boldsymbol{S}_n(t_i) dt_i\right| \quad (6.8)$$

In case of true scattering point, the scattering intensity will be high, as in case of hemorrhage. On the other hand, small values will result from the wrong assumption of the hypothetical point indicating an imaging noise. 2D maps of the scattered energy from the head in multiple levels are reconstructed.

Typically, cross-sectional 2D images are normalized to individual highest intensity because in delay-and-sum approach, after focusing the absolute values of the image do not provide other useful information regarding the images head. However, for the proposed multi-level head imaging system, a scattering threshold is required for differentiating the healthy and unhealthy cases.

Due to the fact that the ICH does not occur in the skin or skull region[3,4,45,46], the skin and skull tissues (which are about 10 *mm* thick) can be considered as a neutral region ($\boldsymbol{\mathcal{N}}$), whereas the rest head interior is considered as the suspected region ($\boldsymbol{\mathcal{S}}$). According to DAS algorithm, ICH targets are expected to scatter strongest signals in unhealthy cases. Therefore, in those cases, the system is expected to detect the strongest scattrer in the suspected region. On the other hand, for healthy cases, the suspected region holds the maximum of the scattered signals. Again, it is concluded from Fig. 6.5 that the maximum scattered signal from an ICH target, is located when scanning the level where it is located. Thus, in both cases, the images can be normalized with the maximum of the all 2D scans, $\boldsymbol{Z}_L$, where L = 1 to 5 the number of scanned levels.

$$Thr_m = \max_{\boldsymbol{Z}_L}[\boldsymbol{I}(\boldsymbol{p})] \quad (6.9)$$

However, in order to determine the threshold, a function, ρ is defined as the ratio of maximum of the neutral region to that of the suspected region for scattering signals from all levels.

$$\rho = \frac{\max_{\boldsymbol{Z}_L}[\boldsymbol{I}(\boldsymbol{a})]}{\max_{\boldsymbol{Z}_L}[\boldsymbol{I}(\boldsymbol{b})]} \quad \begin{matrix} \forall \boldsymbol{a} \in \boldsymbol{\mathcal{N}} \\ \forall \boldsymbol{b} \in \boldsymbol{\mathcal{S}} \,\&\, \boldsymbol{b} \in \boldsymbol{\mathcal{N}} \end{matrix} \quad (6.10)$$

In case of, $\rho > 1$, $Thr_m = \max_{\boldsymbol{Z}_L}[\boldsymbol{I}(\boldsymbol{a})]$, while for $\rho < 1$, $Thr_m = \max_{\boldsymbol{Z}_L}[\boldsymbol{I}(\boldsymbol{b})]$.

Finally, the multi-level images are normalized to 1 with respect to the threshold values. The resulted images illustrate 3D localization of the potential scatterer in multi-level scenario.

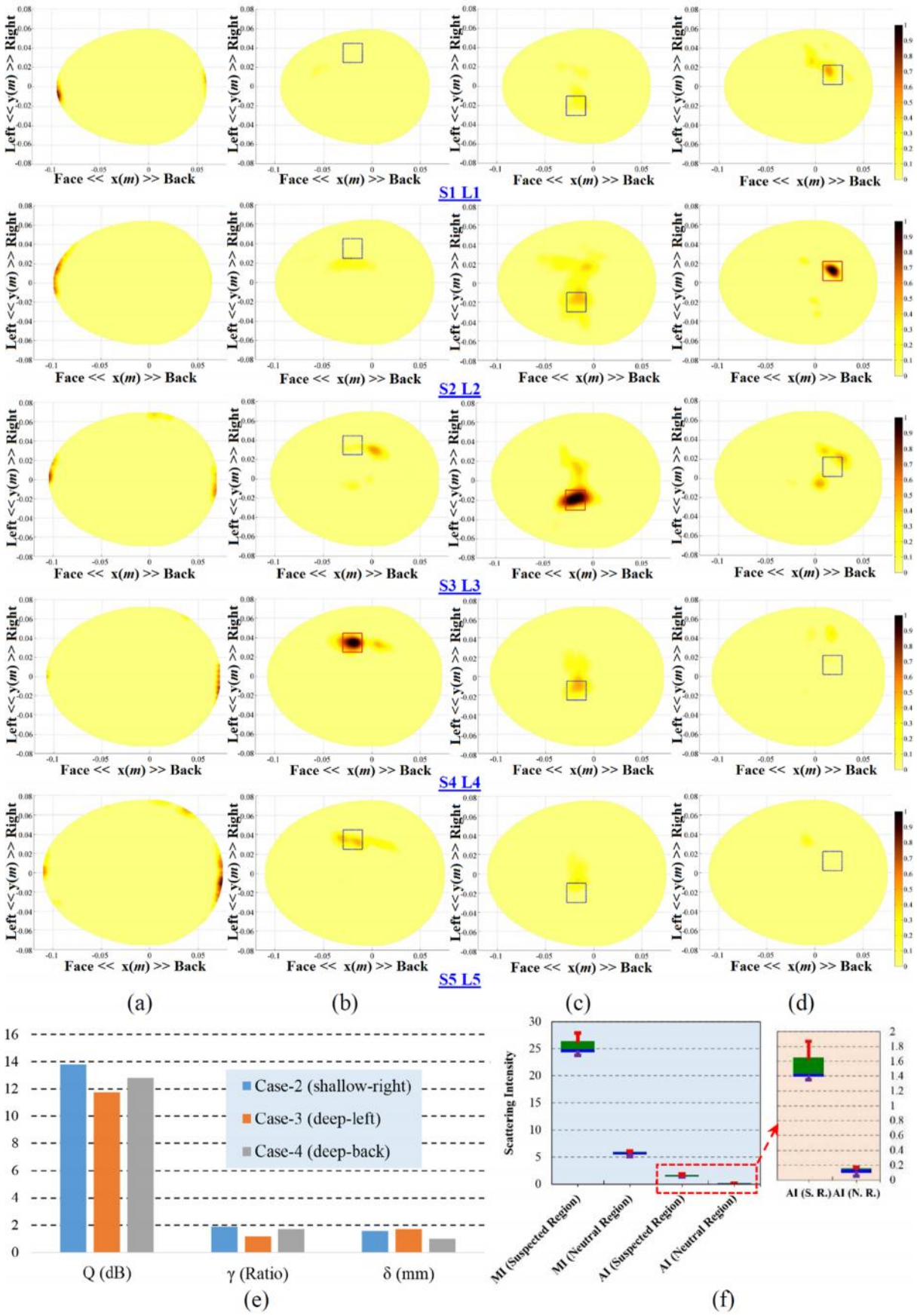

Fig. 6.7 The reconstructed images of realistic human head phantom at five different levels for four different cases: (a) healthy, (b) shallow-right, (c) deep-left, (d) deep-back positions. (e) The quantitative analysis results of the detected targets in the detected level. (f) The statistical analysis

results of the maximum and average intensities in neutral and suspected regions. The green and blue boxes represent the 75th and 25th percentiles respectively and the transitional line between them presents the median. The red and violet lines accordingly states the maximum and minimum magnitudes.

6.4.4 Experimental Results

The reconstructed images of the realistic human head model are depicted in Fig. 6.7. Five scans are presented for each of the four experimental setups. No significant scatterer is noted for the healthy head phantom (Fig. 6.7(a)), which makes it free from false positive detection. In this case, maximum scattering intensity is located near the skin layer. On the other hand, for the ICH affected head phantom (Figs. 6.7(b, c, d)), strong scatterers are located inside the suspected region. Maximum scattering intensities are found at level-4, -3 and-2 accordingly for the shallow-right, deep-left and deep-back target locations, which are the correct vertical scanning position (S4, S3 and S2 accordingly).

Figs. 6.9 and 6.10 illustrates the comparisons of using individual normalization of the reconstructed images with those of the threshold normalization. It is seen that for the healthy head phantom (Figs. 6.9(a, b)), even individual normalization shows that the maximum scattering is located at the neutral layer. Since in this case, $\rho > 1$, the maximum value of the neutral region is defined as the lowest thresholding value. The actual values of the maximum intensities for different scanned levels are mentioned in Fig. 6.8(a). Very low discrepancies among the values are observed.

For the unhealthy head phantoms containing the ICH targets (Figs. 6.9(c, d), 5), when the reconstructed images of each level are normalized to individual maximum, they demonstrate one or multiple targets in different locations of the head. However, from Figs. 6.8(b, c, d), it is evident that the layers have different maximum values in the suspected regions of different scanned levels and the maximum values of the actual target location is highest in each experimental set. However, the maximum values of the neutral region show very low fluctuations.

Quantitative analysis is performed on the reconstructed images with maximum scatterers and the results are presented in Fig. 6.7(e). It is seen that the images yield high values of average signal to clutter ratio (Q), maximum signal to clutter ratio (γ) and accuracy indicator (δ). However, it is noted that for shallow targets, the detection is easier, as the signal to clutter ratio indicators have higher values when compared to the deep targets. This is because in shallow position, the scattered signals suffer comparatively from lower penetration losses due to the lossy head tissues. This phenomenon is also evident from the raw scattering intensity values of the experimental sets (Figs. 6.8(b, c, d)).

However, as low values of accuracy indicator is achieved, it can be said that all experimental sets attain high accuracy of detection when using the proposed multi-level head imaging system and its associated algorithm.

Statistical analysis is also performed on the reconstructed images of all the ICH affected head phantoms. It is noted that both maximum intensity (MI) and average intensity (AI) medians of the suspected regions of all three experimental sets are around 5 times higher than those of the neutral regions. Again, it is observed that the MI and AI of the suspected region exhibit higher fluctuations compared to those of neutral region. This is because depending on the target position (shallow or deep), the scattered energy varies owing to the penetration losses, while the scattering noise of the neutral region has less fluctuations.

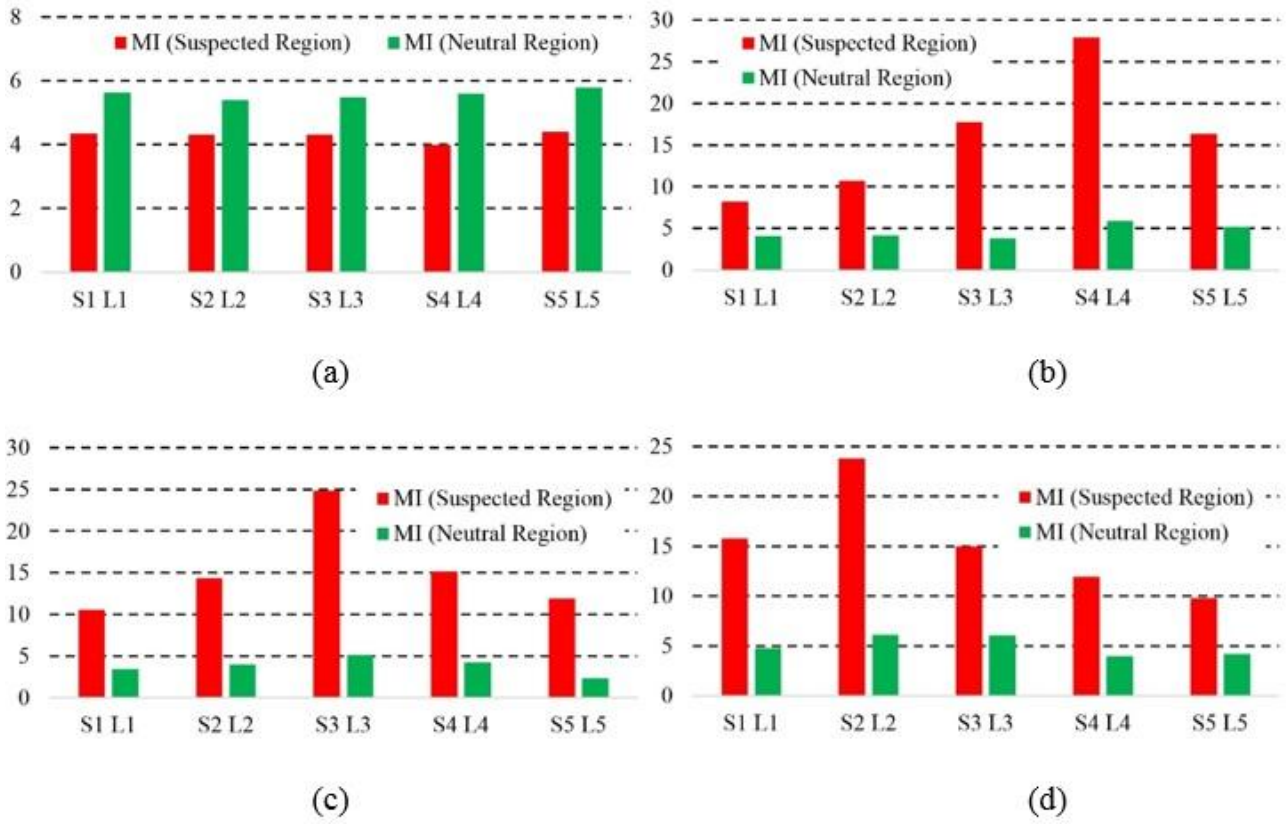

Fig. 6.8 The raw maximum intensity values of different scanning levels for four different cases: (a) healthy, and unhealthy with ICH targets at (b) shallow-right, (c) deep-left, (d) deep-back positions.

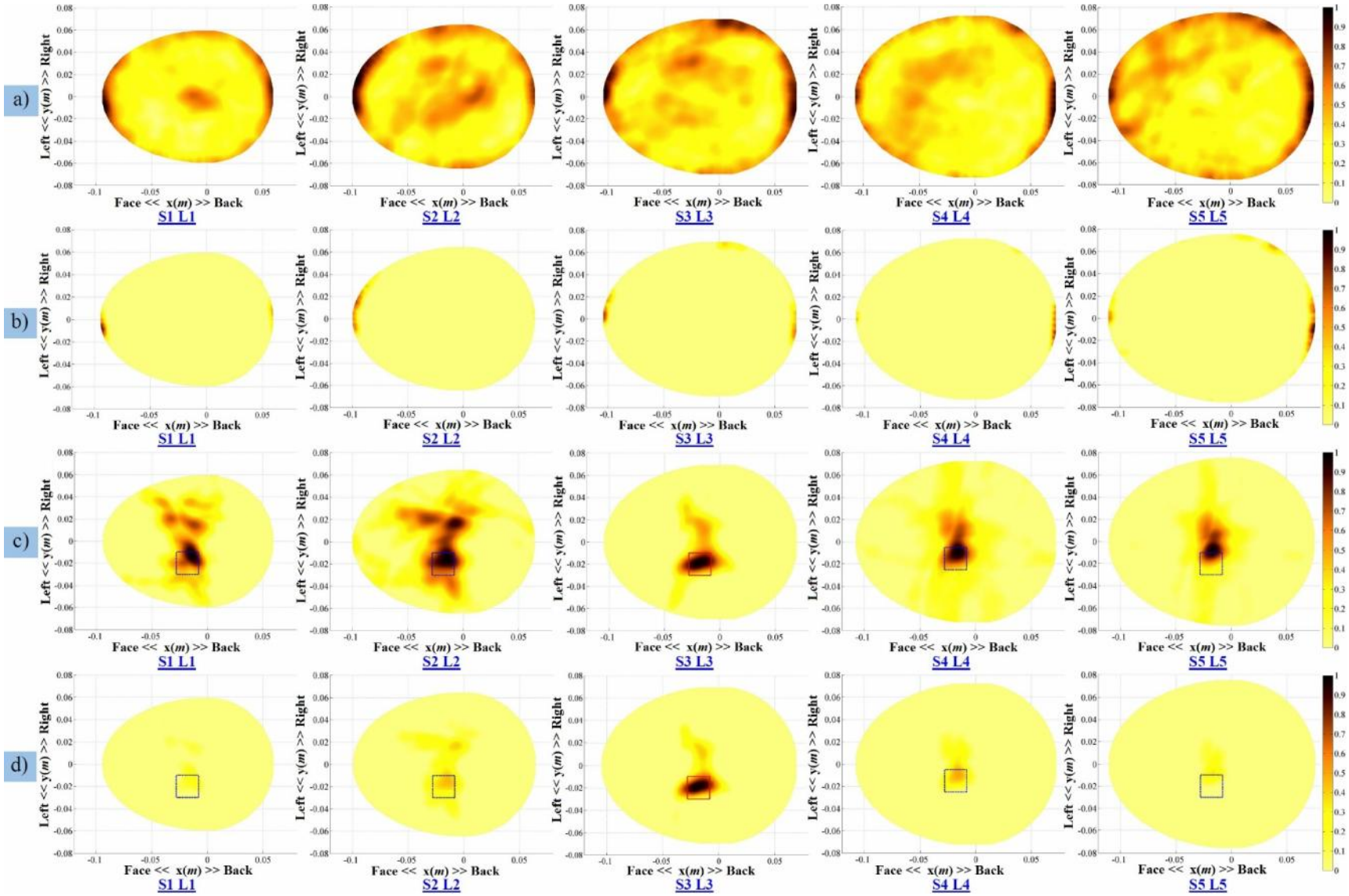

Fig. 6.9 The reconstructed images of five different levels of healthy realistic human head phantom after (a) normalization with respect to individual maximum and minimum of each level, and (b) threshold normalization. The reconstructed images of five different levels of unhealthy realistic human head phantom with target at deep-left location after (a) normalization with respect to individual maximum and minimum of each level, and (b) threshold normalization.

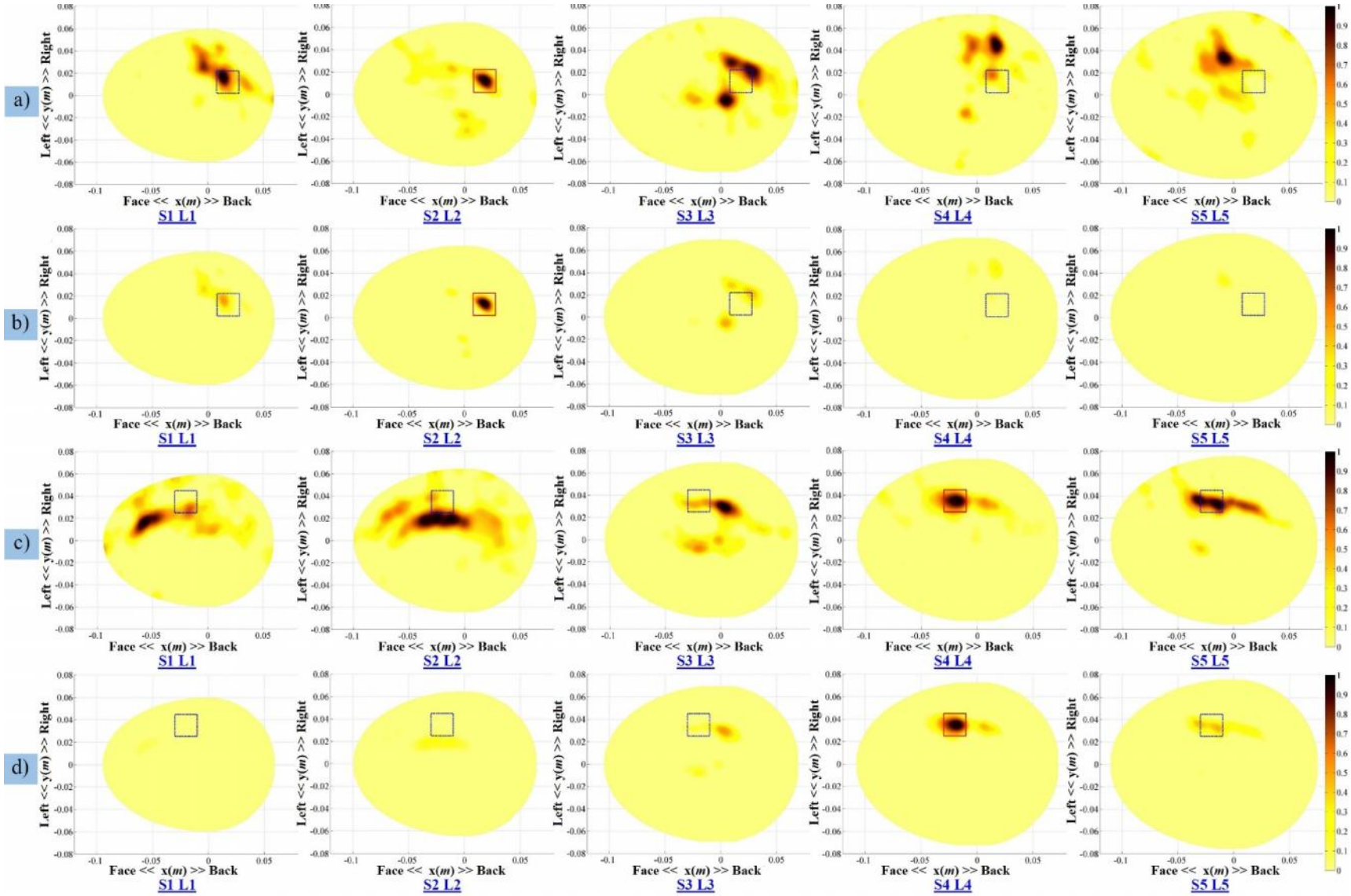

Fig. 6.10 The reconstructed images of five different levels of unhealthy realistic human head phantom with target at deep-back location after (a) normalization with respect to individual maximum and minimum of each level, and (b) threshold normalization. The reconstructed images of five different levels of unhealthy realistic human head phantom with target at shallow-right location after (a) normalization with respect to individual maximum and minimum of each level, and (b) threshold normalization.

6.5 Pilot Human Tests of the System Prototype

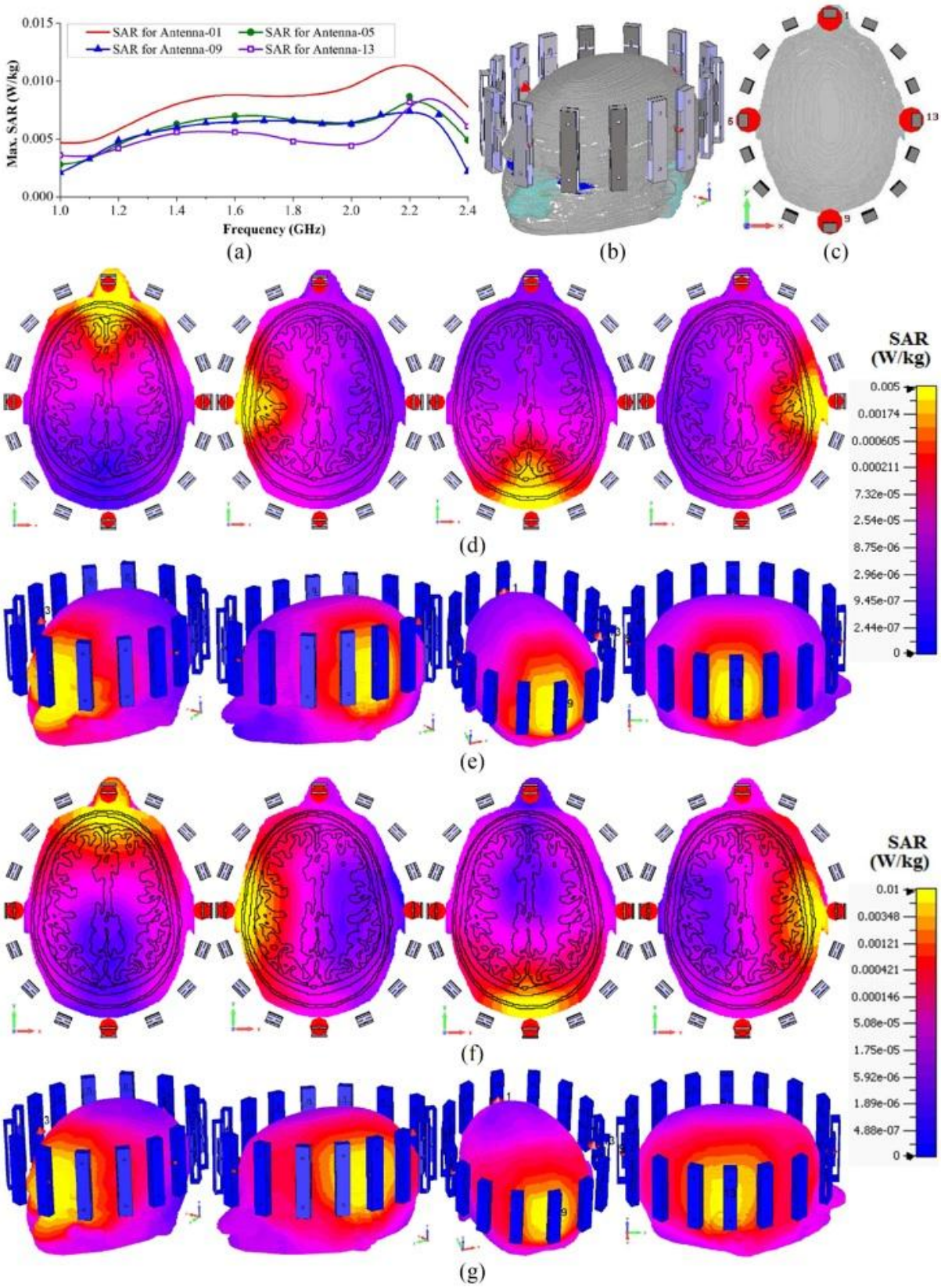

Fig. 6.11 (a-c) The maximum SAR values of realistic human head model for antenna-1, -5, -9 and -13, with the illustration of simulation environment and antenna positions. The SAR distributions of the head phantom at 1.1 GHz for antenna-1, -5, -9 and -13, respectively illustrating (d) cross-sectional

view and (e) the 3D view. The SAR distributions of the head phantom at 2 GHz for antenna-1, -5, -9 and -13, respectively illustrating (d) cross-sectional view and (e) the 3D view.

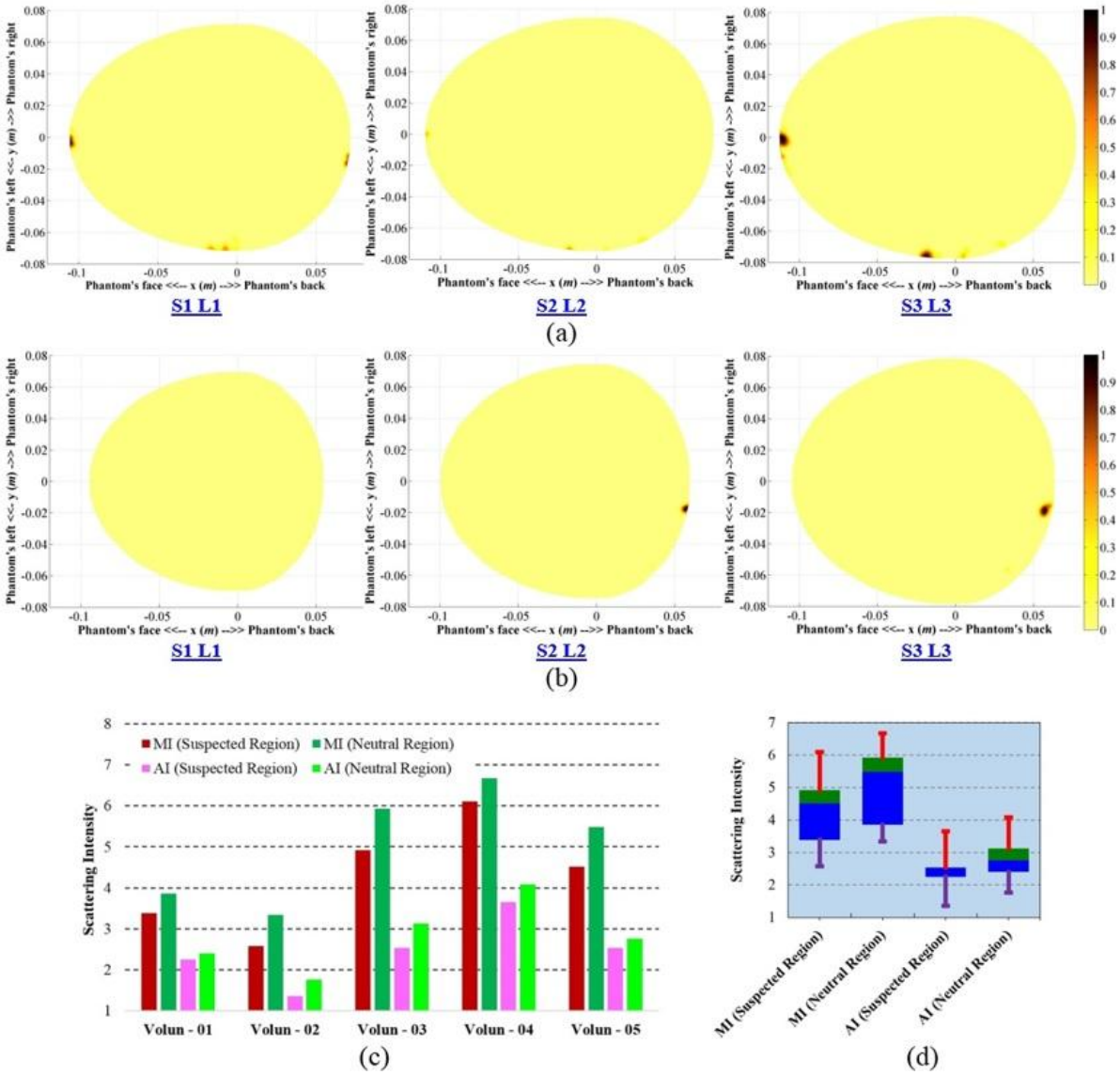

Fig. 6.12 (a, b) The image formation results of two volunteers each having head scanned at three different levels. (c) The maximum and average intensity comparisons between the suspected and neutral regions for five different volunteers. (d) The statistical analysis of the maximum and average intensities of neutral and suspected regions. The green and blue boxes represent the 75th and 25th percentiles respectively and the transitional line between them presents the median. The red and violet lines accordingly states the maximum and minimum magnitudes.

In order to apply the prototyped multi-level head imaging system for pre-clinical volunteer study, the radiation safety of the prototyped system is checked through numerical simulations. Fig. 6.11 illustrates the specific absorption ratio (SAR) simulation setup, which contains the previously discussed MRI-derived numerical head model and various results. In the mono-static system, as only

one antenna is active at a certain moment, SAR of the system is calculated by exciting one antenna at a time. In this case four orthogonally positioned antennas (antenna-1, -5, -9, -13) are considered and excited with 1dBm power, which is the typical power level transmitted from the antennas of the prototyped system. It is observed (from Fig. 6.11(a)) that the calculated SAR values are significantly less than the IEEE defined radiation limit of 2 W/kg [120] indicating the safe use of the presented system. The SAR distributions of the head model (from Figs. 6.11(d-g)) illustrates that for different antenna excitations, maximum SAR values are located on the skin layer and concentrated at the closed point from the phase center location of the antennas.

After verifying the safety issues of the prototyped imaging system, it is applied on healthy volunteers in preclinical trials. The underlying aim of the pilot volunteer study is to verify the conclusions of the realistic phantom measurements as well as to investigate the possibility of building a database of healthy and unhealthy patients which can be utilized as a reference. The preclinical trial is a common practice to prepare a diagnostic system for clinical environment. The performed preclinical trials are performed following the guidelines and protocols of the Ethics Committee of the University of Queensland, who approved the preclinical microwave head imaging system and measurement procedure. Consents of all volunteers are obtained before the study and heads are scanned at three levels having separations of 10 *mm*. The reconstructed images from two volunteers are depicted in Figs. 6.12(a, b). There is no target detected inside the suspected region and the maximum scattering is identified as imaging noise. It is clear that the reconstructed images of all levels are free from false positive detection. Figs. 6.13 to 6.17 demonstrate the imaging comparisons between the reconstructed images with individual normalization and the threshold normalization. Threshold normalization reduces the noise level and makes it clear that most of the scattering signals come from the neutral region. The performed statistical analyses (Figs. 6.12(c, d)) of the reconstructed volunteer images also suggest that the skin reflection is slightly higher than those of the internal scattering from the brain portion.

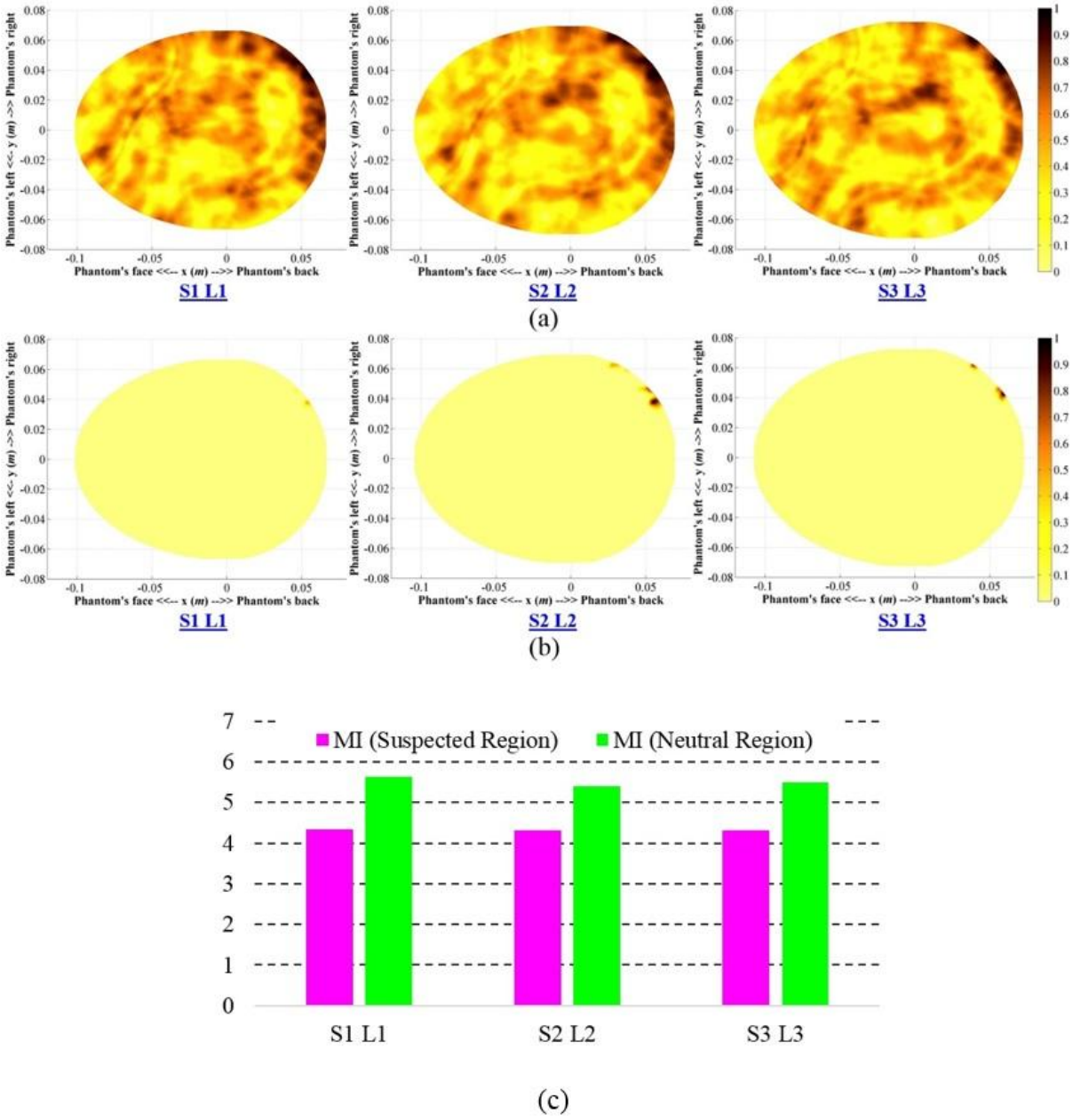

Fig. 6.13 The reconstructed images of three different levels of healthy human volunteer-01 after (a) normalization with respect to individual maximum and minimum of each level, and (b) threshold normalization. (c) The raw maximum intensity values of the suspected and neutral regions at different scanning levels.

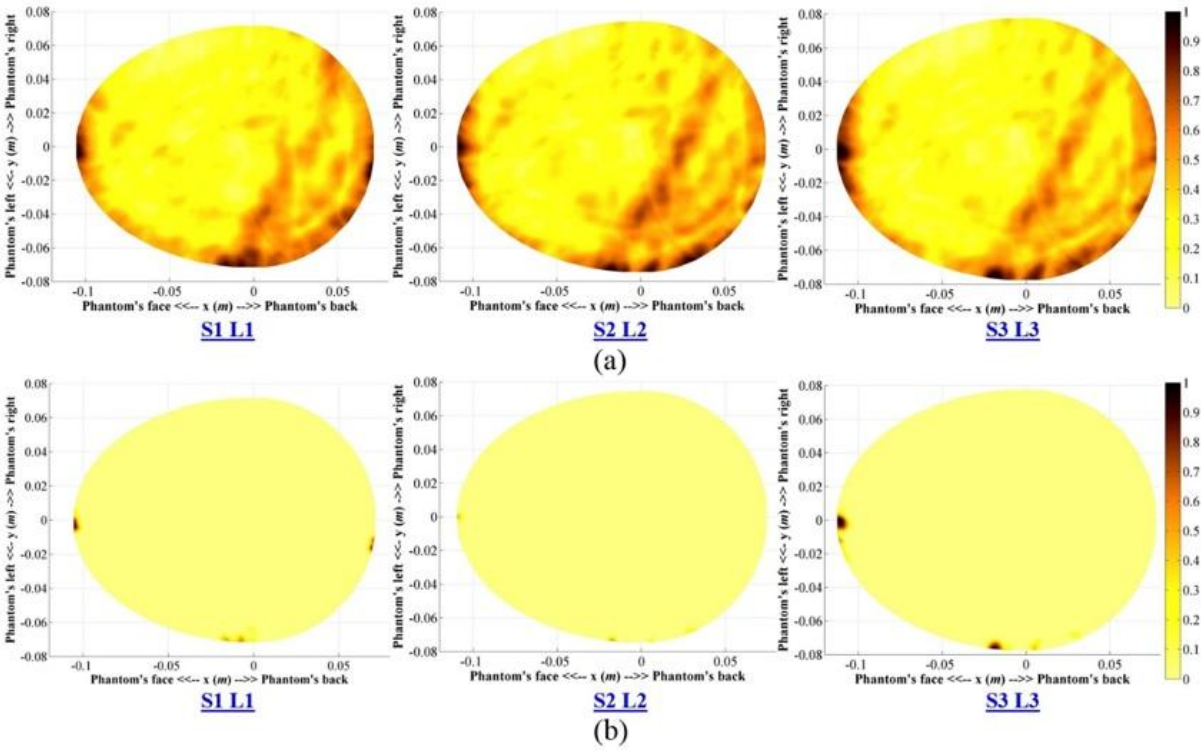

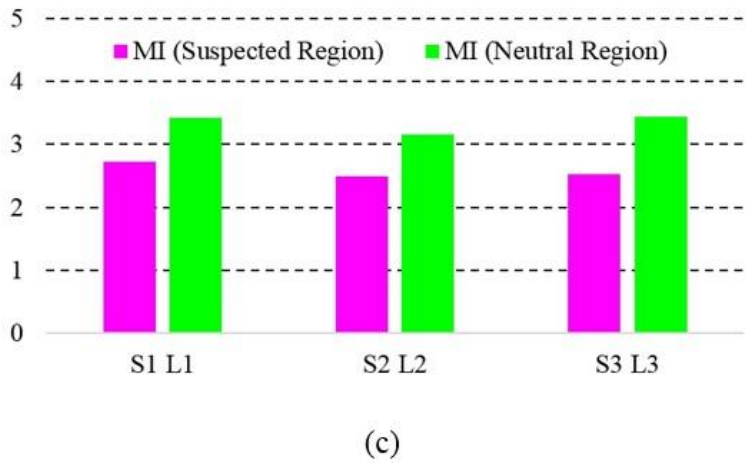

Fig. 6.14 The reconstructed images of three different levels of healthy human volunteer-02 after (a) normalization with respect to individual maximum and minimum of each level, and (b) threshold normalization. (c) The raw maximum intensity values of the suspected and neutral regions at different scanning levels.

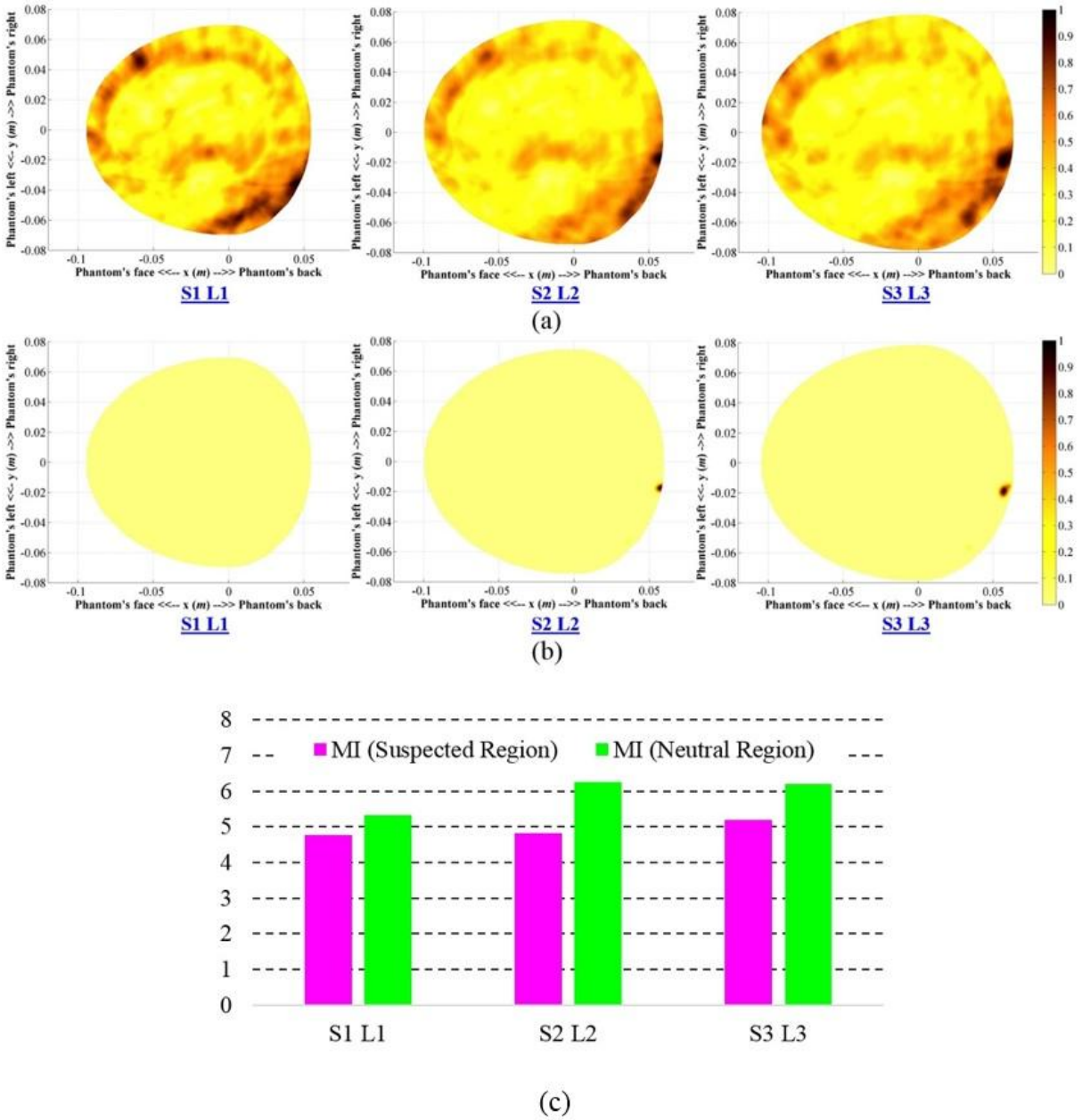

Fig. 6.15 The reconstructed images of three different levels of healthy human volunteer-03 after (a) normalization with respect to individual maximum and minimum of each level, and (b) threshold normalization. (c) The raw maximum intensity values of the suspected and neutral regions at different scanning levels.

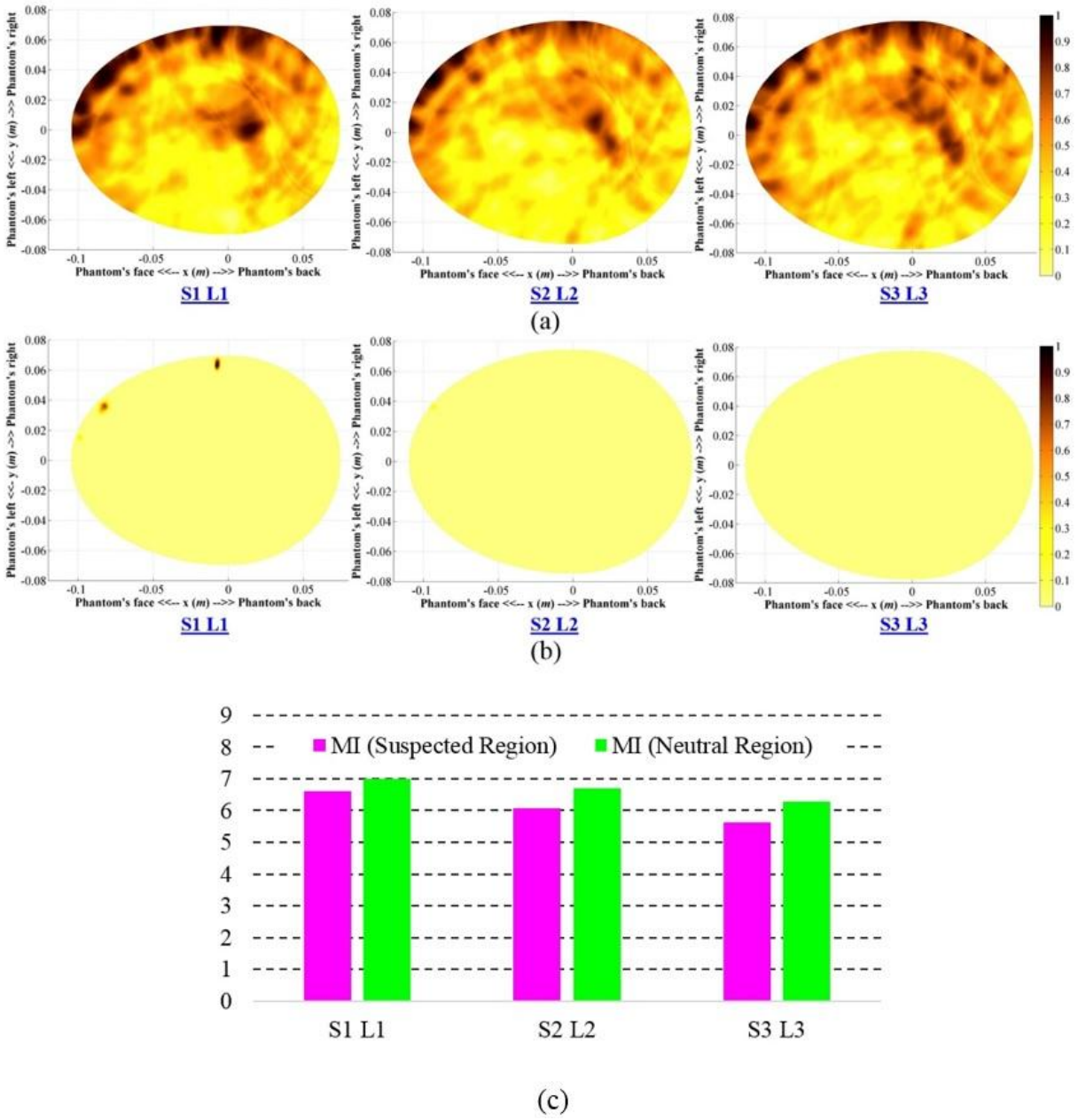

Fig. 6.16 The reconstructed images of three different levels of healthy human volunteer-04 after (a) normalization with respect to individual maximum and minimum of each level, and (b) threshold normalization. (c) The raw maximum intensity values of the suspected and neutral regions at different scanning levels.

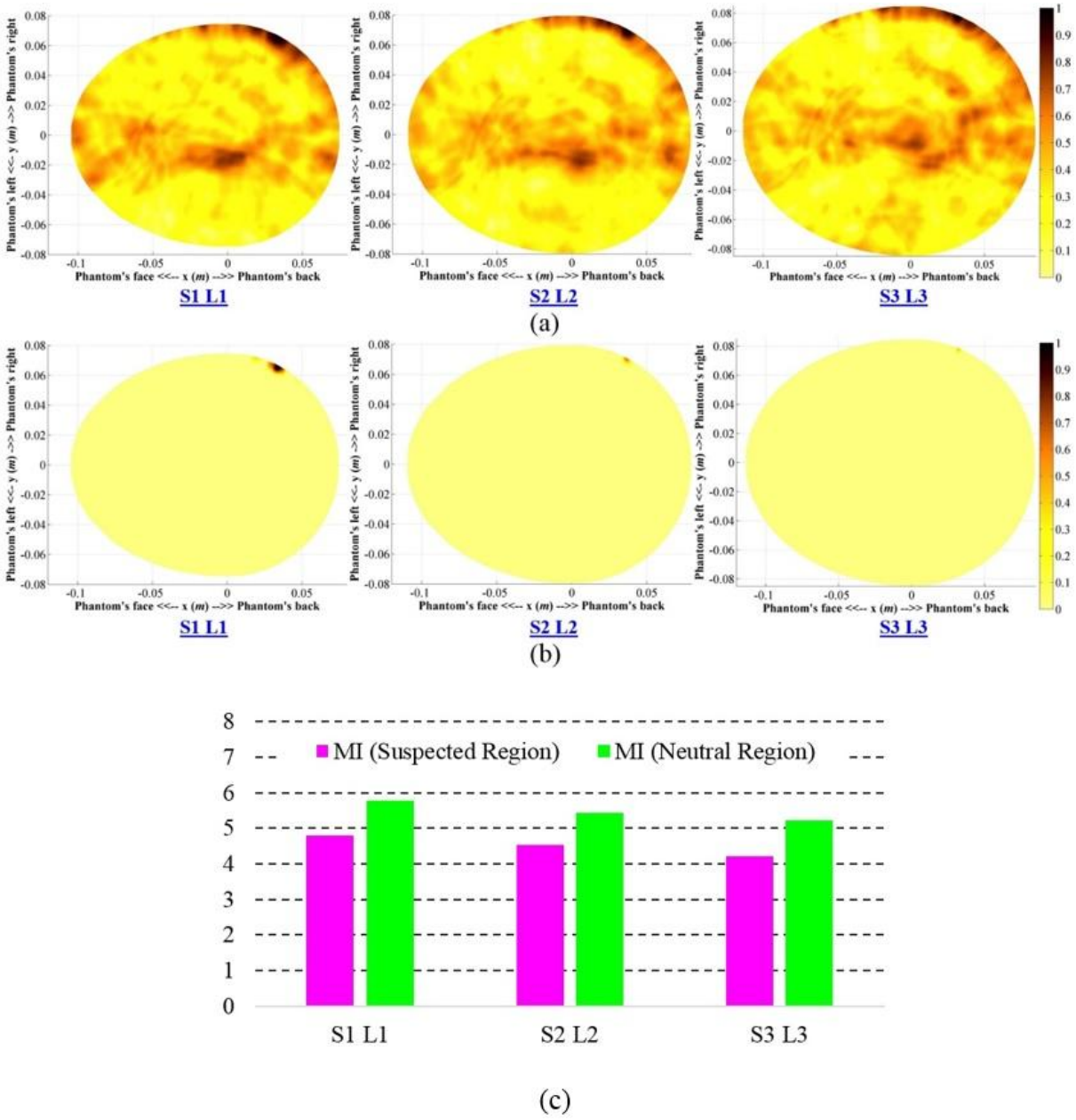

Fig. 6.17 The reconstructed images of three different levels of healthy human volunteer-05 after (a) normalization with respect to individual maximum and minimum of each level, and (b) threshold normalization. (c) The raw maximum intensity values of the suspected and neutral regions at different scanning levels.

6.6 Discussion

A compact and portable multilevel head imaging system prototype operating over the band from 1-2.4 GHz is presented in this section. The head imaging platform that can be adjusted for patient dependent head shapes and sizes, and can be utilized to scan multiple levels of the head. The platform is fabricated using different 3D printed parts. The imaging system consists of an array of compact sensing antennas which are connected to a switching network. A compact microwave transceiver is used for data acquisition. A laptop is used for the data acquisition and post-processing purpose. It takes around 2 seconds for the system to collect data from one scan, while the previous manual scanning system requires 3-4 minutes for data acquisition (Section 5.5). Thus the prototyped system can be used as a portable and fast diagnostic solution for head imaging applications.

In order to satisfy the demands of microwave based head imaging system, an antenna, which is evolved from a typical folded dipole structure, is designed and presented in Section 3.11.2. Both of the near- and far-field radiation performances of the antenna in the time and frequency-domains confirm its potential for head imaging system. The whole system is validated by experimental imaging of various realistic scenarios of healthy and brain injured cases by means of a 3D realistic human head phantom. The acquired data is post-processed and the actual scattering signals are estimated by using a two staged calibration process. A modified DAS based image processing technique relying on a point-of-entry dependent permittivity human head model is utilized to map 2D cross-sections of the head phantom. In order to accumulate the imaging results from multiple different levels, a thresholding is necessary to reduce the incurred imaging noise.

Theoretically, in ideal condition, the two stage subtraction takes care of all reflection and background noise. However, in practice there are several assumptions that might go wrong. Among them is the presumption that all channels have the same characteristics. This assumption can be compromised as the qualities of all connectors, cables and antennas are not exactly the same. Although the first stage of calibration deals with this, in most cases some noise adds up in post-processing. Incorrectness of the assumption that each sensing antenna element is located at a constant distance from the boundary vector and that the skin layer has a uniform thickness can also be another source of noise in post-processing. The noise coherently gets added up at the skin layer. Nevertheless, the permittivity contrast of the internal brain parts also produces scattering signals. However, these scatterings are around 10-20% of the actual ICH target in case of brain injured patient. The thresholding normalization process is very effective in improving the image quality of an unhealthy head as the skin reflection is considered as the minimum threshold signal level. On the other hand, the maximum scattering intensity is selected as the maximum threshold level and it is found that for ICH affected unhealthy head phantoms, maximum scattering is found at the level where ICH target is located. This

phenomenon confirms the numerical results of both time and frequency domain scattering characterizations (Figs. 6.4 to 6.6). However, it is found from the images of the healthy head phantom that the residual skin scattering is the maximum value and thresholding normalization significantly improves the image quality. Compared to the previously reported imaging results (Section 5.5), it can be concluded that the thresholding can attain higher quantitative metrics. Moreover, it is noted that the shallow targets have higher scattering intensities compared to those of the deep targets. Nevertheless, among deep targets, top level located targets yields higher metric values compared to lower level targets. Due to the narrow shape of human head at the top level, the signals have to penetrate less tissue, and are, consequently, confronted by less losses resulting in higher scattering intensities from the ICH target (Fig. 6.7(e)).

The radiation safety of the imaging system is verified and the system is employed in pilot volunteer study. Five different healthy volunteer head images are presented for three different levels and it is observed that the conclusion of the healthy human head phantom are also true for the volunteer data. All the images are found free from false positive responses. This is an important criteria for any medical diagnostic solution.

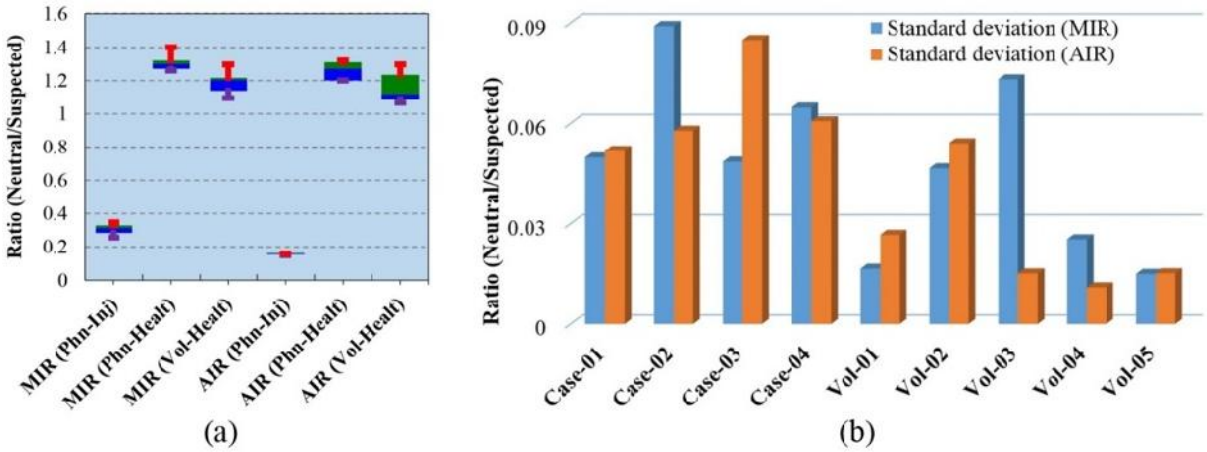

Fig. 6.18 (a) The comparative view of the statistical analyses among the MIR and AIR values of the healthy head phantom and volunteer head, and unhealthy human head phantoms. The green and blue boxes represent the 75th and 25th percentiles respectively and the transitional line between them presents the median. The red and violet lines accordingly states the maximum and minimum magnitudes. (b) The standard deviation results of each individual phantom and volunteer cases in terms of the intensity ratios of neutral and suspected regions.

Extended comparisons between different statistical analyses of the four phantom measurement cases and five volunteer study data are demonstrated in Fig. 6.18. It can be seen that the maximum and average intensity ratios (MIR and AIR) of the healthy scenarios are more than 1. Nevertheless, the

rations are very close to each other, which confirms the imaging similarities between healthy realistic head phantom and volunteer heads as well as among different head sizes and shapes. However, in case of brain injured phantom, medians of MIR and AIR values are around 0.3 and 0.16 respectively indicating huge differences between healthy and unhealthy heads.

The maximum and minimum values of the MIR and AIR are limited up to 15% of the median values. This overall low level of fluctuations indicates the firmness of the image processing algorithm. The standard deviation of MIR and AIR ratios for the individual cases are demonstrated in Fig. 6.18(b). The very low standard deviation values indicate that in case of healthy and unhealthy patients, the MIR and AIR are consistent when compared with different levels of each case.

6.7 Conclusion

This chapter describes the design and developments of compact array based portable head imaging systems. Full wave electromagnetic simulations are performed to verify the safety of the imaging system and the imaging performances are compared between arrays using compact multi-folded 3D antenna (described in Section 3.11.1) and the imaging performances are compared with a miniaturized 3D folded antenna (reported in Section 3.5). It is seen that owing to the small size of the antenna multi-folded 3D antenna performs better in array based wideband microwave imaging systems. A wideband microwave head imaging system with multi-level scanning capabilities is designed and prototyped using 3D printing and custom made nylon parts. The system utilizes a compact multi-folded 3D antenna array and a compact microwave transceiver. The hardware architectures of the prototyped imaging system are described in details. Signal penetration in the head and the hemorrhagic scattering of the target are numerically analyzed from time- and frequency-domain viewpoint, respectively. The wideband head imaging system is applied on the realistic human head phantom and the images are reconstructed by using a threshold normalizing approach. It is seen that the head imaging system is able to locate brain injuries in various 3D positions of human head. The imaging system is found safe from electromagnetic radiation by maintaining SAR values well below the radiation safety limit. The wideband microwave head imaging system is applied on healthy volunteers for performing pilot human tests. The reconstructed images of the healthy volunteers are found to be free from false positive targets. Nevertheless, statistical comparison between the phantom and healthy imaging metrics revel that the values are similar, which indicates that there is a possibility to build a generalized database that can be used as a reference for next generation wideband microwave head imaging that can proceed towards the preclinical trials for diagnosing brain injuries.

Chapter 7 - Conclusions and Future Works

In the previous chapters of this thesis, the performed research works for the design, development and implementation of wideband microwave imaging system for brain injury diagnosis is presented. All conducted research works are directed to fulfil the aims of this thesis that are outlined in Section 1.3 and to overcome the limitations of existing medical imaging systems for brain injury diagnosis as well as to meet the challenges faced by the wideband microwave imaging systems for mentioned in Section 2.3. This chapter summarises the contributions of the research works undertaken in this thesis and suggests some future direction for future investigations.

7.1 Thesis Conclusions

The research work undertaken in this thesis aims to develop a non-ionising, low-cost, compact and mobile wideband microwave imaging system that can be applied to monitor the patient continuously in real time, either at the bedside, in ambulance or emergency room for brain injury diagnosis and in doing so makes multiple contributions to the field of microwave imaging systems.

The background and underlying motivation of this thesis highlights the necessities of for utilizing wideband microwave imaging system for brain injury diagnosis. It is noted that the existing state-of-the-art medical imaging systems and related technologies have several crucial limitations and that wideband microwave imaging have the potential of overcoming these limitations. In the literature most of the systems are studied numerically or with simplified head phantoms. Only handful of head imaging systems are prototyped and tested with realistic head phantom; hence, tiny fraction of them have gone towards the preclinical trials.

A description of the typical wideband microwave imaging system is provided in this thesis along with its advantages and applications. Despite the advantages, wideband microwave imaging systems have to face numerous challenges as the system relies on a diverse range of fields including electromagnetics, signal and image processing, instrumentations, material engineering, software development and so one. In order to make the head-imaging system compact, portable and low-cost which is as well effective in accurately detect the location of brain injury, the system has to meet these challenges.

Design and developments of efficient, compact wideband antennas for microwave imaging systems is very challenging. Antennas are one of the key components of wideband microwave imaging systems as the success of the system depends on these sensing elements. Both omni-directional and directional antennas are initially considered. An antenna miniaturization technique utilizing the plane of symmetry and based on image theory is presented. It is demonstrated that this technique can be

generalized for antennas having both microstrip and co-planar waveguide feeding methods. The operating and radiation mechanism of the miniaturization technique is explained with the help of the characterization mode analysis. A compact omni-directional antenna, utilizing the plane of symmetry, is also introduced afterwards. Furthermore, a folded antenna having directional performance in wide operating frequencies is presented. The plane of symmetry is also applied on it and it is seen that even if the antenna takes half the volume of the previous one, it does not compromise the penetration capability, which is attained by the lowest operating frequency and achieves directional radiation patterns over the wide operating band.

A near-field time-domain characterization technique is proposed in this thesis and it is seen that the directional antennas are more suitable for current application where the antennas mostly operates in near-field. Hence, concentration is given in designing directional antennas for the head imaging systems. A slot-loaded dipole antenna is proposed as a compact solution for directional and wideband operation. It is observed that by different types of feeding and optimization objectives, e.g. antenna profile, operating bandwidth etc. of and this type of antenna has the potential to satisfy the antenna requirements of practical head imaging systems. Afterwards, a cross-feeding technique is presented to be an effective way for correcting the beam-tilting limitation of half-cut antennas. Multi-folding techniques are introduced to reduce the sizes of wideband directional antennas. The design procedures of all antennas are elaborated with supporting theoretical explanations. The antennas are prototyped and performances are verified by both frequency and time-domain analysis for both near and far-field radiations.

Quantitative and explicit validation of the performance and safety of microwave head imaging systems are critical factors of the technological development process. This motivates the developments of realistic human head phantoms as described in the thesis. The previously reported artificial human head phantoms are tabulated in order to understand the utilizations of narrow- and wideband head phantoms in various applications. The types of artificial phantom materials can be classified into four types and each have their own advantages and limitations. The features and functions of different phantom ingredients concludes that semi-solid ATE materials are more suitable for phantom development in microwave head imaging applications. Based on this implication, the development process of a 3D printed realistic human head phantom is demonstrated with the ingredient recipe and step by step depiction of the fabrication procedure with a comparison with the actual tissues and measured electrical properties ATE materials.

The design and development of several single-antenna based wideband microwave head imaging systems for brain injury diagnosis are introduced in this thesis owing to their fast adjustment and calibration facilities, and lower cost. Numerical verification of a preliminary head imaging system by

means of electromagnetic simulation of realistic brain injuries is performed, which is followed by the experimental investigations using two simplified head phantoms. The imaging results attained from both simulation and experiments are found promising. It is noted that in the literature, there are numerous directional and omni-directional antennas reported, but there is no conclusive evidence in the literature to conclude the superiority of one type over another. Hence, the comparative imaging performance of directional and omni-directional antennas for head imaging system is also presented with relative quantitative analyses between the reconstructed images. It can be concluded that directional antenna provides better imaging performance compared to those of omni-directional antenna.

A portable head imaging system based on one transceiver antenna is introduced with the verification on a realistic human head phantom. It is seen that the imaging performance of the portable head imaging system can be significantly improved by using a back-projection algorithm with a model of effective head permittivity. The efficacy of the system along with the imaging algorithm is verified in both simulations and experiments by using realistic numerical head models and 3D printed head phantoms. Nevertheless, results from a pilot human test is also presented and it is found that the head imaging system is safe from electromagnetic radiation and burns pertaining temperature increase, even with long-time exposure when used as a monitoring system. It is to be noted that both frequency domain and time domain based head imaging systems have their merits and demerits over one another. This thesis only considers pulse based time domain imaging. Thus, no conclusion can be drawn to compare between them.

A compact head imaging system with automated scanning capabilities is also presented. It is observed that imaging improvements can be achieved when the surface waves are considered in image reconstruction. The automated scanning system is able to reliably image the interior of human head and it is found that the system is safe from electromagnetic radiation. Moreover, a detection and differentiation system of brain injury types in brain stroke scenario is presented and numerically verified by using spherical and elliptical cylindrical stroke targets inside human head.

A compact array based portable head imaging system is presented. Full wave electromagnetic simulations are performed to verify the safety of the imaging system and the imaging performances are compared between arrays using a compact multi-folded 3D antenna and the imaging performances are compared with a miniaturized 3D folded antenna. It is seen that owing to the small size of the antenna multi-folded 3D antenna performs better in array based wideband microwave imaging systems. A wideband microwave head imaging system with multi-level scanning capabilities is designed and prototyped using 3D printing and custom made nylon parts. The system utilizes a

compact multi-folded 3D antenna array and a compact microwave transceiver. The estimated cost of the system including the receiver is around $15k Australian Dollars, including the receiver.

It is true that the resolution of an imaging environment depends on the bandwidth of the emitted signal from the antenna. However, this definition considers free space as the transmitting medium, where losses are not significant compared to the dynamic range of the system. However, in case of microwave imaging, the transmission and reception vitally depend on the penetration depth in lossy human head tissues. Increasing the bandwidth by extending its the higher frequencies, therefore, is not very helpful, especially the frequencies beyond 2.5 GHz are unable to penetrate through a major part the head. Thus the imaging performance cannot be reliably improved by such increase in bandwidth. As seen from the simulations of Section 6.3, increasing the dynamic range might be a solution regarding the utilization of higher frequencies. However, such systems require quixotic dynamic ranges (>150 dB) for proper reception which eventually makes the system expensive while the overall imaging performance is not significant.

As explained in the measurement procedures of different systems in Chapter 5, that the antennas operate in free space (air) in proximity to human head phantoms and the imaging algorithm post-processes the change in antenna performance with and without the presence of the head phantom by multiple measurements and calibration processes and maps the intensity of scattering from the interior of the head. Thus it is the imaging algorithm which demand such an antenna which operates in free space and changes its performance in presence of the head phantom. However, in case of other imaging algorithm that requires the antenna to operate only in close proximity of human head, optimization is required. Nevertheless, as seen from Fig. 6.2(b), the optimization might not be even necessary, as some designed antennas are still able to operate with good impedance matching in presence of head phantom, although the matching is slightly as they are optimized for free space (air).

The hardware architectures of the prototyped imaging system are described in details. Signal penetration in the head and the hemorrhagic scattering of the target are numerically analyzed from time- and frequency-domain viewpoint, respectively. The wideband head imaging system is applied on the realistic human head phantom and the images are reconstructed by using a threshold normalizing approach. It is seen that the head imaging system is able to locate brain injuries in various 3D positions of human head. The imaging system is found safe from electromagnetic radiation by maintaining SAR values well below the radiation safety limit. The wideband microwave head imaging system is applied on healthy volunteers for performing pilot human tests. The reconstructed images of the healthy volunteers are found to be free from false positive targets. Nevertheless, statistical comparison between the phantom and healthy imaging metrics revel that the values are similar, which indicates that there is a possibility to build a generalized database that can be used as

a reference for next generation wideband microwave head imaging that can proceed towards the preclinical trials for diagnosing brain injuries.

7.2 Suggestions for Future Works

Although the research works performed in this thesis successfully solved a number of important challenges in designing an efficient microwave imaging system, some suggested works can be recommended to further improve the design and efficiency of the preclinical wideband microwave head imaging platform:

1. Classification among different types of brain injuries, for instance, different types of strokes (hemorrhagic and ischemic stroke) is a challenge and can be considered as a future work of this research. Along with the detection and localization of brain injuries, classification is vital, because at early stages, the time when the medication is crucial, patients of both strokes exhibit similar physical symptoms, but the treatments are vastly different and Wrong medical analysis is fatal for the stroke affected patient. However, intensive research and experimental validation is required in differentiating between the types of strokes.
2. Array of reconfigurable antennas can be used to horizontally and vertically scan human head instead of using an array of independent antennas with vertical movement. Extensive research needs to be performed on reconfigurable antennas that are capable to operate in wide bandwidth facilitating directional radiation toward the imaged human head. Additionally, utilizing the reconfigurable antennas, it is possible to increase the number of readings from around the head, which significantly improves the imaging performances.
3. The antennas designed in this thesis are rigid in nature. Flexible and lightweight substrates can be used to design antennas that can be mounted directly on head. However, owing to the limitations of typical flexible substrates it is challenging to design compact structures. Hence, further research on flexible substrates and techniques are required to design wideband compact designs with unidirectional radiation.

References

1. Zasler, N.D., et al., *Brain injury medicine: principles and practice*. 2012: Demos Medical Publishing.
2. Naidech, A.M., *Intracranial hemorrhage.* American Journal of Respiratory and Critical Care Medicine, 2011. **184**(9): p. 998-1006.
3. Coronado, V.G., et al., *Surveillance for traumatic brain injury-related deaths--United States, 1997-2007.* MMWR Surveill Summ, 2011. **60**(5): p. 1-32.
4. Khan, F., I.J. Baguley, and I.D. Cameron, *4: Rehabilitation after traumatic brain injury.* Med J Aust, 2003. **178**(6): p. 290-5.
5. Raghupathi, R., *Cell death mechanisms following traumatic brain injury.* Brain Pathol, 2004. **14**(2): p. 215-22.
6. Luchtmann, M., et al., *Gadolinium-enhanced magnetic resonance angiography in brain death.* Sci Rep, 2014. **4**: p. 3659.
7. Qureshi, A.I., A.D. Mendelow, and D.F. Hanley, *Intracerebral haemorrhage.* Lancet, 2009. **373**(9675): p. 1632-44.
8. Subcommittee, S.S., *AHA statistical update.* Circulation, 2007. **115**: p. e69-e171.
9. Economics, D.A., *The economic impact of stroke in Australia.* Canberra: Access Economics, 2013.
10. Wang, J. and S. Dore, *Inflammation after intracerebral hemorrhage.* J Cereb Blood Flow Metab, 2007. **27**(5): p. 894-908.
11. Baber, U., I. Mastoris, and R. Mehran, *Balancing ischaemia and bleeding risks with novel oral anticoagulants.* Nat Rev Cardiol, 2014. **11**(12): p. 693-703.
12. Palmer, P., G. Hanson, and J. Honeyman-Buck, *Diagnostic imaging in the community: a manual for clinics and small hospitals: Pan-American Health Organization World Health Organization*.
13. Ireland, D. and M. Bialkowski. *Feasibility study on microwave stroke detection using a realistic phantom and the FDTD method*. in *Asia-Pacific Microwave Conference 2010*. 2010. IEEE (Institute for Electrical and Electronic Engineers).
14. Jalilvand, M., et al., *Quantitative imaging of numerically realistic human head model using microwave tomography.* Electronics Letters, 2014. **50**(4): p. 255-256.
15. Ireland, D., K. Bialkowski, and A. Abbosh, *Microwave imaging for brain stroke detection using Born iterative method.* IET Microwaves, Antennas & Propagation, 2013. **7**(11): p. 909-915.
16. Sill, J.M. and E.C. Fear, *Tissue sensing adaptive radar for breast cancer detection-experimental investigation of simple tumor models.* Microwave Theory and Techniques, IEEE Transactions on, 2005. **53**(11): p. 3312-3319.
17. Santorelli, A., et al., *A time-domain microwave system for breast cancer detection using a flexible circuit board.* Instrumentation and Measurement, IEEE Transactions on, 2015. **64**(11): p. 2986-2994.
18. Burfeindt, M.J., et al., *MRI-derived 3-D-printed breast phantom for microwave breast imaging validation.* Antennas and Wireless Propagation Letters, IEEE, 2012. **11**: p. 1610-1613.
19. Nikolova, N., *Microwave imaging for breast cancer.* IEEE Microwave Magazine, 2011. **7**(12): p. 78-94.
20. Mohammed, B.J., et al., *Microwave system for head imaging.* Instrumentation and Measurement, IEEE Transactions on, 2014. **63**(1): p. 117-123.
21. Mustafa, S., B. Mohammed, and A. Abbosh, *Novel preprocessing techniques for accurate microwave imaging of human brain.* Antennas and Wireless Propagation Letters, IEEE, 2013. **12**: p. 460-463.

22. Merino, J.G. and S. Warach, *Imaging of acute stroke.* Nat Rev Neurol, 2010. **6**(10): p. 560-71.
23. deCharms, R.C., *Applications of real-time fMRI.* Nat Rev Neurosci, 2008. **9**(9): p. 720-9.
24. Kidwell, C.S., et al., *Comparison of MRI and CT for detection of acute intracerebral hemorrhage.* JAMA, 2004. **292**(15): p. 1823-30.
25. Pearce, M.S., et al., *Radiation exposure from CT scans in childhood and subsequent risk of leukaemia and brain tumours: a retrospective cohort study.* The Lancet, 2012. **380**(9840): p. 499-505.
26. Mathews, J.D., et al., *Cancer risk in 680 000 people exposed to computed tomography scans in childhood or adolescence: data linkage study of 11 million Australians.* BMj, 2013. **346**.
27. Granot, Y., A. Ivorra, and B. Rubinsky, *A new concept for medical imaging centered on cellular phone technology.* PLoS One, 2008. **3**(4): p. e2075.
28. Zhang, Z., et al., *Intracerebral hemorrhage (ICH) evaluation with a novel magnetic induction sensor: a preliminary study using the Chinese head model.* Bio-medical materials and engineering, 2014. **24**(6): p. 3579-3587.
29. Barai, A., et al., *Magnetic induction spectroscopy: non-contact measurement of the electrical conductivity spectra of biological samples.* Measurement Science and Technology, 2012. **23**(8): p. 085501.
30. Xu, L., et al. *Study of PSSMI for cerebral hemorrhage detection: an experimental simulation*. in *Image and Signal Processing (CISP), 2011 4th International Congress on*. 2011. IEEE.
31. Pastorino, M., *Microwave imaging*. Vol. 208. 2010: John Wiley & Sons.
32. Semenov, S., *Microwave tomography: review of the progress towards clinical applications.* Philosophical Transactions of the Royal Society of London A: Mathematical, Physical and Engineering Sciences, 2009. **367**(1900): p. 3021-3042.
33. Persson, M., et al., *Microwave-based stroke diagnosis making global prehospital thrombolytic treatment possible.* Biomedical Engineering, IEEE Transactions on, 2014. **61**(11): p. 2806-2817.
34. Zhang, H., et al. *Microwave imaging for brain tumour detection using an UWB Vivaldi Antenna array*. in *Antennas and Propagation Conference (LAPC), 2012 Loughborough*. 2012. IEEE.
35. Mobashsher, A.T. and A. Abbosh, *Development of compact directional antenna utilising plane of symmetry for wideband brain stroke detection systems.* Electronics Letters, 2014. **50**(12): p. 850-+.
36. Semenov, S.Y. and D.R. Corfield, *Microwave tomography for brain imaging: Feasibility assessment for stroke detection.* International Journal of Antennas and Propagation, 2008. **2008**.
37. Fhager, A., P. Hashemzadeh, and M. Persson, *Reconstruction quality and spectral content of an electromagnetic time-domain inversion algorithm.* Biomedical Engineering, IEEE Transactions on, 2006. **53**(8): p. 1594-1604.
38. Semenov, S. *Electromagnetic sensing and imaging for medical applications*. in *Antenna Measurements & Applications (CAMA), 2014 IEEE Conference on*. 2014. IEEE.
39. Semenov, S., et al. *Electromagnetic tomography for brain imaging: Initial assessment for stroke detection*. in *Biomedical Circuits and Systems Conference (BioCAS), 2015 IEEE*. 2015. IEEE.
40. Semenov, S., et al. *Electromagnetic tomography for brain imaging: From virtual to human brain*. in *Antenna Measurements & Applications (CAMA), 2014 IEEE Conference on*. 2014. IEEE.
41. Ireland, D. and A. Abbosh, *Modeling human head at microwave frequencies using optimized Debye models and FDTD method.* Ieee Transactions on Antennas and Propagation, 2013. **61**(4): p. 2352-2355.
42. Jalilvand, M., et al. *UWB synthetic aperture-based radar system for hemorrhagic head-stroke detection*. in *Radar Conference (RADAR), 2011 IEEE*. 2011. IEEE.

43. Marimuthu, J., K. Bialkowski, and A. Abbosh. *Stepped frequency continuous wave software defined radar for medical imaging*. in *Antennas and Propagation Society International Symposium (APSURSI), 2014 IEEE*. 2014. IEEE.
44. Mustafa, S., A.M. Abbosh, and P.T. Nguyen, *Modeling human head tissues using fourth-order debye model in convolution-based three-dimensional finite-difference time-domain.* Antennas and Propagation, IEEE Transactions on, 2014. **62**(3): p. 1354-1361.
45. Mobashsher, A.T. and A.M. Abbosh, *Artificial human phantoms: human proxy in testing microwave apparatuses that have electromagnetic interaction with the human body.* Microwave Magazine, IEEE, 2015. **16**(6): p. 42-62.
46. Marimuthu, J., K. Bialkowski, and A. Abbosh. *Reconfigurable software defined radar for medical imaging*. in *Microwave Symposium (AMS), 2014 1st Australian*. 2014. IEEE.
47. Marimuthu, J., K.S. Bialkowski, and A.M. Abbosh, *Software-defined radar for medical imaging.* Microwave Theory and Techniques, IEEE Transactions on, 2016. **PP**(99): p. 1-10.
48. Bialkowski, M., et al. *Ultra-wideband array antenna system for breast imaging*. in *Microwave Conference Proceedings (APMC), 2010 Asia-Pacific*. 2010. IEEE.
49. Ireland, D. and M.E. Bialkowski, *Microwave head imaging for stroke detection.* Progress In Electromagnetics Research M, 2011. **21**: p. 163-175.
50. Karanasiou, I., N. Uzunoglu, and A. Garetsos, *Electromagnetic analysis of a non-invasive 3D passive microwave imaging system-Abstract.* Journal of electromagnetic waves and applications, 2004. **18**(3): p. 379-380.
51. Durney, C.H., H. Massoudi, and M.F. Iskander, *Radiofrequency radiation dosimetry handbook*. 1986, DTIC Document.
52. Scapaticci, R., et al., *A feasibility study on microwave imaging for brain stroke monitoring.* Progress In Electromagnetics Research B, 2012. **40**: p. 305-324.
53. Abtahi, S., J. Yang, and S. Kidborg, *A new compact multiband antenna for stroke diagnosis system over 0.5–3 GHz.* Microwave and Optical Technology Letters, 2012. **54**(10): p. 2342-2346.
54. Mohammed, B., A. Abbosh, and D. Ireland. *Stroke detection based on variations in reflection coefficients of wideband antennas*. in *Antennas and Propagation Society International Symposium (APSURSI), 2012 IEEE*. 2012. IEEE.
55. Semenov, S.Y. and D.R. Corfield, *Microwave tomography for brain imaging: Feasibility assessment for stroke detection.* International Journal of Antennas and Propagation, 2008.
56. Al-Joumayly, M.A., et al., *Dual-band miniaturized patch antennas for microwave breast imaging.* Ieee Antennas and Wireless Propagation Letters, 2010. **9**: p. 268-271.
57. Li, X., et al., *A compact double-layer on-body matched bowtie antenna for medical diagnosis.* Antennas and Propagation, IEEE Transactions on, 2014. **62**(4): p. 1808-1816.
58. Mobashsher, A.T., A.M. Abbosh, and Y.F. Wang, *Microwave system to detect traumatic brain injuries using compact unidirectional antenna and wideband transceiver with verification on realistic head phantom.* Ieee Transactions on Microwave Theory and Techniques, 2014. **62**(9): p. 1826-1836.
59. Stohr, W., *Broadband ellipsoidal dipole antenna*. 1968, Google Patents.
60. Thomas, M. and R.I. Wolfson, *Wideband arrayable planar radiator*. 1994, Google Patents.
61. Abbosh, A., *Ultra-wideband quasi-yagi antenna using dual-resonant driver and integrated balun of stepped impedance coupled structure.* Ieee Transactions on Antennas and Propagation, 2013. **61**(7): p. 3885-3888.
62. Mobashsher, A.T. and A.M. Abbosh, *Wideband unidirectional antenna for head imaging system.* 2013 Ieee Antennas and Propagation Society International Symposium (Apsursi), 2013: p. 674-675.
63. Cappelletti, G., et al., *A low-profile printed drop-shaped dipole antenna for wide-band wireless applications.* Ieee Transactions on Antennas and Propagation, 2011. **59**(10): p. 3526-3535.

64. Mobashsher, A.T. and A. Abbosh, *Slot-loaded folded dipole antenna with wideband and unidirectional performance for L-band applications.* Ieee Antennas and Wireless Propagation Letters, 2014. **13**: p. 798-801.
65. Mobashsher, A.T. and A. Abbosh, *CPW-fed low-profile directional antenna operating in low microwave band for wideband medical diagnostic systems.* Electronics Letters, 2014. **50**(4): p. 246-247.
66. Mobashsher, A.T. and A. Abbosh, *Three- dimensional folded antenna with ultra- wideband performance, directional radiation and compact size.* Iet Microwaves Antennas & Propagation, 2014. **8**(3): p. 171-179.
67. Chen, K.R., C.Y.D. Sim, and J.S. Row, *A compact monopole antenna for super wideband applications.* Ieee Antennas and Wireless Propagation Letters, 2011. **10**: p. 488-491.
68. Radiom, S., et al., *Optimised small-size tapered monopole antenna for pulsed ultra-wideband applications designed by a genetic algorithm.* Iet Microwaves Antennas & Propagation, 2009. **3**(4): p. 663-672.
69. Zaker, R. and A. Abdipour, *A very compact ultrawideband printed omnidirectional monopole antenna.* Antennas and Wireless Propagation Letters, IEEE, 2010. **9**: p. 471-473.
70. Pourahmadazar, J., C. Ghobadi, and J. Nourinia, *Novel modified pythagorean tree fractal monopole antennas for UWB applications.* Antennas and Wireless Propagation Letters, IEEE, 2011. **10**: p. 484-487.
71. Azim, R., M.T. Islam, and A.T. Mobashsher, *Design of a dual band-notch UWB slot antenna by means of simple parasitic slits.* Antennas and Wireless Propagation Letters, IEEE, 2013. **12**: p. 1412-1415.
72. Mobashsher, A.T. and M.T. Islam, *Design, investigation and measurement of a compact ultra wideband antenna for portable applications.* Measurement Science Review, 2013. **13**(4): p. 169-176.
73. Denidni, T. and Z. Weng, *Hybrid ultrawideband dielectric resonator antenna and band-notched designs.* IET microwaves, antennas & propagation, 2011. **5**(4): p. 450-458.
74. Thomas, P., et al., *Compact planar ultra-wideband bevelled monopole for portable UWB systems.* Electronics letters, 2011. **47**(20): p. 1112-1114.
75. Lin, C.-C., P. Jin, and R.W. Ziolkowski, *Single, dual and tri-band-notched ultrawideband (UWB) antennas using capacitively loaded loop (CLL) resonators.* Antennas and Propagation, IEEE Transactions on, 2012. **60**(1): p. 102-109.
76. Koohestani, M., M. Moghadasi, and B. Virdee, *Miniature microstrip-fed ultra-wideband printed monopole antenna with a partial ground plane structure.* Microwaves, Antennas & Propagation, IET, 2011. **5**(14): p. 1683-1689.
77. Azim, R., M.T. Islam, and A.T. Mobashsher, *Dual band-notch UWB antenna with single tri-arm resonator.* Antennas and Wireless Propagation Letters, IEEE, 2014. **13**: p. 670-673.
78. Li, T., et al., *Compact UWB band-notched antenna design using interdigital capacitance loading loop resonator.* Antennas and Wireless Propagation Letters, IEEE, 2012. **11**: p. 724-727.
79. Azim, R., A.T. Mobashsher, and M.T. Islam, *UWB antenna with notched band at 5.5 GHz.* Electronics Letters, 2013. **49**(15): p. 922-923.
80. Azim, R., A.T. Mobashsher, and M.T. Islam, *UWB antenna with notched band at 5.5 GHz.* Electronics Letters, 2013. **49**(15): p. 922-924.
81. Radiom, S., et al., *An effective technique for symmetric planar monopole antenna miniaturization.* Ieee Transactions on Antennas and Propagation, 2009. **57**(10): p. 2989-2996.
82. Liu, W.J. and Q.X. Chu, *Half-cut disc UWB antenna with tapered CPW structure for USB application.* Microwave and Optical Technology Letters, 2010. **52**(6): p. 1380-1384.
83. Prakoso, T., et al. *An evaluation of half-cut technique for microwave-photonic access-point antenna miniaturization*. in *2011 IEEE International RF & Microwave Conference*. 2011.

84. Mobashsher, A.T. and R.W. Aldhaheri, *An improved uniplanar front-directional antenna for dual-band RFID readers.* Antennas and Wireless Propagation Letters, IEEE, 2012. **11**: p. 1438-1441.
85. Bourqui, J., M. Okoniewski, and E.C. Fear, *Balanced antipodal vivaldi antenna with dielectric director for near-field microwave imaging.* Ieee Transactions on Antennas and Propagation, 2010. **58**(7): p. 2318-2326.
86. Xu, Z.W., J. Wu, and Z.S. Wu, *Potential effects of the ionosphere on space-based SAR imaging.* Ieee Transactions on Antennas and Propagation, 2008. **56**(7): p. 1968-1975.
87. Wu, Q., et al., *On the performance of printed dipole antenna with novel composite corrugated-reflectors for low-profile ultrawideband applications.* Ieee Transactions on Antennas and Propagation, 2010. **58**(12): p. 3839-3846.
88. Wang, S.R., Q. Wu, and D.L. Su, *A novel reversed t-match antenna with compact size and low profile for ultrawideband applications.* Ieee Transactions on Antennas and Propagation, 2012. **60**(10): p. 4933-4937.
89. Qu, S.W., et al., *Wideband and unidirectional cavity-backed folded triangular bowtie antenna.* Ieee Transactions on Antennas and Propagation, 2009. **57**(4): p. 1259-1263.
90. Ito, Y., et al., *Unidirectional UWB array antenna using leaf-shaped bowtie elements and flat reflector.* Electronics Letters, 2008. **44**(1): p. 9-10.
91. Azad, M.Z. and M. Ali, *Novel wideband directional dipole antenna on a mushroom like EBG structure.* Ieee Transactions on Antennas and Propagation, 2008. **56**(5): p. 1242-1250.
92. Mobashsher, A.T., N. Misran, and M.T. Islam. *Design analysis of compact dual-band microstrip RFID reader antenna*. in *Space Science and Communication, 2009. IconSpace 2009. International Conference on*. 2009. IEEE.
93. Sabet, K.F., et al., *Compact wireless antennas using an artificial dielectric lens.* 2002 Ieee Aerospace Conference Proceedings, Vols 1-7, 2002: p. 931-938.
94. Kang, C.H., S.J. Wu, and J.H. Tarng, *A novel folded UWB antenna for wireless body area network.* Ieee Transactions on Antennas and Propagation, 2012. **60**(2): p. 1139-1142.
95. Wu, B.Q. and K.M. Luk, *A UWB unidirectional antenna with dual-polarization.* Ieee Transactions on Antennas and Propagation, 2011. **59**(11): p. 4033-4040.
96. Elsherbini, A. and K. Sarabandi, *Dual-polarized coupled sectorial loop antennas for UWB applications.* Ieee Antennas and Wireless Propagation Letters, 2011. **10**: p. 75-78.
97. Qing, X.M. and Z.N. Chen, *A miniaturized directional UWB antenna.* 2011 Ieee International Symposium on Antennas and Propagation (Apsursi), 2011: p. 1470-1473.
98. Yang, J. and A. Kishk, *A novel low-profile compact directional ultra-wideband antenna: The self-grounded bow-tie antenna.* Ieee Transactions on Antennas and Propagation, 2012. **60**(3): p. 1214-1220.
99. Wait, J., *Complex image theory-revisited.* IEEE Antennas and Propagation Magazine, 1991. **4**(33): p. 27-29.
100. Balanis, C.A., *Antenna theory: analysis and design*. Vol. 1. 2005: John Wiley & Sons.
101. Kluskens, M.S. and E.H. Newman, *Image theory for chiral bodies.* Antennas and Propagation, IEEE Transactions on, 1991. **39**(5): p. 676-677.
102. Harrington, R.F. and J.R. Mautz, *Theory of characteristic modes for conducting bodies.* Antennas and Propagation, IEEE Transactions on, 1971. **19**(5): p. 622-628.
103. Cabedo-Fabres, M., et al., *The theory of characteristic modes revisited: A contribution to the design of antennas for modern applications.* Ieee Antennas and Propagation Magazine, 2007. **49**(5): p. 52-68.
104. Wu, W.X. and Y.P. Zhang, *Analysis of ultra-wideband printed planar quasi-monopole antennas using the theory of characteristic modes.* Ieee Antennas and Propagation Magazine, 2010. **52**(6): p. 67-77.
105. Hazdra, P. and P. Hamouz, *On the modal superposition lying under the MoM matrix equations.* Radioengineering, 2008. **17**(3): p. 42-46.

106. Capek, M., et al., *A method for tracking characteristic numbers and vectors.* Progress In Electromagnetics Research B, 2011. **33**: p. 115-134.
107. Li, H., et al., *Characteristic mode based tradeoff analysis of antenna-chassis interactions for multiple antenna terminals.* Ieee Transactions on Antennas and Propagation, 2012. **60**(2): p. 490-502.
108. Garbacz, R.J. and R.H. Turpin, *A generalized expansion for radiated and scattered fields.* Antennas and Propagation, IEEE Transactions on, 1971. **19**(3): p. 348-358.
109. Chen, Y. and C.-F. Wang. *Synthesis of platform integrated antennas for reconfigurable radiation patterns using the theory of characteristic modes*. in *Antennas, Propagation & EM Theory (ISAPE), 2012 10th International Symposium on*. 2012. IEEE.
110. Gautam, A.K., S. Yadav, and B.K. Kanaujia, *A CPW-fed compact UWB microstrip antenna.* Antennas and Wireless Propagation Letters, IEEE, 2013. **12**: p. 151-154.
111. Qu, S.-W. and C.-L. Ruan, *Effect of round corners on bowtie antennas.* Progress In Electromagnetics Research, 2006. **57**: p. 179-195.
112. Antoniades, M. and G.V. Eleftheriades, *Multiband compact printed dipole antennas using NRI-TL metamaterial loading.* Antennas and Propagation, IEEE Transactions on, 2012. **60**(12): p. 5613-5626.
113. Schantz, H.G., *Apparatus for establishing signal coupling between a signal line and an antenna structure*. 2003, Google Patents.
114. Mobashsher, A.T., M.T. Islam, and R. Azim, *A compact shorted wall patch antenna for dual band operation.* Trends in Applied Research, 2011. **6**(9): p. 1071-1077.
115. Elsherbini, A. and K. Sarabandi, *ENVELOP antenna: a class of very low profile UWB directive antennas for radar and communication diversity applications.* Antennas and Propagation, IEEE Transactions on, 2013. **61**(3): p. 1055-1062.
116. Wu, B. and K.-M. Luk, *A UWB unidirectional antenna with dual-polarization.* Antennas and Propagation, IEEE Transactions on, 2011. **59**(11): p. 4033-4040.
117. Yang, J. and A. Kishk, *A novel low-profile compact directional ultra-wideband antenna: the self-grounded Bow-Tie antenna.* Antennas and Propagation, IEEE Transactions on, 2012. **60**(3): p. 1214-1220.
118. Elsherbini, A. and K. Sarabandi, *Compact directive ultra-wideband rectangular waveguide based antenna for radar and communication applications.* Antennas and Propagation, IEEE Transactions on, 2012. **60**(5): p. 2203-2209.
119. Li, Y.-T., et al., *A unidirectional cylindrical conformal monopole antenna designed for impulse radar system.* Antennas and Wireless Propagation Letters, IEEE, 2011. **10**: p. 1397-1400.
120. IEEE Standards Coordinating Committee 28, o.N.-I.R.H., *IEEE standard for safety levels with respect to human exposure to radio frequency electromagnetic fields, 3khz to 300 ghz*. 1992: Institute of Electrical and Electonics Engineers, Incorporated.
121. Quintero, G., J.-F. Zurcher, and A.K. Skrivervik, *System fidelity factor: A new method for comparing UWB antennas.* Antennas and Propagation, IEEE Transactions on, 2011. **59**(7): p. 2502-2512.
122. Sörgel, W. and W. Wiesbeck, *Influence of the antennas on the ultra-wideband transmission.* Eurasip journal on applied signal processing, 2005. **2005**: p. 296-305.
123. Pancera, E., T. Zwick, and W. Wiesbeck, *Spherical fidelity patterns of UWB antennas.* Antennas and Propagation, IEEE Transactions on, 2011. **59**(6): p. 2111-2119.
124. Koohestani, M., et al., *A novel, low-profile, vertically-polarized UWB antenna for WBAN.* Antennas and Propagation, IEEE Transactions on, 2014. **62**(4): p. 1888-1894.
125. Pramanick, P. and P. Bhartia, *Computer-aided design models for millimeter-wave finlines and suspended-substrate microstrip lines.* Microwave Theory and Techniques, IEEE Transactions on, 1985. **33**(12): p. 1429-1435.
126. Klemm, M., et al., *Novel small-size directional antenna for UWB WBAN/WPAN applications.* Antennas and Propagation, IEEE Transactions on, 2005. **53**(12): p. 3884-3896.

127. Zhou, S.-G., *Low-profile and wideband antenna.* Antennas and Wireless Propagation Letters, IEEE, 2011. **10**: p. 373-376.
128. Bukhari, H. and K. Sarabandi, *Ultra-wideband printed slot antenna with graded index superstrate.* Antennas and Propagation, IEEE Transactions on, 2013. **61**(10): p. 5278-5282.
129. Mobashsher, A.T., et al. *Detection and differentiation of brain strokes by comparing the reflection phases with wideband unidirectional antennas*. in *Electromagnetics in Advanced Applications (ICEAA), 2013 International Conference on*. 2013. IEEE.
130. Mobashsher, A.T., et al. *Ultra wideband antenna for portable brain stroke diagnostic system*. in *Microwave Workshop Series on RF and Wireless Technologies for Biomedical and Healthcare Applications (IMWS-BIO), 2013 IEEE MTT-S International*. 2013. IEEE.
131. Mobashsher, A.T. and A. Abbosh, *Utilizing symmetry of planar ultrawideband antennas for size reduction and enhanced performance.* Ieee Antennas and Propagation Magazine, 2015. **57**(2): p. 153-166.
132. Sievenpiper, D.F., et al., *Experimental validation of performance limits and design guidelines for small antennas.* Antennas and Propagation, IEEE Transactions on, 2012. **60**(1): p. 8-19.
133. Yaghjian, A.D. and S.R. Best, *Impedance, bandwidth, and Q of antennas.* Antennas and Propagation, IEEE Transactions on, 2005. **53**(4): p. 1298-1324.
134. Klemm, M. and G. Tröster, *Characterization of small planar antennas for UWB mobile terminals.* Wireless Communications and Mobile Computing, 2005. **5**(5): p. 525-536.
135. Islam, M.T., A.T. Mobashsher, and N. Misran, *A novel feeding technique for a dual band microstrip patch antenna.* IEICE transactions on communications, 2010. **93**(9): p. 2455-2457.
136. Mobashsher, A., M. Islam, and N. Misran, *Triple band RFID reader antenna for handheld applications.* Microwave and optical technology letters, 2011. **53**(7): p. 1629-1632.
137. Mobashsher, A. and A. Abbosh, *Near-field time-domain characterisation of wideband antennas.* Electronics Letters, 2015. **51**(25): p. 2076-2078.
138. Johnson, C.C. and A.W. Guy, *Nonionizing electromagnetic wave effects in biological materials and systems.* Proceedings of the IEEE, 1972. **60**(6): p. 692-718.
139. Watanabe, S.-i., et al., *Characteristics of the SAR distributions in a head exposed to electromagnetic fields radiated by a hand-held portable radio.* Microwave Theory and Techniques, IEEE Transactions on, 1996. **44**(10): p. 1874-1883.
140. Gabriel, S., R. Lau, and C. Gabriel, *The dielectric properties of biological tissues: II. Measurements in the frequency range 10 Hz to 20 GHz.* Physics in medicine and biology, 1996. **41**(11): p. 2251.
141. Gabriel, S., R. Lau, and C. Gabriel, *The dielectric properties of biological tissues: III. Parametric models for the dielectric spectrum of tissues.* Physics in medicine and biology, 1996. **41**(11): p. 2271.
142. Lazebnik, M., et al., *A large-scale study of the ultrawideband microwave dielectric properties of normal, benign and malignant breast tissues obtained from cancer surgeries.* Physics in Medicine and Biology, 2007. **52**(20): p. 6093.
143. Foster, K.R. and H.P. Schwan, *Dielectric properties of tissues.* Handbook of biological effects of electromagnetic fields, 1995. **2**: p. 25-102.
144. O'Halloran, M., et al. *Development of anatomically and dielectrically accurate breast phantoms for microwave breast imaging applications*. in *SPIE Defense+ Security*. 2014. International Society for Optics and Photonics.
145. Schwerdt, H.N., F. Miranda, and J. Chae, *A fully passive wireless backscattering neurorecording microsystem embedded in dispersive human-head phantom medium.* Electron Device Letters, IEEE, 2012. **33**(6): p. 908-910.
146. Sperandio, M., M. Guermandi, and R. Guerrieri, *A four-shell diffusion phantom of the head for electrical impedance tomography*. Biomedical Engineering, IEEE Transactions on, 2012. **59**(2): p. 383-389.

147. Akter, M., et al., *Detection of hemorrhagic hypointense foci in the brain on susceptibility-weighted imaging: clinical and phantom studies.* Academic radiology, 2007. **14**(9): p. 1011-1019.
148. Karanasiou, I.S., N.K. Uzunoglu, and A. Garetsos, *Electromagnetic analysis of a non-invasive 3D passive microwave imaging system.* Progress In Electromagnetics Research, 2004. **44**: p. 287-308.
149. Ibrahim, W., H.M. Algabroun, and M. Almaqtari. *Short review on the used recipes to simulate the bio-tissue at microwave frequencies*. in *4th Kuala Lumpur International Conference on Biomedical Engineering 2008*. 2008. Springer.
150. Hartsgrove, G., A. Kraszewski, and A. Surowiec, *Simulated biological materials for electromagnetic radiation absorption studies.* Bioelectromagnetics, 1987. **8**(1): p. 29-36.
151. Joachimowicz, N., et al., *Breast phantoms for microwave imaging.* Antennas and Wireless Propagation Letters, IEEE, 2014. **13**: p. 1333-1336.
152. Cuyckens, T., *Influence of the human body on the behaviour of monopole and patch antennas*. 2010, UGent.
153. Chou, C.K., et al., *Formulas for preparing phantom muscle tissue at various radiofrequencies.* Bioelectromagnetics, 1984. **5**(4): p. 435-441.
154. Mashal, A., F. Gao, and S.C. Hagness, *Heterogeneous anthropomorphic phantoms with realistic dielectric properties for microwave breast imaging experiments.* Microwave and optical technology letters, 2011. **53**(8): p. 1896-1902.
155. Mobashsher, A.T. and A. Abbosh, *Three-dimensional human head phantom with realistic electrical properties and anatomy.* Antennas and Wireless Propagation Letters, IEEE, 2014. **13**: p. 1401-1404.
156. Kobayashi, T., et al., *Dry phantom composed of ceramics and its application to SAR estimation.* Microwave Theory and Techniques, IEEE Transactions on, 1993. **41**(1): p. 136-140.
157. Nojima, T., et al. *Ceramic dry-phantom and its application to SAR estimation*. in *Microwave Symposium Digest, 1991., IEEE MTT-S International*. 1991. IEEE.
158. Tamura, H., et al., *A dry phantom material composed of ceramic and graphite powder.* Electromagnetic Compatibility, IEEE Transactions on, 1997. **39**(2): p. 132-137.
159. Nikawa, Y., M. Chino, and K. Kikuchi, *Soft and dry phantom modeling material using silicone rubber with carbon fiber.* Microwave Theory and Techniques, IEEE Transactions on, 1996. **44**(10): p. 1949-1953.
160. Hikage, T., et al. *Development of lightweight solid phantom composed of silicone rubber and carbon nanotubes*. in *Electromagnetic Compatibility, 2007. EMC 2007. IEEE International Symposium on*. 2007. IEEE.
161. Mochizuki, S., et al., *Effects of ear shape and head size on simulated head exposure to a cellular phone.* Electromagnetic Compatibility, IEEE Transactions on, 2007. **49**(3): p. 512-518.
162. Hombach, V., et al., *The dependence of EM energy absorption upon human head modeling at 900 MHz.* Microwave Theory and Techniques, IEEE Transactions on, 1996. **44**(10): p. 1865-1873.
163. Picher, C., et al., *Analysis of the human head interaction in handset antennas with slotted ground planes.* Antennas and Propagation Magazine, IEEE, 2012. **54**(2): p. 36-56.
164. Monebhurrun, V., *Conservativeness of the SAM phantom for the SAR evaluation in the child's head.* Magnetics, IEEE Transactions on, 2010. **46**(8): p. 3477-3480.
165. Saraereh, O., et al. *Simulation and experimental SAR and efficiency study for a dual-band PIFA handset antenna (GSM 900/DCS 1800) at varied distances from a phantom head*. in *Antenna Measurements and SAR, 2004. AMS 2004. IEE*. 2004. IET.
166. Rodrigues, D.B., et al., *Design and optimization of an ultra wideband and compact microwave antenna for radiometric monitoring of brain temperature.* Biomedical Engineering, IEEE Transactions on, 2014. **61**(7): p. 2154-2160.

167. Jofre, L., et al., *Medical imaging with a microwave tomographic scanner.* Biomedical Engineering, IEEE Transactions on, 1990. **37**(3): p. 303-312.
168. Ito, K., et al., *Development and characteristics of a biological tissue-equivalent phantom for microwaves.* Electronics and Communications in Japan (Part I: Communications), 2001. **84**(4): p. 67-77.
169. Bini, M.G., et al., *The polyacrylamide as a phantom material for electromagnetic hyperthermia studies.* Biomedical Engineering, IEEE Transactions on, 1984(3): p. 317-322.
170. Okano, Y., et al., *The SAR evaluation method by a combination of thermographic experiments and biological tissue-equivalent phantoms.* Microwave Theory and Techniques, IEEE Transactions on, 2000. **48**(11): p. 2094-2103.
171. Levick, A., D. Land, and J. Hand, *Validation of microwave radiometry for measuring the internal temperature profile of human tissue.* Measurement Science and Technology, 2011. **22**(6): p. 065801.
172. Moon, K.S., et al., *Dielectric properties of epoxy-dielectrics-carbon black composite for phantom materials at radio frequencies.* Journal of applied polymer science, 2000. **77**(6): p. 1294-1302.
173. Ogawa, K. and T. Matsuyoshi, *An analysis of the performance of a handset diversity antenna influenced by head, hand, and shoulder effects at 900 MHz. I. Effective gain characteristics.* Vehicular Technology, IEEE Transactions on, 2001. **50**(3): p. 830-844.
174. Karathanasis, K.T., et al., *Experimental study of a hybrid microwave radiometry—Hyperthermia apparatus with the use of an anatomical head phantom.* Information Technology in Biomedicine, IEEE Transactions on, 2012. **16**(2): p. 241-247.
175. Youngs, I., et al. *Design of solid broadband human tissue simulant materials*. in *Science, Measurement and Technology, IEE Proceedings-*. 2002. IET.
176. Ishido, R., et al. *A study in the solid phantom for 3–6GHz and evaluation of SAR distribution based on the thermographic method*. in *Proceedings of 2004 International Symposium on Electromagnetic Compatibility, EMC*. 2004.
177. Karathanasis, K.T., et al., *Noninvasive focused monitoring and irradiation of head tissue phantoms at microwave frequencies.* Information Technology in Biomedicine, IEEE Transactions on, 2010. **14**(3): p. 657-663.
178. Mohammed, B.a.J. and A.M. Abbosh, *Realistic head phantom to test microwave systems for brain imaging.* Microwave and Optical Technology Letters, 2014. **56**(4): p. 979-982.
179. Latif, S.I., et al., *Design and performance analysis of the miniaturised water-filled double-ridged horn antenna for active microwave imaging applications.* IET Microwaves, Antennas & Propagation, 2015.
180. Bourqui, J. and E.C. Fear, *Shielded UWB sensor for biomedical applications.* Antennas and Wireless Propagation Letters, IEEE, 2012. **11**: p. 1614-1617.
181. van Nieuwstadt, L.M., *Microwave measurement system for breast cancer imaging: An experimental prototype towards time-domain inverse scattering*. 2011, The University of Michigan.
182. Wang, Y., et al., *Synthetic bandwidth radar for ultra-wideband microwave imaging systems.* Antennas and Propagation, IEEE Transactions on, 2014. **62**(2): p. 698-705.
183. Stutzman, W.L. and G.A. Thiele, *Antenna theory and design*. 2012: John Wiley & Sons.
184. Klemm, M., et al., *Evaluation of a hemi-spherical wideband antenna array for breast cancer imaging.* Radio Science, 2008. **43**(6).
185. Solimene, R. and A. Cuccaro, *Front wall clutter rejection methods in TWI.* Geoscience and Remote Sensing Letters, IEEE, 2014. **11**(6): p. 1158-1162.
186. Woody, C.D., *Characterization of an adaptive filter for the analysis of variable latency neuroelectric signals.* Medical and biological engineering, 1967. **5**(6): p. 539-554.
187. Lin, J.C., *A new IEEE standard for safety levels with respect to human exposure to radio-frequency radiation.* Antennas and Propagation Magazine, IEEE, 2006. **48**(1): p. 157-159.

188. Walters, T.J., et al., *Heating and pain sensation produced in human skin by millimeter waves: comparison to a simple thermal model.* Health Physics, 2000. **78**(3): p. 259-267.
189. Birenbaum, D., *Emergency neurological care of strokes and bleeds.* Journal of emergencies, trauma and shock, 2010. **3**(1): p. 52.
190. Mobashsher, A.T. and A. Abbosh. *Microwave imaging system to provide portable-low-powered medical facility for the detection of intracranial hemorrhage*. in *Microwave Symposium (AMS), 2014 1st Australian*. 2014. IEEE.
191. Honner, S.K., et al., *Emergency department control of blood pressure in intracerebral hemorrhage.* The Journal of emergency medicine, 2011. **41**(4): p. 355-361.
192. Cherepenin, V., et al., *A 3D electrical impedance tomography (EIT) system for breast cancer detection.* Physiological measurement, 2001. **22**(1): p. 9.
193. Mobashsher, A.T., P. Nguyen, and A. Abbosh. *Detection and localization of brain strokes in realistic 3-D human head phantom*. in *Microwave Workshop Series on RF and Wireless Technologies for Biomedical and Healthcare Applications (IMWS-BIO), 2013 IEEE MTT-S International*. 2013. IEEE.
194. Gao, F., B. Van Veen, and S. Hagness, *Sensitivity of the distorted born iterative method to the initial guess in microwave breast imaging.*
195. Balami, J.S. and A.M. Buchan, *Complications of intracerebral haemorrhage.* The Lancet Neurology, 2012. **11**(1): p. 101-118.
196. Prima, S., S. Ourselin, and N. Ayache, *Computation of the mid-sagittal plane in 3-D brain images.* Medical Imaging, IEEE Transactions on, 2002. **21**(2): p. 122-138.
197. Presson, N., et al., *Quantifying white matter structural integrity with high-definition fiber tracking in traumatic brain injury.* Military medicine, 2015. **180**(3S): p. 109-121.
198. Khotanlou, H., et al., *3D brain tumor segmentation in MRI using fuzzy classification, symmetry analysis and spatially constrained deformable models.* Fuzzy Sets and Systems, 2009. **160**(10): p. 1457-1473.
199. Jadoon, K.Z., et al., *Analysis of horn antenna transfer functions and phase-center position for modeling off-ground GPR.* Geoscience and Remote Sensing, IEEE Transactions on, 2011. **49**(5): p. 1649-1662.
200. Chalela, J.A., et al., *Magnetic resonance imaging and computed tomography in emergency assessment of patients with suspected acute stroke: a prospective comparison.* The Lancet, 2007. **369**(9558): p. 293-298.
201. Meaney, P.M., et al., *Surface wave multipath signals in near-field microwave imaging.* Journal of Biomedical Imaging, 2012. **2012**: p. 8.